Alma Mater Studiorum - Università di Bologna

DOTTORATO DI RICERCA IN

CHIMICA

Ciclo 34

Settore Concorsuale: 03/B1 - FONDAMENTI DELLE SCIENZE CHIMICHE E SISTEMI INORGANICI

Settore Scientifico Disciplinare: CHIM/03 - CHIMICA GENERALE E INORGANICA

NON-AMBIENT SOLID-STATE CHARACTERIZATION OF CRYSTALLINE
MOLECULAR ORGANIC SEMICONDUCTORS

Presentata da: Francesco Marin

Coordinatore Dottorato

Luca Prodi

Supervisore

Lucia Maini

Esame finale anno 2022

TABLE OF CONTENTS

ABSTRACT

My Ph.D. project was focused on the investigation of the polymorphism of crystalline molecular material for organic semiconductor applications at non-ambient conditions, and the solid-state characterization and crystal structure determination of the different polymorphic forms. In particular, this research project has tackled the investigation and characterization of the polymorphism of perylene diimides (PDIs) derivatives at high temperatures and pressures.

In the framework of molecular organic semiconductors, PDIs are a well-known family of promising *n*-type materials due to their commercial availability, low costs, excellent chemical, thermal, and photostability, high electron affinity, strong absorption in the visible region, low LUMO energies, generally good air-stability, and good charge transport properties. Furthermore, their electronic, optical, and charge transport properties can be tuned over a wide range via functionalization. The combination of these properties makes PDIs promising candidates for several applications such as OFETs, OPV cells, laser dye, sensors, bioimaging, etc. PDIs are also studied for low-temperature thermoelectric generator applications.

Among PDIs, N,N'-dialkyl-3,4,9,10-perylendiimide (PDI-Cn) are commercially available they are known to be highly thermally stable compounds and to exhibit solid-state transitions with temperature. Despite the extensive literature on the investigation of PDI-Cn properties as semiconductors, less is known about their polymorphism and even though the presence of their thermal transitions is reported, they were not investigated in detail.

Herein I present the full thermal characterization of PDI-C5 by a combination of differential scanning calorimetry, variable temperature X-ray diffraction, hot-stage microscopy, and variable temperature Raman spectroscopy (in collaboration with Dr. Tommaso Salzillo). We identified two high-temperature polymorphs, form II and form III; we determined their crystal structure from synchrotron powder data, and we investigated the thermal expansion of the different PDI-C5. Furthermore, a solvate form of PDI-C5 is also reported and characterized.

Here I report also the thorough thermal characterization by differential scanning calorimetry, variable temperature X-ray diffraction, and hot-stage microscopy of PDI-C6, -C7, and -C8. We determined the crystal structure of PDI-C7 form I, which was not previously reported, and we identified PDI-C6, C7, and C8 high-temperature polymorphs. Despite our efforts, it was not possible to solve their crystal structures due to the high degree of freedom and the low intensity of the diffracted peaks at high angles due to the elevated temperature of the data collections. We investigated the thermal expansion also in the case of PDI-C6, -C7, and -C8. Together with their thermal characterization, to further

understand PDI-Cn's polymorphism and the role of different interactions in the crystal packing, I report the study of PDI-Cn high-pressure polymorphism via pressure-dependent UV-Vis absorption spectroscopy and high-pressure Single Crystal X-ray diffraction, although the latter only for PDI-C5 and -C6 (in collaboration with prof. Andrej Katrusiak).

Furthermore, I report the use of a clustering method based on a combination of self-organizing maps (SOM) and principal component analysis (PCA) as a data-driven approach to classify different π-stacking arrangements of PDI derivatives with different types and positions of the substituents into families of similar crystal packing. This investigation was carried out in collaboration with Dr. Alessandro Zappi, who performed the SOM and PCA analysis.

Besides my main project, here I also report two works in which I contributed with the structure-property analysis at non-ambient conditions. The first regards the structural investigation of the water loss in Pt- and Pd- based vapochromic potassium/lithium salts upon temperature, in collaboration with Dr. Rocco Caliandro from IC-CNR of Bari. The second, in collaboration with Dr. Chiara Cappuccino from the Molecular Crystal Engineering group of Bologna, regards the investigation of structure-mechanical property relationships in polymorphs of C4-NT3N, a thienopyrrolyldione end-capped oligothiophene.

CHAPTER 1: INTRODUCTION

ORGANIC SEMICONDUCTORS

The advent of the technology based on semiconducting material and, in particular, the invention and development of metal-oxide-semiconductor field-effect transistors (MOS-FETs) and integrated circuits (microprocessors) caused a revolution that has changed our world and our everyday lives. Nowadays, semiconductors are adopted in almost all modern electronics such as displays, computers, telephones, etc. and for such reason, they become virtually indispensable for daily life.[1] The impact of semiconductors in our lives is once more reflected in the global chip shortage crisis that the world is facing in which the demand for semiconductor chips is greater than the supply, resulted also as one of the consequences of the recent pandemic for COVID, has dramatically influenced the trades and prices affecting several industrial sectors.[2] Moreover, since the discovery of their applications, the field of semiconductors has seen a continuously growing demand for increasingly efficient and performing materials and devices involving considerable effort in research and development in both academic and industry. The semiconductor technology is still mostly based on inorganic materials, and among them, silicon is the most widely used in electronic devices thanks to the combination of cost, performance, and stability; these factors together with the well-established processes of fabrication makes silicon the best choice wherever it can be applied.[3] Nevertheless, the evolution of technology always seeks novel materials with improved performances, and as such organic semiconductors emerged as a vibrant field of research.

Thanks to the work of Shirakawa et al. on polyacetylene[4] which led to the 2000 Nobel Prize in Chemistry for ''The discovery and development of conductive polymers'', the research and development in the field of organic electronics spanning chemistry, physics, materials science, engineering, and technology have exploded due to the potential use of organic semiconducting materials as a low-cost alternative to silicon, fuelled by both academic and industrial interest.[5,6]

In terms of sheer performance, silicon is continuing to dominate the scene of semiconductors and it may be too early to consider organic semiconductors as its competitors; however, even if transport efficiency is usually less favorable than their silicon counterparts,[7] the organic semiconductors brings great promises thanks to their potential advantages over the inorganic ones such as low cost of materials and fabrication also including the possibility of low-temperature solution processability via printing technologies (*e.g.* spin coating, stamping, inkjet printing),[8–10] low weight and mechanical flexibility that could result in ultra-lightweight flexible devices, and the possibility to finely tune the material properties by modifying their chemical structure and/or the crystal packing.[5,6]

Thanks to their potential advantages, currently organic semiconductors are widely used in various organic electronic devices such as organic light-emitting diodes (OLED),[11,12] organic field-effect transistors (OFET),[13–15] and organic photovoltaic cells (OPV).[16–18] OLEDs are devices that emit light when the current is passed through and consist of different layers of different materials. The stack of layers can be very thin and has many variations, including flexible and/or transparent materials, and are currently applied in displays.[19] OFETs are devices consisting of an organic semiconducting layer, a gate insulator layer, and three terminals (drain, source, and gate electrodes). Instead of competing with conventional silicon technologies, they find niche applications in low-performance radio-frequency technologies, sensors, as well as in integrated optoelectronic devices, such as switching elements in displays.[13] OPVs utilize the photovoltaic effect to convert light into electricity; in comparison to traditional silicon-based solar cells, organic solar cells hold the promise to be produced at much lower costs and thus render much shorter payback times possible.[16]

In contrast to inorganic semiconductors as silicon, where charge transport occurs in highly delocalized bands, charge transport in organic semiconductors is more complex. Organic semiconductors possess discrete ''energy levels'' consisting of molecular orbitals, thus charge transport depends on the ability of the charge carriers to pass from one molecule to another. Charge transport in organic semiconductors is influenced by many factors (including molecular packing, disorder, presence of impurities, temperature, electric field, charge-carrier density, size/molecular weight, and pressure) and can occurs through charge hopping or though band-like charge transport. Band-like transport in organic semiconductors involves shallower bands compared to their inorganic counterparts and is more common in crystalline materials at low temperatures. The different nature of charge transport, intrinsic or band-like for traditional and hopping for organic semiconductors, results from the different strength of interaction within the solid; in inorganic semiconductors, the atoms are held together by strong covalent or ionic bonds resulting in strong interactions of the overlapping atomic orbitals, whereas the solid-state structure of organic semiconductors is based on weak interactions, typically van der Waals, hydrogen-bonding, and π-π interactions, between neighboring molecules or polymer chains.[13,20,21] Given the nature of interactions in organic materials, charge delocalization can only occur along with the conjugated backbone of a single molecule or between the π-orbitals of adjacent molecules; therefore, the charge transport in organic materials is closely related to bonding orbitals and quantum mechanical wavefunction overlap, namely, the energy levels of the highest occupied molecular orbital (HOMO), the lowest unoccupied molecular orbital (LUMO) and the energy bandgap between the HOMO and LUMO energy levels (ΔE_g).[7,21]

Organic semiconductors can be broadly classified into two categories: small molecules or oligomers and polymer. Molecular organic semiconductors are attractive because they can be efficiently purified, and their ability to form ordered structures has enabled high charge mobilities; on the other hand, polymers are advantageous for large-area device fabrication and can be utilized as blends of various components performing different functionalities.[22] For both polymeric and molecular organic semiconductors, the various materials that have been designed over the years preferentially transport holes or electrons, thus they are further classified accordingly as hole transporter (or *p*-type) and as electron transporter (*n*-type) respectively. In most instances, this distinction does not rely on the actual ability of the materials to transport charges (*i.e.*, on the actual values of charge mobilities) but rather reflects the ease of charge injection from electrodes traditionally used in devices. In that context, the material is considered *p*-type when its ionization energy closely matches the Fermi level of the electrode material, whereas is considered *n*-type when its electron affinity matches the Fermi level of the electrode. Nevertheless, ambipolar transport (i.e., the ability to transport both electrons and holes) has now been reported for several organic semiconductors.[5] Some examples of *p*-type organic semiconductors are poly(3-hexylthiophene) (P3HT),[23] thieno[3,2-b]thiophene polymers,[24] and poly[9,9-dioctylfluorene-co-bithiophene] (F8T2)[25] as polymers and oligoacenes such as pentacene,[26] oligothiophenes such as dihexylsexithiophene,[27] and thienoacenes, such as [1]benzothieno[3,2-b][1]benzothiophene (BTBT)[28] as small molecules; on the other hand, some examples of *n*-type organic semiconductors are thiophene - naphthalene diimide and thiophene - perylene diimide co-polymers[29,30] as polymeric materials and fullerenes,[31] rylene diimides such as naphthalene (NDI) and perylene (PDI) diimides,[32] and oligothiophenes such as quinoimethane terthiophene (QM3T)[33] or perfluoropentacene,[34] in which the molecular energy levels have been tuned by substitution with electron-withdrawing groups like cyano, perfluoroalkyl/aryl, and alkyl/arylcarbonyl, as molecular organic semiconductors.[13,30] In general, the development of high-performance *n*-type semiconductors significantly lag behind *p*-type; in particular, the vulnerability of the *n*-type charge carrier to air conditions (air stability) is one of the major hurdles that limits the achievement of excellent n-type semiconductor materials, although design strategies for improved materials with better air stabilities has been developed, such as the introduction of strong electron-withdrawing substituents to the π-conjugated core or formation of dense solid-state packing to create kinetic barriers to slow down the diffusion of ambient oxidants into the active channel area.[13,35–37]

The organic semiconductors and the above-mentioned devices share a common trait: in all instances, their performance critically depends on the efficiency with which charge carriers (electrons and/or holes), either injected into the organic semiconductors from the electrodes or generated within the material, move within the π-conjugated materials; hence charge carrier mobility is the key

characteristic that describes the performances and the charge transport properties of semiconductors. The charge carrier mobility depends on intrinsic properties of the material (such as molecular structure and packing), extrinsic properties (such as the nature of defects and their concentration), and external parameters (such as electric field and temperature).[5,22]

One of the advantages of using small molecules is their ability to form ordered structures, and hence the possibility to obtain crystalline material. In this regard, crystals, and in particular single crystals, are particularly beneficial for revealing the intrinsic properties of organic semiconductors.[22] First, from crystal it is possible to have information about the crystal packing, which comprises the packing motif, molecular conformations and arrangement, and intermolecular interactions within the crystals; second, single crystals are generally free of grain boundaries and have long-range periodic order as well as minimal traps and defects which makes them extremely useful tools to probe fundamental information of exciton and charge carrier dynamics. Furthermore, for small-molecule organic semiconductors, long-range intramolecular delocalization is not likely, and as a consequence, the charge transport in these systems is largely determined by the packing of the molecules, the molecular arrangement, and the intermolecular interactions. Therefore, understanding the molecular packing features is beneficial for both the design and synthesis of organic semiconductors and understanding the structure-property relationship and the limits of charge transport.[21]

In organic semiconductor crystals, the molecular packing motifs should have strong and long-range intermolecular interactions (C–H⋯π, π-π, etc.) in order to have efficient charge transport. The typical packing motifs in organic semiconductor crystals, which are herringbone, lamellar packing with one-dimensional (1D) π-π stacking lamellar packing with two-dimensional (2D), are summarized in Figure 1.
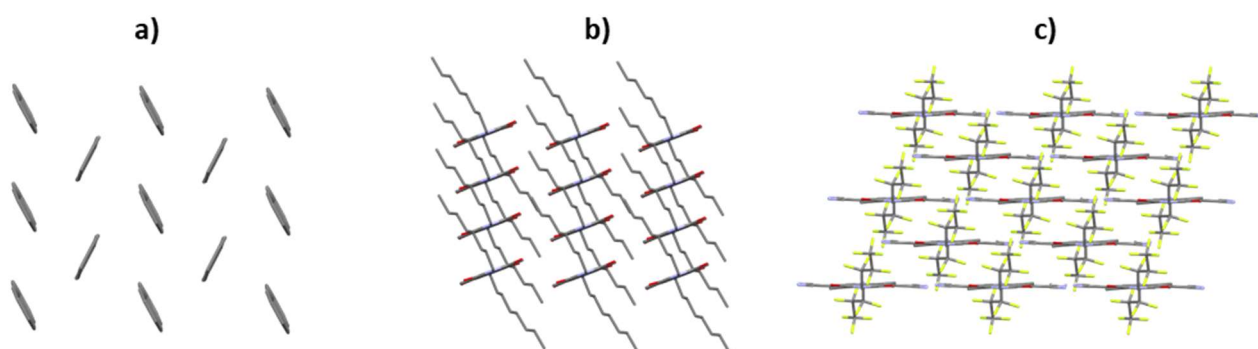

Figure 1. Typical crystal packings in organic crystalline semiconductors: a) herringbone (refcode PENCEN); b) lamellar motif with 1D π-π stacking (refcode GILFUD); c) lamellar motif with 2D π-π stacking (refcode FEHROA). Hydrogen atoms omitted for clarity.

Of these three kinds of packing mode, the 1D π-π stacking is believed to be the most efficient one for transporting charge carriers, as they allow delocalization of the π-electrons across all the aligned π-

orbitals of the molecules. However, a well-defined 1D π-stacking motif might not always be the best choice: it may result in larger dynamic fluctuations of the electronic couplings and site energies along the π-π direction, namely dynamic disorders in intermolecular couplings and energies, leading to less efficient charge transfers. In contrast, 2D π-stacking motifs (as the one in Figure 1c) may be more promising to achieve high electron transport performance.[38,39]

In conclusion, understanding and controlling the crystal packing is fundamental for the development, design, and synthesis of organic semiconductors and to investigate and get insight into the structure-property relationship both at an experimental and theoretical level.

STRUCTURE-PROPERTY RELATIONSHIP

Understanding the structure-properties relationship of materials is one of the key factors for an efficient design of new compounds with tailor-made properties and it is relevant to many fields in science and technology. In particular, the ability to direct the assembly of molecules into crystalline materials with targeted properties is a central goal of the active research field of crystal engineering; however, a deep understanding of the structure-properties relationship required to do so is yet to be achieved. Nevertheless, structural correlation with the properties of crystalline solids has witnessed remarkable growth in recent years from both an experimental and theoretical point of view.[40]

In this framework, a thorough knowledge of X-ray crystallography is indeed necessary to understand the solid-state structure of crystalline materials and subsequently the molecular assembly, together with a robust perception about the intermolecular interactions in play (comprising hydrogen bonding, π-π interactions, and halogen bonding) for effective design of solids with tailored properties.[21,40] To date, researchers have dedicated significant efforts to uncover the correlation between structure and properties of solid materials, exploring a wide range of different properties and applications. Some examples are: the exploration of crystallochromism, *i.e.* the dependence of solid-state color on crystal packing which has direct application in the pigment developments;[41–43] mechanical properties, with brittle, plastic, and elastic crystal for development of novel soft, flexible, and functional materials;[44–47] of course also semiconducting properties and charge transport behavior;[21,38,48,49] gas separation and small molecules recognition, for applications as sensors;[50,51] magnetic properties;[52] and so on.

For organic molecules, a typical strategy to systematically probe into structure-property relationship might involve, for instance, a systematic variation in the model or type of substitution on one part of the molecule in order to test particular hypotheses and behaviors. In this way, it is possible to reduce the structural involved variables and to isolate the few structural parameters which play the most important role in determining the particular property under investigation.[40]

In the field of organic semiconductors, a lot of effort has been made in both experimental and theoretical insight into optoelectronic properties investigating the effects of different substituents on the material performance for a deeper understanding of the relationship among the molecular packing motifs, intermolecular interactions, and properties of molecular materials for efficient design of crystalline material for specific applications.[32,42,53–55] At the same time, driven by experimental insight and thanks to advances in computational power, remarkable growth has been achieved in computational methods to understand structure-properties of organic semiconductors, to evaluate the potential energy surfaces;[56,57] to map relationships between stacking geometry, binding energy, and electronic coupling;[58] and to screen the effect of several different molecular functionalizations in the

material's properties from a computational point of view.[39,59] Such computational approaches are highly attractive for guiding materials discovery as a means of identifying the most promising synthetic targets and, therefore, reducing experimental effort spent on materials with poor properties.[60]

Variations in substituents lead to perturbations in the electronic structure of the target molecule, and they do often result in changes in structure which can be unwanted. In such cases, it is difficult to ascertain if the changes in properties are correlated directly with the changes in the structure or the molecule. Nevertheless, the existence of polymorphic forms provides a unique opportunity for the investigation of structure-property relationships, since, in a polymorphic system, differences in properties must be due to differences in structure.[40]

Thanks to the advances in computational power and the development of smart algorithms in the field of machine learning and artificial intelligence, novel computational approaches are now able to take into account the entire crystal structure, and thus also polymorphism, to investigate the structure-property relationship and to discover and design of OSCs materials with interesting properties.[61] The two main computational approaches in the field of organic semiconductors are multiscale approaches and data-driven searches. Multiscale approaches combine different methods and models for computing the reorganization energies, the electronic couplings, and for evaluating the disorder effects[61–63] and can be integrated with crystal structure prediction (CSP) to screen for interesting packing arrangements.[64–66] Data-driven searches make use of the high amount of data present in databases such as the Cambridge Structural Database (CSD) to carry out large scale screening strategies to predict the semiconducting properties of materials from various computable descriptors and thus to explore their structure-property relationships.[61,67–69]

From their discovery, huge efforts have been paid in investigating optoelectronic properties and structure-property relationship of molecular semiconductors, however, besides some exceptions as pentacene, often the information and knowledge about polymorphism and solid-state transition of these materials are insufficient and although the presence of polymorphs is quite common only a very low number of crystal structures of different polymorphic forms have been reported and fully characterized. Experimental detailed investigation of organic semiconductor's polymorphism is important also to guide computational insight into their structure-property relationship to design and discover novel materials with improved properties.[61] Furthermore, besides further information about molecular packing features and interactions in play, investigating the relationship between polymorphic forms in terms of solid-state transitions dynamic at a microscopic and macroscopic level, can lead to access and understanding several interesting functional properties such as

11

vapochromic,[70,71] mechanochromic,[72,73] and thermochromic behavior,[74,75] thermomechanical[76] and thermosalient behavior,[77,78] and other functional properties in the framework of dynamic and adaptive molecular crystals as potential materials for future applications.[79]

POLYMORPHISM

Polymorphism (Greek: *poly* = many, *morph* = form) specifying the diversity of nature, is a term used in many disciplines. In chemistry, polymorphism denotes the existence of different forms or crystallized structures of a solid substance having different stabilities but with the same stoichiometry. It is a well-known, natural phenomenon common to both organic and inorganic compounds and is present in almost all scientific disciplines involving solid materials.[80] In the case of organic materials, the first example of a polymorphic organic compound was benzamide, which was identified and studied by Liebig and Wohler in 1832[81] by simple observation under the microscope. A recent example of the phenomenon of polymorphism of organic molecules has been reported by Maini's group, where four different crystal forms of NTA (2,2′-(5,5′-(ethyne-1,2-diyl)bis(thiophene-5,2-diyl))bis(5-hexyl-4H-thieno[2,3-c]pyrrole-4,6(5H)-dione)) shows different crystal habits and colours.[82]
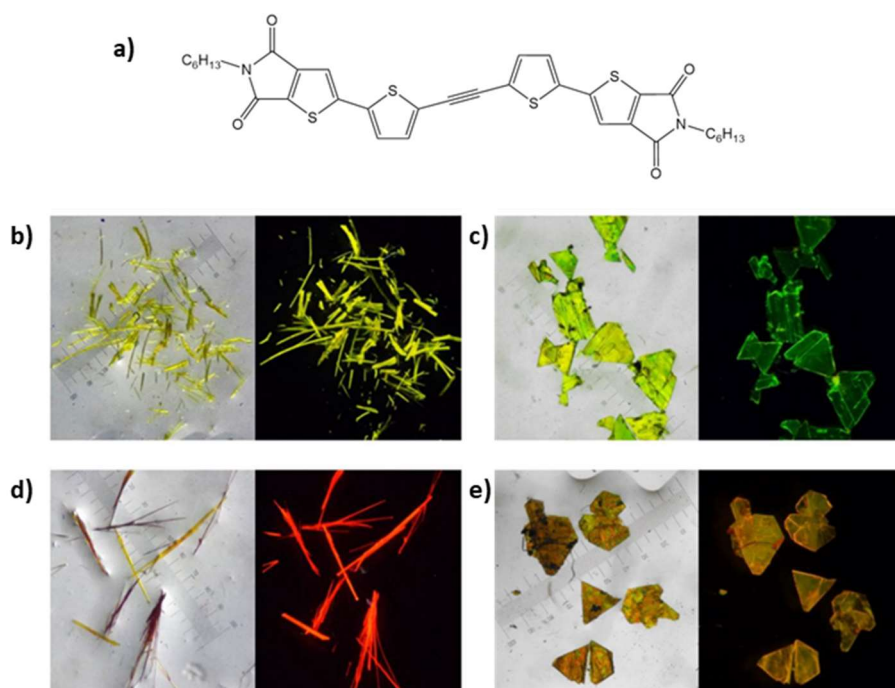

Figure 2. Different polymorphs of NTA taken by optical microscopy, transmitted light on the left and under UV light (365 nm) on the right; (a) structural formula of NTA, (b) phase I, (c) phase II, (d) phase III, (e) phase IV (courtesy of the paper, Cryst. Growth Des. 2019, 19, 2594−2603).

In the past, the investigation of polymorphism was mainly based on simple techniques such as melting point and identification of color and shape, also thanks to the development of the polarizing microscope. The development of structural crystallography caused in the early decades of the twentieth century, a decline of interest in structural polymorphism for two main reasons: first, for many years carrying out a crystal structure determination was a major task and thus solving the crystal structure of another crystal form of the same molecule often was not justified; second, structures with

disorder or that did not grow into ''good'' single crystals, presented major challenges for the crystallographer and were often abandoned. Therefore, although some key contributions to the subject were made in the late 60s and 70s,[83,84] a significant communal interest in the subject did not occur until the early 90s.[80,84] It is worth noting that at that time there were no computers and the crystal structure was determined to know the connectivity and the geometry of the molecule. Only later, with the possibility to visualize the structure, interactions among molecules and crystal packing gained much more attention.

Nowadays, thanks also to the relative ease and decreasing cost in time and money carrying out crystal structure determinations, the use of X-ray crystallography plays a major role in the investigation of polymorphism. Furthermore, besides crystallography, a wide variety of techniques for the identification and characterization of polymorphic systems is used, such as hot-stage microscopy (HSM), differential scanning calorimetry (DSC) and thermogravimetric analysis (TGA), infrared spectroscopy (IR), Raman spectroscopy, solid-state nuclear magnetic resonance spectroscopy (ssNMR), atomic force spectroscopy (AFM) and scanning tunneling microscopy (STM), transmission electron microscopy (TEM), etc.[80]

To understand the formation of polymorphic phases and relationships between polymorphism it is important to take into account thermodynamics and kinetics. In terms of thermodynamics, one of the key questions regarding polymorphic systems is the relative stability of the various crystal modifications at different T and eventually different P and the changes in thermodynamic relationships accompanying phase changes. The molecular packing is the result of the minimization of lattice energy through the cooperative effect of π-π stacking, electrostatic interactions, dispersion interaction, and others; different polymorphs are the result of different relative minima that the molecular compound can reach. Of course, the relative stability of polymorphs depends on their free energies, the most stable form having the lowest free energy. In this respect, it is often useful to represent polymorphic systems with energy vs temperature diagrams; the utility of these diagrams is that they contain a great deal of information in a compact form and provide a one page visual and readily interpretable summary of what can be complex interrelationships among polymorphic modifications.[40,80,85,86]

Generally, polymorphic forms can be in either an enantiotropic or a monotropic relationship; the typical phase diagrams of an enantiotropic and a monotropic dimorphic system are shown in Figure 3. Depending on whether the thermodynamic transition point ($T_{p,I/II}$), defined by the point at which G_I and G_{II} cross, falls at a temperature below the melting point of the lower melting form

14

(enantiotropic polymorphic system); or the free energy curves do not cross at a temperature below the two melting points (monotropic polymorphic system).[80,86]
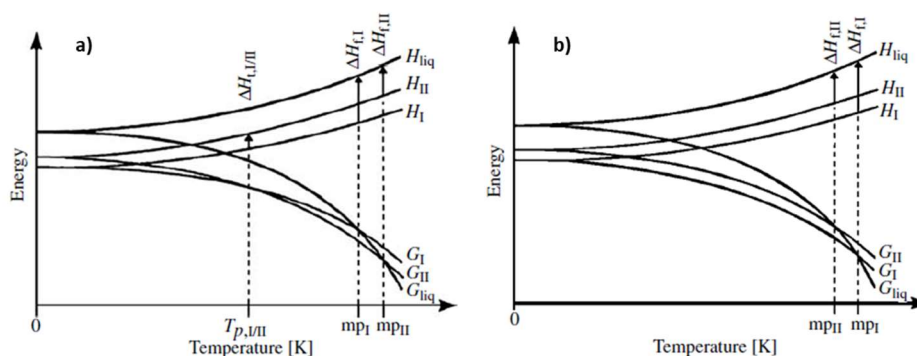

Figure 3. Energy vs temperature (E/T) diagrams of a dimorphic system. G is the Gibbs free energy and H is the enthalpy. These diagrams represent the situation for a) an enantiotropic system and b) a monotropic system.[80]

As already mentioned, the most stable form, namely the thermodynamic form, has the lowest free energy among all the different forms. For this reason, those forms which are less stable will be energetically driven to transform into the most stable form. Nevertheless, kinetic factors may prevent the transformation and kinetic or metastable forms can be achieved instead.[80,86–88]

Systematic variation of the crystallization conditions can be used in order to search for polymorphs, such polymorph screening experiments are common especially for pharmaceutical compounds. Once identified the different polymorphic forms, through proper control of crystallization conditions it is possible to selectively obtain or prevent the crystallization of a particular polymorph.[80,84,85,88]

Two main physical variables governing polymorphism are temperature and pressure. However, the bigger experimental challenges of pressure-dependent investigations compared with temperature-dependent ones make the latter more popular, especially in organic crystals. The identification and investigation of polymorphic systems, in particular in the field of organic molecular crystals, is typically tackled by varying crystallization techniques, concentrations, solvents, or temperature, and as such, energy/temperature diagrams are more popular for organic molecular polymorphic systems compared to the pressure/temperature ones.[40,80,85] Nevertheless, different crystal forms can also be obtained by varying pressure. In this respect, thanks to its development in the last decades, nowadays high-pressure crystallography represents a powerful technique that can be routinely applied in laboratories to investigate the variation of pressure as a new thermodynamic dimension to crystal-structure analyses, and indeed to polymorphism.[89–91]

Combination of pressure, temperature, and crystallographic studies can lead to a detailed understanding of the structural basis of the phase diagram and the mechanisms of the phase transitions, and carrying out those measurements at a variety of temperatures and pressures carries

great potential for the study of polymorphic systems and their utilization for structure-property relationships.[80,84,90–96]

As previously mentioned, the importance of polymorphism derives from the fact that the crystalline structure has a major impact on the solid-state properties of materials, and hence different polymorphs often have distinct physical properties such as the crystal habits, melting point, solubility, electronic, optical, and mechanical properties, and from the fact that polymorphic systems provide a unique opportunity for the investigation of structure-property relationship. As well as other organic compounds, also molecular organic semiconductors exhibit polymorphism, and since small changes in the molecular packing can alter the π orbital overlap and the HOMO and LUMO energies affecting the charge transport and optoelectronic properties, understanding and controlling their polymorphism is fundamental. Consequently, efforts have been made to control molecular packing for improving charge-transport and photophysical properties of organic semiconductors via chemical functionalization and modifications, via control of the crystallization process, and post-deposition processing.[21,97–99]

PERYLENE DIIMIDES

In the framework of organic semiconductors, to achieve good performance *n*-type materials must have high electron affinity to facilitate either injection from contacting electrodes or exciton separation; good intermolecular π-orbital overlap for high mobility; good air-stability.[32,100] Among the n-type materials, perylene diimides (PDIs) derivatives are undoubtedly a family of exceptional and versatile n-type semiconductors for optoelectronic applications due to their commercial availability, low costs, excellent chemical, thermal, and photostability, high electron affinity, strong absorption in the visible region, low LUMO energies, generally good air-stability, and good charge transport properties. Furthermore, their electronic, optical, and charge transport properties can be tuned over a wide range via functionalization.[17,18,30,54,101,102] The combination of these properties makes PDIs promising candidates for several applications such as OFETs,[13–15,30,54] OPV cells,[16–18] laser dye,[103,104] sensors,[105] bioimaging,[106] etc. PDIs are also studied for low-temperature thermoelectric generator applications.[107]

Before becoming interesting as organic semiconductors, PDIs have been an object of research for more than 100 years as a group of high-performance industrial organic pigments, which are currently used in fibers application and industrial paints.[43,108] One of the most important features of these materials in their application as commercial paint pigments that makes PDIs a family of well-known organic pigments is their crystallochromy (*i.e.*, the dependence of color on crystal packing). Crystallochromy of PDIs covers a variety of colors in the solid-state from orange to red, to maroon, and black and it was investigated in-depth, both experimentally and theoretically, for a large number of end functionalized PDI single crystals already in the 1980s and early 1990s. These works by investigating the effect of structure on the pigment's color demonstrated that the intermolecular packing greatly affects their optical properties. In particular, an empirical model to correlate absorption maxima with the π-π contact area between stacked molecules was developed, and theoretically, it was found a strong correlation between crystal color and displacement along the long-(x) and short-axes (y) of the perylene core.[41–43,109–111] In addition to the model, the nature of the optical properties with respect to the electronic structure has been investigated by Jin Mizuguchi et al., whom also describes the different color properties of PR149 polymorphs.[112–115] Besides their application as industrial pigments, in the past 20 years the interest in PDI, as well as other dyes and pigments, moved from traditional colorant toward application as functional solid-state material.[18,116]

Thanks to their planar structure and their peripherical carbonyl oxygen atoms, PDIs typically arrange to form π-π stacking interactions between molecules, which generally promotes efficient charge transport in the solid-state. Like other molecular organic semiconductors, substitution can vary

greatly the extent of intermolecular π-orbital overlap among PDI derivatives, and thus can make a significant effect on the solubility, optical and electrochemical properties, crystal packing, and structural morphology.[21,39,42,59,101,111,117] In particular, the perylene diimide core has ten functionalizable positions: the N,N' positions which are known as the *imide*-; the 1,6,7,12 positions known as the *bay*-; and the 2,5,8,11 positions known as the *ortho*-positions (Figure 4). These numerous positions for introducing functional groups are the reason for the popularity of PDIs, making them versatile for tailoring the properties for specific applications.[54,101] In general, substitution at *imide*-position maintains the planarity of the perylene aromatic core, and can effectively tune solubility, aggregation, and solid-state molecular packing, but shows only limited effects on the molecular-level optical and electronic properties of PDIs.[43,101,111,118] On the other hand, optical and electronic properties of PDIs can be significantly modified via substitution at the perylene core in the *bay*- and *ortho*-positions. Substitution at *bay*-position, besides affecting the optical and electronic properties of the material, may lead to the twisting of the two naphthalene half units in PDIs due to steric effects; however, large geometric distortions of the core may weaken the intermolecular π-π overlap and thus may be detrimental for charge carrier mobilities.[37,54,101,104] Lastly, *ortho*-functionalization creates the possibility to modify the optoelectronic properties while at the same time retaining the planarity of the perylene core.[101,119] The adjustment of the PDI properties can be achieved through combinations of *imide*-, *bay*- and *ortho*- functionalization.
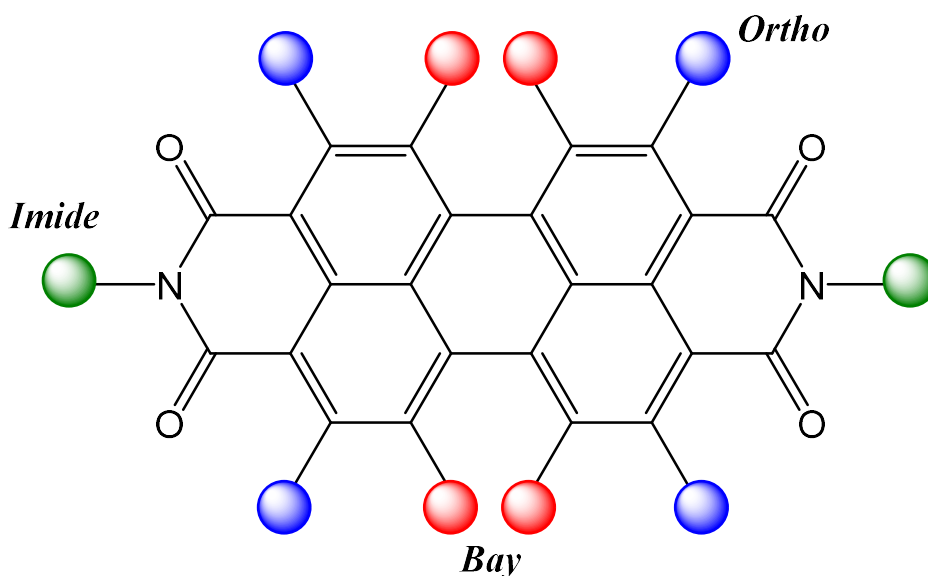

Figure 4. Chemical structure of a generic PDI shows the different substitutions positions: imide-positions highlighted in green, bay-positions in red, and ortho-positions in blue.

The numerous advantages of PDIs as *n*-type material together with a long history of research on PDIs makes them highly valuable as model systems to investigate and understand the relationship among the molecular packing motifs, intermolecular interactions, and properties of molecular materials for

efficient design of crystalline material for specific applications. After the pioneer works on crystallochromy, a lot of effort has been made in the experimental and theoretical insight into optoelectronic properties of PDIs for a deeper understanding of their structure-properties relationship. For instance, Fink et al. and Zhao et al. evaluated the potential energy surfaces (PES) for the ground state of PDI dimers as a function of the shift along the x- and y-axes of the perylene core and as a function of the rotation (φ) between co-facially stacked dimers, and they evaluated excitation energies of PDI crystal structures;[56,57] Vura-Weis et al. mapped the relationships between stacking geometry, binding energy and electronic coupling for dimers of 20 PDI derivatives based on density functional theory (DFT);[58] Delgado et al. investigated the effect of the type, number and position of the substituents on charge-transport properties of 30 imide-substituted PDIs and 7 bay- and bay/imide-substituted PDIs;[59] Geng et al. investigated the influence of substituents on different positions (ortho, bay, and imide) of 17 PDI derivatives on their packing, intermolecular interactions, and electronic properties.[39] Furthermore, several other works, both experimental and theoretical, have been published on PDI derivatives investigating the effects of different substituents on the material performance in specific applications, for example, the use of linear chains,[120,121] fluorinated chains,[122] or branched chains[121,123,124] in imide position, the use of cyano substituent,[125] halogenated substituents,[126] or other substituents at the core.[104,127]

Despite the numerous studies and investigations on PDI derivatives, less is known about their polymorphic behavior, which comprises numerous thermally induced solid-state transitions.[39,59,110,128] It is well known that thermal treatment such as thermal annealing, can be effective in the case of PDIs since can dramatically improve crystallinity and performance in devices, as a consequence of molecular rearrangement induced by temperature, which gives more energy to the molecules to migrate. Furthermore, considering their excellent thermal stability allows thermal treatment to be performed even above 200°C, thermal annealing can be performed at a high temperature in the case of PDIs, in some cases also thermally induced solid-state transition can occur and must be considered.[129–134] However, despite thermal treatments are a common process in fabrication and optimization of devices, as also reported for PDIs,[134] often the effects in the material are not thoroughly investigated, and the thermal annealing could bring to unexpected and undesired phase transition that depends not only on temperature, but also on size and morphology, and affects the final device performance.

Besides temperature, investigating high-pressure PDIs behavior could be beneficial to improve the understanding of the intermolecular interactions and packing motifs of PDIs and in general organic semiconductors. Furthermore, combining high-pressure structural measurement with pressure-

dependent electrical transport measurement would allow a more precise understanding of the role of intermolecular interactions on the optoelectronic properties, shedding further light on the transport mechanisms responsible for charge mobility in organic materials and their structure-property relationship. In the future, it could open the path towards novel functionalities and application technologies of these materials.[90,135–138]

In conclusion, the investigation of the structural behavior at non-ambient conditions of PDIs (temperature and pressure) can drive towards improved knowledge on their polymorphism, crystal packing, and intermolecular interactions in play, which would be beneficial for the design of novel high-performance *n*-type materials.

REFERENCES

(1)   Keyes, R. W. Physical Limits of Silicon Transistors and Circuits. *Reports Prog. Phys.* **2005**, *68* (12), 2701–2746.

(2)   Attinasi, M. G.; De Stefani, R.; Frohm, E.; Gunnella, V.; Koester, G.; Tóth, M.; Melemenidis, A. The Semiconductor Shortage and Its Implication for Euro Area Trade, Production and Prices. *Econ. Bull. Boxes* **2021**, *4*.

(3)   Thompson, S. E.; Parthasarathy, S. Moore's Law: The Future of Si Microelectronics. *Mater. Today* **2006**, *9* (6), 20–25.

(4)   Chiang, C. K.; Fincher, C. R.; Park, Y. W.; Heeger, A. J.; Shirakawa, H.; Louis, E. J.; Gau, S. C.; MacDiarmid, A. G. Electrical Conductivity in Doped Polyacetylene. *Phys. Rev. Lett.* **1977**, *39* (17), 1098–1101.

(5)   Coropceanu, V.; Cornil, J.; da Silva Filho, D. A.; Olivier, Y.; Silbey, R.; Brédas, J. L. Charge Transport in Organic Semiconductors. *Chemical Reviews*. 2007, pp 926–952.

(6)   Anthony, J. E. Organic Electronics: Addressing Challenges. *Nature Materials*. 2014, pp 773–775.

(7)   Murphy, A. R.; Fréchet, J. M. J. Organic Semiconducting Oligomers for Use in Thin Film Transistors. *Chemical Reviews*. 2007, pp 1066–1096.

(8)   Li, Y.; Sun, H.; Shi, Y.; Tsukagoshi, K. Patterning Technology for Solution-Processed Organic Crystal Field-Effect Transistors. *Sci. Technol. Adv. Mater.* **2014**, *15* (2), 24203.

(9)   Ng, T. N. (吳子雅); Sambandan, S.; Lujan, R.; Arias, A. C.; Newman, C. R.; Yan, H. (颜河); Facchetti, A. Electrical Stability of Inkjet-Patterned Organic Complementary Inverters Measured in Ambient Conditions. *Appl. Phys. Lett.* **2009**, *94* (23), 233307.

(10)   Rogers, J. A.; Bao, Z.; Baldwin, K.; Dodabalapur, A.; Crone, B.; Raju, V. R.; Kuck, V.; Katz, H.; Amundson, K.; Ewing, J.; Drzaic, P. Paper-like Electronic Displays: Large-Area Rubber-Stamped Plastic Sheets of Electronics and Microencapsulated Electrophoretic Inks. *Proc. Natl. Acad. Sci.* **2001**, *98* (9), 4835–4840.

(11)   Tang, C. W.; Vanslyke, S. A. Organic Electroluminescent Diodes. *Appl. Phys. Lett.* **1987**, *51* (12), 913–915.

(12)   Brütting, W.; Frischeisen, J. Device Efficiency of Organic Light-Emitting Diodes. In *Physics of Organic Semiconductors: Second Edition*; 2013; Vol. 210, pp 497–539.

(13)   Facchetti, A. Semiconductors for Organic Transistors. *Mater. Today* **2007**, *10* (3), 28–37.

(14)   Mei, J.; Diao, Y.; Appleton, A. L.; Fang, L.; Bao, Z. Integrated Materials Design of Organic Semiconductors for Field-Effect Transistors. *Journal of the American Chemical Society*. 2013, pp 6724–6746.

(15)   Chen, S.; Li, Z.; Qiao, Y.; Song, Y. Solution-Processed Organic Semiconductor Crystals for Field-Effect Transistors: From Crystallization Mechanism towards Morphology Control. *Journal of Materials Chemistry C*. 2021, pp 1126–1149.

(16)   Kippelen, B.; Brédas, J. L. Organic Photovoltaics. *Energy and Environmental Science*. 2009, pp 251–261.

(17)   Anthony, J. E. Small-Molecule, Nonfullerene Acceptors for Polymer Bulk Heterojunction Organic Photovoltaics. *Chem. Mater.* **2011**, *23* (3), 583–590.

(18)   Li, C.; Wonneberger, H. Perylene Imides for Organic Photovoltaics: Yesterday, Today, and Tomorrow. *Adv. Mater.* **2012**, *24* (5), 613–636.

(19)   Gaspar, D. J.; Polikarpov, E. OLED Fundamentals : Materials, Devices, and Processing of Organic Light-Emitting Diodes; 2015.

(20)   Köhler, A.; Bässler, H. The Electronic Structure of Organic Semiconductors. *Electronic Processes in Organic Semiconductors*. May 11, 2015, pp 1–86.

(21)   Wang, C.; Dong, H.; Jiang, L.; Hu, W. Organic Semiconductor Crystals. *Chemical Society Reviews*. Royal Society of Chemistry January 22, 2018, pp 422–500.

(22)   Ostroverkhova, O. Organic Optoelectronic Materials: Mechanisms and Applications. *Chem. Rev.* **2016**, *116* (22), 13279–13412.

(23)   Tsumura, A.; Fuchigami, H.; Koezuka, H. Field-Effect Transistor with a Conducting Polymer Film. *Synth. Met.* **1991**, *41* (3), 1181–1184.

(24)   McCulloch, I.; Heeney, M.; Bailey, C.; Genevicius, K.; MacDonald, I.; Shkunov, M.; Sparrowe, D.; Tierney, S.; Wagner, R.; Zhang, W.; Chabinyc, M. L.; Kline, R. J.; McGehee, M. D.; Toney, M. F. Liquid-Crystalline Semiconducting Polymers with High Charge-Carrier Mobility. *Nat. Mater.* **2006**, *5* (4), 328–333.

(25)   Sirringhaus, H.; Kawase, T.; Friend, R. H.; Shimoda, T.; Inbasekaran, M.; Wu, W.; Woo, E. P. High-Resolution Inkjet Printing of All-Polymer Transistor Circuits. *Science* **2000**, *290* (5499), 2123–2126.

(26)   Klauk, H.; Gundlach, D. J.; Nichols, J. A.; Jackson, T. N. Pentacene Organic Thin-Film Transistors for Circuit and Display Applications. *IEEE Trans. Electron Devices* **1999**, *46* (6), 1258–1263.

(27)   Garnier, F.; Yassar, A.; Hajlaoui, R.; Horowitz, G.; Deloffre, F.; Servet, B.; Ries, S.; Alnot, P. Molecular Engineering of Organic Semiconductors: Design of Self-Assembly Properties in Conjugated Thiophene Oligomers. *J. Am. Chem. Soc.* **1993**, *115* (19), 8716–8721.

(28)   Takimiya, K.; Osaka, I.; Mori, T.; Nakano, M. Organic Semiconductors Based on [1]Benzothieno[3,2- B][1]Benzothiophene Substructure. *Acc. Chem. Res.* **2014**, *47* (5), 1493–1502.

(29)   Zhan, X.; Tan, Z.; Domercq, B.; An, Z.; Zhang, X.; Barlow, S.; Li, Y.; Zhu, D.; Kippelen, B.; Marder, S. R. A High-Mobility Electron-Transport Polymer with Broad Absorption and Its Use in Field-Effect Transistors and All-Polymer Solar Cells. *J. Am. Chem. Soc.* **2007**, *129* (23), 7246–7247.

(30)   Anthony, J. E.; Facchetti, A.; Heeney, M.; Marder, S. R.; Zhan, X. N-Type Organic Semiconductors in Organic Electronics. *Adv. Mater.* **2010**, *22* (34), 3876–3892.

(31)   Kobayashi, S.; Takenobu, T.; Mon, S.; Fujiwara, A.; Iwasa, Y. Fabrication and Characterization of C60 Thin-Film Transistors with High Field-Effect Mobility. *Appl. Phys. Lett.* **2003**, *82* (25), 4581–4583.

(32)   Zhan, X.; Facchetti, A.; Barlow, S.; Marks, T. J.; Ratner, M. A.; Wasielewski, M. R.; Marder, S. R. Rylene and Related Diimides for Organic Electronics. *Advanced Materials*. John Wiley & Sons, Ltd January 11, 2011, pp 268–284.

(33)   Pappenfus, T. M.; Chesterfield, R. J.; Frisbie, C. D.; Mann, K. R.; Casado, J.; Raff, J. D.; Miller, L. L. A π-Stacking Terthiophene-Based Quinodimethane Is an n-Channel Conductor in a Thin Film Transistor. *J. Am. Chem. Soc.* **2002**, *124* (16), 4184–4185.

(34)   Sakamoto, Y.; Suzuki, T.; Kobayashi, M.; Gao, Y.; Fukai, Y.; Inoue, Y.; Sato, F.; Tokito, S. Perfluoropentacene: High-Performance p-n Junctions and Complementary Circuits with Pentacene. *J. Am. Chem. Soc.* **2004**, *126* (26), 8138–8140.

(35)   Zaumseil, J.; Sirringhaus, H. Electron and Ambipolar Transport in Organic Field-Effect

Transistors. *Chem. Rev.* **2007**, *107* (4), 1296–1323.

(36)   Newman, C. R.; Frisbie, C. D.; da Silva Filho, D. A.; Brédas, J.-L.; Ewbank, P. C.; Mann, K. R. Introduction to Organic Thin Film Transistors and Design of N-Channel Organic Semiconductors. *Chem. Mater.* **2004**, *16* (23), 4436–4451.

(37)   Jones, B. A.; Ahrens, M. J.; Yoon, M. H.; Facchetti, A.; Marks, T. J.; Wasielewski, M. R. High-Mobility Air-Stable n-Type Semiconductors with Processing Versatility: Dicyanoperylene-3,4:9,10-Bis(Dicarboximides). *Angew. Chemie - Int. Ed.* **2004**, *43* (46), 6363–6366.

(38)   Wang, C.; Dong, H.; Hu, W.; Liu, Y.; Zhu, D. Semiconducting π-Conjugated Systems in Field-Effect Transistors: A Material Odyssey of Organic Electronics. *Chem. Rev.* **2012**, *112* (4), 2208–2267.

(39)   Geng, Y.; Li, H.-B.; Wu, S.-X.; Su, Z.-M. The Interplay of Intermolecular Interactions, Packing Motifs and Electron Transport Properties in Perylene Diimide Related Materials: A Theoretical Perspective. *J. Mater. Chem.* **2012**, *22* (39), 20840.

(40)   Bernstein, J. Crystal Growth, Polymorphism and Structure-Property Relationships in Organic Crystals. *J. Phys. D. Appl. Phys.* **1993**, *26* (8), B66–B76.

(41)   Graser, F.; Hädicke, E. Kristallstruktur Und Farbe Bei Perylen-3,4:9,10-Bis(Dicarboximid)-Pigmenten. *Liebigs Ann. der Chemie* **1980**, *1980* (12), 1994–2011.

(42)   Klebe, G.; Graser, F.; Hädicke, E.; Berndt, J. Crystallochromy as a Solid-state Effect: Correlation of Molecular Conformation, Crystal Packing and Colour in Perylene-3,4:9,10-bis(Dicarboximide) Pigments. *Acta Crystallogr. Sect. B* **1989**, *45* (1), 69–77.

(43)   Kazmaier, P. M.; Hoffmann, R. A Theoretical Study of Crystallochromy. Quantum Interference Effects in the Spectra of Perylene Pigments. *J. Am. Chem. Soc.* **1994**, *116* (21), 9684–9691.

(44)   Reddy, C. M.; Padmanabhan, K. A.; Desiraju, G. R. Structure-Property Correlations in Bending and Brittle Organic Crystals. *Cryst. Growth Des.* **2006**, *6* (12), 2720–2731.

(45)   Devarapalli, R.; Bhagwan Kadambi, S.; Chen, C.-T.; Rama Krishna, G.; Kammari, B.; Buehler, M. J.; Ramamurty, U.; Malla Reddy, C. Remarkably Distinct Mechanical Flexibility in Three Structurally Similar Semiconducting Organic Crystals Studied by Nanoindentation and Molecular Dynamics.

(46)   Saha, S.; Mishra, M. K.; Reddy, C. M.; Desiraju, G. R. From Molecules to Interactions to Crystal

Engineering: Mechanical Properties of Organic Solids. *Acc. Chem. Res.* **2018**, *51* (11), 2957–2967.

(47) Naumov, P. E.; Chizhik, S.; Panda, M. K.; Nath, N. K.; Boldyreva, E. Mechanically Responsive Molecular Crystals. **2015**.

(48) Melucci, M.; Zambianchi, M.; Favaretto, L.; Gazzano, M.; Zanelli, A.; Monari, M.; Capelli, R.; Troisi, S.; Toffanin, S.; Muccini, M. Thienopyrrolyl Dione End-Capped Oligothiophene Ambipolar Semiconductors for Thin Film- and Light Emitting Transistors. *Chem. Commun.* **2011**, *47* (43), 11840–11842.

(49) Zhang, Y.; Qiao, J.; Gao, S.; Hu, F.; He, D.; Wu, B.; Yang, Z.; Xu, B.; Li, Y.; Shi, Y.; Ji, W.; Wang, P.; Wang, X.; Xiao, M.; Xu, H.; Xu, J.-B.; Wang, X. Probing Carrier Transport and Structure-Property Relationship of Highly Ordered Organic Semiconductors at the Two-Dimensional Limit. *Phys. Rev. Lett.* **2016**, *116* (1), 16602.

(50) Cui, H.; Ye, Y.; Arman, H.; Li, Z.; Alsalme, A.; Lin, R.-B.; Chen, B. Microporous Copper Isophthalate Framework of Mot Topology for C2H2/CO2 Separation. *Cryst. Growth Des.* **2019**, *19* (10), 5829–5835.

(51) Hu, F.; Di, Z.; Wu, M.; Hong, M.; Li, J. A Robust Multifunctional Eu6-Cluster Based Framework for Gas Separation and Recognition of Small Molecules and Heavy Metal Ions. *Cryst. Growth Des.* **2019**, *19* (11), 6381–6387.

(52) Nath, A.; Islam, S. S.; Mukharjee, P. K.; Nath, R.; Mandal, S. Reentrant Spin-Glass Behavior in Cobalt(II) Based Coordination Polymers. *Cryst. Growth Des.* **2019**, *19* (11), 6463–6471.

(53) Inoue, S.; Minemawari, H.; Tsutsumi, J.; Chikamatsu, M.; Yamada, T.; Horiuchi, S.; Tanaka, M.; Kumai, R.; Yoneya, M.; Hasegawa, T. Effects of Substituted Alkyl Chain Length on Solution-Processable Layered Organic Semiconductor Crystals. *Chem. Mater.* **2015**, *27* (11), 3809–3812.

(54) Jones, B. A.; Facchetti, A.; Wasielewski, M. R.; Marks, T. J. Tuning Orbital Energetics in Arylene Diimide Semiconductors. Materials Design for Ambient Stability of n-Type Charge Transport. *J. Am. Chem. Soc.* **2007**, *129* (49), 15259–15278.

(55) Gemayel, M. El; Treier, M.; Musumeci, C.; Li, C.; Müllen, K.; Samorì, P. Tuning the Photoresponse in Organic Field-Effect Transistors. *J. Am. Chem. Soc.* **2012**, *134* (4), 2429–2433.

(56) Fink, R. F.; Seibt, J.; Engel, V.; Renz, M.; Kaupp, M.; Lochbrunner, S.; Zhao, H. M.; Pfister, J.; Würthner, F.; Engels, B. Exciton Trapping in π-Conjugated Materials: A Quantum-Chemistry-Based Protocol Applied to Perylene Bisimide Dye Aggregates. *J. Am. Chem. Soc.* **2008**, *130* (39), 12858–12859.

(57) Zhao, H. M.; Pfister, J.; Settels, V.; Renz, M.; Kaupp, M.; Dehm, V. C.; Würthner, F.; Fink, R. F.; Engels, B. Understanding Ground- and Excited-State Properties of Perylene Tetracarboxylic Acid Bisimide Crystals by Means of Quantum Chemical Computations. *J. Am. Chem. Soc.* **2009**, *131* (43), 15660–15668.

(58) Vura-Weis, J.; Ratner, M. A.; Wasielewski, M. R. Geometry and Electronic Coupling in Perylenediimide Stacks: Mapping Structure - Charge Transport Relationships. *J. Am. Chem. Soc.* **2010**, *132* (6), 1738–1739.

(59) Carmen Ruiz Delgado, M.; Kim, E. G.; Da Silva Filho, D. A.; Bredas, J. L. Tuning the Charge-Transport Parameters of Perylene Diimide Single Crystals via End and/or Core Functionalization: A Density Functional Theory Investigation. *J. Am. Chem. Soc.* **2010**, *132* (10), 3375–3387.

(60) Jain, A.; Shin, Y.; Persson, K. A. Computational Predictions of Energy Materials Using Density Functional Theory. *Nat. Rev. Mater.* **2016**, *1* (1), 15004.

(61) Gryn'Ova, G.; Lin, K. H.; Corminboeuf, C. Read between the Molecules: Computational Insights into Organic Semiconductors. *Journal of the American Chemical Society*. UTC 2018, pp 16370–16386.

(62) Cornil, J.; Verlaak, S.; Martinelli, N.; Mityashin, A.; Olivier, Y.; Van Regemorter, T.; D'Avino, G.; Muccioli, L.; Zannoni, C.; Castet, F.; Beljonne, D.; Heremans, P. Exploring the Energy Landscape of the Charge Transport Levels in Organic Semiconductors at the Molecular Scale. *Acc. Chem. Res.* **2013**, *46* (2), 434–443.

(63) Landi, A.; Troisi, A. Rapid Evaluation of Dynamic Electronic Disorder in Molecular Semiconductors. *J. Phys. Chem. C* **2018**, *122* (32), 18336–18345.

(64) Campbell, J. E.; Yang, J.; Day, G. M. Predicted Energy-Structure-Function Maps for the Evaluation of Small Molecule Organic Semiconductors. *J. Mater. Chem. C* **2017**, *5* (30), 7574–7584.

(65) Yang, J.; De, S.; Campbell, J. E.; Li, S.; Ceriotti, M.; Day, G. M. Large-Scale Computational

Screening of Molecular Organic Semiconductors Using Crystal Structure Prediction. *Chem. Mater.* **2018**, *30* (13), 4361–4371.

(66) Musil, F.; De, S.; Yang, J.; Campbell, J. E.; Day, G. M.; Ceriotti, M. Machine Learning for the Structure-Energy-Property Landscapes of Molecular Crystals. *Chem. Sci.* **2018**, *9* (5), 1289–1300.

(67) Schober, C.; Reuter, K.; Oberhofer, H. Virtual Screening for High Carrier Mobility in Organic Semiconductors. *J. Phys. Chem. Lett.* **2016**, *7* (19), 3973–3977.

(68) Nematiaram, T.; Padula, D.; Landi, A.; Troisi, A. On the Largest Possible Mobility of Molecular Semiconductors and How to Achieve It. *Adv. Funct. Mater.* **2020**, *30* (30), 2001906.

(69) Hofmann, D. W. M.; Kuleshova, L. N. *Data Mining in Crystallography*, 1st ed.; Springer Publishing Company, Incorporated, 2009.

(70) Caliandro, R.; Belviso, B. D.; Cuocci, C.; Fuertes, S.; Sicilia, V.; Hanson, J. C.; Tutuncu, G.; Doorhyee, E.; Altomare, A. Dynamic Characterization of Structural Changes in Vapochromic Compounds by Pair Distribution Function. *Powder Diffr.* **2017**, *32* (S1), S116–S122.

(71) Belviso, B. D.; Marin, F.; Fuertes, S.; Sicilia, V.; Rizzi, R.; Ciriaco, F.; Cappuccino, C.; Dooryhee, E.; Falcicchio, A.; Maini, L.; Altomare, A.; Caliandro, R. Structural Insights into the Vapochromic Behavior of Pt- And Pd-Based Compounds. *Inorg. Chem.* **2021**, *60* (9), 6349–6366.

(72) Xue, P.; Ding, J.; Wang, P.; Lu, R. Recent Progress in the Mechanochromism of Phosphorescent Organic Molecules and Metal Complexes. *J. Mater. Chem. C* **2016**, *4* (28), 6688–6706.

(73) Deshmukh, M. S.; Yadav, A.; Pant, R.; Boomishankar, R. Thermochromic and Mechanochromic Luminescence Umpolung in Isostructural Metal–Organic Frameworks Based on Cu6I6 Clusters. *Inorg. Chem.* **2015**, *54* (4), 1337–1345.

(74) Farinella, F.; Maini, L.; Mazzeo, P. P.; Fattori, V.; Monti, F.; Braga, D. White Luminescence Achieved by a Multiple Thermochromic Emission in a Hybrid Organic–Inorganic Compound Based on 3-Picolylamine and Copper(i) Iodide. *Dalt. Trans.* **2016**, *45* (44), 17939–17947.

(75) Dharmarwardana, M.; Otten, B. M.; Ghimire, M. M.; Arimilli, B. S.; Williams, C. M.; Boateng, S.; Lu, Z.; McCandless, G. T.; Gassensmith, J. J.; Omary, M. A. Strong π-Stacking Causes Unusually Large Anisotropic Thermal Expansion and Thermochromism. *Proc. Natl. Acad. Sci.*

U. S. A. **2021**, *118* (44).

(76)   Dharmarwardana, M.; Welch, R. P.; Kwon, S.; Nguyen, V. K.; Mccandless, G. T.; Omary, M. A.; Gassensmith, J. J.; Li, R.; Chemcomm, /; Communication, C. Thermo-Mechanically Responsive Crystalline Organic Cantilever †. **2017**.

(77)   Park, S. K.; Diao, Y. Martensitic Transition in Molecular Crystals for Dynamic Functional Materials. **2020**.

(78)   Skoko, Z.; Zamir, S.; Naumov, P.; Bernstein, J. The Thermosalient Phenomenon. "Jumping Crystals" and Crystal Chemistry of the Anticholinergic Agent Oxitropium Bromide. *J. Am. Chem. Soc.* **2010**, *132* (40), 14191–14202.

(79)   Naumov, P.; Karothu, D. P.; Ahmed, E.; Catalano, L.; Commins, P.; Mahmoud Halabi, J.; Al-Handawi, M. B.; Li, L. The Rise of the Dynamic Crystals. *J. Am. Chem. Soc.* **2020**, *142* (31), 13256–13272.

(80)   Bernstein, J. *Polymorphism in Molecular Crystals*; Oxford University Press: Oxford, 2007.

(81)   Shtukenberg, A. G.; Drori, R.; Sturm, E. V; Vidavsky, N.; Haddad, A.; Zheng, J.; Estroff, L. A.; Weissman, H.; Wolf, S. G.; Shimoni, E.; Li, C.; Fellah, N.; Efrati, E.; Kahr, B. Crystals of Benzamide, the First Polymorphous Molecular Compound, Are Helicoidal. *Angew. Chemie Int. Ed.* **2020**, *59* (34), 14593–14601.

(82)   Cappuccino, C.; Canola, S.; Montanari, G.; Lopez, S. G.; Toffanin, S.; Melucci, M.; Negri, F.; Maini, L. One Molecule, Four Colors: Discovering the Polymorphs of a Thieno(Bis)Imide Oligomer. *Cryst. Growth Des.* **2019**, *19* (5), 2594–2603.

(83)   Haleblian, J.; McCrone, W. Pharmaceutical Applications of Polymorphism. *J. Pharm. Sci.* **1969**, *58* (8), 911–929.

(84)   Cruz-Cabeza, A. J.; Reutzel-Edens, S. M.; Bernstein, J. Facts and Fictions about Polymorphism. *Chem. Soc. Rev.* **2015**, *44* (23), 8619–8635.

(85)   Bernstein, J. Polymorphism - A Perspective. *Cryst. Growth Des.* **2011**, *11* (3), 632–650.

(86)   Brog, J. P.; Chanez, C. L.; Crochet, A.; Fromm, K. M. Polymorphism, What It Is and How to Identify It: A Systematic Review. *RSC Adv.* **2013**, *3* (38), 16905–16931.

(87)   Herbstein, F. H. Diversity amidst Similarity: A Multidisciplinary Approach to Phase Relationships, Solvates, and Polymorphs. *Crystal Growth and Design*. 2004, pp 1419–1429.

(88) Bučar, D.-K.; Lancaster, R. W.; Bernstein, J. Disappearing Polymorphs Revisited. *Angew. Chemie Int. Ed.* **2015**, *54* (24), 6972–6993.

(89) Szafrafiski, M.; Katrusiak, A. Phase Transitions in the Layered Structure of Diguanidinium Tetraiodoplumbate. *Phys. Rev. B* **2000**, *61* (2), 1026–1035.

(90) Katrusiak, A. High-Pressure Crystallography. *Acta Crystallographica Section A: Foundations of Crystallography*. International Union of Crystallography (IUCr) January 1, 2008, pp 135–148.

(91) Katrusiak, A. High-Pressure X-ray Diffraction Studies on Organic Crystals. *Cryst. Res. Technol.* **1991**, *26* (5), 523–531.

(92) Boldyreva, E. V; Shakhtshneider, T. P.; Vasilchenko, M. A.; Ahsbahs, H.; Uchtmann, H. Anisotropic Crystal Structure Distortion of the Monoclinic Polymorph of Acetaminophen at High Hydrostatic Pressures. *Acta Crystallogr. B.* **2000**, *56 (Pt 2)*, 299–309.

(93) Katrusiak, A. High-Pressure X-Ray Diffraction Study of Pentaerythritol. *Acta Crystallogr. Sect. B* **1995**, *51* (5), 873–879.

(94) Katrusiak, A. Conformational Transformation Coupled with the Order-Disorder Phase Transition in 2-Methyl-1,3-Cyclohexanedione Crystals. *Acta Crystallogr. B.* **2000**, *56 (Pt 5)*, 872–881.

(95) Katrusiak, A. High-Pressure X-Ray Diffraction Study on the Structure and Phase Transition of 1,3-Cyclohexanedione Crystals. *Acta Crystallogr. Sect. B* **1990**, *46* (2), 246–256.

(96) Cruz-Cabeza, A. J.; Bernstein, J. Conformational Polymorphism. *Chemical Reviews*. 2014, pp 2170–2191.

(97) Gentili, D.; Gazzano, M.; Melucci, M.; Jones, D.; Cavallini, M. Polymorphism as an Additional Functionality of Materials for Technological Applications at Surfaces and Interfaces † Key Learning Points. *Chem. Soc. Rev* **2019**, *48*, 2502.

(98) Chung, H.; Diao, Y. Polymorphism as an Emerging Design Strategy for High Performance Organic Electronics. *Journal of Materials Chemistry C*. The Royal Society of Chemistry May 5, 2016, pp 3915–3933.

(99) Milita, S.; Liscio, F.; Cowen, L.; Cavallini, M.; Drain, B. A.; Degousée, T.; Luong, S.; Fenwick, O.; Guagliardi, A.; Schroeder, B. C.; Masciocchi, N. Polymorphism in N , N '-Dialkyl-Naphthalene Diimides. *J. Mater. Chem. C* **2020**, *8* (9), 3097–3112.

(100) Okamoto, T.; Kumagai, S.; Fukuzaki, E.; Ishii, H.; Watanabe, G.; Niitsu, N.; Annaka, T.; Yamagishi, M.; Tani, Y.; Sugiura, H.; Watanabe, T.; Watanabe, S.; Takeya, J. Robust, High-Performance n-Type Organic Semiconductors. *Sci. Adv.* **2020**.

(101) Huang, C.; Barlow, S.; Marder, S. R. Perylene-3,4,9,10-Tetracarboxylic Acid Diimides: Synthesis, Physical Properties, and Use in Organic Electronics. *Journal of Organic Chemistry*. 2011, pp 2386–2407.

(102) Zhan, X.; Facchetti, A.; Barlow, S.; Marks, T. J.; Ratner, M. A.; Wasielewski, M. R.; Marder, S. R. Rylene and Related Diimides for Organic Electronics. *Advanced Materials*. John Wiley & Sons, Ltd January 11, 2011, pp 268–284.

(103) Huang, C.; Sartin, M. M.; Siegel, N.; Cozzuol, M.; Zhang, Y.; Hales, J. M.; Barlow, S.; Perry, J. W.; Marder, S. R. Photo-Induced Charge Transfer and Nonlinear Absorption in Dyads Composed of a Two-Photon-Absorbing Donor and a Perylene Diimide Acceptor. *J. Mater. Chem.* **2011**, *21* (40), 16119–16128.

(104) Mariz, I. F. A.; Raja, S.; Silva, T.; Almeida, S.; Torres, É.; Baleizão, C.; Maçôas, E. Two-Photon Absorption of Perylene-3,4,9,10-Tetracarboxylic Acid Diimides: Effect of Substituents in the Bay. *Dye. Pigment.* **2021**, *193* (May).

(105) Al-Galiby, Q.; Grace, I.; Sadeghi, H.; Lambert, C. J. Exploiting the Extended π-System of Perylene Bisimide for Label-Free Single-Molecule Sensing. *J. Mater. Chem. C* **2015**, *3* (9), 2101–2106.

(106) Ribeiro, T.; Raja, S.; Rodrigues, A. S.; Fernandes, F.; Farinha, J. P. S.; Baleizão, C. High Performance NIR Fluorescent Silica Nanoparticles for Bioimaging. *RSC Adv.* **2013**, *3* (24), 9171–9174.

(107) Cowen, L. M.; Atoyo, J.; Carnie, M. J.; Baran, D.; Schroeder, B. C. Review—Organic Materials for Thermoelectric Energy Generation. *ECS J. Solid State Sci. Technol.* **2017**, *6* (3), N3080–N3088.

(108) Kardos, M. German Patent. DE 276357, 1913.

(109) Hadicke, E.; Graser, F. Structures of 11 Perylene-3,4-9,10-Bis(Dicarboximide) Pigments. *Acta Crystallogr. Sect. C* **1986**, *42*, 189–195.

(110) Langhals, H.; Demmig, S.; Potrawa, T. The Relation between Packing Effects and Solid State

Fluorescence of Dyes. *J. f�r Prakt. Chemie* **1991**, *333* (5), 733–748.

(111) Langhals, H. Cyclic Carboxylic Imide Structures as Structure Elements of High Stability. Novel Developments in Perylene Dye Chemistry. *Heterocycles* **1995**, *40* (1), 477–500.

(112) Mizuguchi, J. Correlation between Crystal and Electronic Structures in Diketopyrrolopyrrole Pigments as Viewed from Exciton Coupling Effects. *J. Phys. Chem. A* **2000**, *104* (9), 1817–1821.

(113) Mizuguchi, J. Polymorph of N,N'-Di-n-Butylperylene-3,4:9,10-Bis(Dicarboximide) and Their Electronic Structure. *Dye. Pigment.* **2006**, *70* (3), 226–231.

(114) Mizuguchi, J. Electronic Characterization of N,N'-Bis(2-Phenylethyl)Perylene-3,4:9, 10-Bis(Dicarboximide) and Its Application to Optical Disks. *J. Appl. Phys.* **1998**, *84* (8), 4479–4486.

(115) Mizuguchi, J.; Hino, K.; Tojo, K. Strikingly Different Electronic Spectra of Structurally Similar Perylene Imide Compounds. *Dye. Pigment.* **2006**, *70* (2), 126–135.

(116) Bialas, D.; Kirchner, E.; Röhr, M. I. S.; Würthner, F. Perspectives in Dye Chemistry: A Rational Approach toward Functional Materials by Understanding the Aggregate State. *Journal of the American Chemical Society*. 2021, pp 4500–4518.

(117) Balakrishnan, K.; Datar, A.; Naddo, T.; Huang, J.; Oitker, R.; Yen, M.; Zhao, J.; Zang, L. Effect of Side-Chain Substituents on Self-Assembly of Perylene Diimide Molecules: Morphology Control. *J. Am. Chem. Soc.* **2006**, *128* (22), 7390–7398.

(118) Würthner, F. Perylene Bisimide Dyes as Versatile Building Blocks for Functional Supramolecular Architectures. *Chem. Commun.* **2004**, *4* (14), 1564–1579.

(119) Nakazono, S.; Easwaramoorthi, S.; Kim, D.; Shinokubo, H.; Osuka, A. Synthesis of Arylated Perylene Bisimides through C - H Bond Cleavage under Ruthenium Catalysis. *Org. Lett.* **2009**, *11* (23), 5426–5429.

(120) Mumyatov, A. V.; Leshanskaya, L. I.; Anokhin, D. V; Dremova, N. N.; Troshin, P. A. Organic Field-Effect Transistors Based on Disubstituted Perylene Diimides: Effect of Alkyl Chains on the Device Performance. *Mendeleev Commun.* **2014**, *24* (5), 306–307.

(121) Ferlauto, L.; Liscio, F.; Orgiu, E.; Masciocchi, N.; Guagliardi, A.; Biscarini, F.; Samorì, P.; Milita, S. Enhancing the Charge Transport in Solution-Processed Perylene Di-Imide Transistors via Thermal Annealing of Metastable Disordered Films. *Adv. Funct. Mater.* **2014**, *24* (35), 5503–5510.

(122) Belova, V.; Wagner, B.; Reisz, B.; Zeiser, C.; Duva, G.; Rozbořil, J.; Novák, J.; Gerlach, A.; Hinderhofer, A.; Schreiber, F. Real-Time Structural and Optical Study of Growth and Packing Behavior of Perylene Diimide Derivative Thin Films: Influence of Side-Chain Modification. *J. Phys. Chem. C* **2018**, *122* (15), 8589–8601.

(123) Hansen, M. R.; Graf, R.; Sekharan, S.; Sebastiani, D. Columnar Packing Motifs of Functionalized Perylene Derivatives: Local Molecular Order despite Long-Range Disorder. *J. Am. Chem. Soc.* **2009**, *131* (14), 5251–5256.

(124) May, F.; Marcon, V.; Hansen, M. R.; Grozema, F.; Andrienko, D. Relationship between Supramolecular Assembly and Charge-Carrier Mobility in Perylenediimide Derivatives: The Impact of Side Chains. *J. Mater. Chem.* **2011**, *21* (26), 9538–9545.

(125) Ahmed, R.; Manna, A. K. Theoretical Insights on Tunable Optoelectronics and Charge Mobilities in Cyano-Perylenediimides: Interplays between -CN Numbers and Positions. *Phys. Chem. Chem. Phys.* **2021**, *23* (27), 14687–14698.

(126) Geng, Y.; Wang, J.; Wu, S.; Li, H.; Yu, F.; Yang, G.; Gao, H.; Su, Z. Theoretical Discussions on Electron Transport Properties of Perylene Bisimide Derivatives with Different Molecular Packings and Intermolecular Interactions. *J. Mater. Chem.* **2011**, *21* (1), 134–143.

(127) Shang, X.; Ahn, J.; Lee, J. H.; Kim, J. C.; Ohtsu, H.; Choi, W.; Song, I.; Kwak, S. K.; Oh, J. H. Bay-Substitution Effect of Perylene Diimides on Supramolecular Chirality and Optoelectronic Properties of Their Self-Assembled Nanostructures. *ACS Appl. Mater. Interfaces* **2021**, *13*.

(128) McKerrow, A. J.; Buncel, E.; Kazmaier, P. M. Molecular Modelling of Photoactive Pigments in the Solid State: Investigations of Polymorphism. *Can. J. Chem.* **1993**, *71* (3), 390–398.

(129) van der Lee, A.; Dumitrescu, D. G. Thermal Expansion Properties of Organic Crystals: A CSD Study. *Chem. Sci.* **2021**, *12*, 8537–8547.

(130) Jeon, H. G.; Hattori, J.; Kato, S.; Oguma, N.; Hirata, N.; Taniguchi, Y.; Ichikawa, M. Thermal Treatment Effects on N-Alkyl Perylene Diimide Thin-Film Transistors with Different Alkyl Chain. *J. Appl. Phys.* **2010**, *108* (12), 124512.

(131) Jang, J.; Nam, S.; Chung, D. S.; Kim, S. H.; Yun, W. M.; Park, C. E. High Tg Cyclic Olefin Copolymer Gate Dielectrics for N,N'-Ditridecyl Perylene Diimide Based Field-Effect Transistors: Improving Performance and Stability with Thermal Treatment. *Adv. Funct. Mater.* **2010**, *20* (16), 2611–2618.

(132) Tatemichi, S.; Ichikawa, M.; Koyama, T.; Taniguchi, Y. High Mobility N-Type Thin-Film Transistors Based on N,N′-Ditridecyl Perylene Diimide with Thermal Treatments. *Appl. Phys. Lett.* **2006**, *89* (11), 112108.

(133) Ma, L.; Guo, Y.; Wen, Y.; Liu, Y.; Zhan, X. High-Mobility, Air Stable Bottom-Contact n-Channel Thin Film Transistors Based on N,N′-Ditridecyl Perylene Diimide. *Appl. Phys. Lett.* **2013**, *103* (20), 203303.

(134) Kuznetsova, L. I.; Piryazev, A. A.; Anokhin, D. V.; Mumyatov, A. V.; Susarova, D. K.; Ivanov, D. A.; Troshin, P. A. Disubstituted Perylene Diimides in Organic Field-Effect Transistors: Effect of the Alkyl Side Chains and Thermal Annealing on the Device Performance. *Org. Electron.* **2018**, *58*, 257–262.

(135) Rang, Z.; Haraldsson, A.; Kim, D. M.; Ruden, P. P.; Nathan, M. I.; Chesterfield, R. J.; Frisbie, C. D. Hydrostatic-Pressure Dependence of the Photoconductivity of Single-Crystal Pentacene and Tetracene. *Appl. Phys. Lett.* **2001**, *79* (17), 2731–2733.

(136) Mailman, A.; Leitch, A. A.; Yong, W.; Steven, E.; Winter, S. M.; Claridge, R. C. M.; Assoud, A.; Tse, J. S.; Desgreniers, S.; Secco, R. A.; Oakley, R. T. The Power of Packing: Metallization of an Organic Semiconductor. *J. Am. Chem. Soc.* **2017**, *139* (6), 2180–2183.

(137) Li, R.; Wang, M.; Zhao, H.; Bian, Z.; Wang, X.; Cheng, Y.; Huang, W. Pressure Effect on Electronic and Excitonic Properties of Purely J-Aggregated Monolayer Organic Semiconductor. *J. Phys. Chem. Lett.* **2020**, *11* (15), 5896–5901.

(138) Wang, Q.; Zhang, H.; Zhang, Y.; Liu, C.; Han, Y.; Ma, Y.; Gao, C. High Pressure Electrical Transport Behavior in Organic Semiconductor Pentacene. *High Press. Res.* **2014**, *34* (4), 355–364.

CHAPTER 2: PROJECT OVERVIEW

The aim of my Ph.D. project was the investigation of the polymorphism of molecular organic semiconductor material at non-ambient conditions and the solid-state characterization and crystal structure determination of the different polymorphic forms.

The first months of my Ph.D. research were not dedicated to the main project, instead, it concerned two different topics in the framework of structure-property investigation and non-ambient measurements. During these projects, I acquired the crystallographic skills and solid-state characterization competencies which were fundamentals for my thesis. The first topic was the solid-state characterization of Pt- and Pd- based vapochromic crystals in collaboration with Dr. Rocco Caliandro from IC-CNR of Bari. These hydrated potassium/lithium salts exhibit a change in color upon heating, and they transform back into the original color upon absorption of water molecules from the environment. The challenging characterization of these vapochromic transitions was carried out by a combination of techniques, such as Single Crystal X-ray diffraction, variable temperature X-ray powder diffraction, and pair distribution function, to underline the structural changes that the material undergoes with water loss upon heating (see Chapter 3). The second topic was the investigation of structure−mechanical property relationships in polymorphs of C4-NT3N, a thienopyrrolyldione end-capped oligothiophene that displays ambipolar n-type charge transport and electroluminescence, in collaboration with Dr. Chiara Cappuccino from the Molecular Crystal Engineering group of Bologna. In this project, the different mechanical properties of the two polymorphs were discussed and related to the different structural arrangements and the thermal behavior, and the enantiotropic relationship of the polymorphs was investigated (see Chapter 4).

The main part of my Ph.D. project was dedicated to the investigation and solid-state characterization of the polymorphism of a series of N,N'-dialkyl-3,4,9,10-perylendiimide (PDI-Cn, with n = 5, 6, 7, 8) at ambient and non-ambient conditions, with a particular focus in their thermal behavior. The PDI-Cn are well-known commercially available n-type molecular organic semiconductors and pigments and have potential applications in organic electronics like OFETs and OPVs. These molecules are known to transform into different crystalline forms upon thermal treatments but no information on the structures has been reported yet and the high-temperature characterization is fragmented and contradictory. To study their behavior at high temperatures I submitted a proposal (ID proposal 2020094632) to ALBA synchrotron for the BL04-MSPD beamline and I was able to collect the data during the spring of 2021.

This series of PDI-Cn was also chosen to understand the role played by alkyl chains in the crystal packing and polymorphism of these materials since the introduction of side chains as alkyl chains is commonly employed to improve solubility and processability.

Out of the four PDI-Cn investigated, the high-temperature polymorphism of N,N'-dipentyl-3,4,9,10-perylendiimide (PDI-C5) was particularly interesting and challenging. For this reason, the thorough investigation of the polymorphs of PDI-C5 was carried out by a combination of the techniques available at the department such as DSC, HSM, and X-ray diffraction variable temperature Raman spectroscopy in collaboration with dr. Tommaso Salzillo (Weizmann Institute) The results are reported and discussed separately from the other PDI-Cn in Chapter 5.

Given the high degree of polymorphism observed for PDI-Cn with temperature, for understanding further the structural characteristics, as intermolecular interactions and packing motifs, and polymorphism of PDI-Cn, we decided to study their behavior at high-pressure. To do so, thanks to the Marco Polo project, I had the opportunity to spend four months (May-July 2021) in the group of Prof. Andrzej Katrusiak at the Uniwersytet im. Adama Mickiewicza in Poznań, Poland. During my stay in Poland, I performed various pressure-dependent UV-Vis absorption spectroscopy and high-pressure Single Crystal X-ray diffraction on the different PDI-Cn. Although for lack of time, these experiments have not yet been completed for all PDI-Cn, the preliminary results of PDI-Cn polymorphism at high temperature and pressure are reported in Chapter 6.

In the last part of my Ph.D. research project, we made use of the large amount of PDI derivatives crystal structure data present in the CSD database to investigate the crystal packing arrangements of PDI derivatives with different types and positions of the substituents to test a clustering method based on a combination of self-organizing maps (SOM) and principal component analysis (PCA) as a data-driven approach to classify different π-stacking arrangements of PDIs. The aim was to identify families of similar stacking arrangements among PDIs through the use of packing descriptors, which could then be used to describe newly solved crystal structures of PDI derivatives, and to give guidelines for predicting the most likely packing family depending on substituents used (see Chapter 7). This part of the project was carried out in collaboration with Dr. Alessandro Zappi, who performed the SOM and PCA analysis.

CHAPTER 3: STRUCTURAL INSIGHTS INTO THE VAPOCHROMIC BEHAVIOR OF Pt- AND Pd- BASED COMPOUNDS

The present work was a part of a project in collaboration with Dr. Rocco Caliandro from IC-CNR in Bari. It was focused on the solid-state characterization of crystals of Pt- and Pd- hydrated potassium/lithium salts that exhibit vapochromic behavior, *i.e.*, they exhibit a change in color upon heating due to loss of hydration water, and they transform back into the original color upon absorption of water molecules from the environment.

My contribution to this project was the structure determination and refinement by single crystal X-ray diffraction of $[K(H_2O)][Pt(ppy)(CN)_2]$, carried out with Dr. Aurelia Falcicchio, and the variable temperature X-ray powder diffraction to relate the color transition to changes in the diffraction pattern and the decrease in sample crystallinity. Our results, combined with results from other techniques such as *in situ* pair distribution function, thermogravimetric analysis, X-ray absorption spectroscopy, and UV-vis spectroscopy, were fundamental to tackle the challenging characterization of these vapochromic transitions and to underline the structural changes that the material undergoes with water loss upon heating.
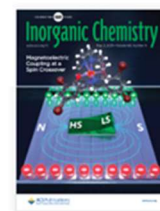
Structural Insights into the Vapochromic Behavior of Pt- and Pd-Based Compounds

Benny Danilo Belviso, Francesco Marin, Sara Fuertes, Violeta Sicilia, Rosanna Rizzi, Fulvio Ciriaco, Chiara Cappuccino, Eric Dooryhee, Aurelia Falcicchio, Lucia Maini, Angela Altomare, and Rocco Caliandro*

For copyright reasons only the link to the original article and the abstract are reported here:

https://pubs.acs.org/doi/10.1021/acs.inorgchem.1c00081
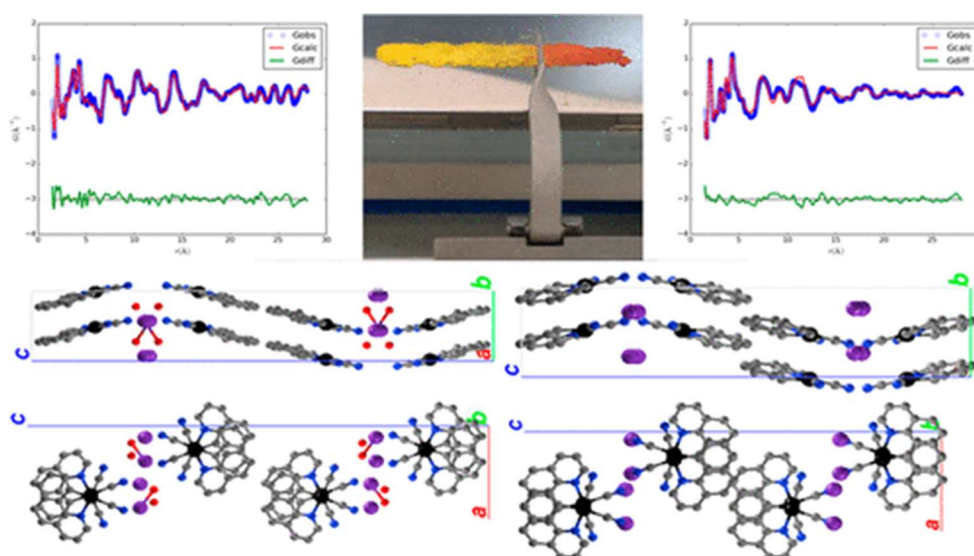
Supplementary information are reported in Appendix A.

ABSTRACT

Anionic complexes having vapochromic behavior are investigated: $[K(H_2O)][M(ppy)(CN)_2]$, $[K(H_2O)][M(bzq)(CN)_2]$, and $[Li(H_2O)_n][Pt(bzq)(CN)_2]$, where ppy = 2-phenylpyridinate, bzq = 7,8-benzoquinolate, and M = Pt(II) or Pd(II). These hydrated potassium/lithium salts exhibit a change in color upon being heated to 380 K, and they transform back into the original color upon absorption of water molecules from the environment. The challenging characterization of their structure in the vapochromic transition has been carried out by combining several experimental techniques, despite the availability of partially ordered and/or impure crystalline material. Room-temperature single-crystal and powder X-ray diffraction investigation revealed that $[K(H_2O)][Pt(ppy)(CN)_2]$ crystallizes in the *Pbca* space group and is isostructural to $[K(H_2O)][Pd(ppy)(CN)_2]$. Variable-temperature

powder X-ray diffraction allowed the color transition to be related to changes in the diffraction pattern and the decrease in sample crystallinity. Water loss, monitored by thermogravimetric analysis, occurs in two stages, well separated for potassium Pt compounds and strongly overlapped for potassium Pd compounds. The local structure of potassium compounds was monitored by *in situ* pair distribution function (PDF) measurements, which highlighted changes in the intermolecular distances due to a rearrangement of the crystal packing upon vapochromic transition. A reaction coordinate describing the structural changes was extracted for each compound by multivariate analysis applied to PDF data. It contributed to the study of the kinetics of the structural changes related to the vapochromic transition, revealing its dependence on the transition metal ion. Instead, the ligand influences the critical temperature, higher for ppy than for bzq, and the inclination of the molecular planes with respect to the unit cell planes, higher for bzq than for ppy. The first stage of water loss triggers a unit cell contraction, determined by the increase in the b axis length and the decrease in the a (for ppy) or c (for bzq) axis lengths. Consequent interplane distance variations and in-plane roto-translations weaken the π-stacking of the room-temperature structure and modify the distances and angles of Pt(II)/Pd(II) chains. The curve describing the intermolecular Pt(II)/Pd(II) distances as a function of temperature, validated by X-ray absorption spectroscopy, was found to reproduce the coordinate reaction determined by the model-free analysis.

CHAPTER 4: STRUCTURE–MECHANICAL RELATIONSHIPS IN POLYMORPHS OF AN ORGANIC SEMICONDUCTOR (C4-NT3N)

The present work was a part of a project carried out by Dr. Chiara Cappuccino from the Molecular Crystal Engineering group of Bologna. It was focused on the investigation of structure-mechanical property relationships in polymorphs of C4-NT3N, a thienopyrrolyldione end-capped oligothiophene that displays ambipolar n-type charge transport and electroluminescence.

My contribution to this project was limited to the investigation of the thermal behavior of the α and β polymorphs of C4-NT4N, in particular the hot-stage microscopy experiments and their correlation with the DSC results. The thermal characterization of C4-NT4N highlighted that the α and β forms are enantiotropically related, with α the stable phase at room temperature, while the β the stable form at high-temperature.

The different mechanical properties of the two polymorphs were characterized and related to the different crystal packing and intermolecular interactions by Dr. Chiara Cappuccino and Dr. Luca Catalano (from New York University Abu Dhabi). The α polymorph, characterized by one-dimensional strong interactions and weak hydrogen bonds between the columns, displays elastic deformation; whereas the β polymorph, characterized by two-dimensional layer packing with very weak interlayer interactions and without interdigitation of the alkyl chains, displays plastic behavior.

Structure−Mechanical Relationships in Polymorphs of an Organic Semiconductor (C4-NT3N)

Chiara Cappuccino, Luca Catalano, Francesco Marin, Ghada Dushaq, Gijo Raj, Mahmoud Rasras, Rachid Rezgui, Massimo Zambianchi, Manuela Melucci, Panče Naumov*, and Lucia Maini*

For copyright reasons only the link to the original article and the abstract are reported here:

https://pubs-acs-org.ezproxy.unibo.it/doi/10.1021/acs.cgd.9b01281
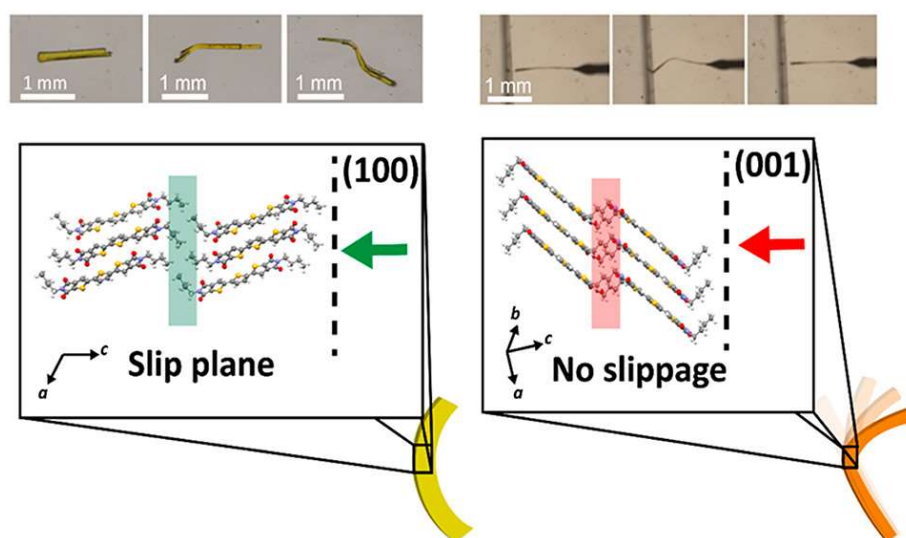
Supporting information are reported in Appendix B.

ABSTRACT

Understanding of polymorphism of organic semiconducting materials is the key to structural control of their electrical and mechanical properties. Motivated by the ambipolar n-type charge transport and electroluminescence of thienopyrrolyldione end-capped oligothiophenes, here we studied the propensity of one representative to crystallize as different polymorphs which display distinctly different mechanically properties. The crystal structures of the two polymorphs (denoted "α" and "β") of the material, 2,2′-(2,2′-thiophene-5,5′-diyl)bis(5-butyl-5*H*-thieno[2,3-*c*]pyrrole-4,6)-dione (C4-NT3N), were determined. In the α phase, the molecules interact strongly by π-stacking, forming columns which are bonded via C–H—O and chalcogen bonds, and this packing is consistent with the

elastic behavior observed with the crystals. Instead, the β phase has the molecules aligned along their core forming layers. While the molecules interact strongly within the layers, they are practically unbound between the layers. The presence of slip planes in this form explains the plastic deformation induced by applying a force perpendicular to the (001). The thermal behavior and the enantiotropic relationship of the polymorphs are reported.

CHAPTER 5: THOROUGH INVESTIGATION ON THE HIGH-TEMPERATURE POLYMORPHISM OF DIPENTYL-PERYLENEDIIMIDE: THERMAL EXPANSION VS POLYMORPHIC TRANSITION.

The present work is focused on the high-temperature polymorphism of N,N'-dipentyl-perylenediimide (PDI-C5); out of the four PDI-Cn investigated, PDI-C5 high-temperature polymorphism was particularly interesting and challenging and for this reason was reported and discussed separately.

In this work, we used a combination of differential scanning calorimetry, variable temperature X-ray diffraction, hot-stage microscopy, and variable temperature Raman spectroscopy to investigate the thermal behavior and polymorphism of PDI-C5. We identified two high-temperature polymorphs, form II and form III and we determined their crystal structure from synchrotron powder data. Furthermore, we investigated the thermal expansion of the different PDI-C5. We also reported and characterized a solvate form of PDI-C5. The variable temperature Raman spectroscopy measurements were carried out by Dr. Tommaso Salzillo from Weizmann Institute.
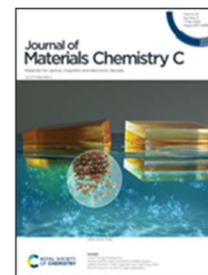
Thorough investigation on the high-temperature polymorphism of dipentyl-perylenediimide: thermal expansion vs polymorphic transition.

Francesco Marin, Serena Tombolesi, Tommaso Salzillo, Omer Yaffe and Lucia Maini

For copyright reasons only the link to the original article and the abstract are reported here:

Supplementary information are reported in Appendix C.

ABSTRACT

N,N'-dipentyl-3,4,9,10-perylendiimide (PDI-C5) is an organic semiconducting material which has been extensively investigated as model compound for its optoelectronic properties. It is known to be highly thermally stable, that it exhibits solid-state transitions with temperature and that thermal treatments lead to an improvement in its performance in devices. Here we report a full thermal characterization of PDI-C5 by combination of differential scanning calorimetry, variable temperature X-ray diffraction, hot stage microscopy, and variable temperature Raman spectroscopy. We identified two high temperature polymorphs, form II and form III, which form respectively at 112 °C and at 221 °C and we determined their crystal structure from powder data. Form II is completely reversible upon cooling with low hysteresis, while form III revealed a different thermal behaviour upon cooling depending on the technique and crystal size. The crystal structure's features of the different polymorphs are discussed and compared, and we looked into the role of the perylene core and alkyl chains during solid-state transitions. The thermal expansion principal axis of PDI-C5 crystal forms is reported showing that all the reported forms possess negative thermal expansion (X1) and large positive thermal expansion (X3) which are correlated to thermal behaviour observed.

CHAPTER 6: EXPLORING POLYMORPHIC LANDSCAPE OF PDI-Cn AT VARIABLE TEMPERATURE AND PRESSURE

High pressure measurements were carried out at Uniwersytet im. Adama Mickiewicza, in Poznań, Poland during my abroad period in collaboration with Prof. Andrzej Katrusiak, Dr. Szymon Sobczak, and Paulina Ratajczyk.

INTRODUCTION

The identification and investigation of polymorphic systems, in particular in the field of organic molecular crystals, is usually tackled by varying crystallization techniques, concentrations, solvents, or temperature. However, different crystal forms can also be obtained by varying another fundamental physical variable, pressure. Thanks to the development of high-pressure techniques in the last decades, nowadays they can be routinely applied in laboratories to analyze the structure-properties relationship of crystalline materials, and indeed to investigate their polymorphism.[1–4]

In the field of organic semiconductors (OSCs), the possibility to understand and control crystal polymorphism is of fundamental importance, as the crystalline structure has a major impact on the properties of materials. Thus, for example, a small change in the molecular packing can lead to dramatic variations in optoelectronic and charge-transport properties. Therefore, the polymorphism of functional materials strongly influences the possible technological applications.[5–8]

In the framework of OSCs, perylene-3,4,9,10-tetracarboxydiimides, also known as perylene diimides (PDIs), are a well-known family of promising n-type materials because of their commercial availability, low costs, high electron affinity, low LUMO energies, and good charge transport properties; moreover, they also display excellent chemical-, thermal-, photo-, as well as good air-stability and strong absorption in the visible light region.[9–13] Due to their properties, PDIs possess several potential applications such as organic field-effect transistors,[14–16] organic photovoltaics,[17,18] laser dye,[19] pigments,[20] etc. As well as other OSC systems, functionalization can greatly influence the final properties of PDIs such as solubility, optical and electrochemical properties, crystal packing, and structural morphology. Among others, the introduction of side chains as alkyl chains is a common procedure used to improve solubility and processability of PDIs and to obtain new functional materials.[5,13,21,22]

This work is focused on the investigation of the polymorphism of a series of four N,N'-dialkyl-PDIs (PDI-Cn) functionalized in a symmetric fashion with alkyl chains of different lengths (C5, C6, C7, and C8). In particular, in this study, we tackle the identification and investigation of PDI-Cn

polymorphs at non-ambient conditions (*i.e.,* at high temperature and pressure). These materials are known to display several solid-solid transitions upon heating;[23,24] however, the characteristics of these transitions have yet not been studied in detail. Furthermore, to our knowledge, no information about their behavior at high-pressure has ever been investigated. Lastly, the investigation of the structural behavior at non-ambient conditions of PDIs with different alkyl chains allows us to look into the role played by alkyl chains in the crystal packing and the polymorphism of these materials.

RESULTS AND DISCUSSION

Polymorph screening

Several crystallization methods from solution (solvent evaporation, triple-layer crystallization, solvothermal processes, fast precipitation) were used to obtain different crystal forms of PDI-Cn and good crystals for single crystal X-ray diffraction measurements. Out of these methods, solvothermal crystallization resulted the most efficient to produce single crystals, also because of the poor solubility of PDI-Cn (less than 1 mg/mL in the used solvents) which hindered the efficiency of the other methods. All crystallizations resulted in the formation of PDI-Cn form I (the crystal form of the commercial material) except PDI-C5 whose solvate crystals were obtained as already reported (add ref submitted)

The crystal structures of PDI-C5 form I, PDI-C6 form I, and PDI-C8 form I, which are their form stable at r.t., were found in the CSD (refcodes: DICMUX, TIXTUS, and GILFUD respectively). On the other hand, no structural model was found for PDI-C7 in the database, thus the crystal structure of PDI-C7 form I was solved from single crystal X-ray diffraction (SCXRD) at room temperature. Furthermore, the PDI-C6 crystal structure was solved at room temperature to better compare it with the other PDI-Cn. Table 1 summarizes the relevant crystallographic data for all the structures.

Crystal structure of PDI-C7 form I. The crystal structure of PDI-C7 form I is triclinic, space group P-1, and cell parameters a = 4.8287(4) Å; b = 8.3567(7) Å; c = 19.320(2) Å; α = 79.591(7) °; β = 88.669(7) °; γ = 81.655(7) °; volume = 758.6 Å^3, with the molecule lying on an inversion centre, and hence half molecule in the asymmetric unit (Z'= 0.5). The perylene core of the molecule is planar, while the heptyl alkyl chains are almost perpendicular to the perylene plane, the alkyl carbon atoms are in staggered conformation, beside the terminal carbon atom which is statically disordered in two positions, one in staggered and one in gauche conformation, with 50% probability each. The torsional angle of the terminal carbon in the two positions is 161.50 ° for the staggered position and 83.29 ° for the gauche one. The PDI molecules are arranged one above the other connected via π−π

interactions, forming columns along the [1 0 0] direction. The neighboring columns of PDI molecules are linked together through π-stacking and weak C-H⋯O interactions.
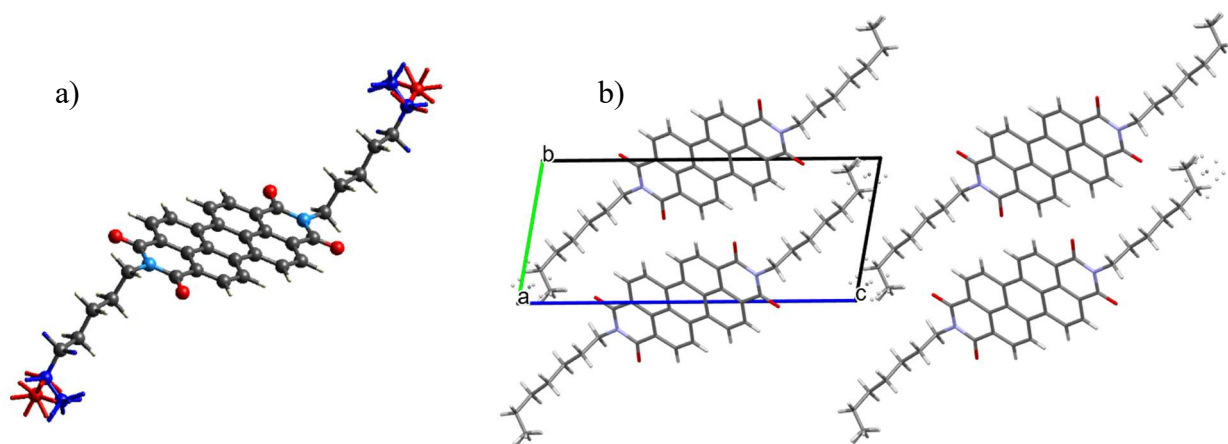
Figure 1. Crystal structure of PDI-C7 a) form I with highlighted in red and blue the two possible disordered positions; b) form I viewed along a-axis.

Table 1. Crystal structure parameters of PDI-Cn form I.

	PDI-C5	PDI-C6	PDI-C7	PDI-C8
SG	$P\bar{1}$	$P\bar{1}$	$P\bar{1}$	$P\bar{1}$
a (Å)	4.754(2)	4.757(1)	4.8287(4)	4.7647(2)
b (Å)	8.479(4)	8.549(2)	8.3567(7)	8.5099(3)
c (Å)	16.30(1)	17.576(2)	19.320(2)	20.2613(6)
α (°)	86.88(5)	81.68(1)	79.591(7)	85.332(2)
β (°)	83.50(5)	84.85(2)	88.669(7)	89.683(2)
γ (°)	83.68(4)	83.17(2)	81.655(7)	82.285(3)
V (Å³)	648.1	700.3	758.6	811.4
Z	1	1	1	1
Z'	0.5	0.5	0.5	0.5
Density (g/cm³)	1.36	1.325	1.284	1.258
T (K)	298	298	298	298
R	6.3	7.2	7.5	5.1

By comparing the crystal structure of PDI-C7 with the known crystal structure of the other PDI-Cn, we observed that they are indeed very similar. All the PDI-Cn crystal structures were solved as triclinic, space group P-1, with half-molecule in the asymmetric unit (Z' = 0.5); the crystal packing of the PDI-Cn is characterized by a one-dimensional lamellar packing motif, with molecules arranged in columns along the [1 0 0] direction characterized by strong π-π stacking interactions between the perylene cores. Different columns are linked to the neighboring columns via π-π stacking interactions and weak C-H⋯O interactions. The overall result is a layered structure in which rigid aromatic core regions alternate with alkyl chain regions (Figure 2). The crystal structure of PDI-C7 differs from the others for the presence of disorder in the terminal carbon atoms of the alkyl chains discussed previously; the PDI-Cn besides PDI-C7 shows alkyl chains in all staggered conformation.
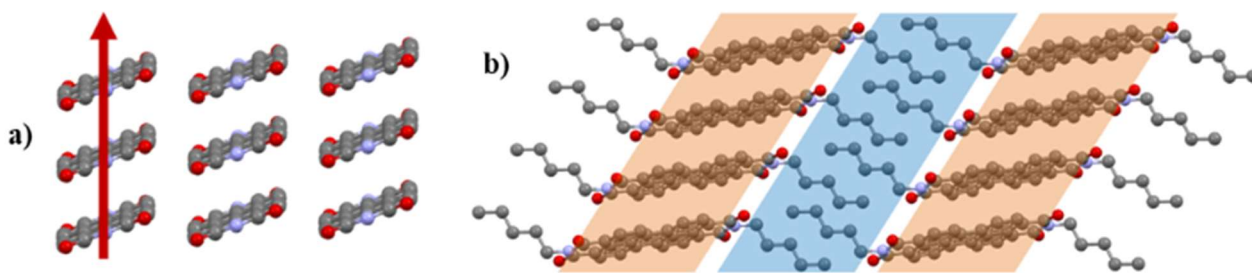
Figure 2. Packing motif in PDI-C5 crystal structure: a) columnar arrangement of π-stacked molecules with the arrow indicating the direction of π-π stacking interactions (alkyl chains omitted for clarity); b) lamellar packing formed by alternated layers of alkyl chains and aromatic cores. Hydrogens are omitted for the sake of clarity.

The overall similarity of these structures is also reflected in their unit cell parameters, in particular of their *a*- and *b*-axis. The *a*-axis corresponds to the stacking vector (SV), which is the distance between the centroids of two closed stacked molecules,[8] and it is almost the same for PDI-C5, PDI-C6, and PDI-C8, and slightly higher for PDI-C7. The *b-axis* correspond to the distance between two neighboring columns of stacked molecules, which is still similar but changes slightly more (from 8.3567 Å to 8.549 Å) among the structure compared to SV, with PDI-C7 displaying the lowest value and PDI-C6 the highest value. The interplanar distance ($d_{\pi-\pi}$) between the perylene core involved in π-stack is characteristic of closed stacking π-π interaction in all the PDI-Cn, varying from 3.337 Å of PDI-C5 to 3.361 Å of PDI-C6. Furthermore, even if we look at their pitch (P) and roll (R) angles, which are the molecular slipping along the long and short molecular axis,[25] they are very similar among the structures; with P having values between 42.6 ° for PDI-C6 and 43.7 for PDI-C7, and R with values between 20.3 ° for PDI-C8 and 21.6 ° for PDI-C6. All these parameters indicate that the perylene cores among the PDI-Cn crystal packings arrange in the same way. To further examine the PDI-Cn packing similarities, the Search on Crystal Packing Similarity tool of the software Mercury[26] of the CCDC package was used with a cluster of 18 molecules. This tool allows comparing multiple structures of the same compound or similar molecules, giving as results the number of molecules in common, together with the root mean square (RMS) deviation in distance and a similarity measure of the simulated powder patterns of the structures. Using PDI-C5 as reference structure, each PDI-Cn showed 9 out of 18 molecules in common, the other 9 molecules were missed matches because separated by alkyl chains of different lengths. The best RMS was found for PDI-C6, with a 0.066 Å deviation, second was PDI-C8 with a 0.151 Å deviation, and lastly, the PDI-C7 with a 0.28 Å deviation, indicating that PDI-C7 is the least similar structure among all, most likely a consequence of its chain conformation. When the PXRD similarity is considered, as expected the PDI-C6 is the most similar (0.96) to PDI-C5, then PDI-C7 (0.88), and the PDI-C8 the least similar one (0.86). The overlay of the form I crystal structure of PDI-Cn used to calculate the crystal packing similarity is shown in Figure 3.
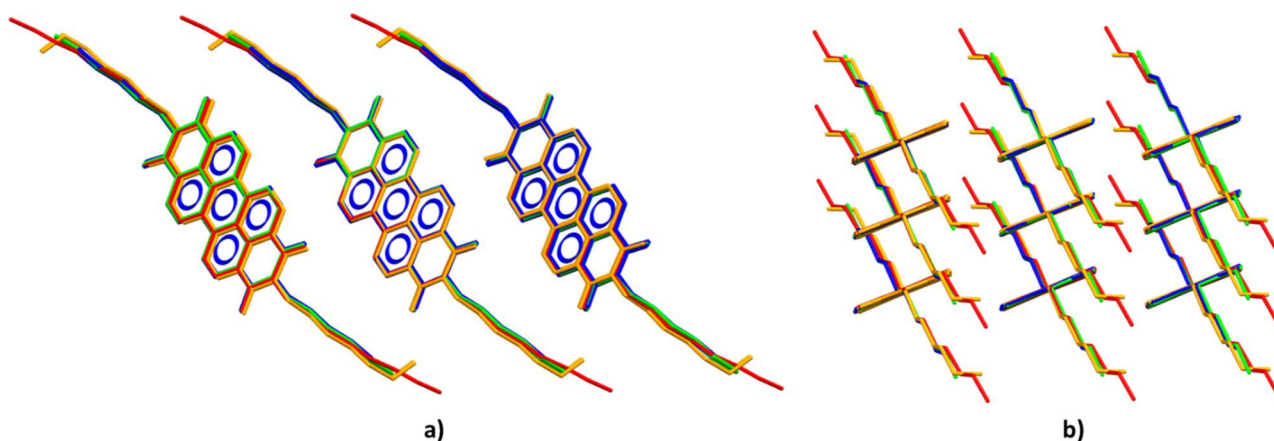
Figure 3. Crystal packing similarity showing the overlay of the different PDI-Cn crystal structures. PDI-C5 is blue, PDI-C6 is green, PDI-C7 in orange, and PDI-C8 in red. a) Structure overlay viewed along [100] direction; b) Structure overlay viewed along the long molecular axis.

PDI-Cn at High-Temperature

The thermal characterization of the PDI-Cn to investigate their high-temperature polymorphism was carried out by a combination of thermogravimetric analysis, differential scanning calorimetry, variable temperature X-ray diffraction, and hot-stage microscopy.

Thermogravimetric analysis

Thermogravimetric analysis (TGA) of PDI-Cn shows that they are stable up to 400°C, displaying the high thermal stability that characterizes these materials (see Figure S1-4 in SI).

Differential Scanning Calorimetry

PDI-Cn were analyzed by Differential Scanning Calorimetry (DSC) to highlight phase transitions that occur with temperature. Besides PDI-C5 behavior that was extensively explained in our previous work,[27] all PDI-Cn displays solid-solid phase transitions with temperature highlighting the presence of high temperature (HT) polymorphism. However, it was not possible to isolate the HT polymorphs at room temperature (RT), because these solid-solid transitions are reversible upon cooling (see Figure 4). The samples were heated until 380-395 °C, just before decomposition and in PDI-C7 and PDI-C8 a reversible peak was observed in the range 360-390°C. Whereas during the VTXRPD the samples decompose at a temperature higher than 300°C, we will not further discuss the transition at a temperature higher than 300°C.
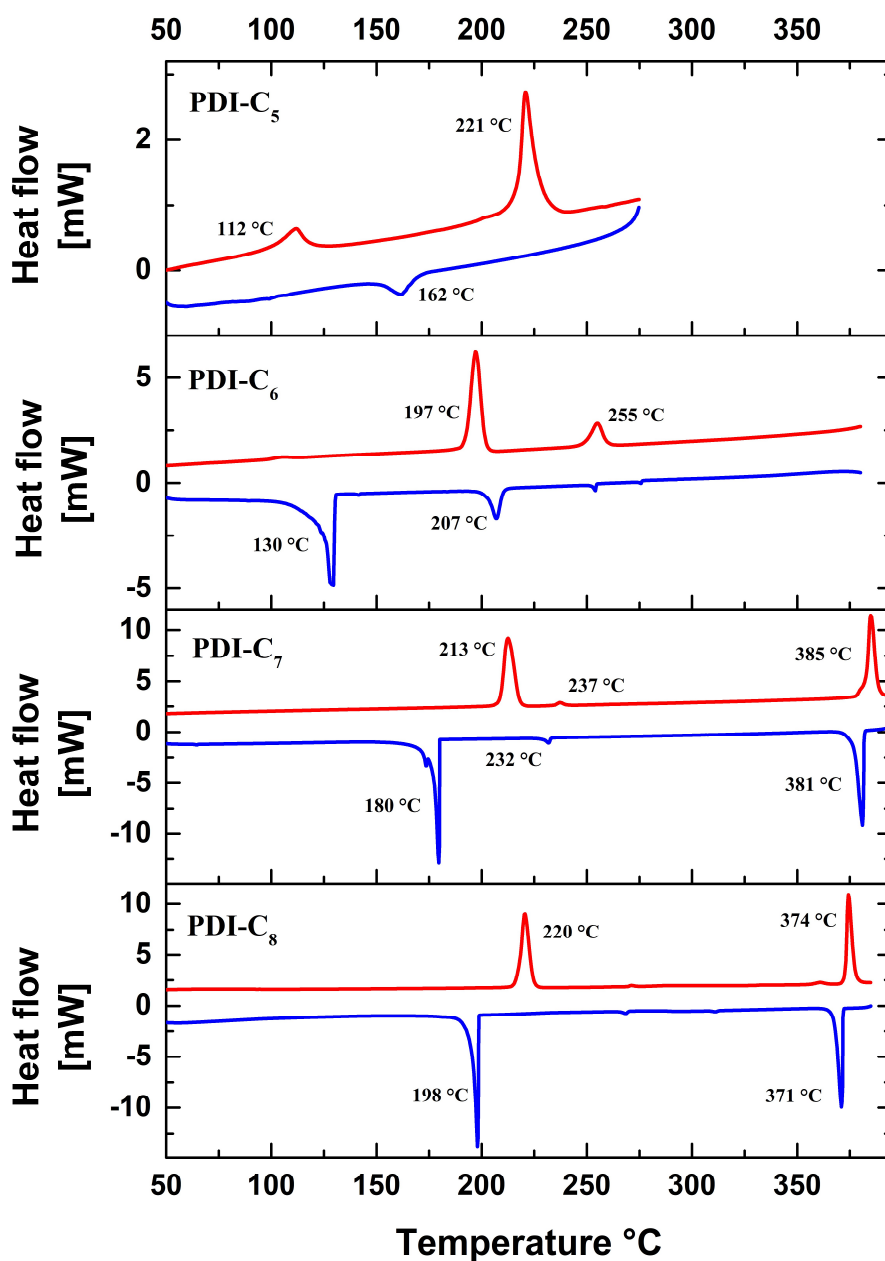
Figure 4. DSC curves of the PDI-Cn; red curves correspond to heating steps, whereas blue curves correspond to cooling steps. The temperature and enthalpy of transition observed are listed in Table 2.

Table 2 summarizes the solid-state transition observed in the DSC curves in Figure 4.

Table 2. Transitions of PDI-Cn observed by DSC upon heating and cooling.

	Cycle	Transition	T (°C)	ΔH (kJ mol^{-1})
PDI-C5	1st Heating	I → II	112	2.8
	1st Cooling	II → I	109	-2.8
	2nd Heating	I → II	112	2.1
		II → III	221	8.8
	2nd Cooling	III → I + II	162	-1.8
PDI-C6	Heating	I → II	197	16.2

		II → III	255	4.4
	Cooling	III → II	207	-4.4
		II → I	130	-19.3
PDI-C7	Heating	I → II	213	24.1
		II → III	237	0.66
	Cooling	III → II	232	-0.85
		II → I	180	-25.3
PDI-C8	Heating	I → II	220	24.7
	Cooling	II → I	198	-26.6

Hot-stage Microscopy

The thermal behavior of PDI-C$_n$ was investigated also with Hot-Stage Microscopy (HSM), to observe the macroscopic changes that occur in the crystals upon heating.

PDI-C6. Single crystals of PDI-C$_6$ were heated up to 280 °C, to observe the macroscopic changes correlated to the transitions into from II and form III (see Figure 5).
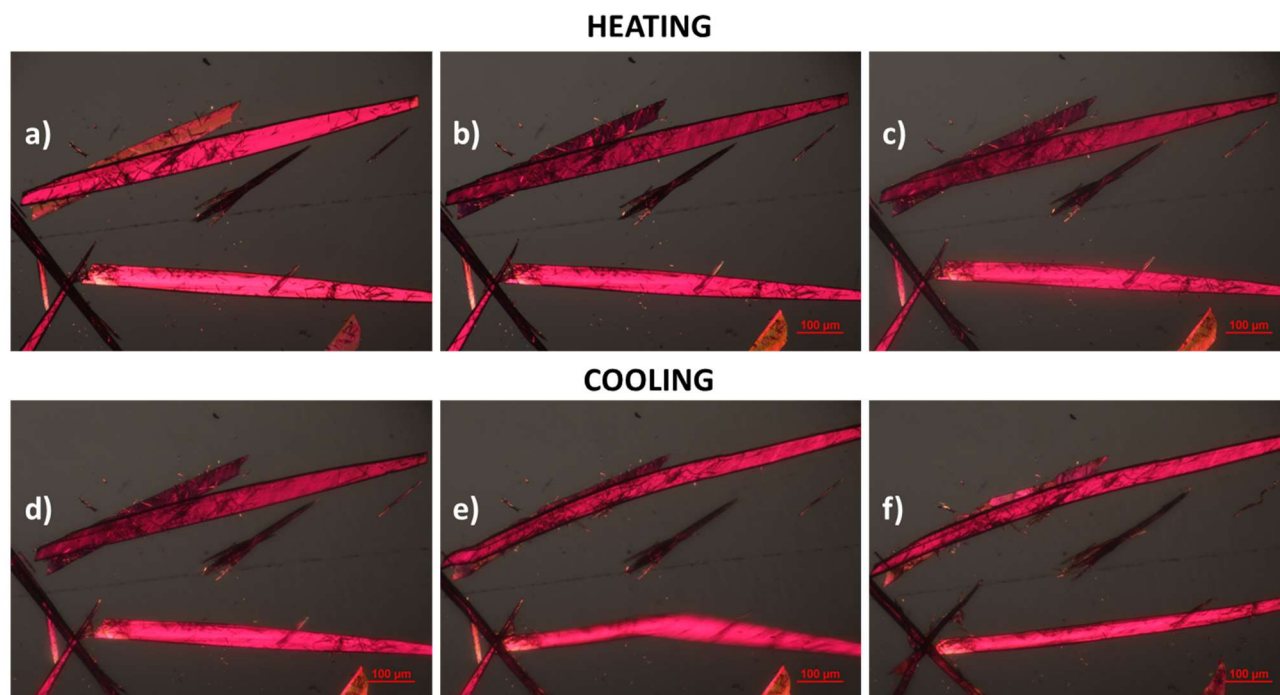
Figure 5. HSM of PDI-C6 crystals: a) 30 °C start of experiment; b) 205 °C after the I → II transition occurs; c) 270 °C after the II → III transition occurs, then the cooling was started; d) 180 °C during cooling; e) 114 °C the reverse transition to form I occurs, although is not possible to separate the reverse transition of form II and form III; f) 50 °C end of cooling. The red bar indicating the scale correspond to 100 μm.

Upon heating, the transition I→II occurs at around 200 °C as expected from DSC (Figure 5b) with clearly visible changes, whereas the II → III transition, which occurs between 250 and 265 °C, causes only slight changes in the crystal shape (Figure 5c). Upon cooling, no changes are observed until 114°C when the crystals undergo a rapid solid-solid transition which is characterized by a clearly visible transition front that propagates throughout the crystal coupled with a dramatic shape change that makes the crystals move on the stage; such behavior is typically associated to martensitic-like

transitions exhibiting thermosalient behavior.[28–31] Considering that at 114°C form I is the stable form and only one solid-state transition is observed, we presume that the transition observed is form III→I. A similar martensitic-like transition upon cooling was also observed in the case of PDI-C5.[27]

PDI-C7. Single crystals of PDI-C7 were heated up to 280 °C, to observe the macroscopic changes correlated to the transition into from II and form III (see Figure 6).

HEATING
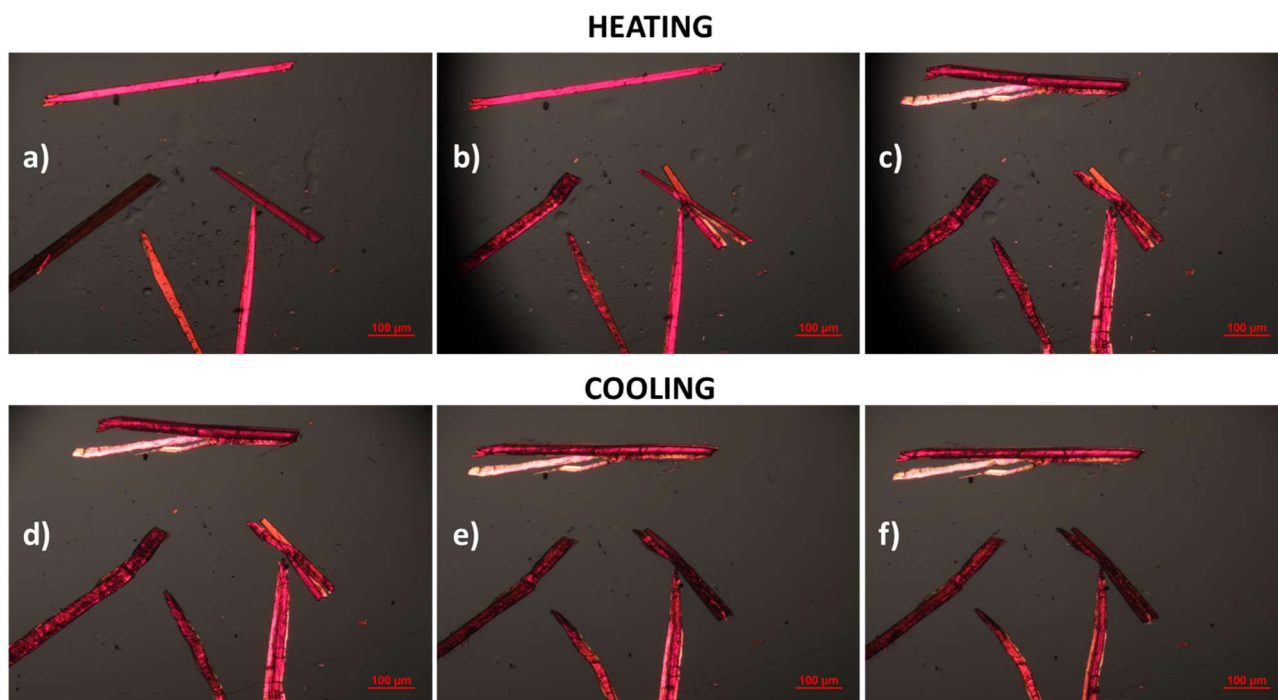
COOLING

Figure 6. HSM of PDI-C7 crystals: a) 30 °C start of experiment; b) 212 °C beginning of the I → II transition; c) 215°C the transition is complete; d) 275 °C no further macroscopic changes that could be addressed to the II → III phase were observed, the cooling was started; e) 102 °C the II → I reverse transition occurs; f) 50 °C end of cooling. The red bar indicating the scale correspond to 100 μm.

Upon heating, the transition I-II occurs at 212°C as expected from DSC (Figure 6b, c), whereas no significant changes were observed that could be correlated with the II → III transition. Upon cooling the reverse transition of form II to form I occurs at 102 °C (Figure 6f) a dramatically lower temperature compared to DSC. The transitions, especially upon cooling, cause crystal breaking and fragmentation.

PDI-C8. Single crystals of PDI-C8 were heated up to 260 °C, to observe the macroscopic changes correlated to the transition to from II (see Figure 7).
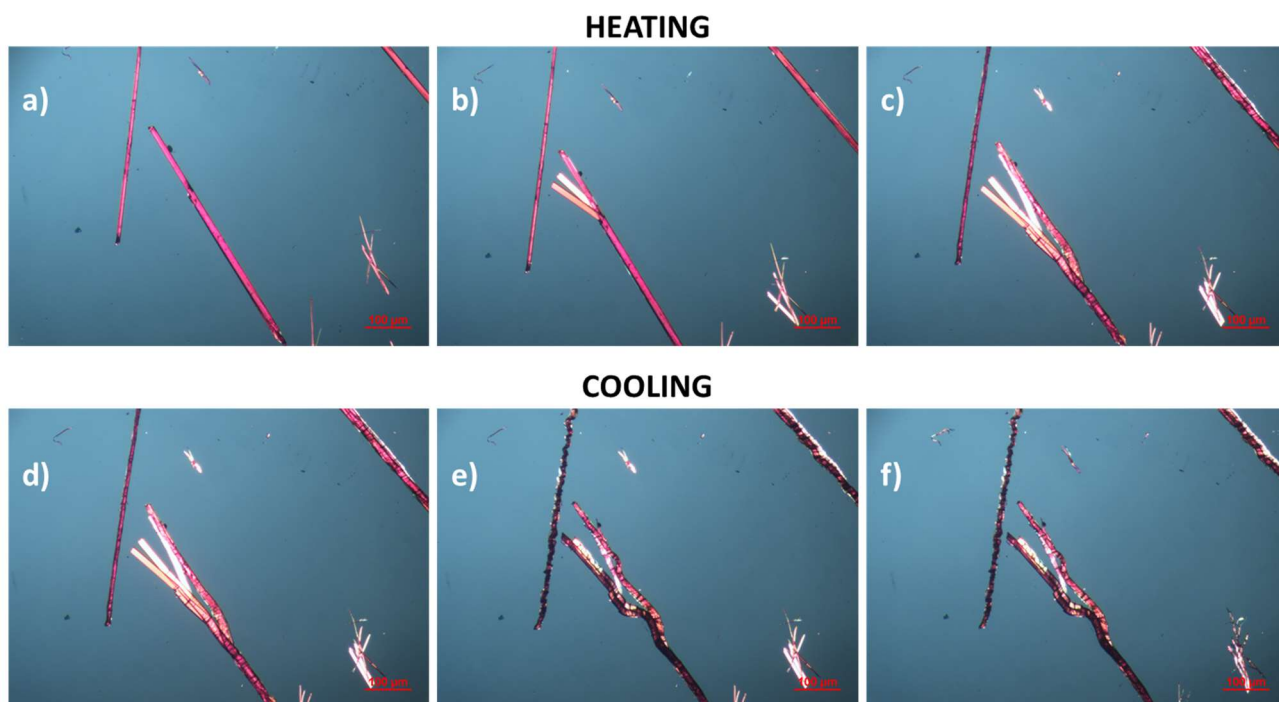
Figure 7. HSM of PDI-C8 crystals: a) 30 °C start of experiment; b) 223 °C beginning of the I → II transition; c) 230°C the transition is complete; d) 250 °C the cooling was started; e) 187 °C the II → I reverse transition occurs; f) 50 °C end of cooling. The red bar indicating the scale correspond to 100 μm.

Upon heating, the transition I-II occurs at 223 °C as expected from DSC (Figure 7b), and upon cooling the reverse transition occurs as at 187 °C (Figure 7f), slightly lower temperature compared to DSC. The transitions, especially upon cooling, cause crystal breaking and fragmentation, as observed for PDI-C8.

Variable temperature X-ray powder diffraction

In order to investigate the structural changes that occur during transitions, variable temperature X-ray powder diffraction (VTXRPD) experiments were carried out at ALBA Synchrotron on all the PDI-Cn.

PDI-C6. The VTXRPD patterns of PDI-C6 upon heating and cooling are reported in Figure 8. This experiment highlights the structural changes that occur with the solid-state transitions observed in DSC. Upon heating, a phase transition ascribable to the I → II transition is observed between 180 and 205 °C, while a second transition ascribable to II → III transition is observed between 225 and 255 °C. Upon cooling, we observe that form III tends to convert back to form I when cooled below 140 °C. The scenario in VTXRD is in some way different from those observed in DSC. In VTXRD a higher hysteresis of the reverse transitions was observed with respect to the DSC curve. Furthermore, in VTXRD we cannot distinguish the III → II and the II → I transition as in DSC; in addition, the transition to form I is not completed at RT, highlighted by some peaks of the HT forms that are still present at the end of the cooling step. This slightly different behavior is probably the result of the

different sample preparation (the powder was further ground for XRD measurements) and from different environmental conditions (N_2 purge during DSC measurement). Lastly, PDI-C6 VTXRD highlights a severe shift of the diffracted peaks due to thermal expansion as observed for PDI-C5.
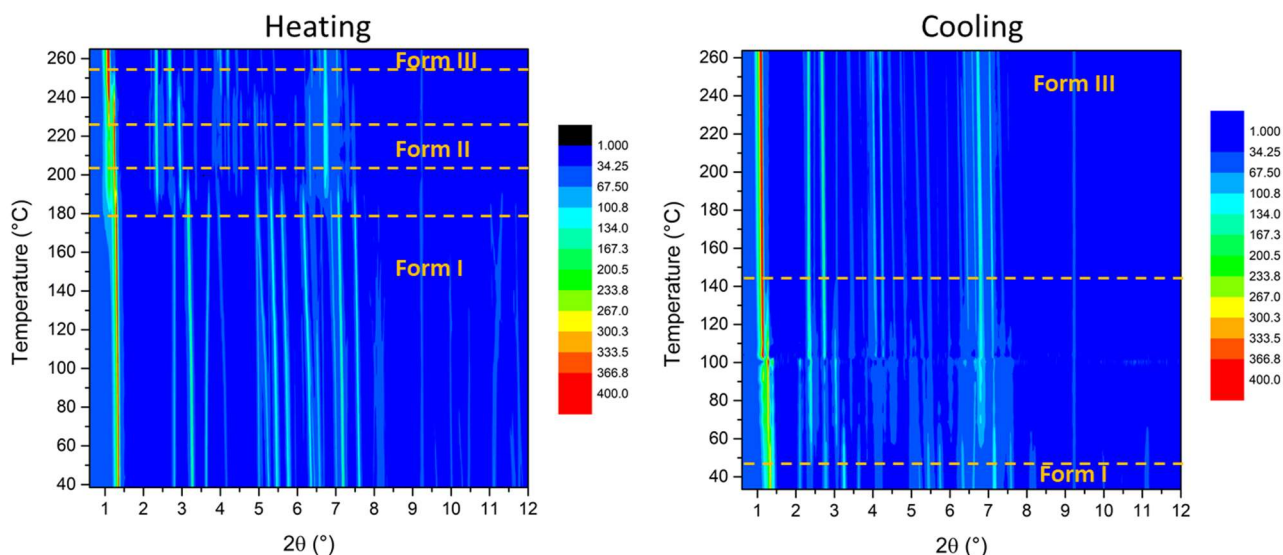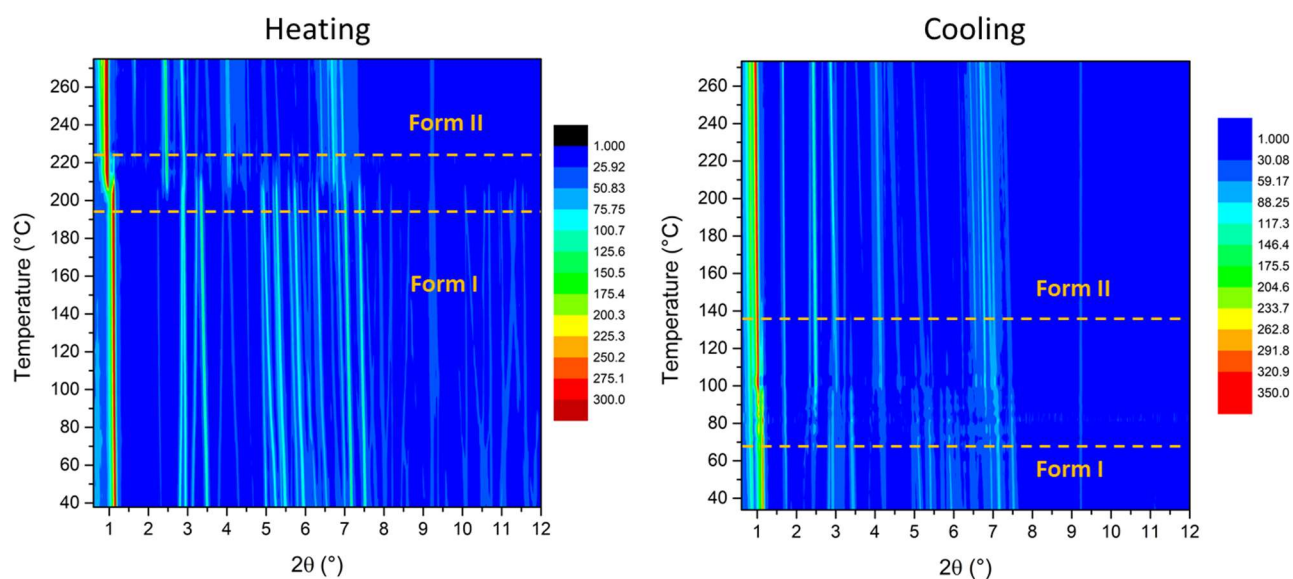

Figure 8. VTXRPD experiment of PDI-C_6 upon heating (left) and cooling (right). Upon heating, drastic changes in the pattern can be observed between 180 and 205 °C ascribable to the transition from form I to form II; then, changes in the pattern can be observed also between 225 °C and 255 °C, where a second solid-solid transition ascribable to the formation of form III occurs. Upon cooling, form III tends to convert back to form I below 140 °C, showing high hysteresis of the transition. In this case, it was not possible to separate the III → II and the II → I transitions; furthermore, the transition to form I is not completed at RT and some peaks of HT forms are still present after cooling. Intensity is plotted in square root scale for the sake of clarity.

PDI-C7. The VTXRPD patterns of PDI-C7 upon heating and cooling are reported in Figure 9. This experiment highlights the structural changes that occur with the solid-state transitions observed in DSC. Upon heating, a first solid-state transition ascribable to the I → II phase transition is observed between 190 and 215 °C, while a second transition ascribable to the II → III transition is observed between 225 and 240 °C, these temperatures correlate with the ones observed in DSC. Upon cooling, we observe that the two transitions observed in heating are reversible and distinguishable; in fact, the transition ascribable to the III → II is observed below 225 °C, with small hysteresis, slightly higher to the hysteresis observed in DSC, while the transition ascribable to the II → I transition is observed below 140 °C, with a high hysteresis of transition. However, the hysteresis observed for II → I transition in VTXRD is considerably higher compared to the one observed in DSC (about 35 °C), which probably result from the different sample preparation (the powder was further ground for XRD measurements) and from different environmental conditions (N_2 purge during DSC measurement). The severe shift of the diffracted peaks due to thermal expansion was observed also in the PDI-C7 VTXRD case.
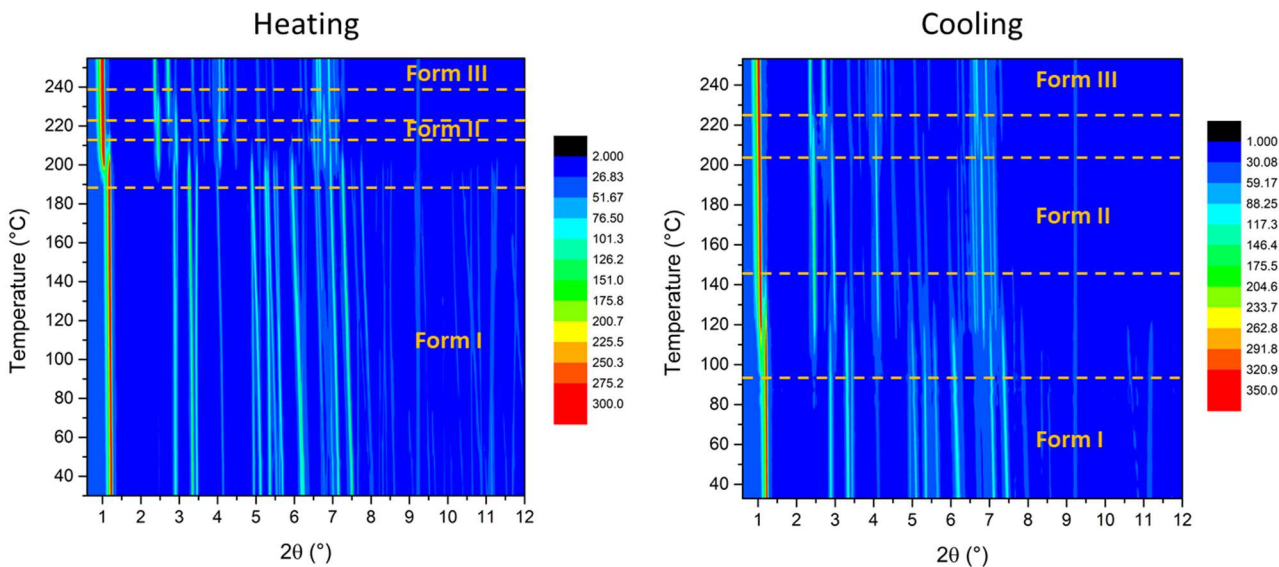
Figure 9. VTXRPD experiment of PDI-C7 upon heating (left) and cooling (right). Upon heating, drastic changes in the pattern can be observed between 190 and 215 °C where the transition ascribable to the transition from form I to form II lies; then, small changes in the pattern can be observed between 225 °C and 240 °C, where a second solid-solid transition ascribable to the formation of form III occurs. Upon cooling, form III converts back to form II below 225 °C, showing low hysteresis of the II → III transition, while the II → I transition occurs below 145 °C with a higher hysteresis. Intensity is plotted in square root scale for the sake of clarity.

PDI-C8. The VTXRPD patterns of PDI-C8 upon heating and cooling are reported in Figure 10. This experiment highlights the structural changes that occur with the solid-state transitions observed in DSC. Upon heating, a solid-state transition ascribable to the I → II phase transition is observed between 200 and 224 °C, in accord with DSC. Upon cooling, the II → I transition is observed below 140 °C, highlighting a high hysteresis of the reverse transition. Even in the PDI-C8 case, the hysteresis observed in VTXRD is considerably higher compared to the one observed in DSC (about 50 °C), which probably result from the different sample preparation (the powder was further ground for XRD measurements) and from different environmental conditions (N_2 purge during DSC measurement). Furthermore, as well as in other PDI-Cn cases, a severe shift of the diffracted peaks due to thermal expansion was observed in VTXRPD.

Figure 10. VTXRPD experiment of PDI-C$_8$ upon heating (left) and cooling (right). Upon heating, drastic changes in the pattern can be observed between 200 and 224 °C ascribable to the transition from form I to form II. Upon cooling, form II converts back to form I below 140 °C, showing high hysteresis of the transition. Intensity is plotted in square root scale for the sake of clarity.

High-Temperature polymorphs indexing

Even though it was not possible to isolate the HT forms at RT due to reverse transition, after assessing the temperature at which the transitions to HT polymorphs occur, we collected the PXRD of each HT polymorph in isothermal conditions in the temperature range of its stability. Despite the high temperature at which the PDI-Cn HT polymorphs data are available in this way, we attempted to index and solve their crystal structure from powder to have more information on the changes these materials undergo with temperature, as we did in our previous work on PDI-C5.[27] However, despite our efforts, we were able to only index some of their unit cells. The high temperature of the collection (over 200 °C) and probably the high level of disorder present in the crystal at these temperatures hindered the feasibility of the structure solution. The cell parameters of the indexed phases are reported in Table 3.

As commonly used, the cell found are validated by comparing the molecular volume. Since the patterns are collected at high temperatures and since these materials present high thermal expansion, we expect considerably higher volumes compared to the ones observed at RT. Therefore, the accepted volumes are higher and the densities lower than the structures collected at RT. All the indexed unit cells were found in a triclinic space group. From our knowledge of PDI-Cn and considering the molecules are symmetrically functionalized, we expect triclinic cells to be P-1, although the confirmation of the space group can be obtained only by the structure determination.

PDI-C6 shows two transitions upon heating at 197 °C and 255 °C. Therefore, we collected and indexed the patterns at 226 °C for form II and 265 °C for form III, the temperature at which we assessed that the transition was completed.

PDI-C6 form II 226 °C. Despite several indexing attempts on this pattern, it was not possible to define unambiguously a unit cell; only Z > 2 with P-1 space group cells.

PDI-C6 form III 265 °C. We were able to successfully index PDI-C6 form III using TOPAS. The unit cell found has a volume of 1659 Å^3, which agrees with 2 molecules in the cell, corresponding to a Z = 2, which results in a Z' = 1 for a P-1 space group, and an estimated density of 1.12 g/cm^3. Unit cell parameters refined using Pawley refinement, are reported in Table 3. The Pawley refinement of PDI-C6 at 265 °C, displaying the experimental and calculated pattern together with the difference pattern is shown in Figure S5.

PDI-C7 shows two transitions upon heating at 213 °C and 237°C. Therefore, we collected and indexed the patterns at 218 °C for form II and 255 °C for form III, the temperature at which we assessed that the transitions were completed.

PDI-C7 form II 218 °C. We were able to successfully index PDI-C7 form II at 218 °C using EXPO software.[32] The unit cell found has a volume of 2455 Å^3, which agrees with 3 molecules in the cell, corresponding to a Z = 3, which results in a Z' =1.5 for a P-1 space group (similar to C5 form III case), and estimated density of 1.19 g/cm^3. The unit cell parameters refined using Pawley refinement in TOPAS, are reported in Table 3. The Pawley refinement of PDI-C7 form II at 218 °C, showing the experimental and calculated pattern together with the difference pattern is shown in Figure S6.

PDI-C7 form III 255 °C. We were able to successfully index PDI-C7 form III at 255 °C using TOPAS. The unit cell found has a volume of 1774 Å^3, which agrees with 2 molecules in the cell, corresponding to a Z = 2, which results in a Z' =1 for a P-1 space group, and an estimated density of 1.10 g/cm^3. The unit cell parameters refined using Pawley refinement in TOPAS, are reported in Table 3. The Pawley refinement of PDI-C7 form III at 255 °C, showing the experimental and calculated pattern together with the difference pattern is shown in Figure S7.

PDI-C8 shows a transition upon heating at 217 °C. Therefore, we collect and index the patterns at 224 °C. By observing the VTXRPD of PDI-C8, we observed that even after this transition was completed, some changes in the pattern were observed when the temperature was further increased, which comprises mainly the appearance of two peaks at small 2θ values.

PDI-C8 form II 224 °C. We were able to successfully index PDI-C8 form II at 224 °C using EXPO software, however, two peaks were omitted with the unit cell found. The intensity of the unindexed

peaks (0.806 and 1.660 of 2θ) increases upon further increasing the temperature and suggests the possible presence of another phase. The unit cell found has a volume of 1880 Å^3, which agrees with 2 molecules in the cell, corresponding to a Z = 2, which results in a Z' =1 for a P-1 space group, and an estimated density of 1.09 g/cm^3. The unit cell parameters refined using Pawley refinement in TOPAS, are reported in Table 3. The Pawley refinement of PDI-C7 form III at 255 °C, showing the experimental and calculated pattern together with the difference pattern is shown in Figure S8.

Table 3. Cell parameters of the indexed HT polymorphs of PDI-Cn refined by Pawley refinement.

	PDI-C6	PDI-C7		PDI-C8
Temperature (°C)	265	218	255	224
Form	III	II	III	II
SG	$P\bar{1}$	$P\bar{1}$	$P\bar{1}$	$P\bar{1}$
a (Å)	7.681(3)	10.790(9)	7.696(2)	7.738(1)
b (Å)	10.130(1)	11.067(5)	10.088(1)	9.979(2)
c (Å)	21.504(2)	23.202(4)	23.117(2)	24.783(3)
α (Å)	84.47(2)	94.03(5)	81.86(2)	83.92(2)
β (Å)	85.11(5)	97.84(5)	86.73(3)	81.17(2)
γ (Å)	90.46(4)	115.35(5)	89.86(3)	88.96(2)
V (Å^3)	1659	2455	1774	1880
Z	2	3	2	2
Z'	1	1.5	1	1
Density (g/cm^3)	1.12	1.19	1.10	1.09
Rwp	4.65	4.09	4.17	3.79
Rp	3.13	2.63	2.50	2.62

Interestingly, the indexed unit cells of PDI-C6 form III, PDI-C7 form III, and PDI-C8 form II have some common traits, in a similar way to what was observed with the cell parameters of form I of the three materials. The *a*- and *b*-axis are again quite similar, while the *c*-axis is longer in the case of longer chains. However, without the crystal structure is not possible to further discuss these crystal forms.

Thermal Expansion

As before mentioned, a severe shift of the diffracted peaks due to thermal expansion was observed in VTXRPD. For this reason, we performed a sequential Rietveld refinement on PDI-Cn form I, to observe the variation of its crystal structure parameters with temperature and to investigate the thermal expansion of these materials. Then, after obtaining the crystal structure parameters at variable temperature from Rietveld refinement over PDI-Cn XRD data, we used the software PASCal (Principal Axis Strain Calculations)[33] to quantify the observed thermal expansion effect on PDI-Cn form I. From variable temperature lattice parameter data as input, PASCal calculates in linear approximation and returns as output the principal axis expansivities, the orientation of the principal axes relative to the crystallographic axes, and the expansivity indicatrix. The expansivity indicatrix is the visual representation of the material's thermal expansivity tensor and is constructed as a

smoothly varying surface centered at the unit-cell origin, where the distance between the surface and the origin in each direction is equal to the magnitude of α (linear thermal expansion coefficient) in that direction.

Starting from the results obtained with sequential Rietveld refinement over PDI-C6 VTXRPD patterns (Figure 11), it is clear that above 180 °C the transition to form II occurs since the R_{wp} rapidly increases above that temperature, indicating a worsening of the match between calculated and experimental pattern. Furthermore, the volume increases rapidly with temperature, indicating once again the high thermal expansion of this material.
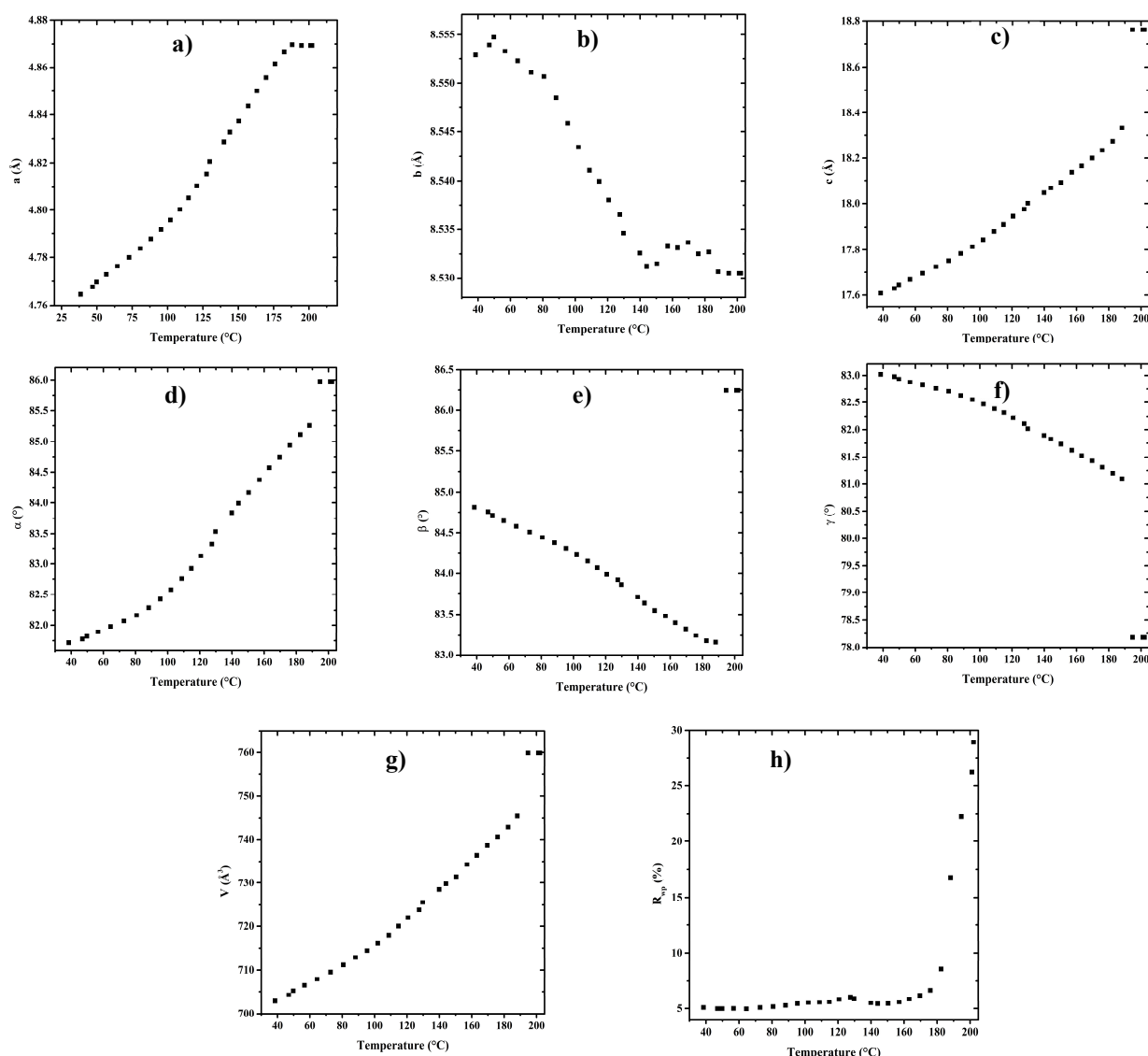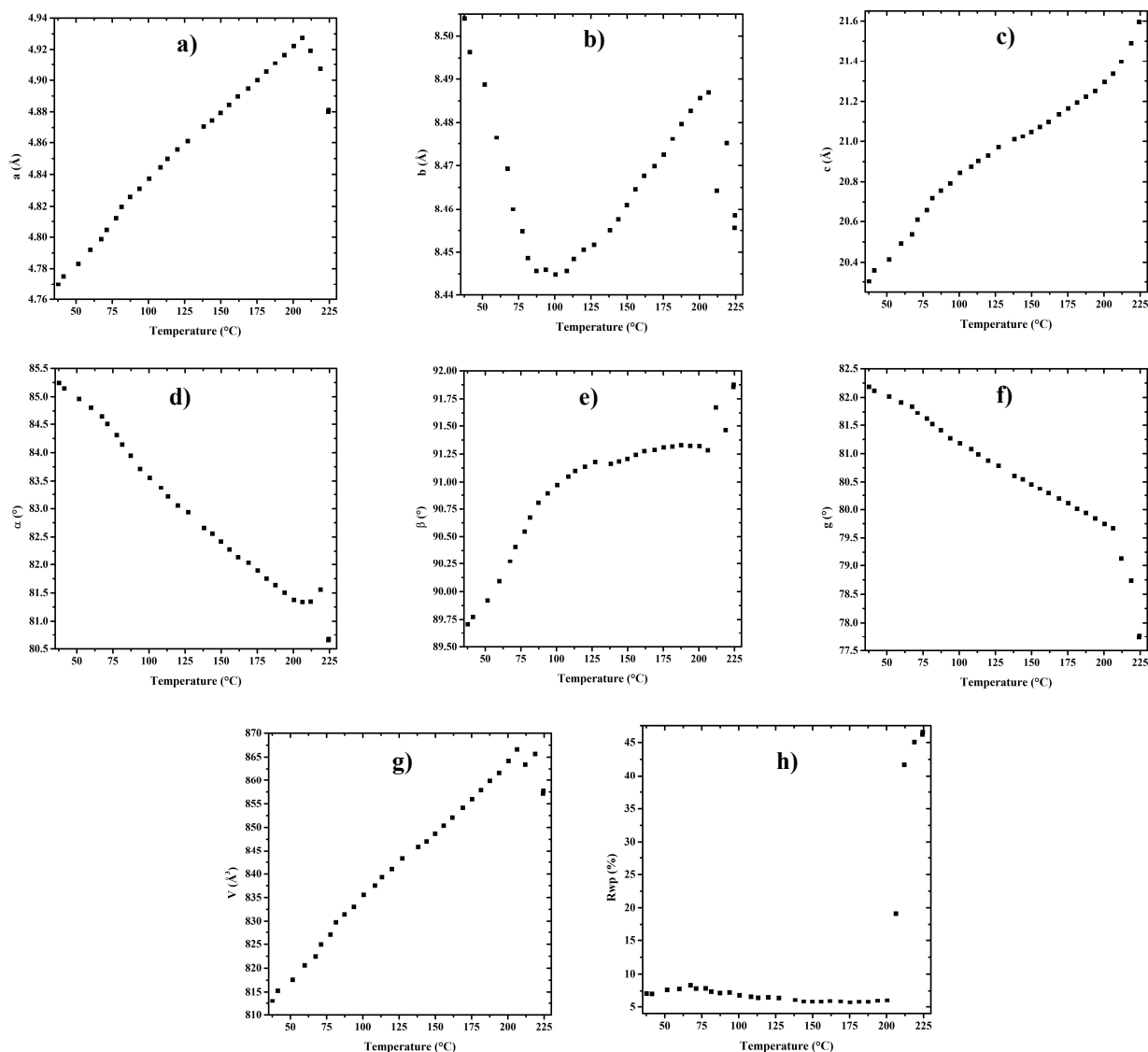

Figure 11. Sequential Rietveld refinement of PDI-C6 form I, variation of unit cell parameters in the temperature range 30 – 205 °C. a) a-axis with T; b) b-axis with T; c) c-axis with T; d) α with T; e) β with T; f) γ with T; g) volume with T; h) R_{wp} with T. The discontinuity in the trend of unit cell parameter with temperature, which indicates the transition to form II, is observed above 180 °C.

The crystal structure parameters of PDI-C6 form I at different temperatures obtained by Rietveld refinement were then used to investigate the thermal expansion of this material with PASCal.

Linear coefficients of thermal expansion and corresponding principal axes determined for PDI-C6 form I are listed in Table 4 and the relative expansivity indicatrix is shown in Figure 12.

Table 4. Linear thermal expansion coefficients along the corresponding principal axes and volumetric thermal expansion coefficient calculated using PASCal for PDI-C6 form I in the range of temperature between 38 and 176 °C; a, b, c gives the orientation of the principal axis with respect to the unit cell axes.

| Axes	α_i [10^{-6} K^{-1}]	$\sigma\alpha$ [10^{-6} K^{-1}]	a	b	c
X_1	-203	9	-0.7457	0.6481	0.1544
X_2	192	8	0.9552	0.2941	-0.0330
X_3	416	13	0.5518	-0.5750	0.6040
V	400	11			
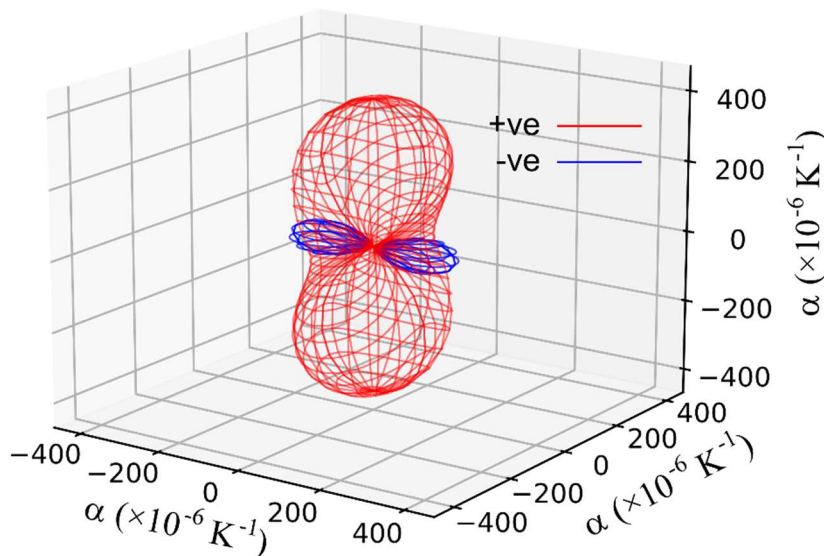
Figure 12. Expansivity indicatrix of PDI-C$_6$ form I determined using the PASCal program, showing the spatial orientation of positive (red) and negative (blue) thermal expansion.

PDI-C6 form I shows a large NTE (negative thermal expansion) along the principal axis X_1, which is probably to compensate for the large positive thermal expansion along the X_2 and X_3 principal axis. The overall effect is a large thermal expansion α_V of about 400 MK^{-1} (the mean value for volumetric thermal expansion of organic compounds is α_V = 168.6 MK^{-1}, with a standard deviation σ of 72.5 MK^{-1});[34] therefore, in the range of temperature investigated (38 – 176 °C), the overall volume increase is about 5.4 % of the initial volume. This large thermal expansion effect is reflected in the observed shift of the diffracted peaks with temperature.

Second, from the results obtained with sequential Rietveld refinement over PDI-C7 VTXRPD patterns (Figure 13), it is clear that above 190 °C the transition occurs since the R_{wp} rapidly increases above that temperature, indicating a worsening of the match between calculated and experimental pattern. Furthermore, the volume increases rapidly with temperature, indicating once again the high thermal expansion of this material.
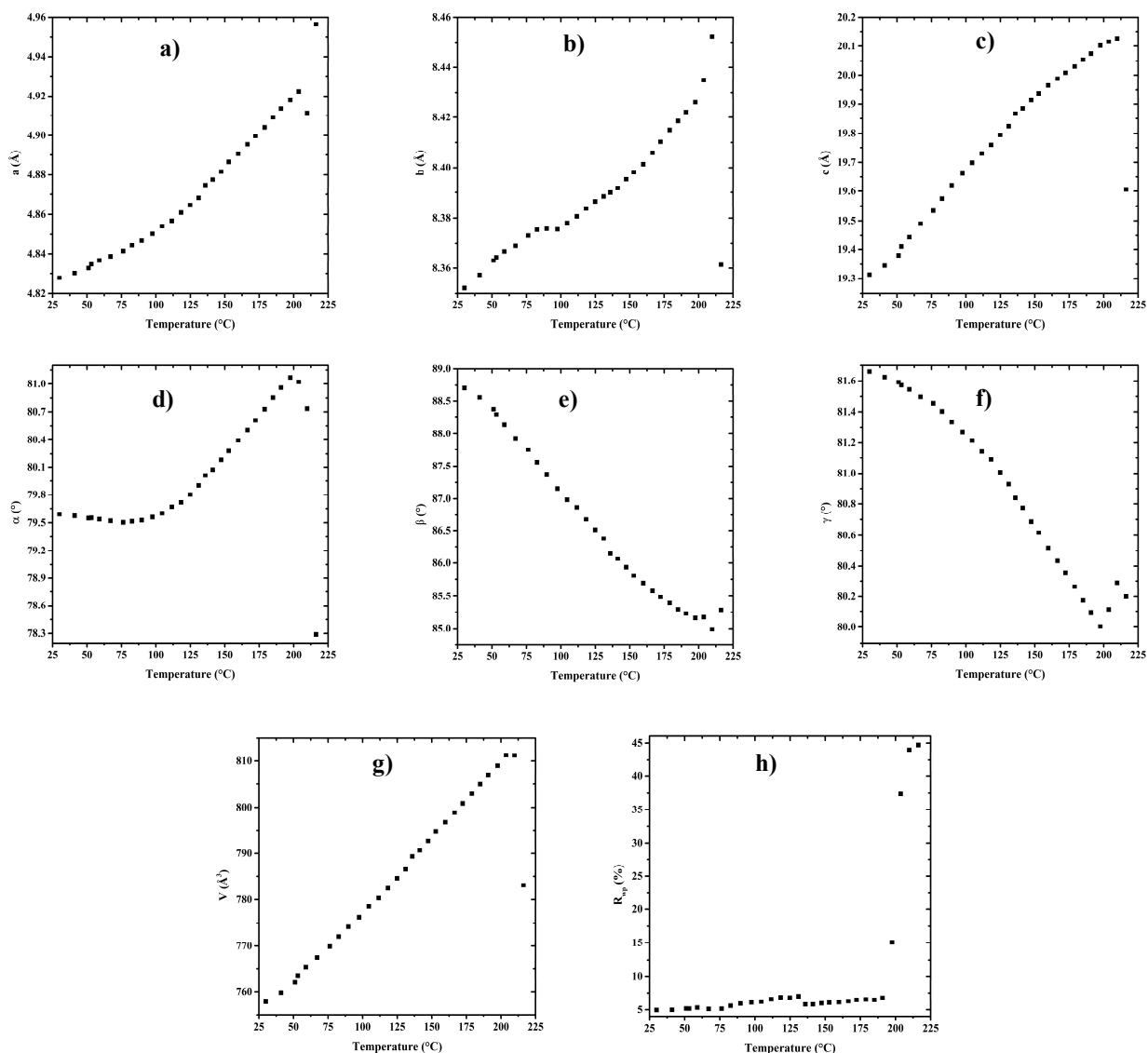
Figure 13. Sequential Rietveld refinement of PDI-C7 form I, variation of unit cell parameters in the temperature range 25 – 225 °C. a) a-axis with T; b) b-axis with T; c) c-axis with T; d) α with T; e) β with T; f) γ with T; g) volume with T; h) R_{wp} with T. The discontinuity in the trend of unit cell parameter with temperature, which indicates the transition to form II, is observed above 190 °C.

The crystal structure parameters at different temperatures obtained by Rietveld refinement were then used to investigate the thermal expansion of this material with PASCal.

Linear coefficients of thermal expansion and corresponding principal axes determined for PDI-C7 form I are listed in Table 5 and the relative expansivity indicatrix is shown in Figure 14.

Table 5. Linear thermal expansion coefficients along the corresponding principal axes and volumetric thermal expansion coefficient calculated using PASCal for PDI-C7 form I in the range of temperature between 30 and 191 °C; a, b, c gives the orientation of the principal axis with respect to the unit cell axes.

Axes	α_i [10^{-6} K^{-1}]	$\sigma\alpha$ [10^{-6} K^{-1}]	a	b	c
X_1	-113	4	-0.9534	0.2690	0.1366
X_2	118	9	0.4297	0.8954	-0.1167
X_3	411	5	0.9212	-0.1256	0.3683
V	414	4			
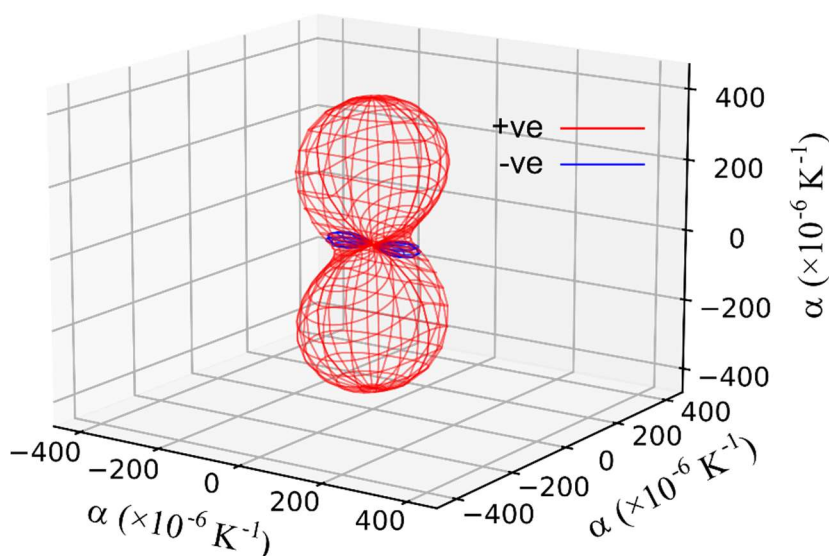
Figure 14. Expansivity indicatrix of PDI-C7 form I determined using the PASCal program, showing the spatial orientation of positive (red) and negative (blue) thermal expansion.

PDI-C7 form I shows a large NTE (negative thermal expansion) along the principal axis X_1, which is probably to compensate for the large positive thermal expansion along the X_2 and X_3 principal axis. The overall effect is a large thermal expansion $\alpha_V > 400$ MK^{-1}, which means that in the range of temperature investigated (30 – 191 °C) the overall volume increase is about 6.5% of the initial volume. This large thermal expansion effect is reflected in the observed shift of the diffracted peaks with temperature.

Lastly, from the results obtained with sequential Rietveld refinement over PDI-C8 VTXRPD patterns (Figure 15), it is clear that above 200 °C the transition occurs since the R_{wp} rapidly increases above that temperature, indicating a worsening of the match between calculated and experimental pattern. Furthermore, the volume increases rapidly with temperature, indicating once again the high thermal expansion of this material.

Figure 15. Sequential Rietveld refinement of PDI-C$_8$ form I, variation of unit cell parameters in the temperature range 35 – 230 °C. a) a-axis with T; b) b-axis with T; c) c-axis with T; d) α with T; e) β with T; f) γ with T; g) volume with T; h) R$_{wp}$ with T. The discontinuity in the trend of unit cell parameter with temperature, which indicates the transition to form II, is observed above 200 °C.

The crystal structure parameters at different temperatures obtained by Rietveld refinement were then used to investigate the thermal expansion of this material with PASCal.

Linear coefficients of thermal expansion and corresponding principal axes determined for PDI-C8 form I are listed in Table 6 and the relative expansivity indicatrix is shown in Figure 16.

Table 6. Linear thermal expansion coefficients along the corresponding principal axes and volumetric thermal expansion coefficient calculated using PASCal for PDI-C8 form I in the range of temperature between 35 and 200 °C; a, b, c gives the orientation of the principal axis with respect to the unit cell axes.

Axes	α_i [10^{-6} K^{-1}]	$\sigma\alpha$ [10^{-6} K^{-1}]	a	b	c
X$_1$	-236	10	-0.6627	0.7323	-0.1568
X$_2$	247	2	0.9537	0.2947	0.0599
X$_3$	378	15	-0.8623	0.2827	0.4202
V	376	5			
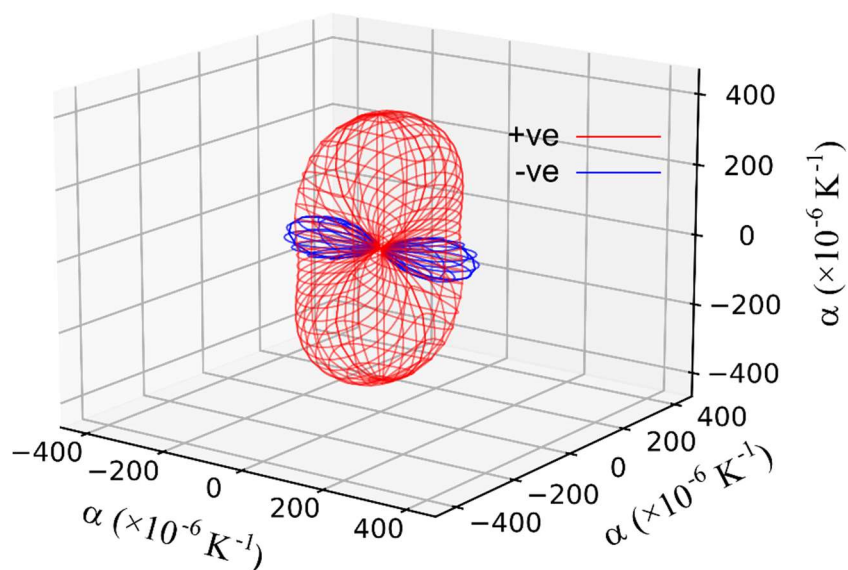
Figure 16. Expansivity indicatrix of PDI-C8 form I determined using the PASCal program, showing the spatial orientation of positive (red) and negative (blue) thermal expansion.

PDI-C8 form I shows a large NTE (negative thermal expansion) along the principal axis X_1, which is probably to compensate for the large positive thermal expansion along the X_2 and X_3 principal axis. The overall effect is a large thermal expansion $\alpha_V > 350$ MK^{-1}, which means that in the range of temperature investigated (35 – 200 °C) the overall volume increase is about 6.3% of the initial volume. This large thermal expansion effect is reflected in the observed shift of the diffracted peaks with temperature.

Figure 17 shows the packing of PDI-C6, -C7, and -C8 with indicated the directions of the thermal expansion principal axes. Overall, the direction of the three principal axes is similar in the three structures, which was expected given the similarity of these crystal structures.
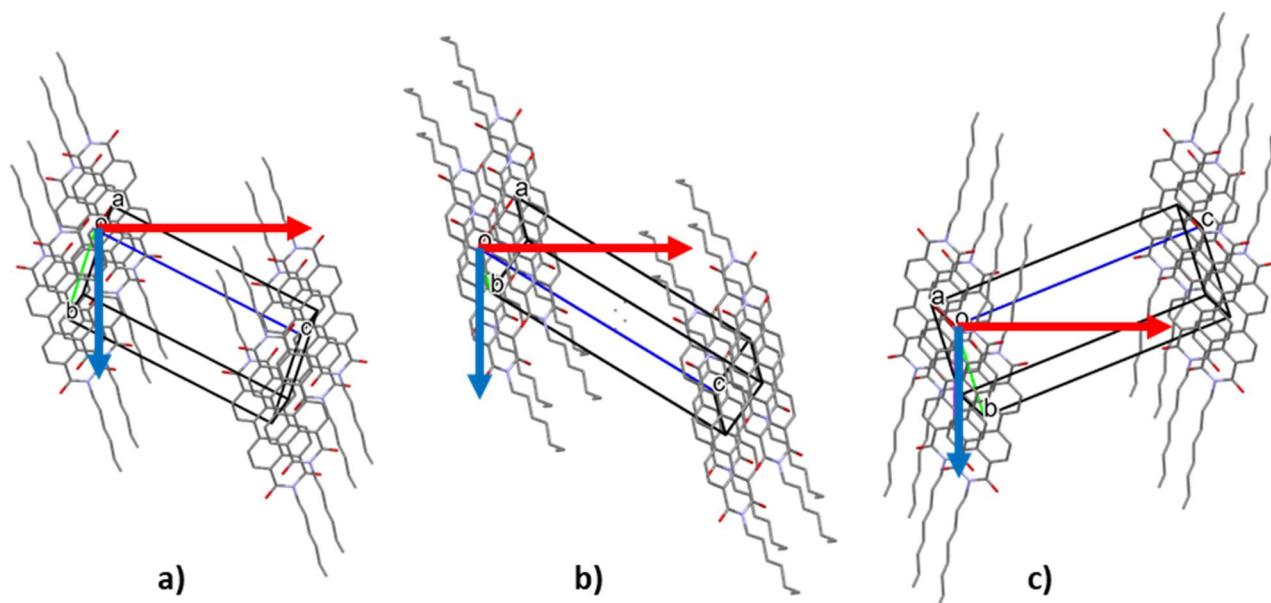
Figure 17. Packing of the PDI-Cn form I structures a) PDI-C6, b) PDI-C7 and c) PDI-C8 with indicated the orientation of the thermal expansion principal axes calculated by PASCal: X_2 is perpendicular to the figure, while X_1 is indicated by the blue arrow and X_3 is indicated by the red arrow.

PDI-Cn at High-Pressure

UV-Vis-NIR measurements

The variation of the absorption spectra of the material upon increasing pressure can be an important index to investigate the changes that occur in the material. In particular, the investigation of the absorption edge upon compression allows identifying the possible pressure-induced phase transition and if these transformations are reversible upon releasing pressure. The absorption measurements were thus carried out on all PDI-Cn upon increasing and releasing pressure.

The absorption measurements of the PDI-C5 upon increasing pressure are shown in Figure 18 and the related macroscopic color changes are shown in Figure 19. These measurements highlight a significant red-shift of the absorption spectra with compression and consequently, the PDI-C5 film color tends to darken from red to black.
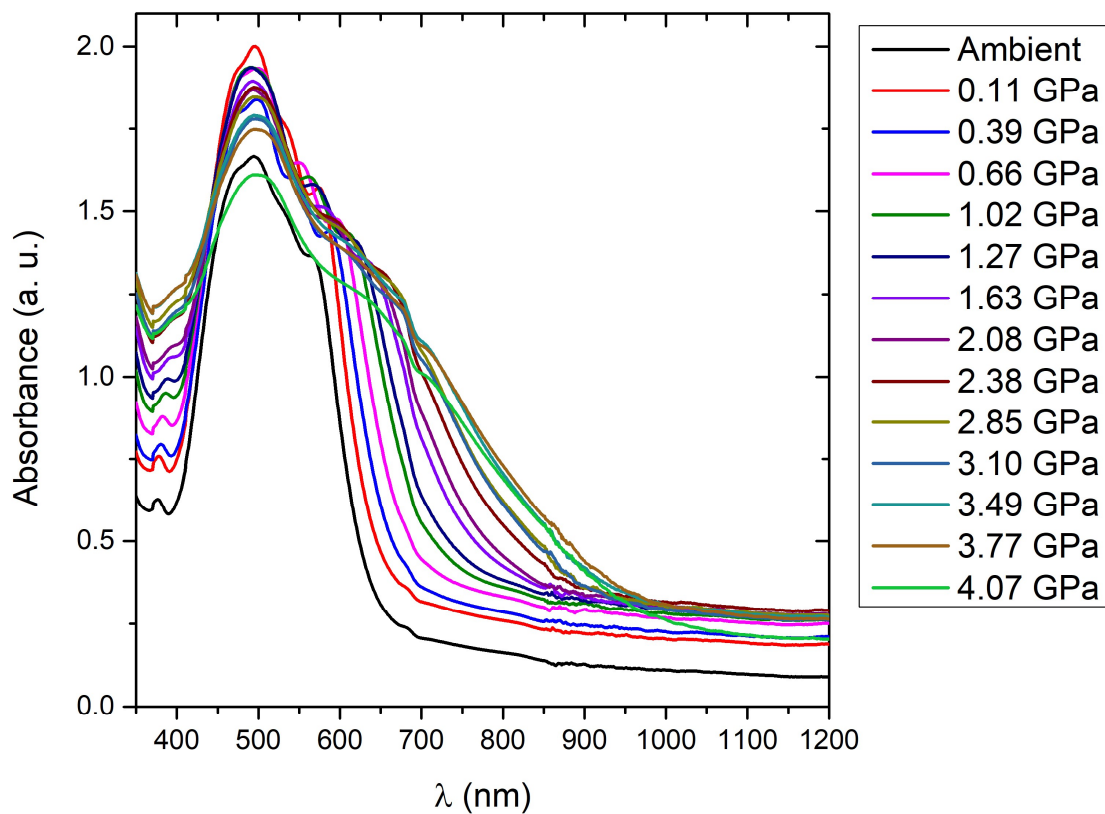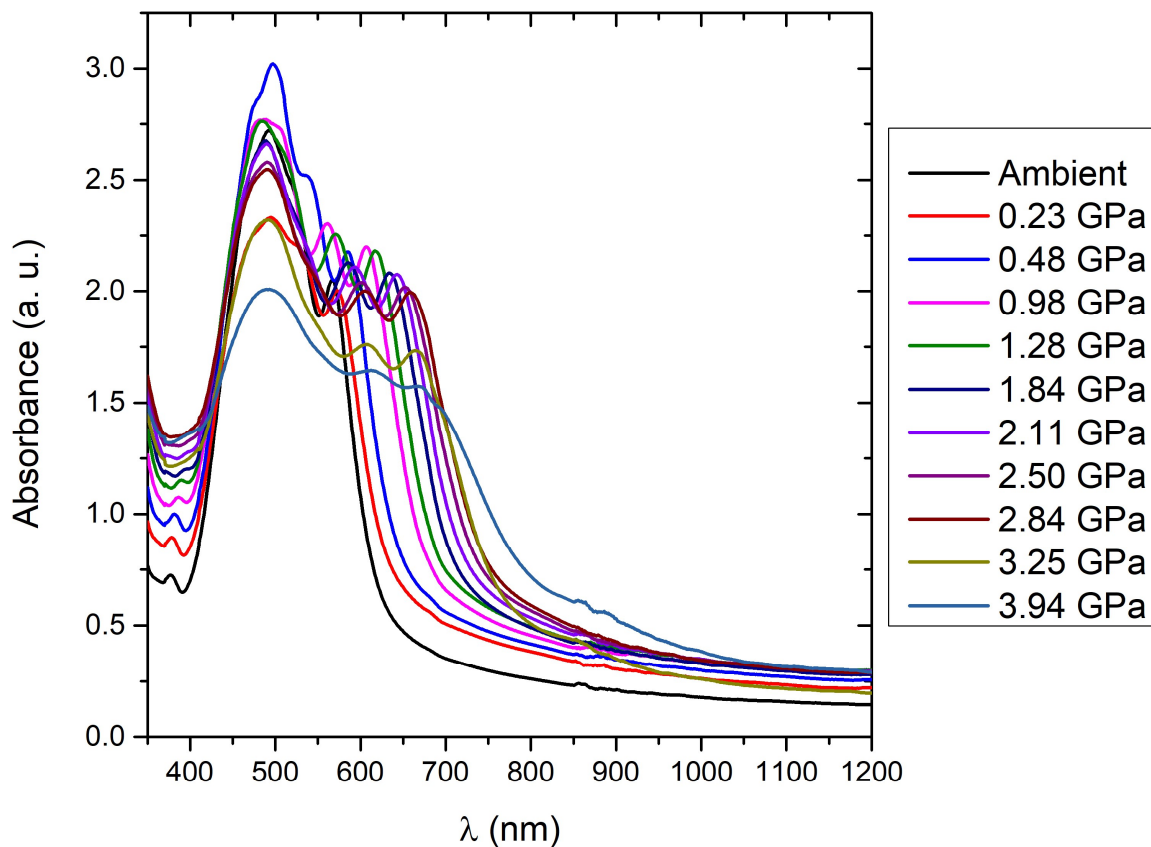
Figure 18. UV-Vis-NIR absorption spectra of PDI-C5 upon increasing pressure.
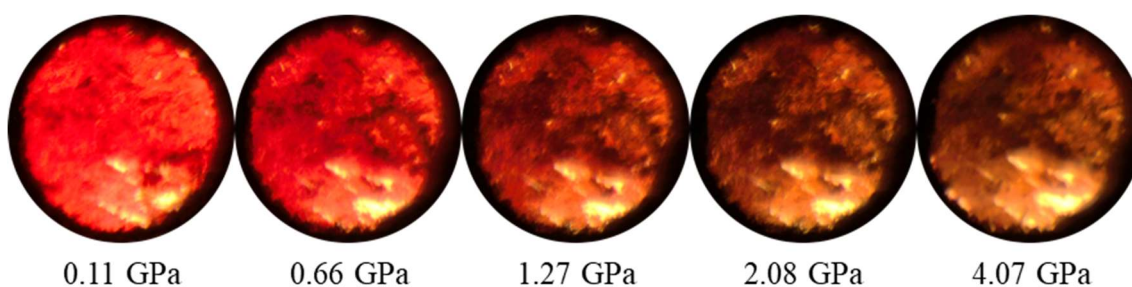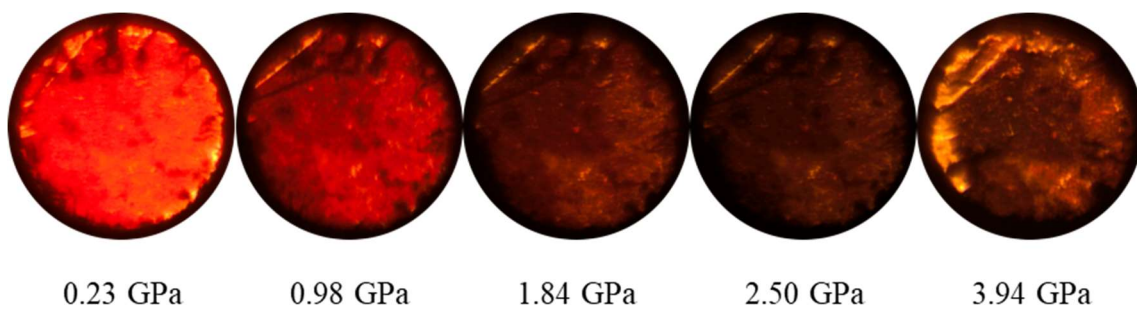

Figure 19. Images of PDI-C5 film with increasing pressure.

The red-shift of the absorption spectra resulted to be reversible upon releasing pressure (Figure S9) and consequently, the color returns red when pressure is released (Figure 20).
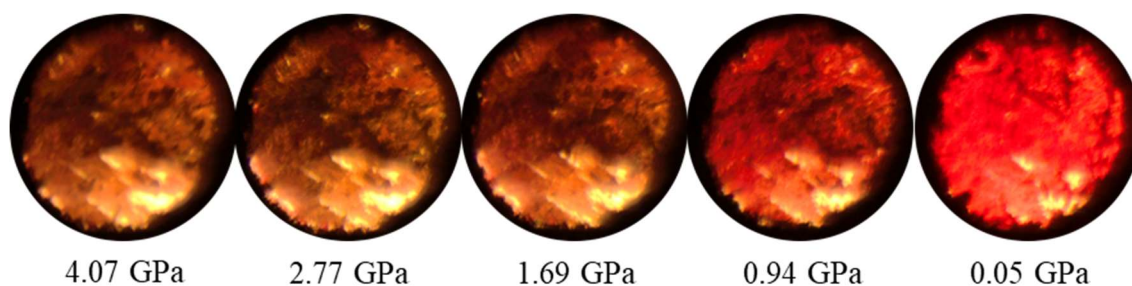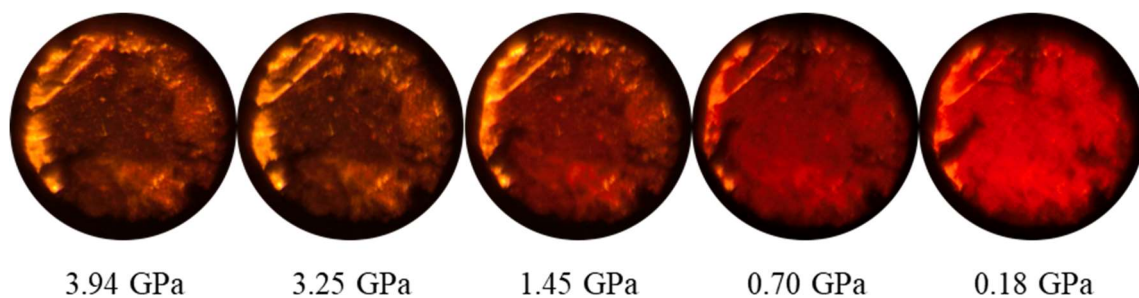

Figure 20. Images of PDI-C5 film upon releasing pressure.

The absorption edges at different pressure were extrapolated from the absorption spectra and listed in Table 7; furthermore, the variation of absorption edge with pressure is shown in Figure 21.

Table 7. Variation of the absorption edge of PDI-C5 with increasing and releasing pressure.

INCREASING PRESSURE			RELEASING PRESSURE		
Pressure (GPa)	Absorption Edge (nm)	Absorption Edge (cm^{-1})	Pressure (GPa)	Absorption Edge (nm)	Absorption Edge (cm^{-1})
Ambient	635	15700	4.07	913	11000
0.11	641	15600	3.3	870	11500
0.39	661	15100	2.77	832	12000
0.66	679	14700	2.16	799	12500
1.02	704	14200	1.69	756	13200
1.27	719	13900	0.95	707	14100
1.63	748	13400	0.05	640	15600
2.08	789	12700			
2.38	812	12300			
2.85	837	11900			
3.1	846	11800			
3.49	875	11400			
3.77	899	11100			
4.07	913	11000			
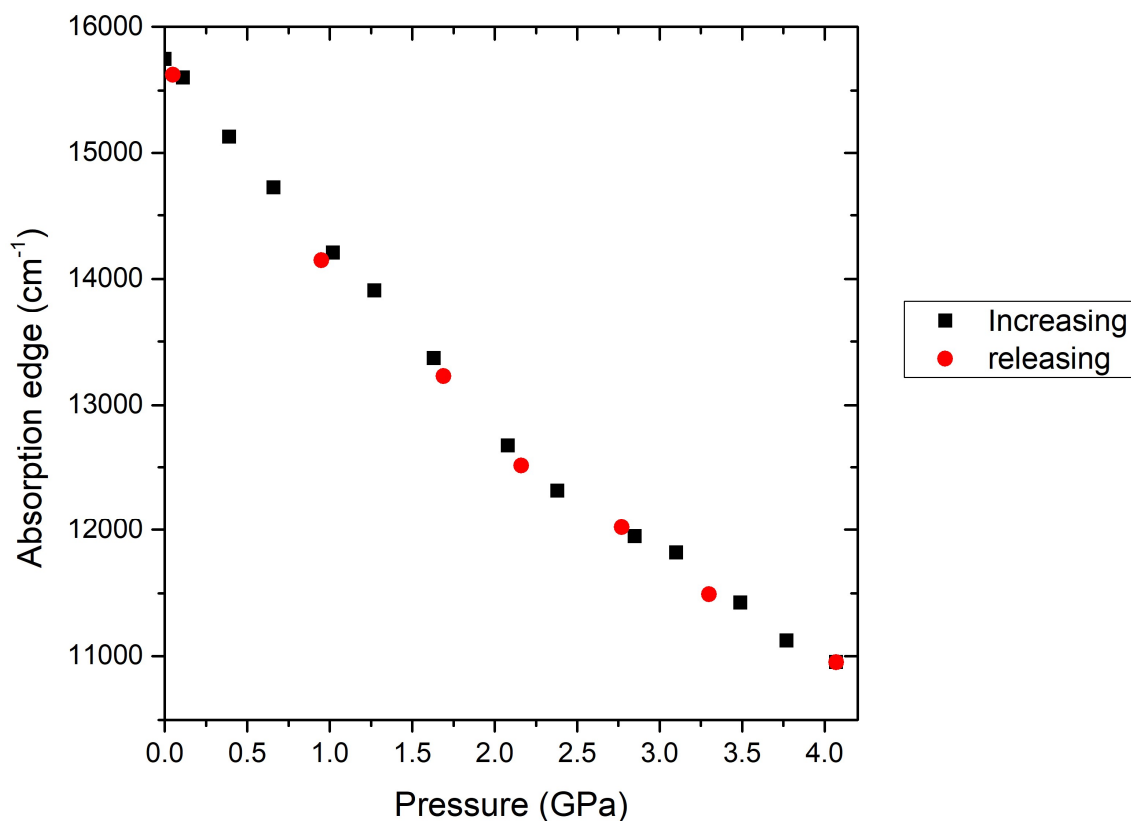
Figure 21. Absorption edge of PDI-C5 with increasing (black) and with releasing (red) pressure.

A slight discontinuity in the trend of PDI-C5 absorption edge as a function of pressure applied can be observed between 1.5 and 2.5 GPa, which indicates the possible presence of a phase transition. This will be verified by XRD at high pressure. Nevertheless, the observed changes seem to be reversible upon releasing pressure. In fact, the absorption edge value after releasing pressure is very close to the initial value and the film color changes from red to black when the pressure is increased and returns to red when pressure is released.

In conclusion, from the variation of the absorption edge, we expect that PDI-C5 form I is stable up to 1.5 GPa. However, upon further compression, we can expect to observe a pressure-induced phase transition to a new crystal form, hereafter referred to as form IV, which should be the most stable form above 2.5 GPa. We do not exclude yet the presence of more than one pressure-induced phase transition in this range.

The absorption measurements of the PDI-C6 upon increasing pressure are shown in Figure 22 and the related macroscopic color changes are shown in Figure 23. Unfortunately, the gasket deformed when the pressure was increased to 3.85 GPa (can be seen by looking at the pictures and by the lower absorbance at 3.85GPa). For this reason, the following measurements at higher pressures were not performed. Nevertheless, these measurements highlight a significant red-shift of the absorption spectra with compression and consequently, the PDI-C6 film color tends to darken from red to black.
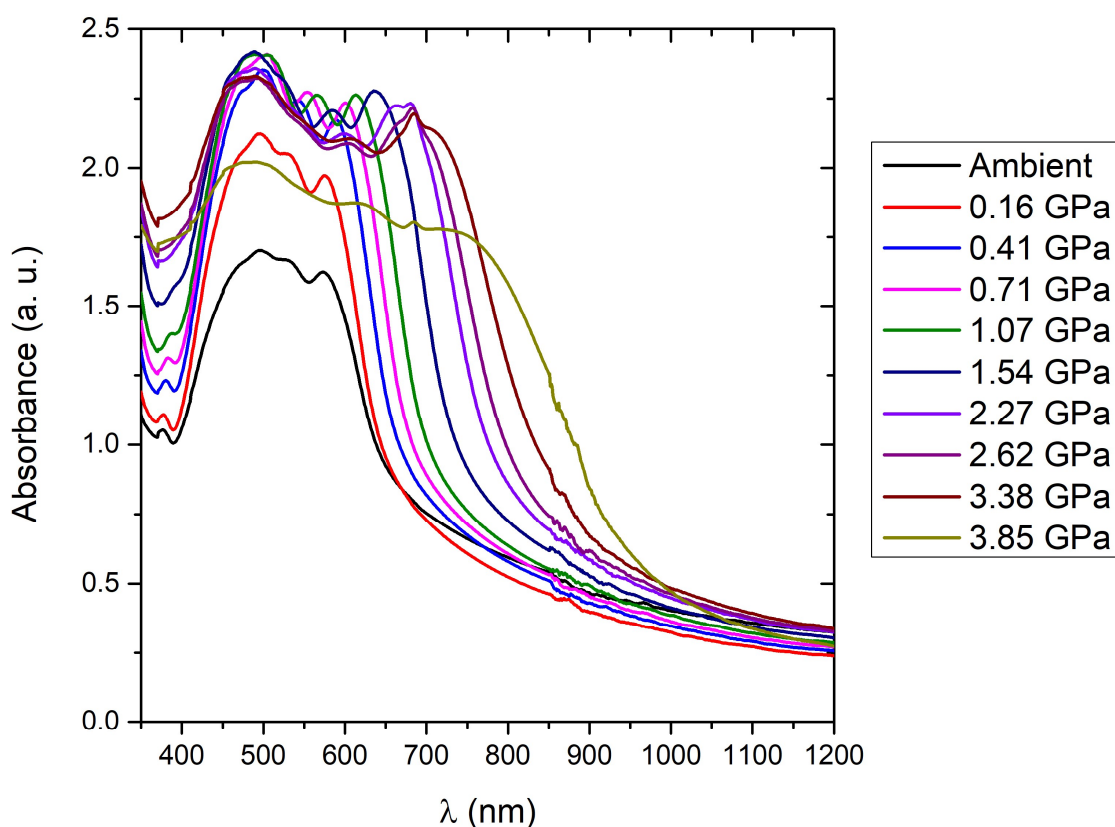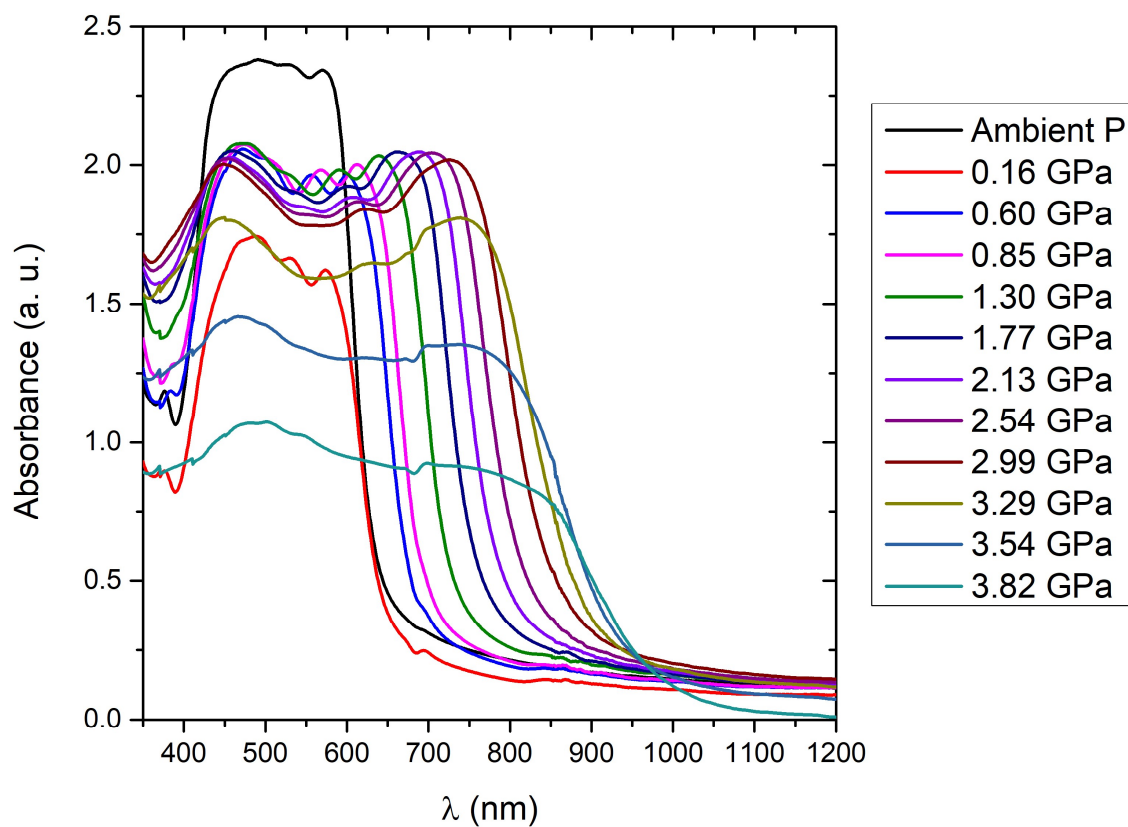

Figure 22. UV-Vis-NIR absorption spectra of PDI-C6 upon increasing pressure.
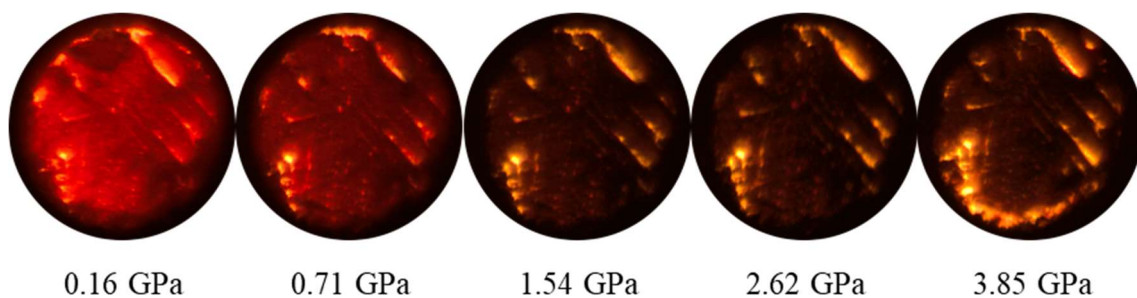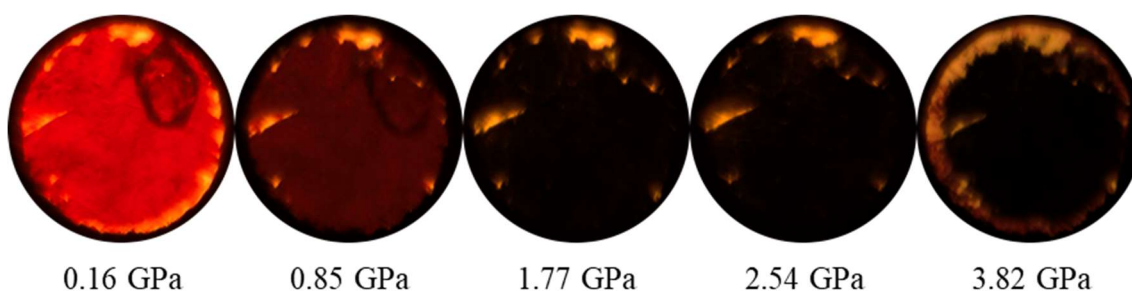
Figure 23. Images of PDI-C6 film with increasing pressure.

The red-shift of the absorption spectra resulted to be reversible upon releasing pressure (Figure S10) and consequently, the color returns red when pressure is released (Figure 24).
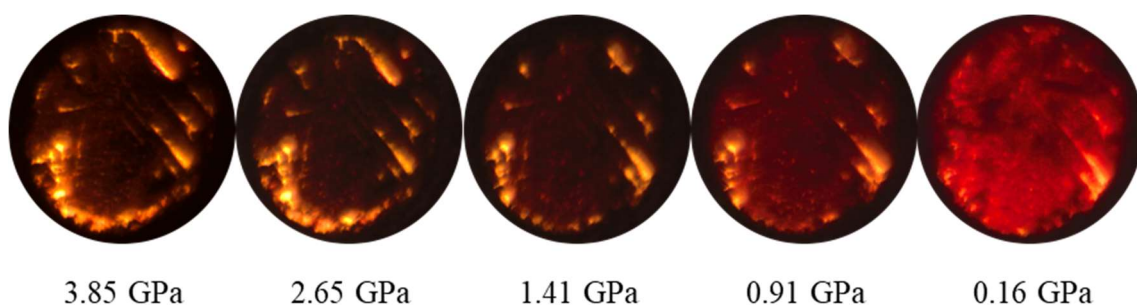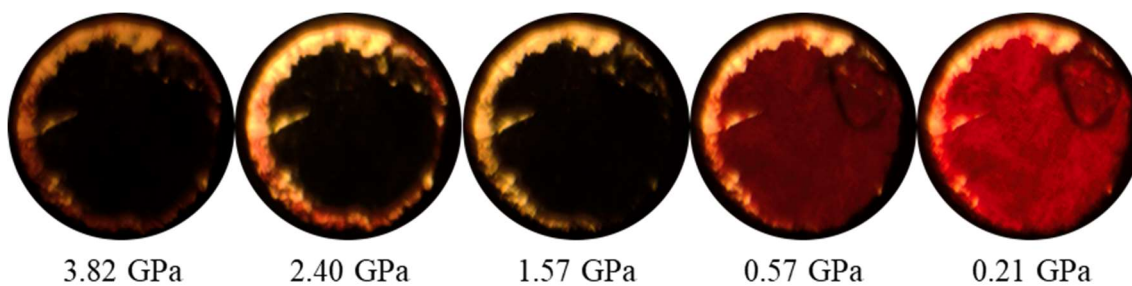

Figure 24. Images of PDI-C6 film upon releasing pressure.

The absorption edges at different pressure were extrapolated from the absorption spectra and listed in Table 8; furthermore, the variation of absorption edge with pressure is shown in Figure 25.

Table 8. Variation of the absorption edge of PDI-C6 with increasing and releasing pressure.

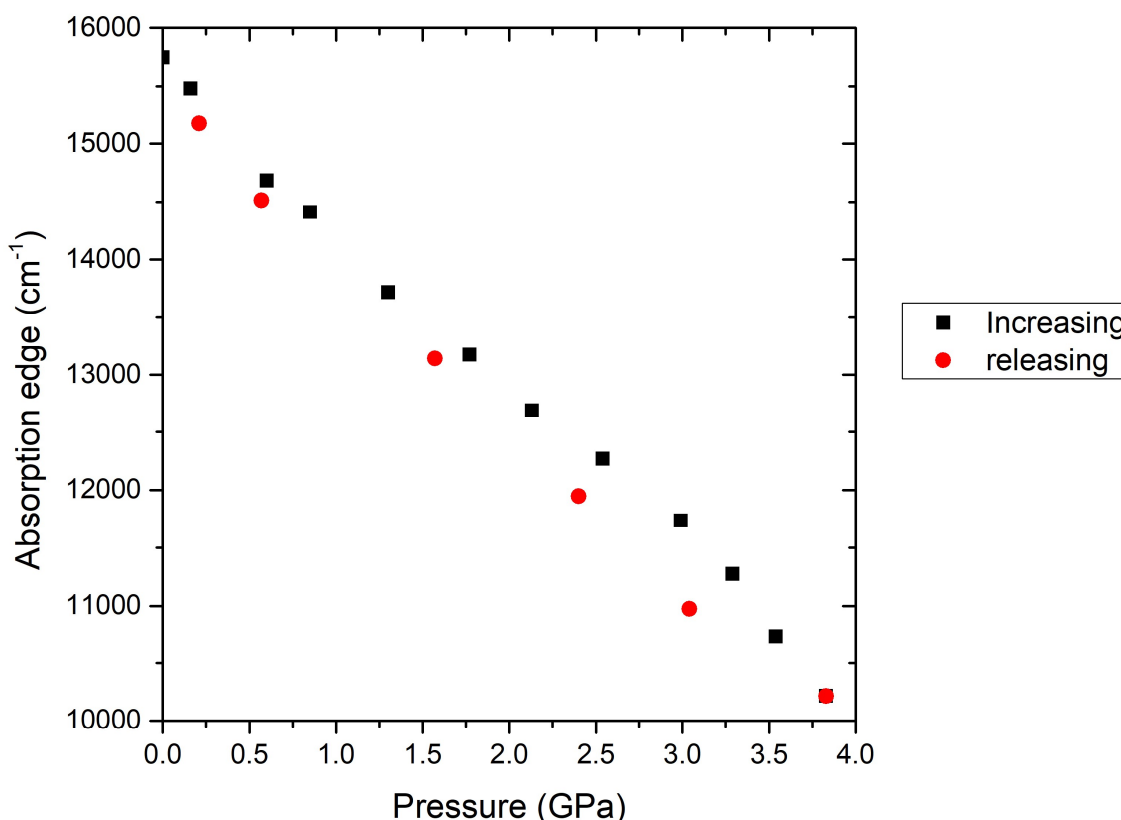| INCREASING PRESSURE			RELEASING PRESSURE		
Pressure (GPa)	Absorption Edge (nm)	Absorption Edge (cm^{-1})	Pressure (GPa)	Absorption Edge (nm)	Absorption Edge (cm^{-1})
Ambient	657	15200	3.85	948	10500
0.16	667	15000	2.65	834	12000
0.41	679	14700	1.96	784	12800
0.71	694	14400	1.41	737	13600
1.07	710	14100	0.91	711	14100
1.54	743	13500	0.38	671	14900
2.27	788	12700	0.16	656	15200
2.62	816	12300			
3.38	855	11700			
3.85	948	10500			
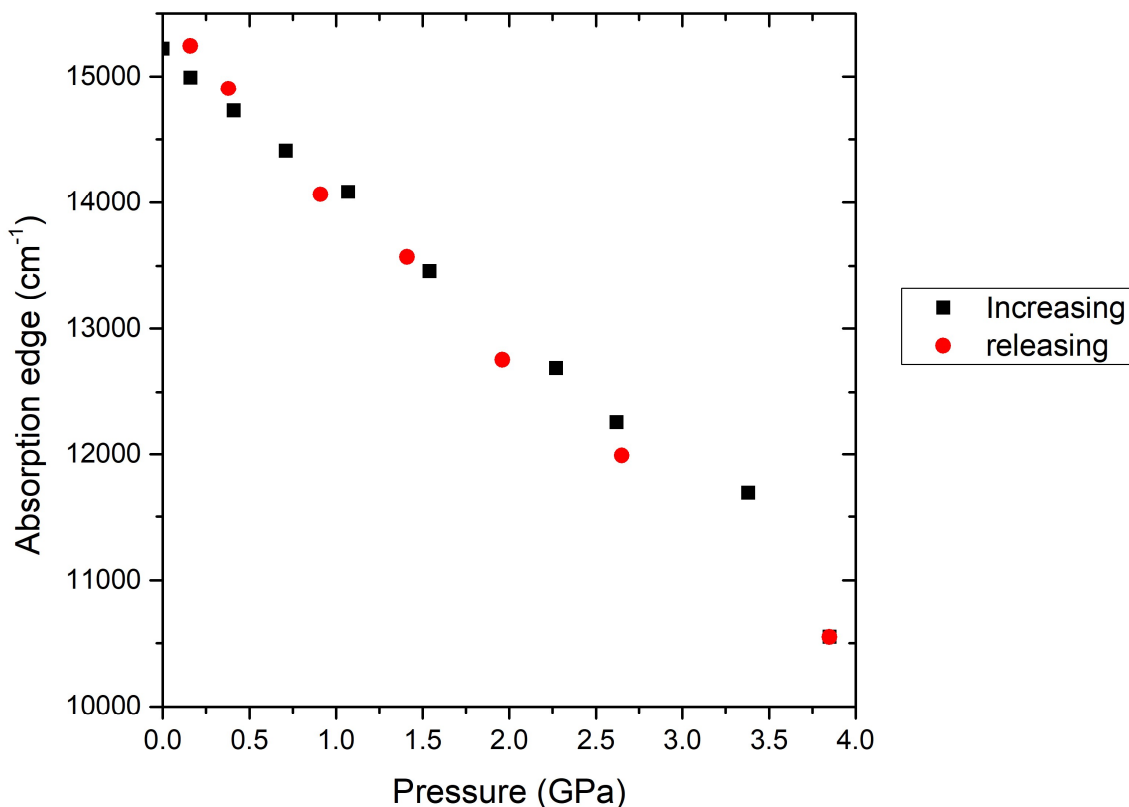
Figure 25. Absorption edge of PDI-C6 with increasing (black) and with releasing (red) pressure.

A slight discontinuity in the trend of the absorption edge as a function of pressure applied can be observed between 1.0 and 2.0 GPa, indicating the presence of a phase transition. This will be verified by XRD at high pressure. Nevertheless, the observed transformation seems to be reversible upon releasing pressure. In fact, the absorption edge value after releasing pressure is very close to the initial value and the film color changes from red to black when the pressure is increased and returns to red when pressure is released.

In conclusion, from the variation of the absorption edge, we expect that PDI-C6 form I is stable up to 1.0 Gpa, above what we expect to observe a pressure-induced phase transition to a new crystal form, form IV, which should be the preferred form above 2.0 GPa. However, we do not exclude the possible presence of more than one pressure-induced phase transition in this range.

The absorption measurements of the PDI-C7 upon increasing pressure are shown in Figure 26 and the related macroscopic color changes are shown in Figure 27. These measurements highlight a significant red-shift of the absorption spectra with compression and consequently, the PDI-C7 film color tends to darken from red to black.

Figure 26. UV-Vis-NIR absorption spectra of PDI-C7 upon increasing pressure.

Figure 27. Images of PDI-C7 film upon increasing pressure.

The red-shift of the absorption spectra resulted to be reversible upon releasing pressure (Figure S11) and consequently, the color returns red when pressure is released (Figure 28).

Figure 28. Images of PDI-C7 film upon releasing pressure.

The absorption edges at different pressure were extrapolated from the absorption spectra and listed in Table 9; furthermore, the variation of absorption edge with pressure is shown in Figure 29.

Table 9. Variation of the absorption edge of PDI-C7 with increasing and releasing pressure.

INCREASING PRESSURE			RELEASING PRESSURE		
Pressure (GPa)	Absorption Edge (nm)	Absorption Edge (cm^{-1})	Pressure (GPa)	Absorption Edge (nm)	Absorption Edge (cm^{-1})
Ambient	622	16100	3.94	822	12200
0.23	638	15700	3.25	798	12500
0.48	647	15500	1.45	713	14000
0.98	683	14600	0.7	677	14800
1.28	696	14400	0.18	640	15600
1.84	716	14000			
2.11	723	13800			
2.5	735	13600			
2.84	760	13200			
3.25	773	12900			
3.94	822	12200			
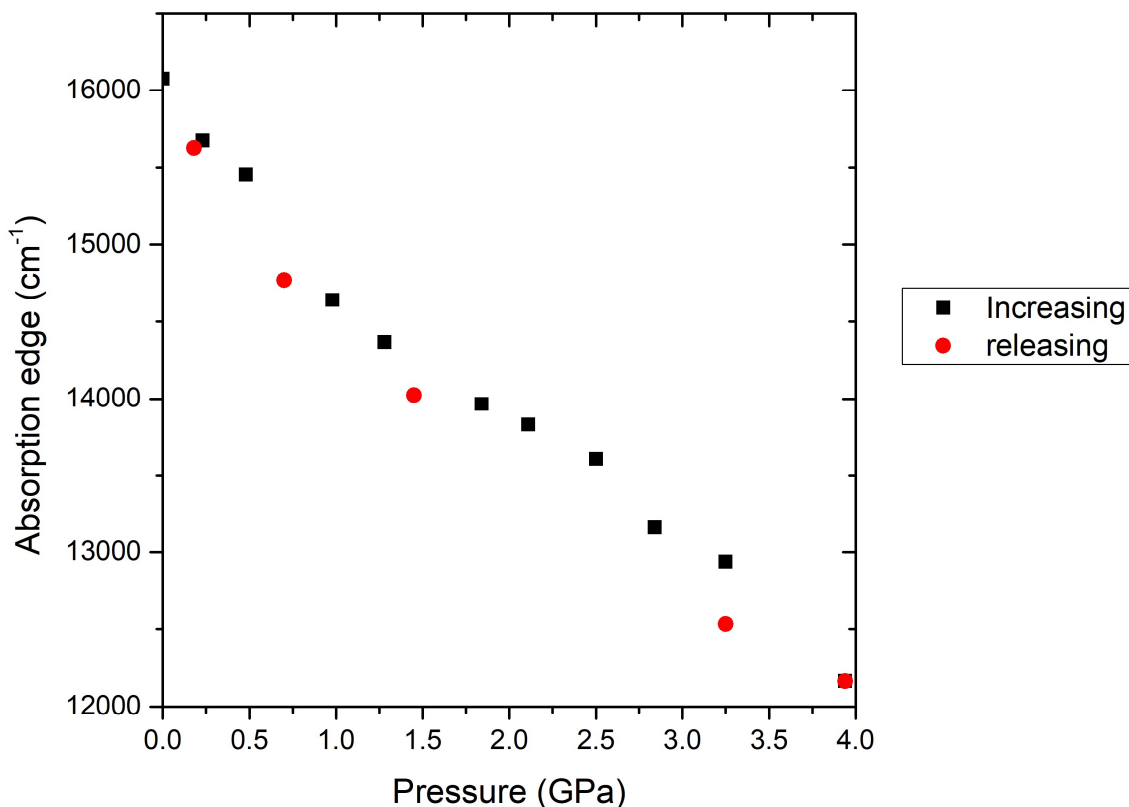
Figure 29. Absorption edge of PDI-C7 with increasing (black) and with releasing (red) pressure.

In this case, the values of the absorption edge are a bit more scattered, making it more difficult to underline possible solid-state transitions with pressure, or might be an indication of more than one phase transition. According to the observed changes, one could assign a phase transition somewhere between 0.5 and 1.5 GPa and another one between 2.0 and 3.0 GPa. However, it must be verified by XRD experiments. Nevertheless, the system seems to be reversible upon releasing pressure as the other PDI-Cn.

In conclusion, from the variation of the absorption edge, we expect that PDI-C7 form I is stable up to 0.5 Gpa, and then, with further increasing pressure, we expect to observe one or more pressure-induced phase transitions.

The absorption measurements of the PDI-C8 upon increasing pressure are shown in Figure 30 and the related macroscopic color changes are shown in Figure 31. These measurements highlight a significant red-shift of the absorption spectra with compression and consequently, the PDI-C8 film color tends to darken from red to black. Unfortunately, the gasket deformed when the pressure was increased above 3 GPa (can be seen by looking at the pictures and by the decrease in absorbance above 3 GPa). Nevertheless, the pressure was further increased up to 3.82 GPa.

Figure 30. UV-Vis-NIR absorption spectra of PDI-C8 upon increasing pressure.

Figure 31. Images of PDI-C8 film with increasing pressure.

The red-shift of the absorption spectra resulted to be reversible upon releasing pressure (Figure S12) and consequently, the color returns red when pressure is released (Figure 32).

Figure 32. Images of PDI-C8 film with releasing pressure.

The absorption edges at different pressure were extrapolated from the absorption spectra and listed in Table 10; furthermore, the variation of absorption edge with pressure is shown in Figure 33.

Table 10. Variation of the absorption edge of PDI-C8 with increasing and releasing pressure.

INCREASING PRESSURE			RELEASING PRESSURE		
Pressure (GPa)	Absorption Edge (nm)	Absorption Edge (cm⁻¹)	Pressure (GPa)	Absorption Edge (nm)	Absorption Edge (cm⁻¹)
Ambient	635	15700	3.82	979	10200
0.16	646	15500	3.04	911	11000
0.6	681	14700	2.4	837	11900
0.85	694	14400	1.57	761	13100
1.3	729	13700	0.57	689	14500
1.77	759	13200	0.21	659	15200
2.13	788	12700			
2.54	815	12300			
2.99	852	11700			
3.29	887	11300			
3.54	932	10700			
3.82	979	10200			

Figure 33. Absorption edge of PDI-C8 with increasing (black) and with releasing (red) pressure.

A slight discontinuity in the trend seems to be present between 0.8 and 1.8 GPa, probably an indication of the presence of a transition. Also, above 2.5 GPa there seems to be something happening. The presence of transitions will be verified by XRD at high pressure. Nevertheless, the system seems to be reversible upon releasing pressure. In fact, the absorption edge value after releasing pressure is

very close to the initial value and the film color changes from red to black when the pressure is increased and reverts to red when pressure is released.

In conclusion, from the variation of the absorption edge, we expect that PDI-C8 form I is stable up to 0.8 Gpa, and then, with further increasing pressure, we expect to observe a pressure-induced phase transition to a new crystal form, called form III, which should be the form stable above 2.0 GPa. However, we do not exclude the possible presence of more than one pressure-induced phase transition in this range.

The absorption edge as a function of pressure for all the PDI-Cn together is shown and compared in Figure 34.
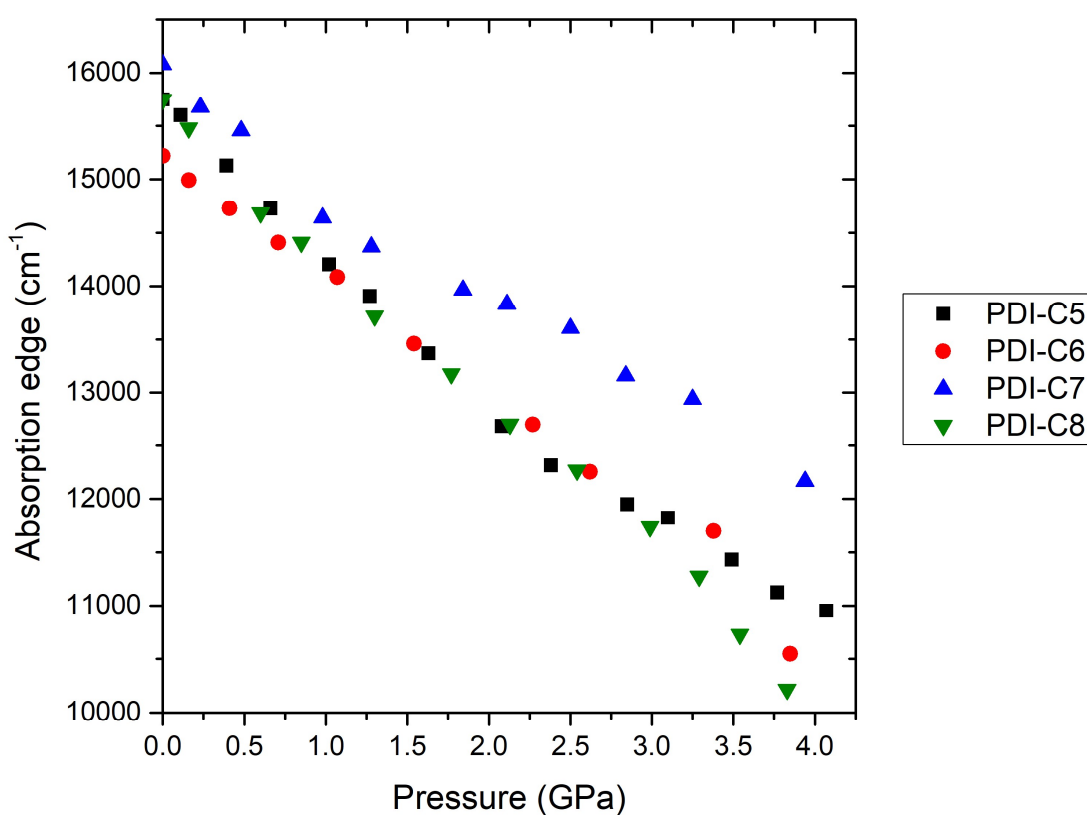
Figure 34. Absorption edge of the four PDI-Cn with increasing (black) and with releasing (red) pressure.

From this graph it is possible to observe that the behaviour of the four PDI-Cn is indeed similar, with a redshift of the absorption edge upon increasing pressure. Out of this four, PDI-C7 is the one with the lowest redshift, and with the highest energy of the absorption edge, this can be observed also from its colour changes in Figure 27. On the other hand, PDI-C8 has the highest redshift.

Single crystal XRD in DAC

To investigate the structural changes in compressed PDI-Cn, a series of high-pressure SCXRD experiments were performed. However, these high-pressure SCXRD experiments have not been carried out for PDI-C7 and PDI-C8 yet, and thus, only the results for PDI-C5 and PDI-C6 are reported.

Form I crystals of PDI-C5 can be compressed up to ~ 1.9 GPa without any signs of phase transition. Above this point, the phase transition to form IV occurs. The critical pressure observed for PDI-C5 form I by SCXRD agrees with the UV-Vis results, which highlighted a possible transition in the range 1.5 - 2.5 GPa. The structure determination for data collected at 2.17 GPa revealed the new high-pressure form IV, as suggested by the absorption edge measurements. The crystal structure parameters of PDI-C5 at different pressure are reported in Table 11.

Table 11. Crystal structure parameters of PDI-C5 at different pressure.

Pressure (GPa)	Ambient	0.05	0.66	1.04	1.40	1.78	2.17	2.70	3.84
Form	I	I	I	I	I	I	IV	IV	IV
SG	$P\bar{1}$	$P\bar{1}$	$P\bar{1}$	$P\bar{1}$	$P\bar{1}$	$P\bar{1}$	$P\bar{1}$	$P\bar{1}$	$P\bar{1}$
a	4.754(2)	4.727(3)	4.6264(6)	4.5647(6)	4.5115(6)	4.4654(6)	3.7606(6)	3.7203(3)	3.639(3)
b	8.479(4)	8.493(3)	8.4339(8)	8.394(1)	8.3676(9)	8.345(1)	8.5729(5)	8.5616(7)	8.536(7)
c	16.30(1)	16.308(9)	15.907(7)	15.735(7)	15.611(7)	15.480(7)	18.044(6)	17.928(7)	17.49(3)
α	86.88(5)	86.78(8)	85.85(2)	85.66(3)	85.44(3)	85.34(3)	87.22(2)	87.10(2)	87.5(2)
β	83.50(5)	83.3(1)	82.97(2)	83.20(3)	83.40(2)	83.71(2)	74.48(3)	74.75(2)	76.4(2)
γ	83.68(4)	84.12(4)	85.09(1)	85.60(1)	85.96(1)	86.22(1)	101.631(8)	101.539(7)	101.09(7)
Volume (Å³)	648.1	646.1	612.5	595.5	582.4	570.5	545.8	536.6	515.8
Z	1	1	1	1	1	1	1	1	1
Z'	0.5	0.5	0.5	0.5	0.5	0.5	0.5	0.5	0.5
R	6.3	10.7	10.0	10.7	10.5	10.3	8.8	7.9	23.23

The changes in the unit-cell volume plotted as a function of pressure are shown in Figure 35. A clear drop in the unit cell volume indicates a phase transition. A clear drop in the volume is observed as expected above the critical pressure of 1.9 GPa. The high R factor for the measurement collected at 3.84 GPa can be related to the high-pressure instrumentation, especially disadvantageous for the low-symmetry samples and to the decreasing quality of single-crystal due to the progressing structural strain accumulated during monotonic compression.
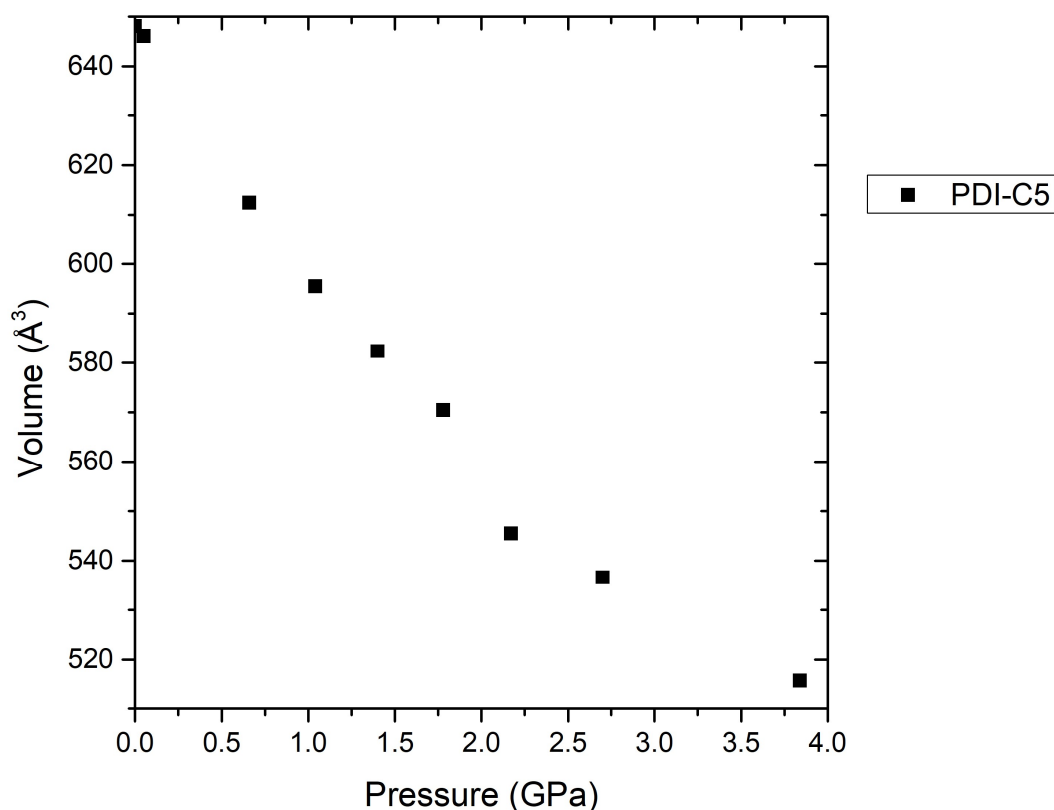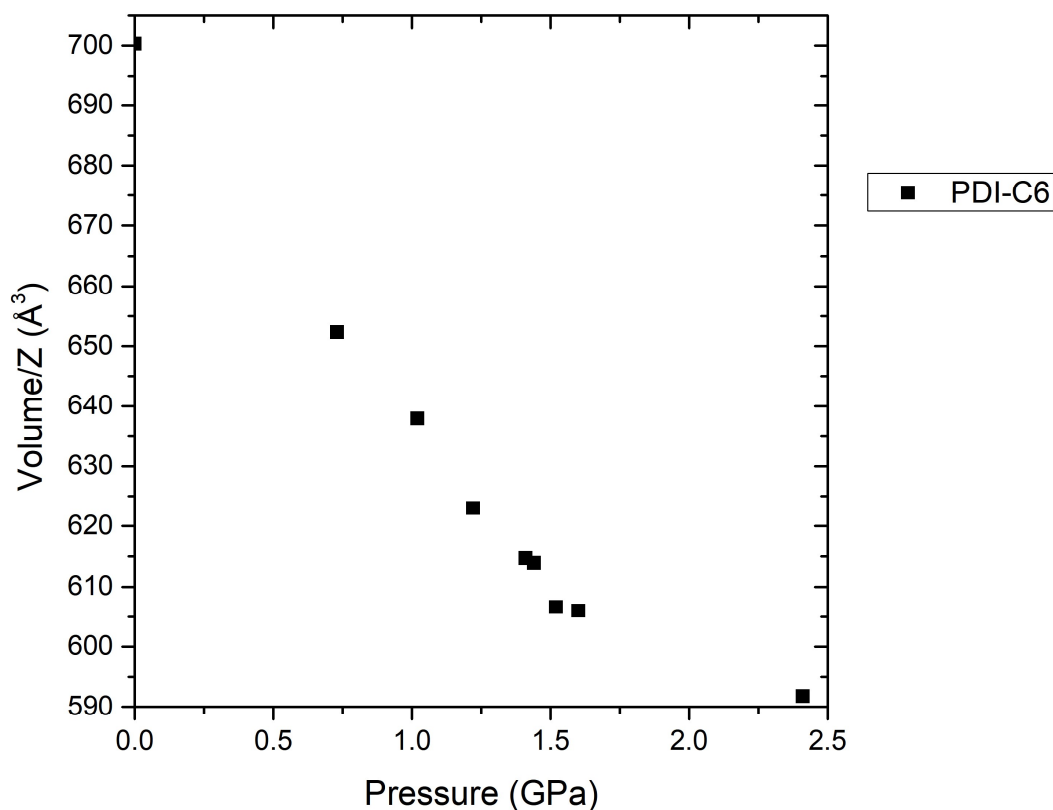
Figure 35. Variation of unit cell volume of PDI-C5 upon increasing pressure.

Both PDI-C5 form I and IV, crystallize in triclinic space-group P-1, with half molecule in the asymmetric part of the unit-cell.

The form I crystal is soft along the *a*-axis direction, which decreases by about 0.3 Å upon compression up to 1.78 GPa. This direction corresponds to the SV (distance between the centroids of two closed stacked molecules) direction, which means that upon compression, the interplanar distance ($d_{\pi-\pi}$) between the π-stacked perylene cores and the displacement along the x- and y- molecular axes (respectively long and short axes of the perylene core) decrease. Like in form I, also in form IV the *a*-axis corresponds. Upon further compression from 1.78 GPa to 2.17 GPa, the transition occurs with a severe drop of the SV distance of about 0.7 Å due to the decrease of the displacement along the molecular x-axis, which decreases from 2.9 to 1.0 Å; in contrast, the displacement along the y-axis increases from 1.14 to 1.72 Å and also the $d_{\pi-\pi}$ increases slightly (~0.05 Å).

Another change lies in the molecular conformation. The torsion angle that the alkyl chains form with the aromatic core plane varies from 82° for the ambient phase form I to 52° for the high-pressure phase form IV, whereas the conformation within the chains in form IV remains all staggered as in the form I phase. The crystal structures of form I and form IV are shown in Figure 36together with the single crystal images. The comparison between molecular conformations in forms I and IV is shown in Figure 37.
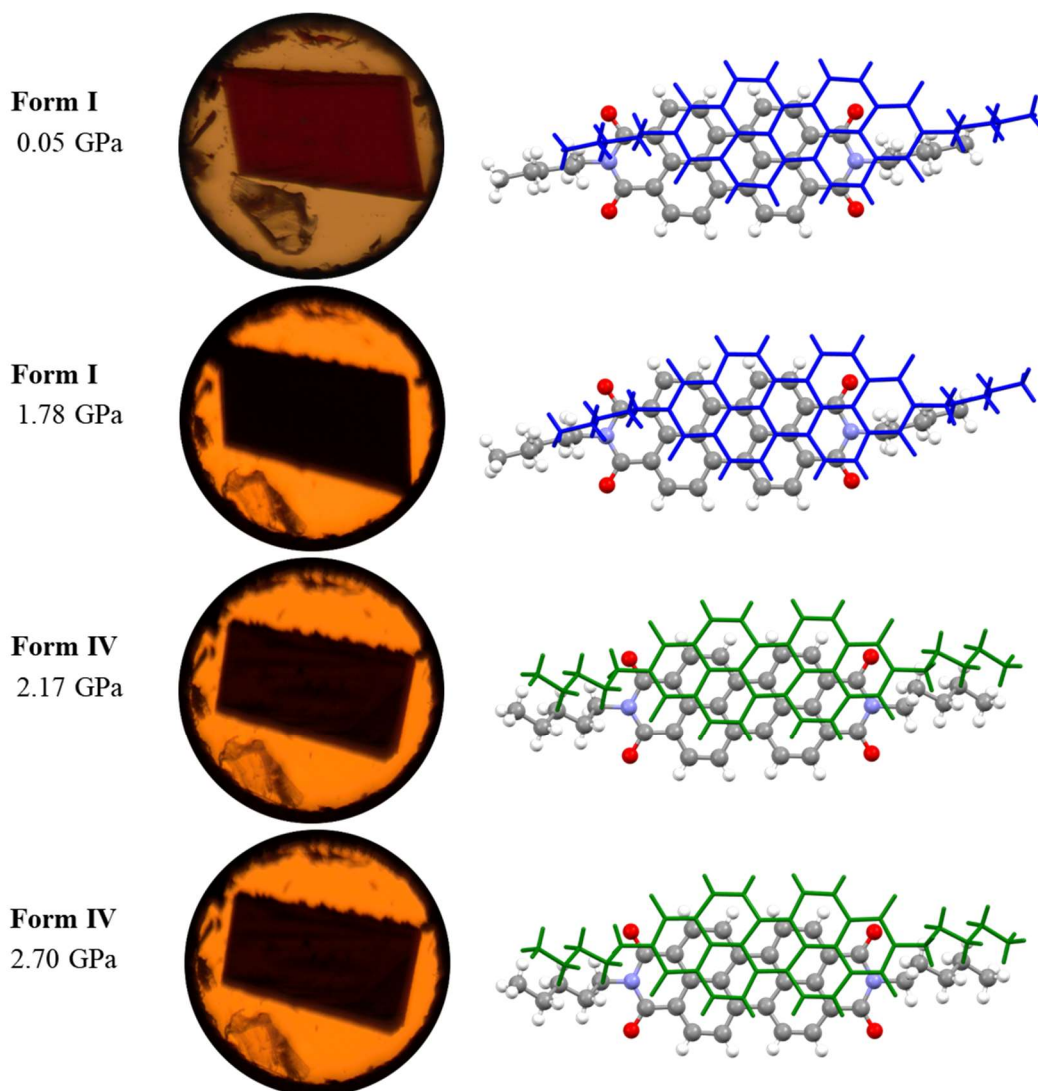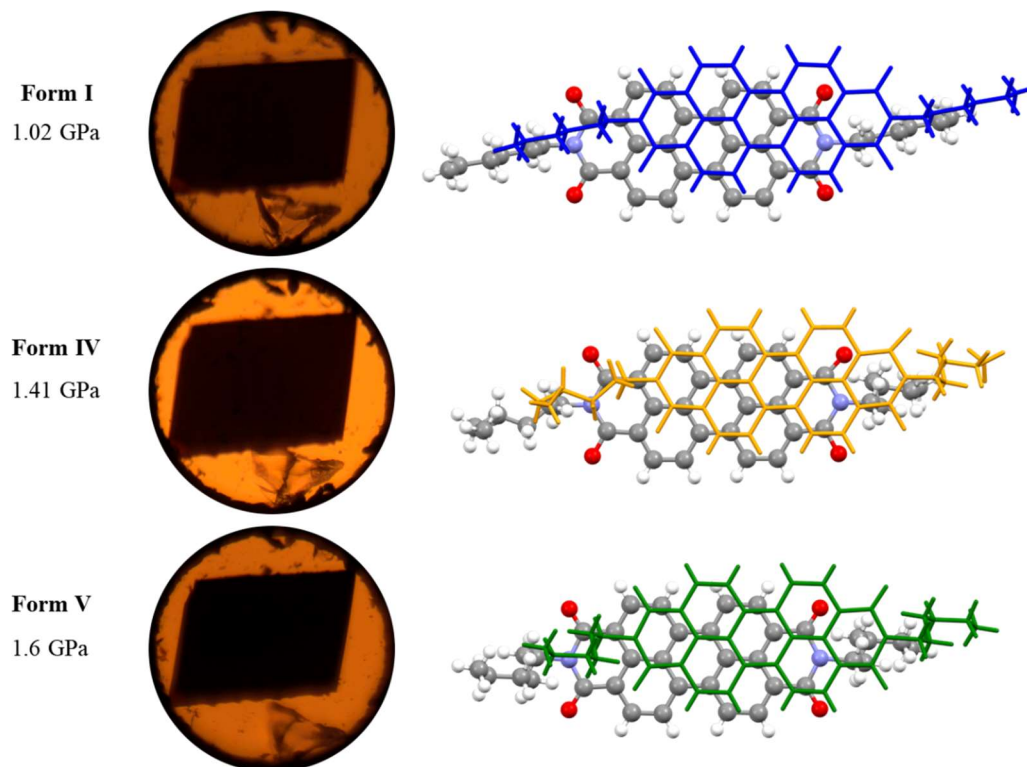
Figure 36. Crystal morphology and color shift of PDI-C5 at different pressures (on the left) and the corresponding crystal structure (on the right), two molecules are displayed to show the variation of the molecular stacking upon transition. The ambient phase form I is stable up to 1.78 GPa, whereas at 2.17 GPa the high-pressure phase form IV is present.
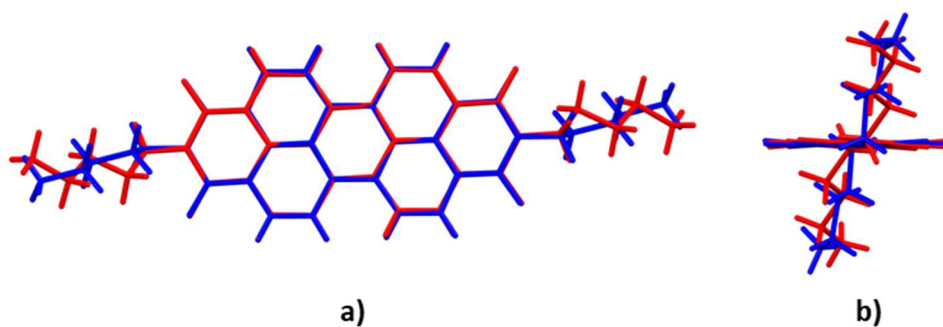
Figure 37. Comparison between ambient phase (in blue, at 1.78 GPa) and high-pressure phase (in red, at 2.17 GPa) crystal structures of PDI-C5 to highlight the different alkyl chain conformation. a) View perpendicular to the perylene plane of the two overlapped molecules; b) molecules viewed along the perylene x-axis.

As shown in Figure 36, the phase transition is also accompanied by a change in the crystal morphology.

Form I crystals of PDI-C6 can be compressed up to ~ 1.1 GPa without any signs of phase transition. Above this point, the phase transition to form IV occurs. The critical pressure observed for PDI-C6 form I by SCXRD agrees with the UV-Vis results, which highlighted a possible transition in the range 1.0 - 2.0 GPa. The structure determination for data collected at 1.22 GPa revealed the new high-pressure form IV, as suggested by the absorption edge measurements. Form IV can be compressed up to ~ 1.5 GPa without any signs of other phase transitions. Above this point, a second phase transition to form V occurs. The critical pressure observed for PDI-C6 form IV by SCXRD agrees with the UV-Vis results since also this second transition is in the range of 1.0 - 2.0 GPa. The structure determination for data collected at 1.52 GPa revealed the new high-pressure form IV, as suggested by the absorption edge measurements. The crystal structure parameters of PDI-C6 at different pressure are reported in Table 11.

Table 12. Crystal structure parameters of PDI-C6 at different pressure.

Pressure (GPa)	Ambient	0.73	1.02	1.22	1.41	1.44	1.52	1.6	2.41
Form	I	I	I	IV	IV	IV	V	V	V
SG	$P\bar{1}$	$P\bar{1}$	$P\bar{1}$	$P\bar{1}$	$P\bar{1}$	$P\bar{1}$	$P\bar{1}$	$P\bar{1}$	$P\bar{1}$
a	4.757(1)	4.5966(4)	4.5465(4)	4.5331(5)	4.5053(5)	4.5031(5)	4.4907(5)	4.4771(8)	4.4179(4)
b	8.549(2)	8.565(2)	8.5662(9)	16.936(4)	16.867(3)	16.866(3)	8.5886(7)	8.597(1)	8.5938(6)
c	17.576(2)	16.886(7)	16.687(6)	17.871(9)	17.770(5)	17.761(6)	15.877(5)	15.89(1)	15.738(6)
α	81.68(1)	80.89(3)	80.69(2)	66.39(4)	66.56(2)	66.52(3)	90.69(2)	90.70(4)	90.80(2)
β	84.85(2)	86.38(2)	86.89(2)	84.57(3)	84.51(2)	84.51(3)	92.05(2)	92.11(4)	92.62(2)
γ	83.17(2)	84.27(1)	84.487(8)	83.76(2)	83.73(1)	83.71(2)	97.523(8)	97.50(1)	97.410(7)
Volume (Å³)	700.3	652.4	637.9	1247.8	1229.5	1227.8	606.6	606.0	591.8
Z	1	1	1	2	2	2	1	1	1
Z'	0.5	0.5	0.5	1	1	1	0.5	0.5	0.5
R	7.2	7.6	7.7	28.6	19.7	30.4	7.9	8.4	7.7

The changes in the unit-cell volume normalized by Z are plotted as a function of pressure are shown in Figure 38. A clear drop in the unit cell volume indicates a phase transition. As expected, two clear drops of the unit cell volume are observed in the plot: the first above the critical pressure of form I (1.1 GPa); the second above the critical pressure of form IV (1.5 GPa). The high R factor for the measurement collected for form IV can be related to the high-pressure instrumentation, especially disadvantageous for the low-symmetry samples; this is indeed the case of form IV, which has a doubled unit cell and asymmetric unit and thus more parameters to refine for structure determination compared to form I and form V.

Figure 38. Variation of unit cell volume of PDI-C6 upon increasing pressure.

PDI-C6 form I, IV, and V, crystallize in triclinic space-group P-1, with half molecule in the asymmetric part of the unit-cell for form I and V, whereas in form IV the asymmetric unit is one molecule.

The form I crystal is soft along the *a*-axis direction, which decreases by about 0.2 Å upon compression up to 1.02 GPa. As in PDI-C5, in PDI-C6 form I the direction of *a*-axis corresponds to the SV direction, which means that upon compression, the interplanar distance ($d_{\pi\text{-}\pi}$) between the π-stacked perylene cores and the displacement along the x- and y- molecular axes decrease. Upon further compression from 1.02 GPa to 1.22 GPa, the transition occurs; however, in the case of PDI-C6, the severe drop of the SV distance is not observed. The pressure-induced transition to form IV does not involve the slipping of the perylene cores as in PDI-C5; instead, the transition to form IV leads to a change in the alkyl chain conformation. The same is true for the second pressure-induced phase transition to form V upon compression above 1.5 GPa, which results in no significant change in the SV, but only on the alkyl chain conformation. The alkyl chain conformation goes from a staggered conformation in form I to a gauche conformation in form V; form IV represents an intermediate situation between the ambient phase form I and the high-pressure phase form V.

The crystal structures of the ambient phase form I and high-pressure phases form IV and V are shown in Figure 39 together with the single crystal images, whereas, the comparison between molecular conformations of form I and form V, displaying the different conformation of the alkyl chains (staggered conformation in form I and gauche conformation in form V), is shown in Figure 40.

Figure 39. Crystal morphology and color shift of PDI-C6 at different pressures (on the left) and the corresponding crystal structure (on the right), two molecules are displayed to show the variation of the molecular stacking upon transition. On top is shown the ambient phase form I, stable up to 1.02 GPa; in the middle the first high-pressure phase form IV at 1.41 GPa; at the bottom the second high-pressure phase form V at 1.6 GPa.
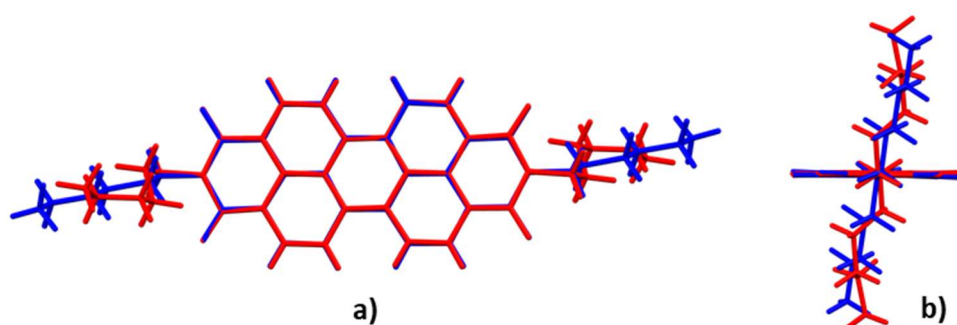
Figure 40. Comparison between ambient phase form I (in blue, at 1.02 GPa) and high-pressure phase form V (in red, at 1.6 GPa) crystal structures of PDI-C6 to highlight the different alkyl chain conformation. a) View perpendicular to the perylene plane of the two overlapped molecules; b) molecules viewed along the perylene x-axis.

EXPERIMENTAL METHODS

Crystallization

PDI-Cn were purchased from Aldrich and used without further purification. Single crystals of PDI-Cn were obtained inside a solvothermal reactor, where a supersaturated solution of the PDI was heated up for one night and then slowly cooled down to room temperature. Toluene, p-xylene, CHCl3, and CH2Cl2 were used as solvents and the solutions were heated up to 180°C in the case of toluene and p-xylene solutions, while CHCl3 and CH2Cl2 were heated up to 100°C.

Single-Crystal X-ray Diffraction

Single crystal data of PDI-C6 and PDI-C7 at ambient conditions were collected on an Oxford Xcalibur S instrument with MoKα radiation ($\lambda = 0.71073$ Å) and graphite monochromator, equipped with a Cryostream800 for temperature control. SHELXT[35] was used for structure solution and SHELXL[36,37] for the refinement based on F^2. The non-hydrogen atoms were refined anisotropically, and the hydrogen atoms were added at calculated positions. The software Mercury was used to generate the molecular packing representation and for the calculation of the diffraction pattern from the crystal structures.

X-ray Powder Diffraction

The synchrotron radiation PXRD measurements of PDI-C5 were performed at the ALBA Synchrotron light facility in Barcelona at Material Science and Powder Diffraction beamline BL04-MSPD equipped with the High-throughput Position Sensitive Detector (PSD) MYTHEN53 and an FMB Oxford hot air blower for variable temperature measurements. End station with a nominal photon energy of 30 keV. Fine Si NIST standard refinement returned a wavelength of 0.41235(1) Å and a residual zero error of 0.008(3) 2θ, step size of 0,004°. The measurements were performed in transmission geometry. The material was loaded inside a glass capillary with a diameter of 0.5 mm, spun during measurement, and exposed to X-rays for 10 s for measurements in continuous heating with 5 °C/min heating rate for measurement in continuous during variable temperature experiment.

Synchrotron PXRD data for indexing the HT polymorphs of PDI-Cn were collected at isothermal conditions, at 226 °C and 265 °C for PDI-C6, at 218 °C and 255 °C for PDI-C7, and 224 °C for PDI-C8, with a 30s X-rays exposition over the range 0.8°–15° 2θ. The data for PDI-C6 form II at 226 °C were not indexed because it was not possible to unambiguously assess a unit cell. The data for PDI-C6 form III at 265 °C were indexed to a triclinic P-1 cell (a = 7.681 Å, b = 10.130 Å, c = 21.504 Å, α = 84.47 °, β = 85.11 °, γ = 90.46 ° and V = 1659 Å^3), and were Pawley fitted in Topas-Academic V5(TOPAS)[38]. Consideration of the cell volume, molecular volume, and space group symmetry

suggested $Z' = 1$. The data for PDI-C7 form II at 218 °C were indexed to a triclinic P-1 cell (a = 10.790 Å, b = 11.067 Å, c = 23.202 Å, α = 94.30 °, β = 97.84 °, γ = 115.35 ° and V = 2455 Å^3), and were Pawley fitted in TOPAS. Consideration of the cell volume, molecular volume, and space group symmetry suggested $Z' = 1.5$. The data for PDI-C7 form III at 255 °C were indexed to a triclinic P-1 cell (a = 7.696 Å, b = 10.088 Å, c = 23.117 Å, α = 81.86 °, β = 86.73 °, γ = 89.86 ° and V = 1774 Å^3), and were Pawley fitted in TOPAS. Consideration of the cell volume, molecular volume, and space group symmetry suggested $Z' = 1$. The data for PDI-C8 form II at 255 °C were indexed to a triclinic P-1 cell (a = 7.738 Å, b = 9.979 Å, c = 24.783 Å, α = 83.92 °, β = 81.17 °, γ = 88.96 ° and V = 1880 Å^3), and were Pawley fitted in TOPAS. Consideration of the cell volume, molecular volume, and space group symmetry suggested $Z' = 1$.

Thermogravimetric analysis (TGA)

TGA measurements were performed using a Perkin Elmer TGA7 in the temperature range 35-550°C under N_2 gas flow and heating was carried out at 20 °C min^{-1}.

Differential Scanning Calorimetry (DSC)

The DSC analysis was performed with an instrument PerkinElmer PyrisDiamond DSC-7 equipped with a PII intracooler, in N_2 atmosphere and a scanning speed of 20 °C/min.

Hot-Stage Microscopy (HSM)

The HSM analysis was performed using an OLYMPUS BX41 microscope equipped with a VISICAM 5.0 and a NIKON DS FI3 camera. A Linkam TMS-94 stage was used for the temperature control. The images were taken under polarized light to highlight modifications in the crystals due to solid-state transition, with a 40× magnification.

High-pressure experiments

All high-pressure experiments were performed with a modified Merrill-Bassett diamond anvil cell (DAC) with diamond anvils supported on steel discs.[39] The diamond culets were 0.8 mm in diameter. The gasket was made of 0.3 mm thick tungsten foil with sparked-eroded holes of 0.4 to 0.5 mm in diameter. The pressure was calibrated using the ruby fluorescence method.[40,41] Daphne Oil 7575 was used as the pressure transmitting medium.

High-pressure Single-Crystal X-ray Diffraction

Single-crystal X-ray diffraction measurements were performed using a 4-circle diffractometer equipped with a CCD detector and MoKα X-ray source (λ=0.71073 Å). The DAC chamber was centered using the gasket-shadowing method[42]. The CrysAlisPro software was used for the data

collection and processing. All the structures were solved with direct methods using Shelxs and refined with Shelxl using the Olex2 suite.[36,43]

High-pressure UV-Vis spectroscopy

The measurements of UV-Vis spectra were performed in a DAC equipped with low-fluorescence synthetic AII diamond anvils. To minimize the light diffusion from the sample, on the diamond culet the investigation sample was spread into a thin film. The UV-vis spectra at high pressure were measured with a Jasco V-770 spectrophotometer adapted for using the DAC. The absorbance was measured at a scan speed of 200 nm min^{-1} in the 1200 - 350 nm range.

Absorption edges were extrapolated from the UV-Vis spectra at different pressures and were calculated from the interception between the extrapolated tangent of that absorption edge and the tangent on x-axis such that absorption is zero. The absorption egdes values were converted from nm to cm^{-1} to be directly related to energy.

CONCLUSIONS

The screening for PDI-C6, -C7, and -C8 polymorphs by solution techniques did not result in the observation of new crystal forms. However, the crystal structure of PDI-C7 form I, previously unreported, was determined from Single Crystal X-ray diffraction. The crystal structures of the different PDI-Cn form I were compared using Mercury, showing that all PDI-Cn form I structures are very similar and display the same 1D packing motif dominated by strong π-π interactions.

The thermal characterization of PDI-C6, -C7, and -C8 was thoroughly investigated by a combination of differential scanning calorimetry, variable temperature X-ray diffraction, and hot-stage microscopy, leading to the identification of several high-temperature polymorphs that forms above 190 °C. Two high-temperature polymorphs are reported for PDI-C6 (form II and form III) and PDI-C7 (form II and form III), whereas only one has been identified for PDI-C8 (form II). Despite our efforts, it was not possible to solve their crystal structures due to the elevated temperature of the data collections; hence, we reported only the phase indexing for these forms. The thermal expansion of PDI-C6, -C7, and -C8 has also been studied, highlighting a high and anisotropic thermal expansion. The high-temperature polymorphs of PDI-C6, -C7, and -C8 are completely reversible upon cooling. Although the reverse transition is always observed upon cooling, the transition's hysteresis is different depending on the technique used; such behavior might derive from strains and energy accumulation in the crystal induced by thermal contraction as in the PDI-C5 case.

Together with the thermal characterization, to further understand PDI-Cn's polymorphism and the role of different interactions in the crystal packing, we investigated the polymorphisms PDI-C5, -C6,

-C7, and -C8 at high-pressure by pressure-dependent UV-Vis absorption spectroscopy and high-pressure Single Crystal X-ray diffraction. The presence of one or more pressure-induced phase transitions was identified in all PDI-Cn by UV-Vis measurements. High-pressure Single Crystal X-ray diffraction experiments were carried out only for PDI-C5 and PDI-C6. From SCXRD we observed that form I crystals of PDI-C5 can be compressed up to ~ 1.9 GPa without transition. When the pressure is increased above this critical pressure, a pressure-induced phase transition to form IV occurs, in agreement with UV-Vis results. We determined the crystal structure of form IV and we compared it with form I, highlighting a severe drop of the stacking vector with transition due to a decrease in the displacement between stacked perylene cores. Instead, form I crystals of PDI-C6 can be compressed up to ~ 1.1 GPa without transition. When the pressure is increased above this critical pressure, a pressure-induced phase transition to form IV occurs, which can be further compressed up to ~ 1.5 GPa. Further compression causes a second pressure-induced phase transition to form V. The pressure observed for these transitions are again in agreement with UV-Vis results. The transitions in PDI-C6 do not cause a severe drop in the stacking vector as in PDI-C5, but leads to a change in the alkyl chain conformation, from a staggered conformation in form I to a gauche conformation in form V. The investigation of non-ambient polymorphism of PDI-Cn highlighted that the crystal packing is indeed dominated by the strong π-π interactions between the perylene cores, however, the alkyl chains have a major role in determining their polymorphic behavior.

ACKNOWLEDGEMENTS

NOTES

Supplementary information are reported in Appendix D.

REFERENCES

(1)   Bernstein, J. *Polymorphism in Molecular Crystals*; Oxford University Press: Oxford, 2007.

(2)   Bernstein, J. Polymorphism - A Perspective. *Cryst. Growth Des.* **2011**, *11* (3), 632–650.

(3)   Bernstein, J. Crystal Growth, Polymorphism and Structure-Property Relationships in Organic Crystals. *J. Phys. D. Appl. Phys.* **1993**, *26* (8), B66–B76.

(4)   Katrusiak, A. High-Pressure Crystallography. *Acta Crystallographica Section A: Foundations of Crystallography*. International Union of Crystallography (IUCr) January 1, 2008, pp 135–148.

(5)   Wang, C.; Dong, H.; Jiang, L.; Hu, W. Organic Semiconductor Crystals. *Chemical Society Reviews*. Royal Society of Chemistry January 22, 2018, pp 422–500.

(6)   Gentili, D.; Gazzano, M.; Melucci, M.; Jones, D.; Cavallini, M. Polymorphism as an Additional

Functionality of Materials for Technological Applications at Surfaces and Interfaces † Key Learning Points. *Chem. Soc. Rev* **2019**, *48*, 2502.

(7)   Cappuccino, C.; Catalano, L.; Marin, F.; Dushaq, G.; Raj, G.; Rasras, M.; Rezgui, R.; Zambianchi, M.; Melucci, M.; Naumov, P.; Maini, L. Structure-Mechanical Relationships in Polymorphs of an Organic Semiconductor (C4-NT3N). *Cryst. Growth Des.* **2020**, *20* (2), 884–891.

(8)   Milita, S.; Liscio, F.; Cowen, L.; Cavallini, M.; Drain, B. A.; Degousée, T.; Luong, S.; Fenwick, O.; Guagliardi, A.; Schroeder, B. C.; Masciocchi, N. Polymorphism in N , N '-Dialkyl-Naphthalene Diimides. *J. Mater. Chem. C* **2020**, *8* (9), 3097–3112.

(9)   Klebe, G.; Graser, F.; Hädicke, E.; Berndt, J. Crystallochromy as a Solid-state Effect: Correlation of Molecular Conformation, Crystal Packing and Colour in Perylene-3,4:9,10-bis(Dicarboximide) Pigments. *Acta Crystallogr. Sect. B* **1989**, *45* (1), 69–77.

(10)   Jones, B. A.; Facchetti, A.; Wasielewski, M. R.; Marks, T. J. Tuning Orbital Energetics in Arylene Diimide Semiconductors. Materials Design for Ambient Stability of n-Type Charge Transport. *J. Am. Chem. Soc.* **2007**, *129* (49), 15259–15278.

(11)   Anthony, J. E.; Facchetti, A.; Heeney, M.; Marder, S. R.; Zhan, X. N-Type Organic Semiconductors in Organic Electronics. *Adv. Mater.* **2010**, *22* (34), 3876–3892.

(12)   Zhan, X.; Facchetti, A.; Barlow, S.; Marks, T. J.; Ratner, M. A.; Wasielewski, M. R.; Marder, S. R. Rylene and Related Diimides for Organic Electronics. *Advanced Materials*. John Wiley & Sons, Ltd January 11, 2011, pp 268–284.

(13)   Huang, C.; Barlow, S.; Marder, S. R. Perylene-3,4,9,10-Tetracarboxylic Acid Diimides: Synthesis, Physical Properties, and Use in Organic Electronics. *Journal of Organic Chemistry*. 2011, pp 2386–2407.

(14)   Facchetti, A. Semiconductors for Organic Transistors. *Mater. Today* **2007**, *10* (3), 28–37.

(15)   Mei, J.; Diao, Y.; Appleton, A. L.; Fang, L.; Bao, Z. Integrated Materials Design of Organic Semiconductors for Field-Effect Transistors. *Journal of the American Chemical Society*. 2013, pp 6724–6746.

(16)   Chen, S.; Li, Z.; Qiao, Y.; Song, Y. Solution-Processed Organic Semiconductor Crystals for Field-Effect Transistors: From Crystallization Mechanism towards Morphology Control. *Journal of Materials Chemistry C*. 2021, pp 1126–1149.

(17)   Li, C.; Wonneberger, H. Perylene Imides for Organic Photovoltaics: Yesterday, Today, and Tomorrow. *Adv. Mater.* **2012**, *24* (5), 613–636.

(18)   Kippelen, B.; Brédas, J. L. Organic Photovoltaics. *Energy and Environmental Science*. 2009, pp 251–261.

(19)   Huang, C.; Sartin, M. M.; Siegel, N.; Cozzuol, M.; Zhang, Y.; Hales, J. M.; Barlow, S.; Perry, J. W.; Marder, S. R. Photo-Induced Charge Transfer and Nonlinear Absorption in Dyads Composed of a Two-Photon-Absorbing Donor and a Perylene Diimide Acceptor. *J. Mater. Chem.* **2011**, *21* (40), 16119–16128.

(20)   Hadicke, E.; Graser, F. Structures of 11 Perylene-3,4-9,10-Bis(Dicarboximide) Pigments. *Acta Crystallogr. Sect. C* **1986**, *42*, 189–195.

(21)   Balakrishnan, K.; Datar, A.; Naddo, T.; Huang, J.; Oitker, R.; Yen, M.; Zhao, J.; Zang, L. Effect of Side-Chain Substituents on Self-Assembly of Perylene Diimide Molecules: Morphology Control. *J. Am. Chem. Soc.* **2006**, *128* (22), 7390–7398.

(22) Carmen Ruiz Delgado, M.; Kim, E. G.; Da Silva Filho, D. A.; Bredas, J. L. Tuning the Charge-Transport Parameters of Perylene Diimide Single Crystals via End and/or Core Functionalization: A Density Functional Theory Investigation. *J. Am. Chem. Soc.* **2010**, *132* (10), 3375–3387.

(23) Mumyatov, A. V.; Leshanskaya, L. I.; Anokhin, D. V; Dremova, N. N.; Troshin, P. A. Organic Field-Effect Transistors Based on Disubstituted Perylene Diimides: Effect of Alkyl Chains on the Device Performance. *Mendeleev Commun.* **2014**, *24* (5), 306–307.

(24) Kuznetsova, L. I.; Piryazev, A. A.; Anokhin, D. V.; Mumyatov, A. V.; Susarova, D. K.; Ivanov, D. A.; Troshin, P. A. Disubstituted Perylene Diimides in Organic Field-Effect Transistors: Effect of the Alkyl Side Chains and Thermal Annealing on the Device Performance. *Org. Electron.* **2018**, *58*, 257–262.

(25) Curtis, M. D.; Cao, J.; Kampf, J. W. Solid-State Packing of Conjugated Oligomers: From π-Stacks to the Herringbone Structure. *J. Am. Chem. Soc.* **2004**, *126* (13), 4318–4328.

(26) MacRae, C. F.; Sovago, I.; Cottrell, S. J.; Galek, P. T. A.; McCabe, P.; Pidcock, E.; Platings, M.; Shields, G. P.; Stevens, J. S.; Towler, M.; Wood, P. A. Mercury 4.0: From Visualization to Analysis, Design and Prediction. *J. Appl. Crystallogr.* **2020**, *53*, 226–235.

(27) Marin, F.; Tombolesi, S.; Salzillo, T.; Yaffe, O.; Maini, L. Thorough Investigation on the High-Temperature Polymorphism of Dipentyl-Perylenediimide: Thermal Expansion vs Polymorphic Transition. **2021**.

(28) Park, S. K.; Diao, Y. Martensitic Transition in Molecular Crystals for Dynamic Functional Materials. *Chem. Soc. Rev* **2020**, *49*, 8287.

(29) Khalil, A.; Karothu, D. P.; Naumov, P. Direct Quantification of Rapid and Efficient Single-Stroke Actuation by a Martensitic Transition in a Thermosalient Crystal. *J. Am. Chem. Soc.* **2019**, *141* (8), 3371–3375.

(30) Chung, H.; Dudenko, D.; Zhang, F.; D'Avino, G.; Ruzié, C.; Richard, A.; Schweicher, G.; Cornil, J.; Beljonne, D.; Geerts, Y.; Diao, Y.; D'Avino, G.; Ruzié, C.; Richard, A.; Schweicher, G.; Cornil, J.; Beljonne, D.; Geerts, Y.; Diao, Y. Rotator Side Chains Trigger Cooperative Transition for Shape and Function Memory Effect in Organic Semiconductors. *Nat. Commun.* **2018**, *9* (1), 278.

(31) Sun, H.; Park, S. K.; Diao, Y.; Kvam, E. P.; Zhao, K. Molecular Mechanisms of Superelasticity and Ferroelasticity in Organic Semiconductor Crystals. *Chem. Mater.* **2021**, *33* (5), 1883–1892.

(32) Altomare, A.; Cuocci, C.; Giacovazzo, C.; Moliterni, A.; Rizzi, R.; Corriero, N.; Falcicchio, A. EXPO2013: A Kit of Tools for Phasing Crystal Structures from Powder Data. *J. Appl. Crystallogr.* **2013**, *46* (4), 1231–1235.

(33) Cliffe, M. J.; Goodwin, A. L. PASCal : A Principal Axis Strain Calculator for Thermal Expansion and Compressibility Determination. *J. Appl. Crystallogr.* **2012**, *45* (6), 1321–1329.

(34) van der Lee, A.; Dumitrescu, D. G. Thermal Expansion Properties of Organic Crystals: A CSD Study. *Chem. Sci.* **2021**, *12*, 8537–8547.

(35) Sheldrick, G. M. SHELXT - Integrated Space-Group and Crystal-Structure Determination. *Acta Crystallogr. Sect. A Found. Crystallogr.* **2015**, *71* (1), 3–8.

(36) Sheldrick, G. M. Crystal Structure Refinement with SHELXL. *Acta Crystallogr. Sect. C Struct. Chem.* **2015**, *71*, 3–8.

(37) Sheldrick, G. M. A Short History of SHELX. *Acta Crystallographica Section A: Foundations of Crystallography*. International Union of Crystallography (IUCr) January 1, 2008, pp 112–122.

(38) Coelho, A. A. TOPAS and TOPAS-Academic: An Optimization Program Integrating Computer Algebra and Crystallographic Objects Written in C++: An. *J. Appl. Crystallogr.* **2018**, *51* (1), 210–218.

(39) Merrill, L.; Bassett, W. A. Miniature Diamond Anvil Pressure Cell for Single Crystal X-ray Diffraction Studies. *Rev. Sci. Instrum.* **1974**, *45* (2), 290–294.

(40) Piermarini, G. J.; Block, S.; Barnett, J. D.; Forman, R. A. Calibration of the Pressure Dependence of the R1 Ruby Fluorescence Line to 195 Kbar. *J. Appl. Phys.* **1975**, *46* (6), 2774–2780.

(41) Mao, H. K.; Xu, J.; Bell, P. M. Calibration of the Ruby Pressure Gauge to 800 Kbar under Quasi-Hydrostatic Conditions. *J. Geophys. Res. Solid Earth* **1986**, *91* (B5), 4673–4676.

(42) Budzianowski, A.; Katrusiak, A. High-Pressure Crystallographic Experiments with a CCD-Detector. **2004**, *140*, 101–112.

(43) Dolomanov, O. V; Bourhis, L. J.; Gildea, R. J.; Howard, J. A. K.; Puschmann, H. OLEX2: A Complete Structure Solution, Refinement and Analysis Program. *J. Appl. Crystallogr.* **2009**, *42* (2), 339–341.

CHAPTER 7: SELF-ORGANIZING MAPS AS A DATA-DRIVEN APPROACH TO REVEALS THE VARIETY OF PACKING MOTIVES OF PDI DERIVATIVES.

The SOM and PCA analyses were carried out by Dr. Alessandro Zappi and Prof. Dora Melucci from department of Chemistry "G. Ciamician", University of Bologna.

The manuscript is going to be submitted to the journal *Molecular Systems Design & Engineering (MSDE)*.

ABSTRACT

The possibility to efficiently classify observed or predicted crystals structures into a small number of families of related structures can be extremely important in the design of materials with specific packing and properties. In this respect, the traditional way to classify the crystal packing of organic semiconductors as herringbone, sandwich-herringbone, β- and γ-sheets by visual inspection can be limited and inadequate. Herein, we present the use of a clustering method based on a combination of self-organizing maps (SOM) and principal component analysis (PCA) as a data-driven approach to classifying different π-stacking arrangements into families of similar crystal packing. We explore the π-stacking arrangements within the crystal structures deposited in the CSD database of perylene diimides (PDIs) derivatives with different types and positions of the substituents. The structures were characterized by a set of descriptors that were then used for the clustering. Six different packing families of PDIs were identified and their characteristics were discussed. Finally, the effects of different substituent types and positions on the resulting packing arrangement were discussed.

KEYWORDS

Cambridge Structural Database (CSD), perylene diimide (PDI), self-organizing maps (SOM), principal component analysis (PCA), packing motives, molecular organic semiconductors.

INTRODUCTION

Organic electronics have received an increasing amount of academic and industrial interest in recent decades involving research and development across various fields such as chemistry, physics, material science, and engineering. This rapid growth in the interest given to π-conjugated materials and in particular to organic semiconductors (OSCs) originates from their numerous attractive features including mechanical flexibility, low-cost, solution processability, molecular-level tunability, and so on. These properties make OSCs highly versatile functional materials to be incorporated as building

blocks for the design of high-performing flexible optoelectronic devices.[1–5] Currently, they are widely used in various organic electronic devices such as organic light-emitting diodes (OLED),[6,7] organic field-effect transistors (OFET),[8–10] and organic photovoltaic cells (OPV)[11–13]. These devices' performances depend critically on the efficiency of charge transport within the material, therefore the key to success in the development of OSCs for everyday life applications are OSCs displaying high charge carrier mobility, together with air stability and solubility in commonly used solvents to be easily processed by low-cost techniques.[1,3,14]

Since their discovery, a large number of OSCs have been developed, reported and investigated, such as oligoacenes (like pentacene and rubrene),[1,8,9] oligothiophenes,[1,8] thiazole derivatives,[1,15] benzothienobenzothiophenes,[9,16] fullerenes,[1,8,15] perylenes,[1,2,8,17] and so on.

Among the OSCs, perylene diimides (PDIs) have been an object of research for more than 100 years and have been known as a group of high-performance industrial organic pigments, which are currently used in fibre application and industrial paints.[18,19] Besides their application as industrial pigments, in the past 20 years the interest in PDI, as well as other dyes and pigments, moved from traditional colourant toward application as functional solid-state material.[13,20] In fact, PDI derivatives are currently well-known as a family of very promising and versatile n-type materials for organic optoelectronic applications due to their commercial availability, low costs, excellent chemical, thermal and photostability, high electron affinity, strong absorption in the visible region, low LUMO energies and good charge transport properties. Furthermore, their electronic, optical and charge transport properties can be tuned over a wide range via functionalization.[2,12,13,17,21,22] The combination of these properties makes PDIs promising candidates for several applications such as OFETs,[2,8–10,21] OPV cells,[11–13] laser dye,[23,24] sensors,[25] bioimaging,[26] etc. PDIs are also studied for low-temperature thermoelectric generator applications.[27]

Thanks to their planar structure and peripherally rich oxygen atoms, PDIs typically arrange to form π-π stacking interactions between molecules. Nevertheless, substitution can vary greatly the extent of intermolecular π-orbital overlap among PDI derivatives, and thus can make a significant effect on the solubility, optical and electrochemical properties, crystal packing and structural morphology.[5,17,28–32] The perylene diimide core has ten functionalizable positions: the N,N' positions which are known as the *imide*-; the 1,6,7,12 positions known as the *bay*-; and the 2,5,8,11 positions known as the *ortho*-positions (Figure 1). These numerous positions for introducing functional groups are the reason for the popularity of PDIs, making them versatile for tailoring the properties for specific applications.[17,21] In general, substitution at *imide*-position maintains the planarity of the perylene aromatic core, and can effectively tune solubility, aggregation, and solid-state molecular packing, but shows only limited

effects on the molecular-level optical and electronic properties of PDIs.[17,19,29,33] On the other hand, optical and electronic properties of PDIs can be significantly modified via substitution at the perylene core in the *bay-* and *ortho*-positions. Substitution at *bay*-position, besides affecting the optical and electronic properties of the material, may lead to the twisting of the two naphthalene half units in PDIs due to steric effects; however, large geometric distortions of the core may weaken the intermolecular π-π overlap and thus may be detrimental for charge carrier mobilities.[17,21,24,34] Lastly, *ortho*-functionalization creates the possibility to modify the optoelectronic properties while at the same time retaining the planarity of the perylene core.[17,35] The adjustment of the PDI properties can be achieved through combinations of *imide-*, *bay-* and *ortho-* functionalization.
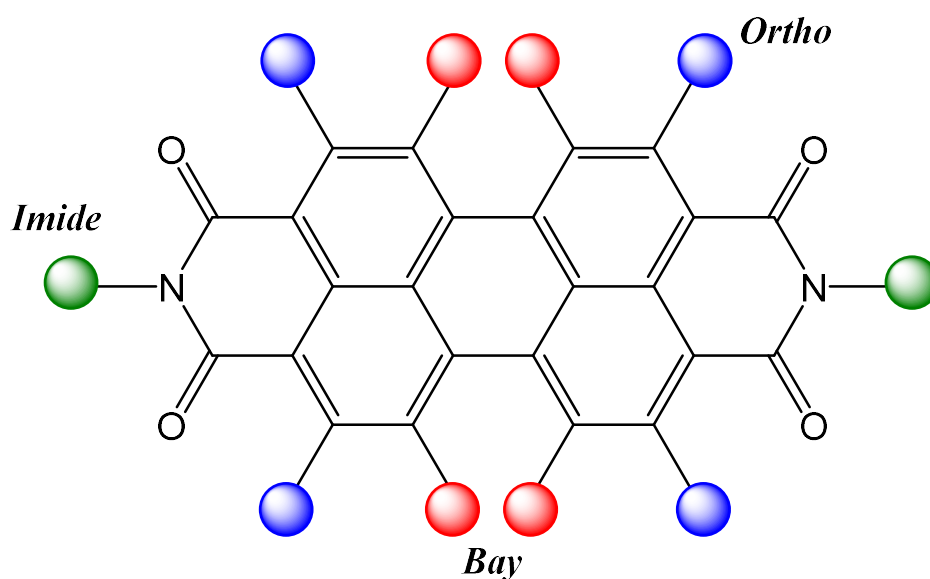
Figure 1. Chemical structure of a generic PDI showing the different positions for substitutions: *imide*-positions highlighted in green, *bay*-positions in red, and *ortho*-positions in blue.

A long-standing goal and challenge of OSCs materials and of crystal engineering that has been involving a lot of experimental and computational effort, is understanding the relationship among the molecular packing motifs, intermolecular interactions, and properties of molecular materials for efficient design of crystalline material for specific applications. Attempts to correlate structural arrangements to specific properties in order to predict solid-state materials with tailored properties have been made already in the 1980s and early 1990s, where the crystallochromy (i.e., the dependence of colour on crystal packing) of PDIs with varying substituents in the imide position was investigated in depth both experimentally and theoretically, highlighting that intermolecular packing greatly impacts the optical properties. In particular, an empirical model to correlate absorption maxima with the π-π contact area between stacked molecules was developed and theoretically was found a strong correlation between crystal colour and displacement along the long- (x) and short-axes (y) of the perylene core.[19,28,36] After these pioneer works, a lot of effort has been made in the theoretical insight

into optoelectronic properties for a deeper understanding of the structure-properties relationship. For instance, Fink et al. and Zhao et al. evaluated the potential energy surfaces (PES) for the ground state of PDI dimers as a function of the shift along the x- and y-axes of the perylene core and as a function of the rotation (φ) between co-facially stacked dimers, and they evaluated excitation energies of PDI crystal structures;[37,38] Vura-Weis et al. mapped the relationships between stacking geometry, binding energy and electronic coupling for dimers of 20 PDI derivatives based on density functional theory (DFT);[39] Delgado et al. investigated the effect of the type, number and position of the substituents on charge-transport properties of 30 imide-substituted PDIs and 7 bay- and bay/imide-substituted PDIs;[31] Geng et al. investigated the influence of substituents on different positions (ortho, bay and imide) of 17 PDI derivatives on their packing, intermolecular interactions, and electronic properties.[32] Furthermore, several other works, both experimental and theoretical, have been published on PDI derivatives investigating the effects of different substituents on the material performance in specific applications, for example, the use of linear chains,[3,40] fluorinated chains,[41] or branched chains[3,42,43] in imide position, the use of cyano substituent,[44] halogenated substituents,[45] or other substituents at the core.[24,46]

Most of the works above mentioned are mainly based on dimer approaches on reduced data sets of similar molecules due to the large molecular size of the involved molecules that leads to high computational costs. More recently, to overcome the limitations of the dimeric approach and thanks to recent advances in computational power and the development of smart algorithms in the field of machine learning and artificial intelligence, the discovery and design of OSCs materials with interesting properties and the investigation of their structure-property relationship are going towards two main computational approaches that take into account the entire crystal structure: multiscale approaches and data-driven searches.[47] Multiscale approaches combine different methods and models for computing the reorganization energies, the electronic couplings, and for evaluating the disorder effects;[47–49] they can be combined with crystal structure prediction to screen for interesting packing arrangements.[50–52] Data-driven searches make use of the high amount of data present in databases such as CSD to carry out large scale screening strategies to predict the semiconducting properties of materials from various computable descriptors and thus to explore their structure-property relationships.[47,53–55]

The mentioned recent advances in predicting OSCs with interesting properties make use of prior knowledge on the crystal structures, either experimental[54] or calculated from CSP;[51] in fact, the knowledge of the crystal packing is very important for investigating the property of a material, because it reveals the intrinsic properties of organic semiconductors, providing a powerful tool for

examining structure-property relationships. Therefore, understanding the molecular packing features is beneficial for both the design and synthesis of OSCs and understanding the structure-property relationship and the limits of charge transport.[5] Furthermore, the possibility to efficiently classify observed or predicted molecular crystals into a small number of families of related structures can be extremely important in the design of materials and crystal phases with specific packing and properties. In this respect, the traditional way to classify the crystal packing of OSCs is to describe the π-stacking interactions responsible for the charge carrier mobility such as herringbone, sandwich-herringbone, β- and γ-sheets by visual inspection can be limited and inadequate.

In this work, we investigate the packing arrangements over 103 PDI derivatives crystal structures deposited in the CSD database to test a clustering method based on a combination of self-organizing maps (SOM) and principal component analysis (PCA) as a data-driven approach to classify different π-stacking arrangements of PDIs. This method aims to identify families of PDIs stacking arrangements using a number of descriptors that were chosen to characterize each PDI's crystal structure and aims to give guidelines for predicting the most likely packing family depending on substituents used and for assessing the families of new crystal structures of PDI derivatives. Furthermore, we believe that this way of crystal structure clustering can be applied also to other types of OSCs and could help theoretical studies to achieve efficient and data-driven clustering of structures to identify the model systems that best describe each specific family of packing arrangements. Lastly, this clustering-based classification of crystal structures can be used in the future to correlate different families of structures with OSC's properties, however, investigation of the PDIs properties in different clusters is beyond the scope of this work.

RESULTS AND DISCUSSION

The search for PDI derivative's structures in CSD resulted in the selection of 103 different crystal structures for the analysis. For these structures, the variables indicating the temperature of the data collection (Temperature), Z, and Z' were used to give information about the crystal structure. The variables indicating the molecular volume (V_{mol}), the substituent position, the type of substituent at the *imide-*, the type of substituent at the core, the torsional angle of the PDI's perylene core resulting from the twisting of the two naphthalene half units (torsion), and the molecular aspect ratio (with the three variables S, S/L, and M/L) are used to describe the molecule within the crystal structure. Lastly, the π-stacking arrangement within the crystal packing was described by considering the stacking between a dimer formed by two neighbouring PDI molecules in the packing, thus the variables are calculated to give the relative position of one molecule in the dimer with respect to the other one. The variables describing the stacking arrangement are the distance between the centroids of the perylene

cores (SV); the interplanar distance between the perylene planes ($d_{\pi\text{-}\pi}$); the displacement of the perylene units along the long (Δx) and short (Δy) molecular axis; the directions cosines of the SV (χ with the x-axis and ψ with the y-axis); the angles of the perylene unit slipping along the x- and y-directions (P and R respectively); the tilt angle between the plane of the two perylene cores within the dimer (tilt); the degree of criss-cross of the molecules in the dimer (rotation). These variables were collected and calculated, resulting in a dataset of 142 different sets of descriptors. See Experimental Section for further details on the dataset and descriptors.

From the collection and calculation of the different variables, we observed two different strategies in PDIs to minimize repulsion between the aromatic units and achieve a tighter stacking compared to the face-to-face situation: a shifted cofacial alignment, that means non-zero Δx and Δy, and/or a rotation between the stacked aromatic cores, *i.e.* non-zero rotation.

After collecting and calculating the variables for all the 142 samples (from now on called "objects"), we used the SOM method[56] to find families of packing arrangements. SOM is an unsupervised machine learning technique (that does not require previously indication about the samples' pertaining group) aimed at finding groups of objects with similar features. The computation was carried out with the R package *SOMEnv*,[57] adapting the algorithms developed by Licen et al. for environmental problems to our use for crystallographic purposes.

Since the SOM output and the final objects' grouping may depend on the map dimensionality and the number of clusters in which the SOM units are divided, we trained and clusterized 4 different maps. Once trained the map, moreover, with *SOMEnv* it is possible to automatically calculate several numbers of clusters for the SOM units and to choose the best number as the one minimizing the DB index.[58] For all trained maps, up to eight clusters were calculated.

The first two eigenvalues calculated by PCA on the original dataset are 4.38 and 3.51. These values (together with the number of samples) were then used as the guidelines to define the map's dimensions, following the empirical rules of Nakagawa et al.[59] The trained maps had then the following dimensions and clusters number: 5x3 with 8 clusters; 9x7 with 5 and 8 clusters (the two BD indexes were very close, making difficult to choose between one of them as the best); 10x6 with 5 clusters; 17x4 with both 6 and 7 clusters. Therefore, six different results of objects' grouping were obtained. In order to obtain reliable groups of objects, the SOM results were compared and the structures that were grouped together by all trained SOMs were considered as pertaining to the same family. In this way, six main families of structures were identified, describing 109 out of the starting 142 objects. The remaining objects were, in general, at the border between these families and were either grouped into minor families (less than five objects always grouped together by SOMs) or not

grouped at all. To best visualize the result of SOM grouping, the PCA scores plot was used. The scores of PC1 vs PC2 are shown in Figure 2, the colour of the scores correspond to the family in which each structure was categorized.
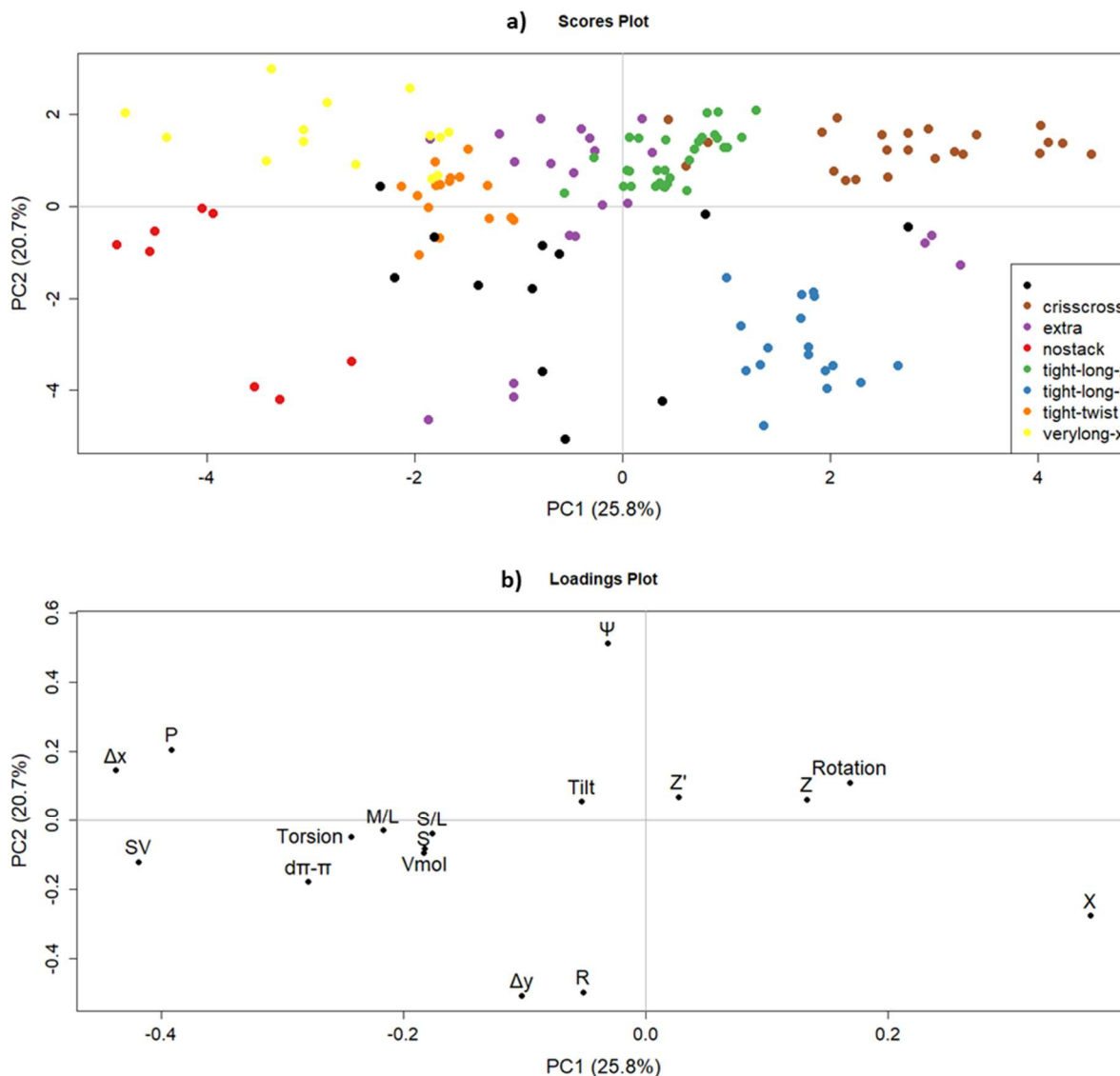
Figure 2. a) PC1-PC2 scores plot obtained by PCA, with the scores categorized by the family they belong to. The 6 major families are: *tight-long-x* (green), *crisscross* (brown), *tight-long-y* (blue), *nostack* (red), *tight-twist* (orange) and *verylong-x* (yellow). The "*extra*" group (purple) contains all the minor groups that do not entirely fit in one of the 6 major families, whereas the black dots are the scores that do not belong to any major or minor group. b) PCA loadings plot that gives visual inspection of the variables most influencing each family.

From the scores plot in Figure 2, we observe that different families obtained using SOM are found in different areas of the PC1-PC2 plot. We named the different groups depending on the area of the scores plot they lie in. The 6 major families identified are *tight-long-x* (green coloured), which lies close to the origin; *crisscross* (brown) that lies at positive values of both PC1 and PC2; *tight-long-y* (blue) that lies at positive PC1 and negative PC2 values; *tight-twist* (orange) that lies at moderate negative PC1; *verylong-x* (yellow) lies at negative PC1 and positive PC2 values; *nostack* (red) lies at

negative values of both PC1 and PC2. The *extra* group (purple) contains all the minor clusters found in the SOM, whereas the black scores are the ones that did not fit unambiguously in any of the other major or minor groups. Interestingly, the scores at negative PC1 tend to be more scattered compared to the positive ones, *i.e.*, the families in the right part of the scores plot are more homogeneous than the ones in the left part.

Once established the different families, we investigated in detail the principal characteristics of each of them and their typical structure. A visual inspection of the variables most influencing each family can be given by the PCA loadings plot reported in Figure 2b. Indeed, there exists a quadrant correspondence between scores and loading plots: the variables in a certain quadrant of the loadings plot are the ones most directly influencing the scores in the same quadrant. Therefore, for example, the families *tight-twist* and *verylong-x* are the ones with higher values of Δx and P, while the *crisscross* family is the one with higher Rotation and Z values. However, in order to better visualize important insight into the variation of the variables in each group, boxplots of the most important variables were created and are shown in Figure 3. In the boxplots, the variation range of each variable is plotted for each family, and these can give information about the range and distribution of each variable. The use of boxplots, coupled with the inspection of the scores in each family allowed us to identify the families' most important characteristics.

The *tight-long-x* group comprehend 31/142 objects and is characterized by a very narrow distribution of all the variables (Figure 3). This group is characterized by short $d_{\pi-\pi}$ distance, in the range 3.31-3.52 Å, typical of effective π-π interactions between aromatic cores.[60] Similar $d_{\pi-\pi}$ distances can be found in the *crisscross* (3.32-3.55 Å) and *tight-long-y* (3.36-3.70 Å) families. The groups with short $d_{\pi-\pi}$ distances are the ones in the right area of the scores plot, at positive PC1, besides a couple with small negative PC1. The other variables characteristic of *tight-long-x* are Δx and Δy. In *tight-long-x*, Δx has values in the range 2.45-3.46 Å and Δy in the range 0-1.33 Å, which means that this family is characterized by a displacement with rather high Δx and small Δy ($\Delta x >> \Delta y$). Lastly, no molecules with non-zero torsion angles are present in this family, and it is the only group with such characteristics.

The *tight-long-y* family, which comprehend 17/142 scores, beside the short $d_{\pi-\pi}$ distances (3.36-3.70 Å) already mentioned, like the *tight-long-x* group, is characterized by a displacement along the x- and y-direction to achieve a tighter packing; however, in this cluster, the displacement is higher along the y-direction compared to the x-direction ($\Delta x < \Delta y$). Indeed, in this cluster, Δx values are in the range 0.18-2.03 Å and Δy in the range 2.41-4.35 Å. Nevertheless, as a consequence of their similar $d_{\pi-\pi}$

distances and their displacement (even if in different directions), *tight-long-x* and *tight-long-y* also have similar SV values. Finally, 5/17 samples of this group have non-zero torsion.
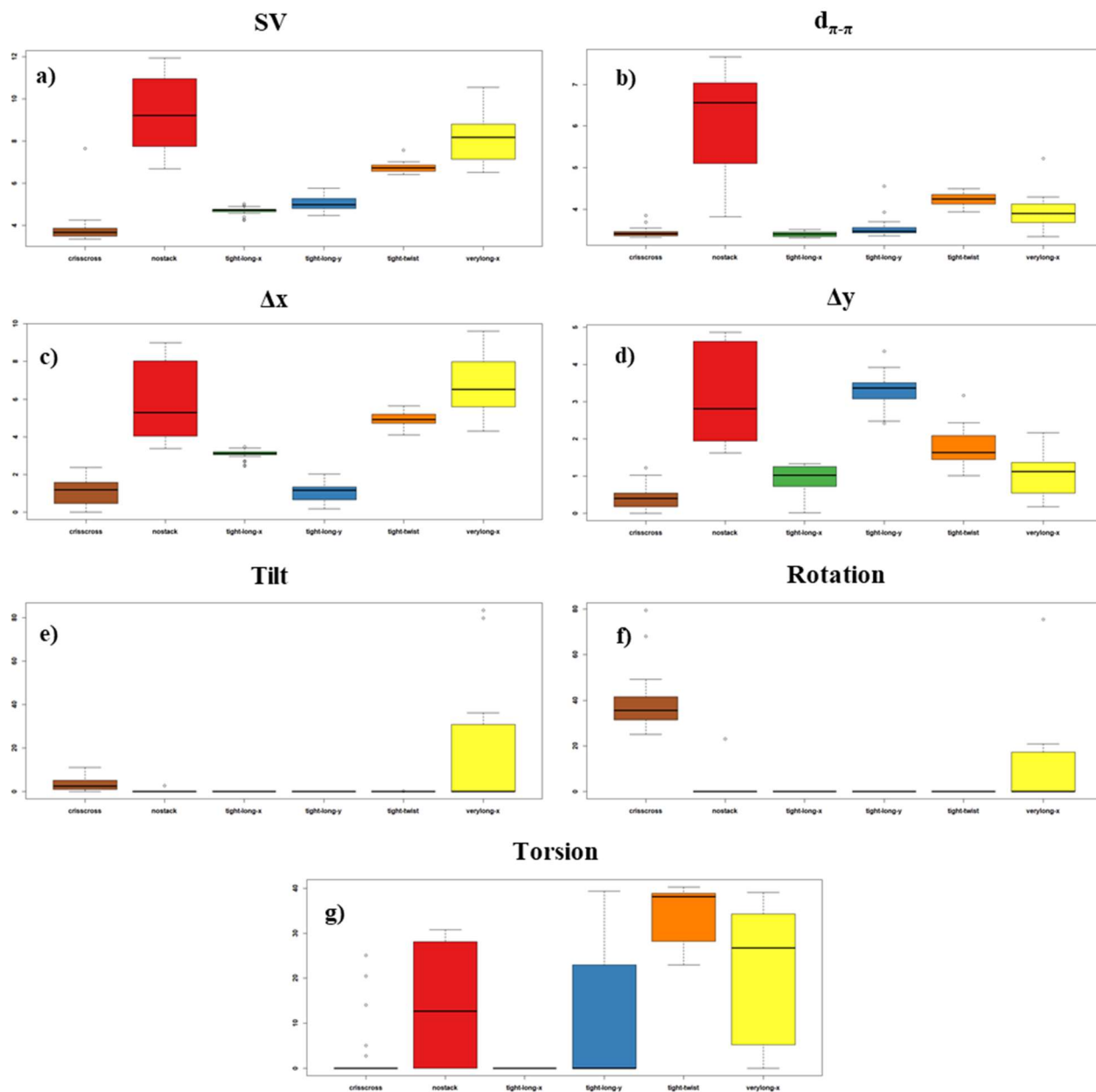
Figure 3. Boxplots of the variable's distributions among the identified families. These boxplots are relative to a) SV; b) $d_{\pi-\pi}$; c) Δx; d) Δy; e) tilt; f) Rotation; g) torsion.

The *crisscross* family comprehend 23/142 scores. The principal characteristics of this group are highlighted by Figure 3e and 3f, which shows that *crisscross,* together with *verylong-x,* is one of the only two families showing non-zero rotation and tilt. In particular, *crisscross* is the only group with all the structures in criss-cross (non-zero rotation). Furthermore, *crisscross* is the family with the shortest SV; such feature is a consequence of the criss-cross arrangement. Since rotation between the aromatic cores allows a closer packing, a displacement such as in *tight-long-x* or *tight-long-y* is not

necessary for a close packing in the *crisscross* family. Thus, Δx (0-2.4 Å) and Δy (0-0.75 Å) are both very small in this group, and because of this and of similar short $d_{\pi-\pi}$ distances (3.32-3.55 Å), the distance between the molecular centroids (SV) is also small. Even in this group, some objects present torsion, but only 5/23, so it's not a common feature of the group.

In the *tight-twist* family, there are 16/142 samples. This group lies in an area of the scores plot between *tight-long-x*, *verylong-x* and *nostack*, at small negative PC1 and between small positive and small negative PC2, which means that it is a cluster with intermediate characteristics between those three. Its peculiar characteristic is that this family is the only one with all the structures with twisted perylene core and the group with the highest torsion angles. Furthermore, in this family, the distribution of values of the different variables are quite narrow like in the previously described ones. This group is characterized by rather high $d_{\pi-\pi}$ distances (3.94-4.50 Å). Furthermore, Δx (4.1-5.64 Å) and Δy (1-3.16 Å) are higher than in *tight-long-x*, though Δy values are not as high as in the *tight-long-y* family. Indeed, considering high values for $d_{\pi-\pi}$, Δx, and Δy, this group is characterized by a higher SV compared to the previously described groups where very close π-π distances were observed.

The *verylong-x* family comprehend 14/142 scores. This group is characterized by the very high SV (6.51-10.55 Å) and Δx (4.29-9.62 Å), but small Δy (0.17-2.16 Å). Within the group, generally, $d_{\pi-\pi}$ has slightly lower values than in *tight-twist* (3.34-4.29 Å) beside one object with a high one (5.22 Å). As before mentioned, some of the objects within this group have non-zero rotation and/or tilt, however, they are a minority within the group (4/14 with tilt and 6/14 with rotation) and they are not in the *crisscross* group because they differ in the other parameters.

The last major family, *nostack*, comprehend 8/142 scores. As Figure 3 clearly shows, this group has the highest SV, Δx, Δy and $d_{\pi-\pi}$, which means that for the structures within this group, the π-stack interactions are not important anymore, while other intermolecular interactions are dominant. Furthermore, despite the low number of objects in it, this group has the largest distribution for the variables' values; therefore, it seems that these objects are grouped together not because they share real common traits, but because they share the fact that they have very different characteristics from the other families.

Out of the 33/142 objects that did not fit in any of the major families, 12 were not addressed to any group, whereas 21 are in the *extra* group, divided into five minor groups (see Figure S15). As before mentioned, these five *extra* groups do not fit unambiguously in any of the six major families, because they have some parameters that would fit in a group, but other parameters that fit into another group. The *extra1* (4 objects) objects were addressed to *tight-twist*, to *nostack*, or none of the major families by the various SOMs; this is because they have high $d_{\pi-\pi}$ (4.05-4.09 Å), a non-zero torsion and

intermediate Δy values that could fit in these groups, but their Δx and their SV are too small. Also, the *extra2* (3 objects) group fitted to either *tight-twist*, *nostack*, or none of the major families in different SOMs, but for different parameters: they have high SV, Δy and $d_{\pi\text{-}\pi}$ (closer to *nostack* values), but small Δx that do not fit in these groups, resulting in high R values (R > 38 °, higher than P), only typical of the *tight-long-y* family, they were never clustered together though. The *extra3* groups (3 objects) lies between the *crisscross* and *tight-long-y* families and in various SOMs it was fitted to either one of these two families. This group have small SV, $d_{\pi\text{-}\pi}$, and Δx values that could fit in *crisscross*, but the objects in this group do not have rotation nor tilt (characteristic of *crisscross* family) and their Δy is slightly too high; at the same time Δy and SV are too low to fit in the *tight-long-y* family, despite $d_{\pi\text{-}\pi}$ and Δx are similar. The *extra4* group (8 objects), as the *extra5* group (3 objects) have parameters that could fit into *tight-long-x* and *tight-twist*. These objects have $d_{\pi\text{-}\pi}$ values higher than *tight-long-x* and lower than *tight-twist*, some of them are twisted, their SV is similar to the one found in *tight-long-x*, besides a couple of *extra4* scores; Δx and Δy values are similar to *tight-long-x* and not to *tight-twist*.

A visual representation of the different typical stacking in crystal structures of the major families identified, that best summarize the characteristics of each group, is given in Figure 4.
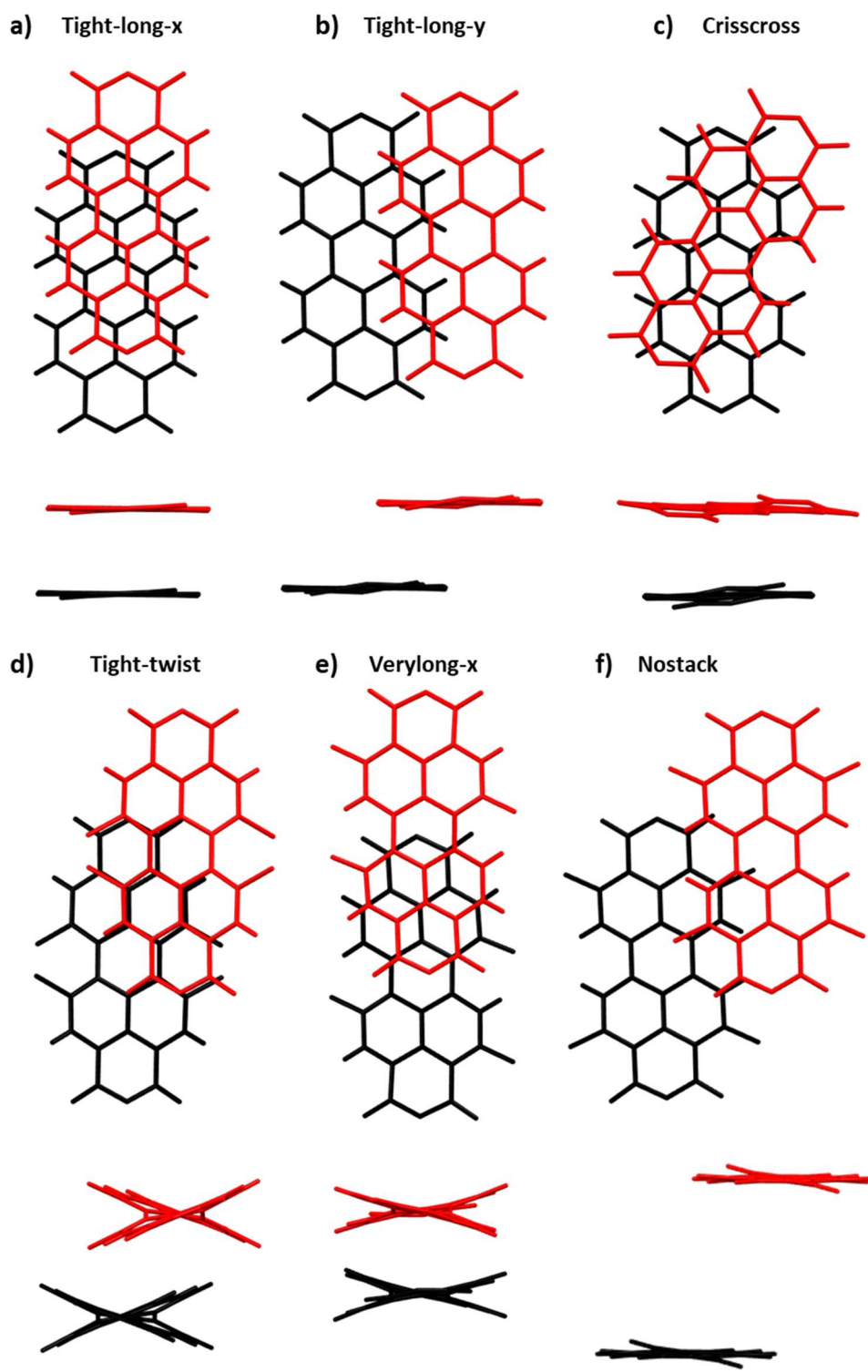
Figure 4. Stacking of the perylene core in the different major clusters identified viewed along z (top) and x (bottom) axis. a) *tight-long-x*, refcode DICNIM; b) *tight-long-y*, refcode SAGWEC; c) *crisscross*, refcode MIWHEF; d) *tight-twist*, refcode NIXWIC02; e) *verylong-x*, refcode KUWXOR; f) *nostack*, refcode USAFEB01.

Figure 4 shows that the overlay between perylene cores in the *tight-long-x* and *crisscross* families (Figure 4a and 4c) is high; the structures within these two groups are indeed characterised by a well-defined 1D packing motif along the direction of the π-stacking. Instead, in the case of *tight-long-y* (Figure 4b), the large displacement along the y-direction leads to a minor overlay of the perylene

cores, however, higher displacement lead also to a 2D packing motif, which can be beneficial for charge mobility.[32] Looking at the *tight-twist* family (Figure 4d), it clearly resembles the characteristics described previously, which are high torsion, higher displacement along x and y direction that result in a lower core overlay and a higher $d_{\pi-\pi}$; nevertheless, some degree of π-stacking is still important in this group, even though it is clear that the packing is driven also by other types of interactions. Finally, although the objects within *nostack* and *verylong-x* families are always clustered together by SOMs, they differ from each other, especially in the case of *nostack* ones; thus, the structures given in Figure 4e and 4f are meant to show the main stacking characteristics that group the objects together in these two groups. In the *nostack* this is reflected in the high variability of the parameters within the group, in addition, some objects have torsions or rotation, while some do not. Instead, in *verylong-x* most of the objects are similar, besides the ones with high rotation and/or twist that differ from the majority of the group. In particular, two objects (refcode YIWMEY and XAPRIQ) have extremely high tilt values (~80 °). In these cases, there are no π-stacking interactions between the perylene cores, because they are almost perpendicular to each other. Instead, a dipole-π interaction is observed between the perylene core and the carbonyl oxygen of the closest molecule (Figure S16).
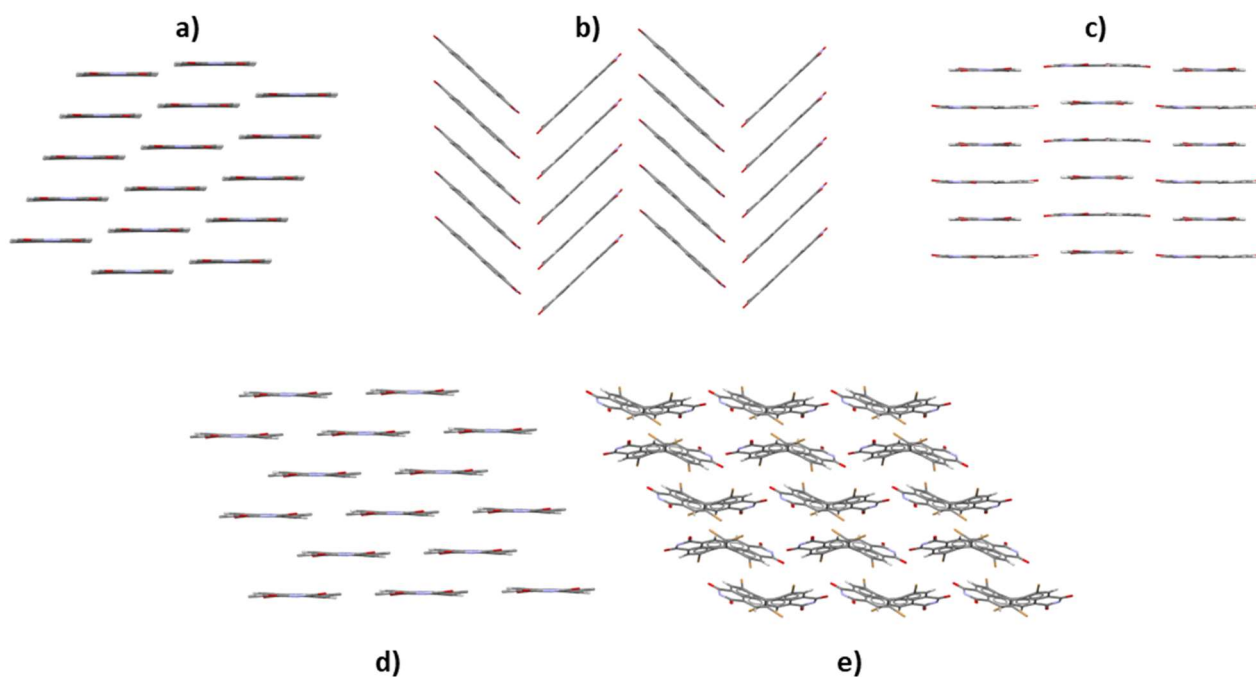
Figure 5. Common molecular packing motifs observed in the PDI's crystal structure investigated. a) DICMUX, *tight-long-x* family; b) DICNIM, *tight-long-x* family; c) FEDPOU, *crisscross* family; d) FEHROA, *tight-long-y* family; e) OWOMEU, *tight-twist* family.

Some examples of common molecular packing motifs of the PDI's crystal structures are reported in Figure 5. The packing motif in Figure 5a,b are common in the *tight-long-x* family and are two ways in which their well defined 1D stacking can be achieved in the structure; despite the same 1D packing motif, they can be differentiated as β-sheets (Figure 5a) and γ-sheets (Figure 5b). Another way of 1D

stacking is shown in Figure 5c, where the packing of a *crisscross* structure is given showing the criss-cross molecules along the π-stacked columns. Figure 5d shows a packing from the *tight-long-y* family, where its high displacement along y leads to a 2D packing motif, which can be also described as a β-sheet packing motif Figure 5e shows a typical 1D packing motif with a twisted core that can be found in the *tight-twist* family.

One limitation of this work is that the descriptors for the structures to investigate the stacking interactions are calculated by considering the dimer of one molecule with the closest molecule. Therefore, few cases within the considered PDIs show good π-stacking interactions within the dimer, but weaker interactions with other neighbouring molecules due to steric hindrance effects or other interactions caused by substituents. An example of such structures is shown in Figure 6.
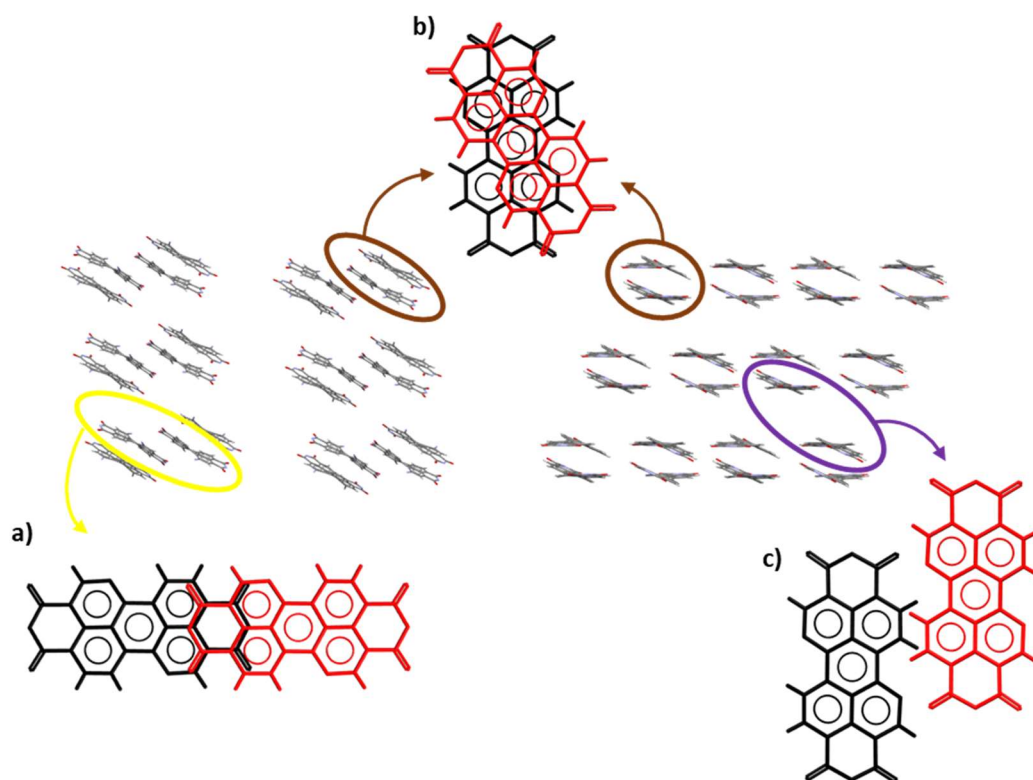
Figure 6. Example of crystal packing with good π-stacking interactions within the dimer, but weaker interactions with other neighbouring molecules. In the figure is shown the crystal structure of BAMCAV, viewed along two perpendicular slices of the packing, described by three different objects that were clustered in three different groups: a) *verylong-x* family; b) *crisscross* family; c) *extra2* group. Substituents are omitted for clarity sake.

These results clearly show that for the PDIs there are a lot of different structures that can be achieved through different functionalization, leading to a very rich landscape of possible packing arrangements and stacking interactions. The simple traditional description of the packing motif can not fully grasp such complexity, for example, Figure 5a, Figure 5c and Figure 5d show structures that can all be described as β-sheets even though the stacking is quite different.

To investigate the role of different functionalization in the packing of different PDI derivatives, we investigated first how different positions for substitution (*i.e., imide-, bay-* and *ortho-*position) can influence the packing, and then how different types of substituents can determine in which group they are more likely to fit.

First, we considered the PDIs substituted only in *imide*-position (68/142 objects). In these PDIs, two of the major families are strongly preferred over the others: *tight-long-x* and *crisscross*. 29 out of 68 objects with only *imide*-substitution are in the *tight-long-x* family and 20 out of 68 are in *crisscross*, which also means that almost all the scores within these groups are substituted only in the *imide*-position (besides 2 objects for *tight-long-x* and 3 for *crisscross*). Third for importance for *imide* substituted PDIs is the *tight-long-y* group with 7 objects. While the 12 remaining objects are divided between the other groups. From these findings, we observe that most of the *imide* objects are found in the tight-long-x-right area of the scores plot (Figure 7) where the clusters are characterised by closer stacking between perylene cores.
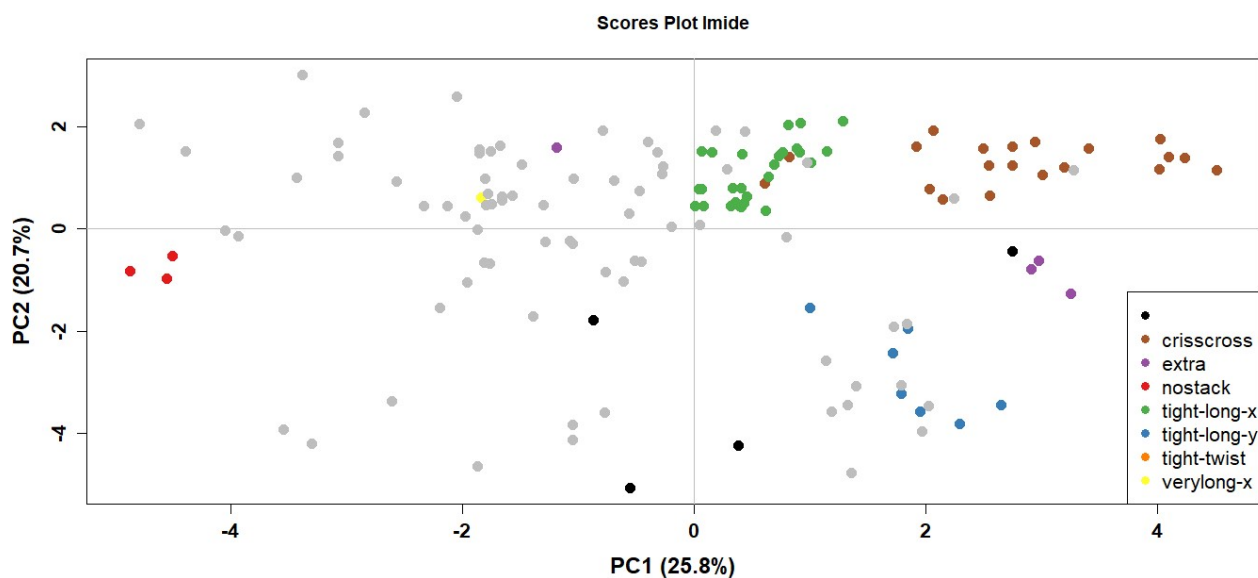
Figure 7. PC1-PC2 scores plot obtained by PCA, with the *imide*-substituted objects categorized by the family they belong to by the colour. The core-substituted objects are coloured in grey. Most of the *imide* objects are at positive PC1 values, where the objects are characterised by closer stacking between perylene cores.

We observed some patterns between the type of substituents at *imide-* used and the resulting stacking arrangement and thus the family they belong to. When the substituents are linear chains, especially long chains, are most likely going to have a packing with the characteristic of the *tight-long-x* group; only few PDIs with linear chains fit in different groups, and all of them have short chains: only chains with 1, 2, 3 or 5 atoms in the chain are found in other groups, and in case of 5 atoms the structures correspond to different polymorphs of DICMUX that instead belong to the *tight-long-x* group. Therefore, we can conclude that short chains allow more possible packing motifs than longer chains,

maybe because the higher volume occupied by the chains limits the formation of different interactions between the PDI's cores; for the same reason short chains might be more prone to polymorphism. The outcome is different when a branched chain is used. It is reported in literature that the presence of branched chains causes the molecules to rotate along the stacking direction to reduce the steric hindrance between the chains;[42,43] in fact, most of the *imide* scores substituted with branched chains have non-zero rotation. The only object with no rotation despite the branched chain is because the branching is not on the carbon atom bonded to the imide nitrogen. However, only five structures with branched chains are deposited, three of them for a total of five objects are in *crisscross*, whereas one is in *verylong-x* and the non-rotated one is part of the *extra4* group. When an aromatic ring is present on the *imide* substituent group, the possible outcome depends on whether it is directly bonded to the imide nitrogen or there are atoms between them and on the ring substitution. If the aromatic ring is directly linked to the nitrogen, typically it has a nearly 90° torsion angle with the PDI core; such conformation causes a steric hindrance for the perylene cores to stack one above the other. Therefore, two outcomes driven by the tendency of the perylene unit to form close π-stacking interactions are possible: either the PDIs rotate along the stacking direction, like for branched chains, and it results in *crisscross* family, or the molecules are stacked with a higher Δy, resulting in the *tight-long-y* family (or *extra3*). This occurs except in the case in which the aromatic core is substituted in *ortho* with respect to the nitrogen, the steric hindrance, in this case, does not allow close packing and the structure results in the *nostack* group or no group. When the aromatic ring is not directly bonded to the hydrogen, there is no more steric effect and the resulting packing is usually the *tight-long-x* one, except when the aromatic ring is substituted with halogens, that in some cases could form interactions that result in different packing, or when the atom between the nitrogen and the aromatic ring has other substituents, which cause again the steric hindrance and results in the *tight-long-y* or *crisscross* families. In conclusion, the most likely stacking arrangement can be predicted when substitution only in *imide*-position is concerned. However, substituents in this position are not able to tune the HOMO and LUMO energies of PDIs.[31]

Substituents at the core, instead, can efficiently tune HOMO and LUMO energies. However, when the substitution in the core positions is considered, the situation becomes more complicated. First, core substitution usually introduces functional groups in the PDIs that can form different interactions that can compete with the π-π interactions and can induce twisting of the perylene core; furthermore, they are generally substituted also in *imide*-position, therefore the variety of possible PDIs is higher. The core substituted PDI's structures in this work are 55 only *bay*-; 11 *bay*- and *ortho*-; 8 only *ortho*-substituted. The PC1-PC2 scores plot with highlighted only the core-substituted PDIs is shown in Figure S17.

Out of the 55 *bay*-, 27 are substituted only in two positions, whereas 28 in all four the *bay*-positions. Most of the 28 objects (21/28) with four substituents in *bay* have halogen atoms as functional groups because bulky groups do not allow the full *bay* functionalization due to steric effects. This substitution always causes elevated torsion in the core; in fact, the most likely group for these objects is *tight-twist*, which comprises 10/28 objects and all with halogens at the core (F, Cl and Br), with linear chains or aromatic substituents in *imide*-position. The other objects with four halogens in *bay* are in *extra1* (4), with branched chains in *imide*, and *tight-long-y* (4).

When only two *bay*-positions are occupied, there is more freedom on the substituent type, and for some substituents, the planarity of the core could be maintained. For these reasons, structures substituted in this way can be found in all the major families and thus it is difficult to predict the outcome of this type of substitution. Even though the number of structures with these characteristics is too small to make strong assumptions, we can still see some patterns between the objects. First, the *crisscross* objects of this type are mostly structures that show this packing within the dimer and not in all the structure, so it is not a likely group. When the substituents allow to maintain the planarity, like halogens or cyano groups, it is possible to result in the *tight-long-x*, *tight-long-y*, or other groups depending also on the *imide* substitution. Otherwise, when the core is twisted, usually scores with the *tight-twist* and *verylong-x* characteristics are obtained.

Unfortunately, there are only few structures with *ortho* functionalization in CSD with the characteristics included in this investigation. Nevertheless, we observed that the few structures substituted both in *bay* and *ortho* result mostly in *tight-twist* and *verylong-x* groups, as expected from their highly twisted cores and the different competing interactions brought by substituents. Instead, when only *ortho*-substituted PDIs are considered, the planarity of the core is generally maintained, or a slight twist can be present. Therefore, the few objects with only *ortho* substitution do not belong to either *tight-twist* or *verylong-x*, but in other groups such as *tight-long-y*, *extra4* and *extra5*.

From looking into the resulting stacking with different positions and types of the substituents, we observed that as far as only the *imide* functionalization is concerned, the most likely stacking arrangement that the PDI would adopt in the crystal structure can be predicted to some extent, because the molecular packing is mainly driven by the formation of closed π-π stacking interactions. However, when substitution in *bay* and *ortho* position are considered, the formation of π-π stacking interactions must compete with the formation of different interactions brought by substituents at the core; thus, the high variety of different substituent and interaction combinations makes clustering more difficult and less efficient and, as a consequence, prediction of the possible packing arrangements becomes more difficult. Moreover, the number of structures deposited in CSD of similar PDI derivatives is not

yet sufficient to carry out efficient data-driven clustering of structures carrying substituents at the core, especially in the case of *ortho* substitution.

Besides different substitutions, another way in which different stacking arrangements could be obtained is with polymorphism. However, despite it being known that PDIs can exhibit polymorphism, information about different PDI polymorphs in CSD are very limited. Only 5 PDIs investigated in this study have different polymorphs deposited in CSD, making a total of 12 structures (over 103 structures investigated). Nevertheless, two of the PDIs displaying polymorphism has objects for different polymorphs that belong to different major families, showing that it is possible to move to the desired stacking arrangement through polymorphism. Investigating the PDI derivative's polymorphism, and in general polymorphism of OSCs, could be beneficial to both experimental and theoretical work to find OSCs with good semiconducting properties, to design novel semiconductors, and to improve the efficiency of calculation of structure and property of semiconducting material.

CONCLUSIONS

In this work, we successfully found six groups of PDI derivatives crystal structures deposited in CSD with similar stacking arrangements by using a method based on self-organizing maps. The characteristics of the packing of the different clusters were discussed and compared based on the descriptors used. Furthermore, we investigated the effect of different substituent positions and types on the molecular stacking of the PDIs, based on the characteristics of the PDIs clustered together in the six identified groups. We observed that if PDIs are substituted only in *imide*-position, the packing is mainly driven by the formation of closed π-π stacking interactions, and hence the most likely stacking arrangement that the PDI would adopt in the crystal structure can be predicted to some extent; whereas, when *bay-* and *ortho-* substitution are considered, the observed packing is the result of the competition between the interactions brought by these substituents and the formation of π-π stacking interactions between the perylene core. Thus, when multiple substituents are introduced at the perylene core, at some point the formation of closed π-stacking interaction is not the driving force of the packing anymore, but the driving force becomes the interactions with the substituents. Therefore, introducing substituent to the core, despite being beneficial to tune HOMO and LUMO energies, makes it more difficult to predict the possible packing outcome and can be detrimental to achieving efficient stacking interactions for charge transport.

Moreover, the lack of deposited crystal structures, especially when polymorphism is considered, hinder the efficiency of these data-driven methods and the design of novel materials with desired property and packing. Of course, the lack of structures can be overcome by using crystal structure

prediction methods, however, improved knowledge of the experimental crystal structure can also increase the accuracy of such methods.

We believe that clustering-based classification of crystal structure such as the one used in this study can be used in the future to correlate different families of structures with OSC's properties and could help both theoretical and experimental studies to achieve improved knowledge on the structure and property of materials to efficiently design novel semiconducting material with desired property and packings.

EXPERIMENTAL SECTION

Dataset

The search for PDI derivatives structures in CSD resulted in more than 300 structures. From these structures, only organic ones were selected. Furthermore, we discarded solvates, polymers, duplicated structures (for structures collected in different conditions, the structure with the best R factor and/or lower temperature of data collection was chosen), and PDIs with extended fused aromatic cores. Furthermore, we considered PDIs substituted either at *imide-*, *bay-* and *ortho-*positions; however, since the focus of this work was about the π-stacking interactions between the perylene's core of the PDI molecule, we limited the type of substituent considered in this study. At *imide-*position we considered only linear chains, branched chains (even though very bulky groups were excluded), chains containing small cyclic groups and aromatic rings, and halogen-substituted aromatics and chains; the choice of substituents at the core (*ortho-* and *bay-*positions) was even more strict, in fact, only halogens, cyano-groups, short chains, and small cyclic groups and aromatic rings were considered.

In this way, a total of 103 structures of PDI derivatives were selected, out of which 53 were substituted only in *imide-*position (besides one of these with no substitution) and 50 structures with PDIs substituted at the perylene core. Out of these 50 core-substituted PDIs, 35 were substituted in *bay-*position, 6 in *ortho-*position, and 9 in both *bay-* and *ortho-*positions; out of these 50 core-substituted PDIs structures, only 3 do not have substitution in *imide-*position.

From the 103 PDI's crystal structures evaluated, 142 samples were obtained for the analysis. The increase in the number of samples derives from structures with Z' > 1, thus for samples with more than one molecule in the asymmetric units, and from structures with Z' = 1 in which the asymmetric unit is formed by two halves of PDI molecules in different configurations; in these cases, more than one set of descriptors was necessary to describe the π-stacking arrangement between PDI dimers in the structure (different scores corresponding to a single structure are labelled as A, B, etc.).

Descriptors

The descriptors or variables used for the analysis can be differentiated into two different types of variables: numerical variables, which are the variables used by the algorithm to perform the clustering, and categorical variables, which are variables that do not have a numeric value but are used to describe in detail the specific characteristics of the structure and the molecule in order to find patterns between clustering and the object characteristics. The numerical variables comprise Z, Z', V_{mol}, torsion, S, S/L, M/L, SV, $d_{\pi\text{-}\pi}$, χ, ψ, Δx, Δy, P, R, tilt and rotation. The category variables comprise Temperature, substituent position, substituent at the *imide-*, substituent at the core and packing type. Out of these variables, Temperature, Z and Z' are used to give information about the crystal structures and were easily retrieved by information deposited by CSD. All the other variables were not available as simple information from CSD and hence were calculated using the software Mercury[61] of the CCDC package. The variables V_{mol}, substituent position, substituent at the *imide-*, substituent at the core, torsion, S, S/L and M/L are descriptors used to give information about the molecule, whereas SV, $d_{\pi\text{-}\pi}$, χ, ψ, Δx, Δy, P, R, tilt, rotation and packing type are variables that give information about the packing of the PDIs, calculated by considering the stacking between a dimer formed by two neighbouring PDI molecules.

Z. The number of molecules (or formula units) in the unit cell.

Z'. The number of molecules (or formula units) in the unit cell divided by the number of independent general positions, which corresponds to the number of molecules in the asymmetric unit in the case of PDIs.

V_{mol}. Molecular volume in the crystal structure, which correspond to the unit cell volume divided by Z.

Torsion. The torsional angle of the PDI's perylene core resulting from the twisting of the two naphthalene half units. The value was calculated from Mercury, as the average between the two torsion angles formed by the naphthalene half units with respect to the molecular x-axis.

S, S/L and M/L. Are simple descriptors of molecular shape and size, where the molecule is enclosed in a rectangular box where S, M and L are respectively its short, medium, and long axis. Their ratio (*i.e.,* S/L and M/L) give information about molecular shape. These parameters are calculated using the molecular complementary tool of Mercury.[62]

SV. This variable is the stacking vector modulus, which is the distance between the centroid of the two closest perylene units involved in the stacking. The description of the SV and its components is like the one used by Milita et al. in their work about NDI derivatives polymorphism.[63]

$d_{\pi\text{-}\pi}$. Correspond to the interplanar distance between the planes of the perylene cores involved in the stacking. In the case of non-parallel planes, it was calculated as the average of the distance between the centroid of the perylene cores with the plane formed by the plane of the other perylene core involved in the stacking.

χ *and* ψ. Are the angles of the direction cosines of the SV. Where χ is calculated with the x-axis and ψ with the y-axes.

Δx and Δy. Respectively correspond to the displacement of the perylene unit along the x- and y-direction.

P and R. Respectively the pitch and roll angles. The pitch angle is used to assess the molecular slipping along the x-axis, while the roll angle is used to assess the slipping along the y-axis[64]. These two angles can be calculated from Δx, Δy and $d_{\pi\text{-}\pi}$ using the following equation 1:

$$P = \arctan\left(\frac{\Delta x}{d_{\pi-\pi}}\right); \quad R = \arctan\left(\frac{\Delta y}{d_{\pi-\pi}}\right) \qquad (1)$$

Tilt. This variable is non-zero when the perylene core planes are non-parallel. It corresponds to the angle between the normal of the two perylene planes involved in the stacking.

Rotation. Also referred to as "helical pitch" in some works with perylene substituted with swallow-tail alkyl-chains,[42,43] correspond to the angle of respective rotation between the perylene core, calculated viewing along the z-direction of the perylene core plane (perpendicular to the xy-plane).
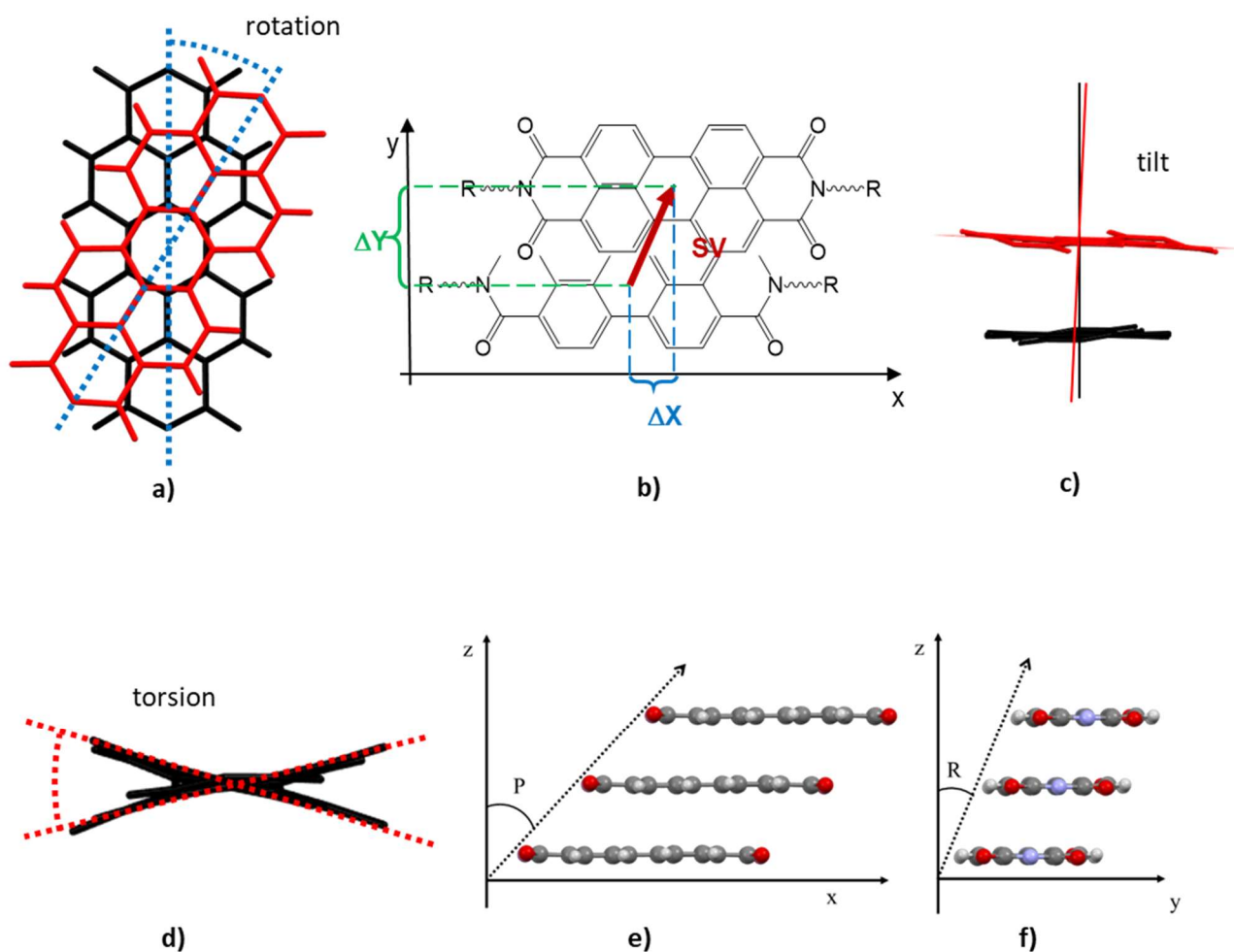
Figure 8. Visual representation of some of the descriptors used to describe the crystal packing: a) rotation angle; b) SV, Δx and Δy; c) tilt angle; d) torsion angle; e) pitch angle; f) roll angle.

Temperature. The temperature (expressed in K) reported for the data collection of the crystal structure.

Substituent position. Indicates in which position the PDI is substituted, *i.e.*, *imide-*, *bay-*, *ortho-* or *bay-/ortho-* (in case of core substitution the imide- is omitted).

Imide- substituents. Indicates the type of substituent in *imide*-position. The types of substituents are grouped as linear, branched, cyclic, aromatic, fluorinated and combination of these groups.

Core substituents. Indicates the type of substituent in the *bay-* and *ortho*-position. The types of substituents are grouped as linear, branched, cyclic, aromatic, fluorinated, halogen, cyano and combinations of these groups.

Packing type. The type of traditional packing arrangement to describe the π-stacking. In this work, we used 1D, 2D, H (as herringbone) to describe the type of packing arrangement, whereas "no" was

used in case the PDI molecules were too distant to create π-stacking interaction, and none of the previous packing types could be used to describe it.

PCA

Principal component analysis (PCA)[65] is one of the most important chemometric methods. The mathematical procedure can be summarized in a rotation of the original variables of the dataset to convert them into new variables, called principal components (PCs). The PCs are orthogonal to each other and oriented in the most informative directions for the data. In this way, the coordinates of the first two or three PCs of objects and variables can be used to describe, with good approximation, the entire behaviour of the data. Each PC carry a percentage of information (explained variance) that can be used to check if enough information is maintained in the considered PCs. Therefore, the two main results of PCA are the scores plot and the loadings plot. Scores plot shows the behaviour of objects, indicating possible groups (objects close to each other) or outliers (objects far from all the others), while loadings plot shows the behaviour of variables, indicating correlation (variable loadings close to each other) or anti-correlation (loadings at the opposite side of the graph).

Self-Organizing Maps

Self-organizing maps (SOM)[56] were used in the present work to find patterns of crystal structures. SOM is a multivariate analysis based on the artificial neural networks (ANN) method[57] which calculates clusters from the dataset objects in an iterative way. The output of the SOM computation can be viewed as a 2D rectangular map divided into several adjacent circles (or hexagons), each of which represents a SOM unit and in which some objects of the starting dataset are aggregated. The starting point of SOM computation is the definition of the number of units and the sizes of the map. Some empirical rules have been proposed to define such parameters, as the one reported by Nakagawa et al..[59] In that work, the number of SOM units is chosen as the one closest to five times the squared root of the number of objects. The dimensions of the rectangle, instead, are chosen in proportion to the first two eigenvalues calculated by a PCA performed on the original data.

The SOM computation starts from a random point once defined the map dimensions. Each SOM unit is actually a vector with length equal to the number of original variables and the first computation step have random values for these vectors. Each object is presented to each vector, the Euclidean distance between object and vector is calculated, and the object is assigned to the closest unit. Once all objects have been assigned, the second step starts using as unit vectors the mean of the previously assigned objects and repeats the same procedure of presenting the objects to the units and assigning them to the closest one. This procedure is repeated for a pre-determined number of steps (called epochs) or until a convergence is reached, which means that the results do not change for two or three

consecutive epochs. At the end, each unit of the map represents a "cluster" of starting objects. The units can be further grouped by performing a cluster analysis[66] on the final vectors. In this way, a lower number of clusters is calculated (generally 5 to 8 clusters starting from at least dozens of units), simplifying the further considerations.

However, it does not exist a general rule to define the map dimensions and the optimal number of clusters, and the final result may depend on such choices. Therefore, for the present work, we decided to perform six SOM computations modifying each time the map dimensions and using the Davies-Bouldin index[58] to determine the best number of clusters. The results of the SOMs were then compared at the end to evaluate the best families of crystal structures that can be derived from the dataset.

SOM computations were performed using the package *SOMEnv*[57] of the R environment (R Core Team, Vienna, Austria).

NOTES

Supplementary information are reported in Appendix E.

REFERENCES

(1)   Coropceanu, V.; Cornil, J.; da Silva Filho, D. A.; Olivier, Y.; Silbey, R.; Brédas, J. L. Charge Transport in Organic Semiconductors. *Chemical Reviews*. 2007, pp 926–952.

(2)   Anthony, J. E.; Facchetti, A.; Heeney, M.; Marder, S. R.; Zhan, X. N-Type Organic Semiconductors in Organic Electronics. *Adv. Mater.* **2010**, *22* (34), 3876–3892.

(3)   Ferlauto, L.; Liscio, F.; Orgiu, E.; Masciocchi, N.; Guagliardi, A.; Biscarini, F.; Samorì, P.; Milita, S. Enhancing the Charge Transport in Solution-Processed Perylene Di-Imide Transistors via Thermal Annealing of Metastable Disordered Films. *Adv. Funct. Mater.* **2014**, *24* (35), 5503–5510.

(4)   Ostroverkhova, O. Organic Optoelectronic Materials: Mechanisms and Applications. *Chem. Rev.* **2016**, *116* (22), 13279–13412.

(5)   Wang, C.; Dong, H.; Jiang, L.; Hu, W. Organic Semiconductor Crystals. *Chemical Society Reviews*. Royal Society of Chemistry January 22, 2018, pp 422–500.

(6)   Tang, C. W.; Vanslyke, S. A. Organic Electroluminescent Diodes. *Appl. Phys. Lett.* **1987**, *51* (12), 913–915.

(7)   Brütting, W.; Frischeisen, J. Device Efficiency of Organic Light-Emitting Diodes. In *Physics*

of Organic Semiconductors: Second Edition; 2013; Vol. 210, pp 497–539.

(8)   Facchetti, A. Semiconductors for Organic Transistors. *Mater. Today* **2007**, *10* (3), 28–37.

(9)   Mei, J.; Diao, Y.; Appleton, A. L.; Fang, L.; Bao, Z. Integrated Materials Design of Organic Semiconductors for Field-Effect Transistors. *Journal of the American Chemical Society*. 2013, pp 6724–6746.

(10)   Chen, S.; Li, Z.; Qiao, Y.; Song, Y. Solution-Processed Organic Semiconductor Crystals for Field-Effect Transistors: From Crystallization Mechanism towards Morphology Control. *Journal of Materials Chemistry C*. 2021, pp 1126–1149.

(11)   Kippelen, B.; Brédas, J. L. Organic Photovoltaics. *Energy and Environmental Science*. 2009, pp 251–261.

(12)   Anthony, J. E. Small-Molecule, Nonfullerene Acceptors for Polymer Bulk Heterojunction Organic Photovoltaics. *Chem. Mater.* **2011**, *23* (3), 583–590.

(13)   Li, C.; Wonneberger, H. Perylene Imides for Organic Photovoltaics: Yesterday, Today, and Tomorrow. *Adv. Mater.* **2012**, *24* (5), 613–636.

(14)   Anthony, J. E. Organic Electronics: Addressing Challenges. *Nature Materials*. 2014, pp 773–775.

(15)   Ando, S.; Murakami, R.; Nishida, J. I.; Tada, H.; Inoue, Y.; Tokito, S.; Yamashita, Y. N-Type Organic Field-Effect Transistors with Very High Electron Mobility Based on Thiazole Oligomers with Trifluoromethylphenyl Groups. *J. Am. Chem. Soc.* **2005**, *127* (43), 14996–14997.

(16)   Takimiya, K.; Osaka, I.; Mori, T.; Nakano, M. Organic Semiconductors Based on [1]Benzothieno[3,2- B][1]Benzothiophene Substructure. *Acc. Chem. Res.* **2014**, *47* (5), 1493–1502.

(17)   Huang, C.; Barlow, S.; Marder, S. R. Perylene-3,4,9,10-Tetracarboxylic Acid Diimides: Synthesis, Physical Properties, and Use in Organic Electronics. *Journal of Organic Chemistry*. 2011, pp 2386–2407.

(18)   Kardos, M. German Patent. DE 276357, 1913.

(19)   Kazmaier, P. M.; Hoffmann, R. A Theoretical Study of Crystallochromy. Quantum Interference Effects in the Spectra of Perylene Pigments. *J. Am. Chem. Soc.* **1994**, *116* (21), 9684–9691.

(20) Bialas, D.; Kirchner, E.; Röhr, M. I. S.; Würthner, F. Perspectives in Dye Chemistry: A Rational Approach toward Functional Materials by Understanding the Aggregate State. *Journal of the American Chemical Society*. 2021, pp 4500–4518.

(21) Jones, B. A.; Facchetti, A.; Wasielewski, M. R.; Marks, T. J. Tuning Orbital Energetics in Arylene Diimide Semiconductors. Materials Design for Ambient Stability of n-Type Charge Transport. *J. Am. Chem. Soc.* **2007**, *129* (49), 15259–15278.

(22) Zhan, X.; Facchetti, A.; Barlow, S.; Marks, T. J.; Ratner, M. A.; Wasielewski, M. R.; Marder, S. R. Rylene and Related Diimides for Organic Electronics. *Advanced Materials*. John Wiley & Sons, Ltd January 11, 2011, pp 268–284.

(23) Huang, C.; Sartin, M. M.; Siegel, N.; Cozzuol, M.; Zhang, Y.; Hales, J. M.; Barlow, S.; Perry, J. W.; Marder, S. R. Photo-Induced Charge Transfer and Nonlinear Absorption in Dyads Composed of a Two-Photon-Absorbing Donor and a Perylene Diimide Acceptor. *J. Mater. Chem.* **2011**, *21* (40), 16119–16128.

(24) Mariz, I. F. A.; Raja, S.; Silva, T.; Almeida, S.; Torres, É.; Baleizão, C.; Maçôas, E. Two-Photon Absorption of Perylene-3,4,9,10-Tetracarboxylic Acid Diimides: Effect of Substituents in the Bay. *Dye. Pigment.* **2021**, *193* (May).

(25) Al-Galiby, Q.; Grace, I.; Sadeghi, H.; Lambert, C. J. Exploiting the Extended π-System of Perylene Bisimide for Label-Free Single-Molecule Sensing. *J. Mater. Chem. C* **2015**, *3* (9), 2101–2106.

(26) Ribeiro, T.; Raja, S.; Rodrigues, A. S.; Fernandes, F.; Farinha, J. P. S.; Baleizão, C. High Performance NIR Fluorescent Silica Nanoparticles for Bioimaging. *RSC Adv.* **2013**, *3* (24), 9171–9174.

(27) Cowen, L. M.; Atoyo, J.; Carnie, M. J.; Baran, D.; Schroeder, B. C. Review—Organic Materials for Thermoelectric Energy Generation. *ECS J. Solid State Sci. Technol.* **2017**, *6* (3), N3080–N3088.

(28) Klebe, G.; Graser, F.; Hädicke, E.; Berndt, J. Crystallochromy as a Solid-state Effect: Correlation of Molecular Conformation, Crystal Packing and Colour in Perylene-3,4:9,10-bis(Dicarboximide) Pigments. *Acta Crystallogr. Sect. B* **1989**, *45* (1), 69–77.

(29) Langhals, H. Cyclic Carboxylic Imide Structures as Structure Elements of High Stability. Novel Developments in Perylene Dye Chemistry. *Heterocycles* **1995**, *40* (1), 477–500.

(30) Balakrishnan, K.; Datar, A.; Naddo, T.; Huang, J.; Oitker, R.; Yen, M.; Zhao, J.; Zang, L.

Effect of Side-Chain Substituents on Self-Assembly of Perylene Diimide Molecules: Morphology Control. *J. Am. Chem. Soc.* **2006**, *128* (22), 7390–7398.

(31)   Carmen Ruiz Delgado, M.; Kim, E. G.; Da Silva Filho, D. A.; Bredas, J. L. Tuning the Charge-Transport Parameters of Perylene Diimide Single Crystals via End and/or Core Functionalization: A Density Functional Theory Investigation. *J. Am. Chem. Soc.* **2010**, *132* (10), 3375–3387.

(32)   Geng, Y.; Li, H.-B.; Wu, S.-X.; Su, Z.-M. The Interplay of Intermolecular Interactions, Packing Motifs and Electron Transport Properties in Perylene Diimide Related Materials: A Theoretical Perspective. *J. Mater. Chem.* **2012**, *22* (39), 20840.

(33)   Würthner, F. Perylene Bisimide Dyes as Versatile Building Blocks for Functional Supramolecular Architectures. *Chem. Commun.* **2004**, *4* (14), 1564–1579.

(34)   Jones, B. A.; Ahrens, M. J.; Yoon, M. H.; Facchetti, A.; Marks, T. J.; Wasielewski, M. R. High-Mobility Air-Stable n-Type Semiconductors with Processing Versatility: Dicyanoperylene-3,4:9,10-Bis(Dicarboximides). *Angew. Chemie - Int. Ed.* **2004**, *43* (46), 6363–6366.

(35)   Nakazono, S.; Easwaramoorthi, S.; Kim, D.; Shinokubo, H.; Osuka, A. Synthesis of Arylated Perylene Bisimides through C - H Bond Cleavage under Ruthenium Catalysis. *Org. Lett.* **2009**, *11* (23), 5426–5429.

(36)   Graser, F.; Hädicke, E. Kristallstruktur Und Farbe Bei Perylen-3,4:9,10-Bis(Dicarboximid)-Pigmenten. *Liebigs Ann. der Chemie* **1980**, *1980* (12), 1994–2011.

(37)   Fink, R. F.; Seibt, J.; Engel, V.; Renz, M.; Kaupp, M.; Lochbrunner, S.; Zhao, H. M.; Pfister, J.; Würthner, F.; Engels, B. Exciton Trapping in π-Conjugated Materials: A Quantum-Chemistry-Based Protocol Applied to Perylene Bisimide Dye Aggregates. *J. Am. Chem. Soc.* **2008**, *130* (39), 12858–12859.

(38)   Zhao, H. M.; Pfister, J.; Settels, V.; Renz, M.; Kaupp, M.; Dehm, V. C.; Würthner, F.; Fink, R. F.; Engels, B. Understanding Ground- and Excited-State Properties of Perylene Tetracarboxylic Acid Bisimide Crystals by Means of Quantum Chemical Computations. *J. Am. Chem. Soc.* **2009**, *131* (43), 15660–15668.

(39)   Vura-Weis, J.; Ratner, M. A.; Wasielewski, M. R. Geometry and Electronic Coupling in Perylenediimide Stacks: Mapping Structure - Charge Transport Relationships. *J. Am. Chem. Soc.* **2010**, *132* (6), 1738–1739.

(40) Mumyatov, A. V.; Leshanskaya, L. I.; Anokhin, D. V; Dremova, N. N.; Troshin, P. A. Organic Field-Effect Transistors Based on Disubstituted Perylene Diimides: Effect of Alkyl Chains on the Device Performance. *Mendeleev Commun.* **2014**, *24* (5), 306–307.

(41) Belova, V.; Wagner, B.; Reisz, B.; Zeiser, C.; Duva, G.; Rozbořil, J.; Novák, J.; Gerlach, A.; Hinderhofer, A.; Schreiber, F. Real-Time Structural and Optical Study of Growth and Packing Behavior of Perylene Diimide Derivative Thin Films: Influence of Side-Chain Modification. *J. Phys. Chem. C* **2018**, *122* (15), 8589–8601.

(42) Hansen, M. R.; Graf, R.; Sekharan, S.; Sebastiani, D. Columnar Packing Motifs of Functionalized Perylene Derivatives: Local Molecular Order despite Long-Range Disorder. *J. Am. Chem. Soc.* **2009**, *131* (14), 5251–5256.

(43) May, F.; Marcon, V.; Hansen, M. R.; Grozema, F.; Andrienko, D. Relationship between Supramolecular Assembly and Charge-Carrier Mobility in Perylenediimide Derivatives: The Impact of Side Chains. *J. Mater. Chem.* **2011**, *21* (26), 9538–9545.

(44) Ahmed, R.; Manna, A. K. Theoretical Insights on Tunable Optoelectronics and Charge Mobilities in Cyano-Perylenediimides: Interplays between -CN Numbers and Positions. *Phys. Chem. Chem. Phys.* **2021**, *23* (27), 14687–14698.

(45) Geng, Y.; Wang, J.; Wu, S.; Li, H.; Yu, F.; Yang, G.; Gao, H.; Su, Z. Theoretical Discussions on Electron Transport Properties of Perylene Bisimide Derivatives with Different Molecular Packings and Intermolecular Interactions. *J. Mater. Chem.* **2011**, *21* (1), 134–143.

(46) Shang, X.; Ahn, J.; Lee, J. H.; Kim, J. C.; Ohtsu, H.; Choi, W.; Song, I.; Kwak, S. K.; Oh, J. H. Bay-Substitution Effect of Perylene Diimides on Supramolecular Chirality and Optoelectronic Properties of Their Self-Assembled Nanostructures. *ACS Appl. Mater. Interfaces* **2021**, *13*.

(47) Gryn'Ova, G.; Lin, K. H.; Corminboeuf, C. Read between the Molecules: Computational Insights into Organic Semiconductors. *Journal of the American Chemical Society*. UTC 2018, pp 16370–16386.

(48) Cornil, J.; Verlaak, S.; Martinelli, N.; Mityashin, A.; Olivier, Y.; Van Regemorter, T.; D'Avino, G.; Muccioli, L.; Zannoni, C.; Castet, F.; Beljonne, D.; Heremans, P. Exploring the Energy Landscape of the Charge Transport Levels in Organic Semiconductors at the Molecular Scale. *Acc. Chem. Res.* **2013**, *46* (2), 434–443.

(49) Landi, A.; Troisi, A. Rapid Evaluation of Dynamic Electronic Disorder in Molecular

Semiconductors. *J. Phys. Chem. C* **2018**, *122* (32), 18336–18345.

(50) Campbell, J. E.; Yang, J.; Day, G. M. Predicted Energy-Structure-Function Maps for the Evaluation of Small Molecule Organic Semiconductors. *J. Mater. Chem. C* **2017**, *5* (30), 7574–7584.

(51) Yang, J.; De, S.; Campbell, J. E.; Li, S.; Ceriotti, M.; Day, G. M. Large-Scale Computational Screening of Molecular Organic Semiconductors Using Crystal Structure Prediction. *Chem. Mater.* **2018**, *30* (13), 4361–4371.

(52) Musil, F.; De, S.; Yang, J.; Campbell, J. E.; Day, G. M.; Ceriotti, M. Machine Learning for the Structure-Energy-Property Landscapes of Molecular Crystals. *Chem. Sci.* **2018**, *9* (5), 1289–1300.

(53) Schober, C.; Reuter, K.; Oberhofer, H. Virtual Screening for High Carrier Mobility in Organic Semiconductors. *J. Phys. Chem. Lett.* **2016**, *7* (19), 3973–3977.

(54) Nematiaram, T.; Padula, D.; Landi, A.; Troisi, A. On the Largest Possible Mobility of Molecular Semiconductors and How to Achieve It. *Adv. Funct. Mater.* **2020**, *30* (30), 2001906.

(55) Hofmann, D. W. M.; Kuleshova, L. N. *Data Mining in Crystallography*, 1st ed.; Springer Publishing Company, Incorporated, 2009.

(56) Kohonen, T. The Self-Organizing Map. *Neurocomputing* **1998**, *21* (1), 1–6.

(57) Licen, S.; Franzon, M.; Rodani, T.; Barbieri, P. SOMEnv: An R Package for Mining Environmental Monitoring Datasets by Self-Organizing Map and k-Means Algorithms with a Graphical User Interface. *Microchem. J.* **2021**, *165*, 106181.

(58) Davies, D. L.; Bouldin, D. W. A Cluster Separation Measure. *IEEE Trans. Pattern Anal. Mach. Intell.* **1979**, *PAMI-1* (2), 224–227.

(59) Nakagawa, K.; Yu, Z.-Q.; Berndtsson, R.; Hosono, T. Temporal Characteristics of Groundwater Chemistry Affected by the 2016 Kumamoto Earthquake Using Self-Organizing Maps. *J. Hydrol.* **2020**, *582*, 124519.

(60) Hunter, C. A.; Sanders, J. K. M. The Nature of π-π Interactions. *J. Am. Chem. Soc.* **1990**, *112*, 5525–5534.

(61) MacRae, C. F.; Sovago, I.; Cottrell, S. J.; Galek, P. T. A.; McCabe, P.; Pidcock, E.; Platings, M.; Shields, G. P.; Stevens, J. S.; Towler, M.; Wood, P. A. Mercury 4.0: From Visualization to Analysis, Design and Prediction. *J. Appl. Crystallogr.* **2020**, *53*, 226–235.

(62) Fábián, L. Cambridge Structural Database Analysis of Molecular Complementarity in Cocrystals. *Cryst. Growth Des.* **2009**, *9* (3), 1436–1443.

(63) Milita, S.; Liscio, F.; Cowen, L.; Cavallini, M.; Drain, B. A.; Degousée, T.; Luong, S.; Fenwick, O.; Guagliardi, A.; Schroeder, B. C.; Masciocchi, N. Polymorphism in N , N ′- Dialkyl-Naphthalene Diimides. *J. Mater. Chem. C* **2020**, *8* (9), 3097–3112.

(64) Curtis, M. D.; Cao, J.; Kampf, J. W. Solid-State Packing of Conjugated Oligomers: From π- Stacks to the Herringbone Structure. *J. Am. Chem. Soc.* **2004**, *126* (13), 4318–4328.

(65) Bro, R.; Smilde, A. K. Principal Component Analysis. *Anal. Methods* **2014**, *6* (9), 2812–2831.

(66) Everitt, B. S.; Landau, S.; Leese, M. *Cluster Analysis*, 5th ed.; Wiley Publishing, 2011.

CHAPTER 8: CONCLUSIONS

The first two chapters of the thesis cover the first part of my thesis, when, during my training, I was involved in different projects. I was able to acquire the fundamental skill and knowledge on crystallography and solid-state characterization. Then I focused mainly on my t my Ph.D. project which was the investigation of the polymorphism of a series of N,N'-dialkyl-3,4,9,10-perylendiimide (PDI-Cn, with n = 5, 6, 7, 8) at ambient and non-ambient conditions and the solid-state characterization and crystal structure determination of the different polymorphic forms.

A p-xylene and a toluene solvate form of PDI-C5 have been obtained by polymorph screening from solution and the crystal structure of the p-xylene solvate was determined by Single Crystal X-ray diffraction; the presence of the solvent was confirmed by hot-stage measurements and ^{1}H-NMR. No other new forms were achieved by polymorph screening from solution. Solvothermal crystallization resulted the most efficient method to produce single crystals of PDI-Cn. From Single Crystal X-ray diffraction, we determined the crystal structure of PDI-C7 form I, which was not previously reported. The crystal structures of the different PDI-Cn have been analyzed and compared using Mercury, showing that all PDI-Cn form I structures are indeed very similar and display the same packing motif dominated by strong π-π interactions.

The full thermal characterization of PDI-C5 by a combination of differential scanning calorimetry, variable temperature X-ray diffraction, hot-stage microscopy, and variable temperature Raman spectroscopy have been tackled and reported. Two high-temperature polymorphs have been identified: form II which is completely reversible upon cooling and form III which revealed a different thermal behavior upon cooling depending on the technique and crystal size. The crystal structure of PDI-C5 forms II and III have been determined from synchrotron powder data, and the crystal structures of the PDI-C5 different polymorphs have been discussed and compared using Mercury and CrystalExplorer. Form I, form II are extremely similar, they are characterized by a lamellar mono-dimensional (1D) packing motif dominated by strong π-π interactions between aromatic cores and differ mostly in the alkyl chains conformation; only the formation of form III above 220 °C cause a variation in the π-stacking arrangement to an alternation of shifted and criss-crossed stacking, showing the strong propensity of the material to maintain the stacking arrangement of form I. The thermal expansion of the different PDI-C5 forms has been studied, highlighting a high and anisotropic thermal expansion, especially for form III. We hypothesize that this thermal expansion could be responsible for the different thermal behavior observed with different analyses upon cooling, due to strains and energy accumulation induced by thermal contraction.

The thermal characterization of PDI-C6, -C7, and -C8 by differential scanning calorimetry, variable temperature X-ray diffraction, and hot-stage microscopy have also been reported. Several high-temperature polymorphs have been identified by the combination of these techniques, two for PDI-C6 and PDI-C7, whereas only one has been identified for PDI-C8. The formation of these polymorphs occurs only at temperatures above 190 °C and they are completely reversible upon cooling. Despite our efforts, it was not possible to solve their crystal structures due to the elevated temperature of the data collections. Hence, only the phase indexing for these forms has been reported. The thermal expansion of PDI-C6, -C7, and -C8 has also been studied, highlighting once again a high and anisotropic thermal expansion. Although the reverse transition is always observed upon cooling, the hysteresis observed for such transitions is different depending on the technique used; such behavior might derive from strains and energy accumulation in the crystal induced by thermal contraction as in the PDI-C5 case.

Together with the thermal characterization, the study of PDI-Cn high-pressure polymorphism by pressure-dependent UV-Vis absorption spectroscopy and high-pressure Single Crystal X-ray diffraction has been reported to further understand PDI-Cn's polymorphism and the role of different interactions in the crystal packing. The presence of one or more pressure-induced phase transitions has been identified in all PDI-Cn by UV-Vis measurements. High-pressure Single Crystal X-ray diffraction experiments have been carried out only for PDI-C5 and PDI-C6. One high-pressure polymorph of PDI-C5 (form IV) and two high-pressure polymorphs of PDI-C6 (form IV and form V) have been identified by X-ray diffraction and their crystal structure has been determined.

The investigation of non-ambient polymorphism of PDI-Cn highlighted that the crystal packing is indeed dominated by the strong π-π interactions between the perylene cores, however, the alkyl chains have a major role in determining their polymorphic behavior.

Lastly, the clustering method based on a combination of self-organizing maps (SOM) and principal component analysis (PCA) used as a data-driven approach to classifying different π-stacking arrangements of PDI derivatives with different types and positions of the substituents have been able to successfully identify six different families characterized by similar crystal packing within the structures considered. The main characteristics of these packing families have been reported and the influence of the type and position of the PDI's substituents on the resulting packing has been discussed.

ACKNOWLEDGEMENTS

APPENDIX A

SUPPLEMENTARY INFORMATION

Structural insights into the vapochromic behavior of Pt and Pd-based compounds

Benny Danilo Belviso,[1] Francesco Marin,[2] Sara Fuertes,[3] Violeta Sicilia,[3] Rosanna Rizzi,[1] Fulvio Ciriaco,[4] Chiara Cappuccino,[5] Eric Dooryhee,[6] Aurelia Falcicchio,[1] Lucia Maini,[2] Angela Altomare[1] and Rocco Caliandro[1,]*

1 Institute of Crystallography, CNR, via Amendola 122/o, Bari, 70126, Italy.

2 Dipartimento di Chimica "Giacomo Ciamician", Università di Bologna Via Selmi 2, 40126, Bologna, Italy.

3 Departamento de Química Iorgánica, Universidad de Zaragoza-CSIC, Zaragoza, Spain.

4 Dipartimento di Chimica, Università di Bari, via Orabona, 70125, Bari, Italy.

5 Departement of Chemical Science, Bernal Institute, University of Limerick.

6 NSLS II, Photon Science Division, Brookhaven National Laboratory, New York.

SUPPLEMENTARY INFORMATION

Structural insights into the vapochromic behavior of Pt- and Pd-based compounds

Benny Danilo Belviso,[1] Francesco Marin,[2] Sara Fuertes,[3] Violeta Sicilia,[3] Rosanna Rizzi,[1] Fulvio Ciriaco,[4]

Chiara Cappuccino,[5] Eric Dooryhee,[6] Aurelia Falcicchio,[1] Lucia Maini,[2] Angela Altomare[1] and Rocco

Caliandro[1,]*

1 Institute of Crystallography, CNR, via Amendola 122/o, Bari, 70126, Italy.
2 Dipartimento di Chimica "Giacomo Ciamician", Università di Bologna Via Selmi 2, 40126, Bologna, Italy.
3 Departamento de Química Iorgánica, Universidad de Zaragoza-CSIC, Zaragoza, Spain.
4 Dipartimento di Chimica, Università di Bari, via Orabona, 70125, Bari, Italy.
5 Departement of Chemical Science, Bernal Institute, University of Limerick.
6 NSLS II, Photon Science Division, Brookhaven National Laboratory, New York.

Corresponding author's email address: rocco.caliandro@ic.cnr.it

Section 1. Spectroscopic characterization of compounds
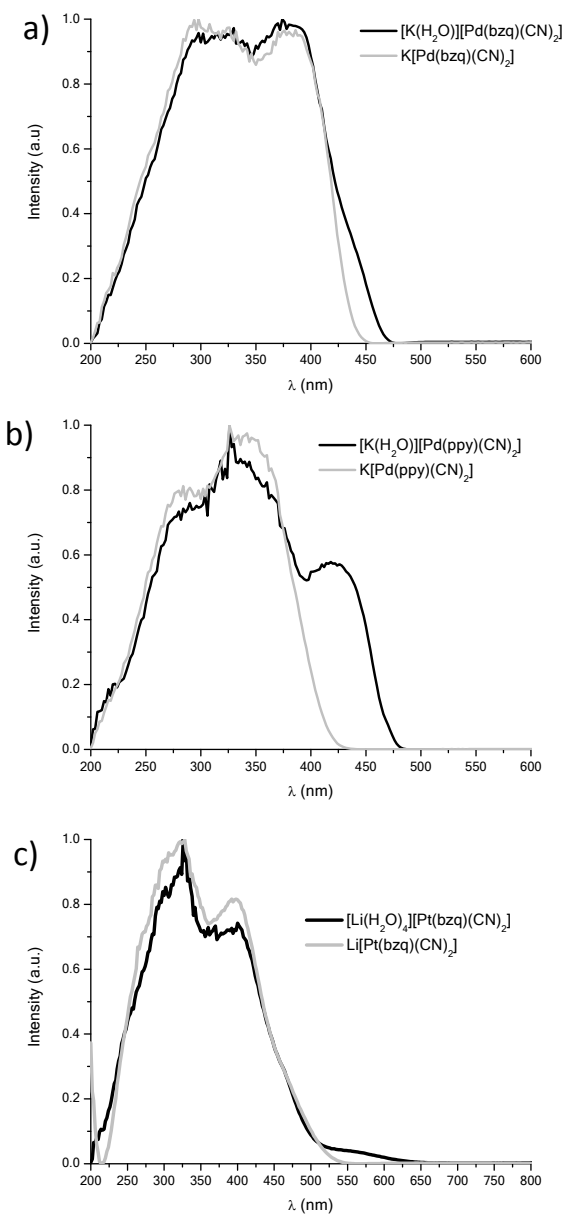
Figure S1. Normalized diffuse reflectance UV-visible spectra of Pd(bzq) (a), Pd(ppy)(b) and Pt(bzq)Li (c) in the solid state at 298 K.
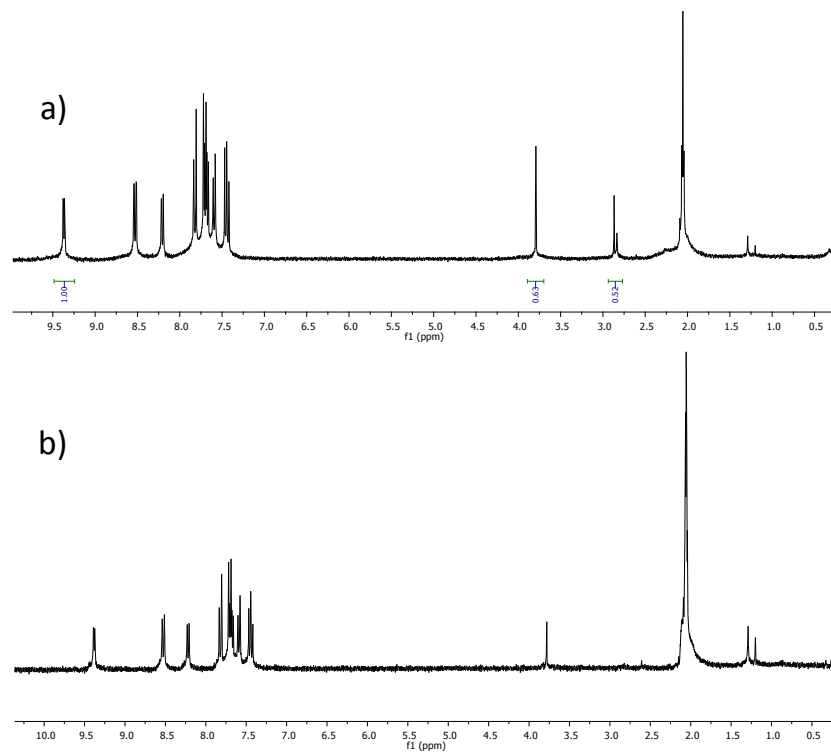
Figure S2: ^1H NMR of Pd(bzq)K·H_2O (a) and Pd(bzq)K (b) in anhydrous acetone-d_6, 300 MHz, 293 K.
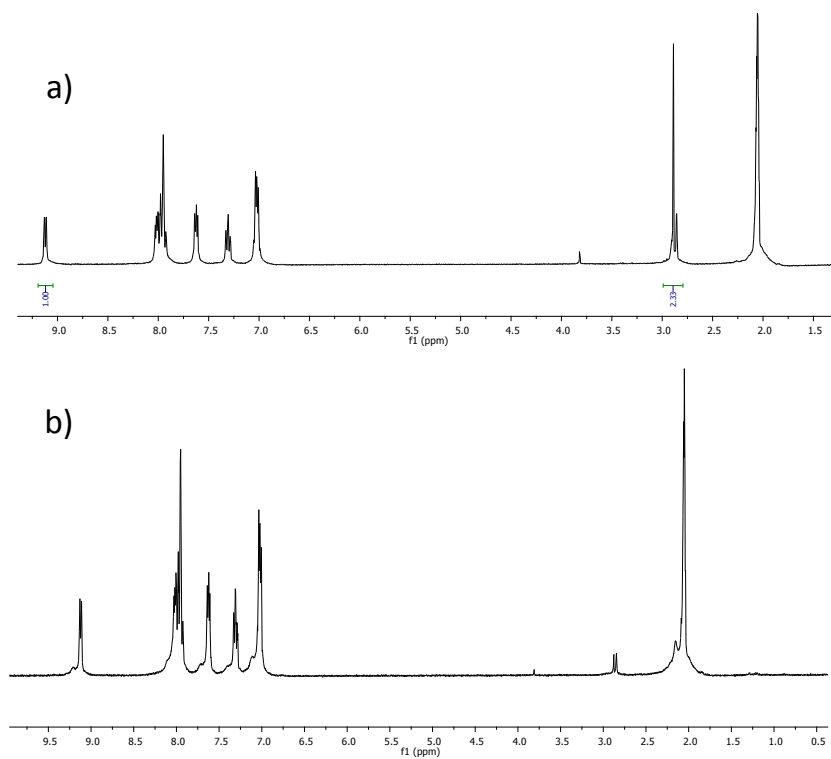
Figure S3: ^1H NMR of Pd(ppy)K·H_2O (a) and Pd(ppy)K (b) in anhydrous acetone-d_6, 300 MHz, 293 K.
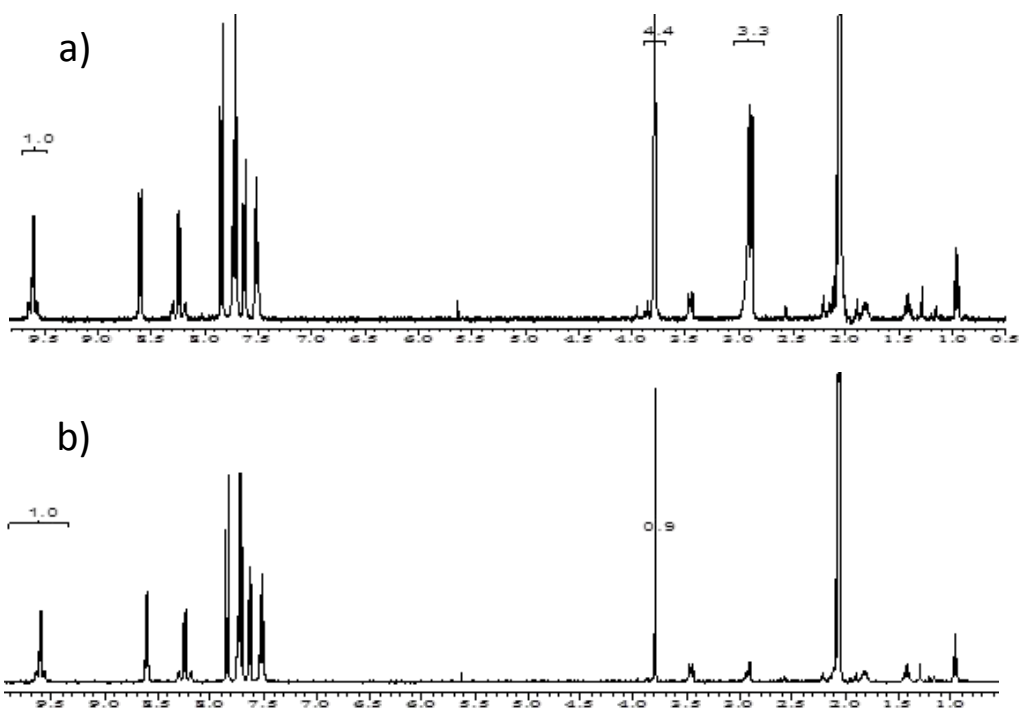
Figure S4: ^{1}H NMR of Pt(bzq)Li·4H$_2$O (a) and Pt(bzq)Li (b) in anhydrous acetone-d_6, 400 MHz, 293 K.

Section 2. Single crystal structure solution
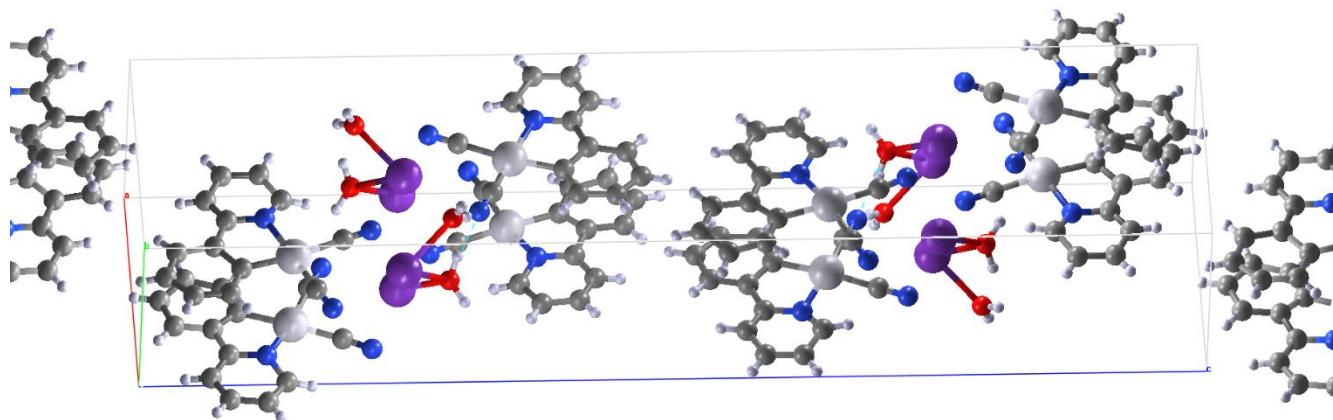
Figure S5. Crystal structure solution of Pt(ppy)K• compound, with crystal symmetry expanded within the unit cell.

Table S1. Computational parameters used in DFT calculations.

Adopted pseudopotentials:	
Pt	Pt.pbe-n-rrkjus_psl.0.1.UPF
K	K.pbe-n-mt.UPF
N	N.pbe-rrkjus.UPF
C	C.pbe-rrkjus.UPF
O	O.pbe-rrkjus.UPF
H	H.pbe-rrkjus.UPF
k-grid for Pca2$_1$ (y is the shortest axis)	
Rough	1 2 1
Refined	1 4 1
k-grid for Pbca (y is the shortest axis)	
Rough	1 1 1
refined	1 2 1
Van der Waals terms	
rough	*none*
refined	grimme-d3
dft energy convergence threshold	0.5e-5 hartree/cell
energy cutoff	25 hartree
density cutoff	800 hartree

Section 3. Thermogravimetric analysis
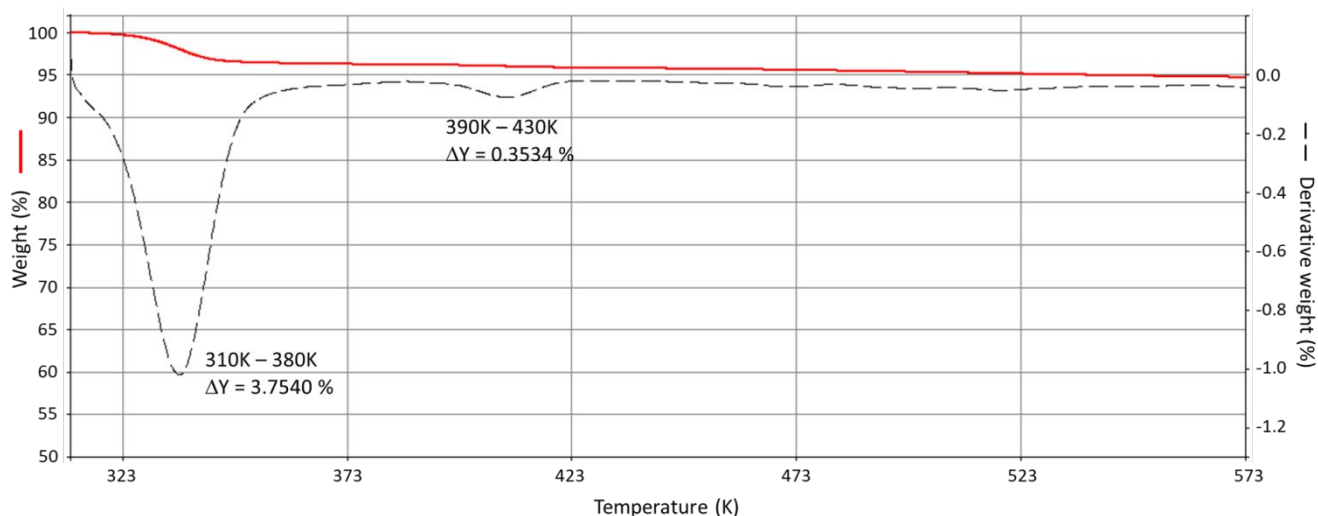
Figure S6. TGA curve of Pt(bzq)K. Two processes are detected: one between 310 K and 380 K, corresponding to a 3.75% weight loss, and the second between 390 K and 430 K, corresponding to a 0.35% weight loss. The overall weight loss is 4.1%, which corresponds to a total loss of 1 water molecule.
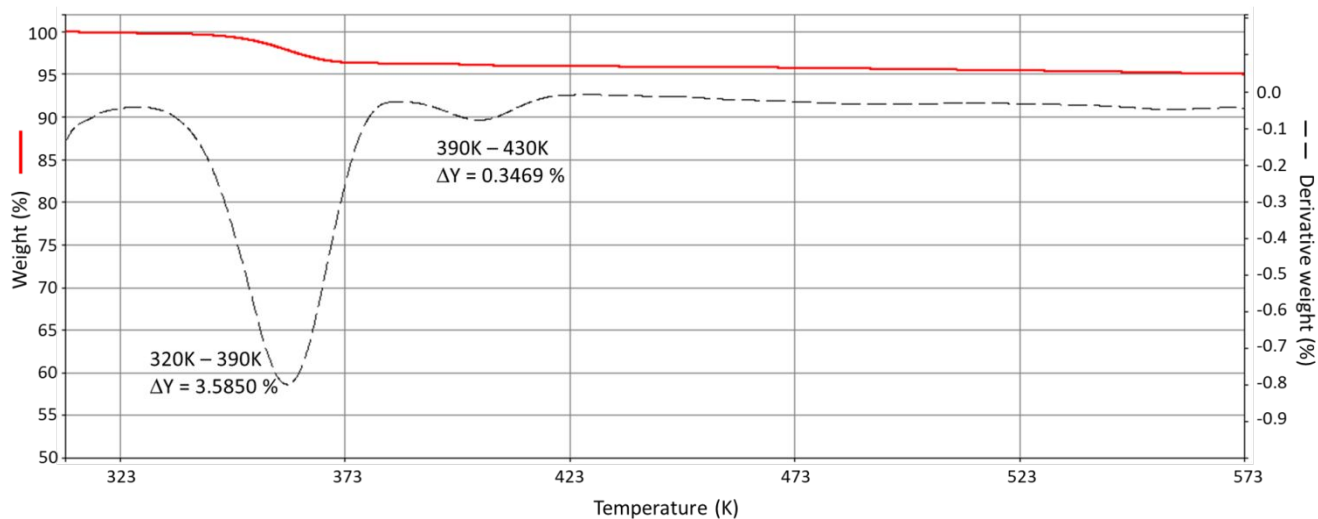
Figure S7. TGA curve of Pt(ppy)K. Two processes are detected: one between 320 K and 390 K, corresponding to a 3.59% weight loss, and the second between 390 K and 430 K, corresponding to a 0.35% weight loss. The overall weight loss is 3.9%, which corresponds to a total loss of 1 water molecule.
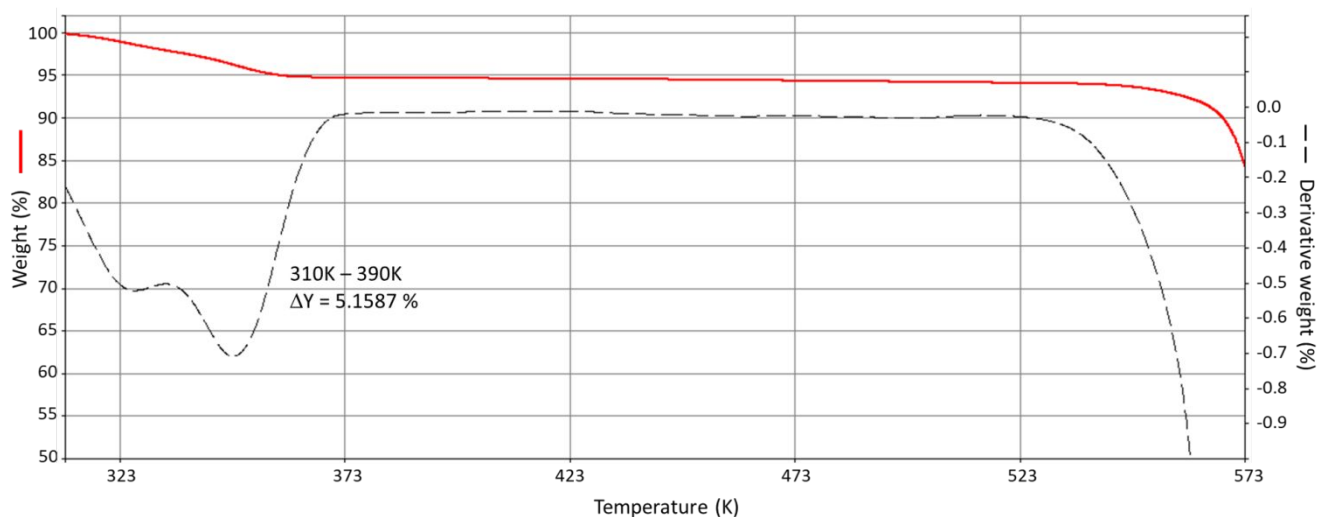
Figure S8. TGA curve of Pd(ppy)K. Two superimposed processes are detected between 310 K and 390 K. The overall weight loss is 5.2%, which corresponds to a total loss of 1 water molecule.
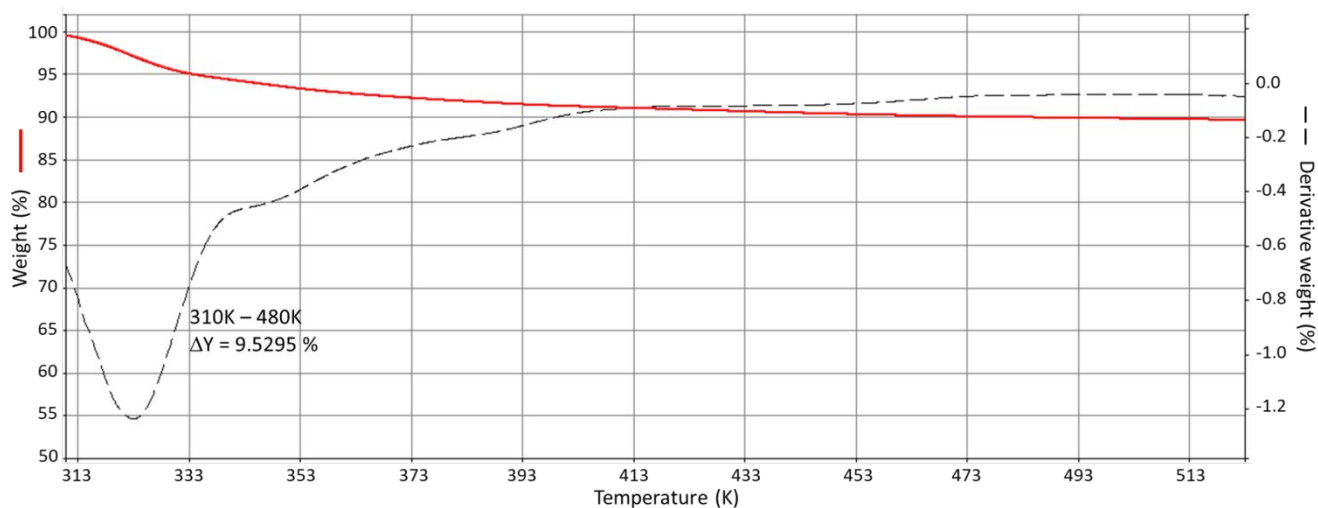
Figure S9. TGA curve of Pt(bzq)Li. Several superimposed processes are detected between 310 K and 480 K. The overall weight loss is 9.5%, which corresponds to a total loss of 2.5 water molecules. In an attempt to improve the crystallinity of Pt(bzq)Li, the sample was placed in a 100%HR environment. However, after few hours the sample liquefied. This behavior highlights the high hygroscopicity of the lithium salt, and therefore, that the pre-treatment of the sample highly affects the determination of the amount of water.

Section 4. Variable-temperature X-ray powder diffraction analysis
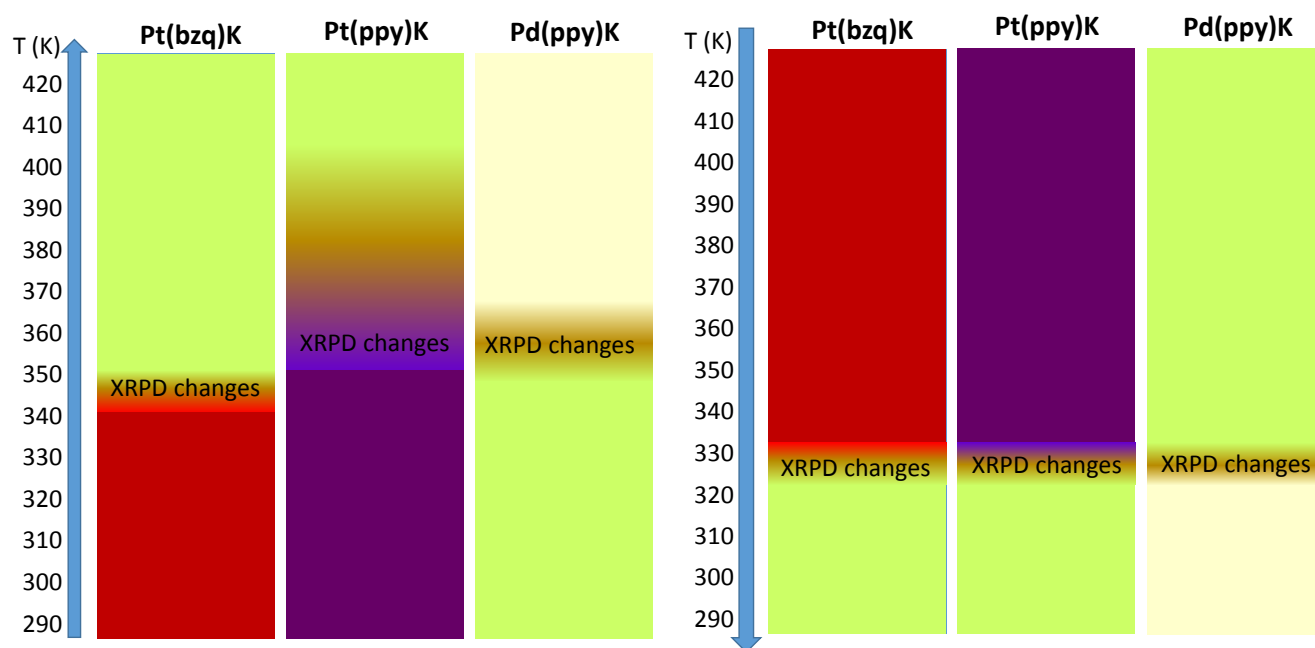
Figure S10. Schematic representation of structural and color variations occurring during heating (left) and cooling (right). "XRPD changes" identifies temperature ranges where X-ray powder diffraction patterns undergo variations.
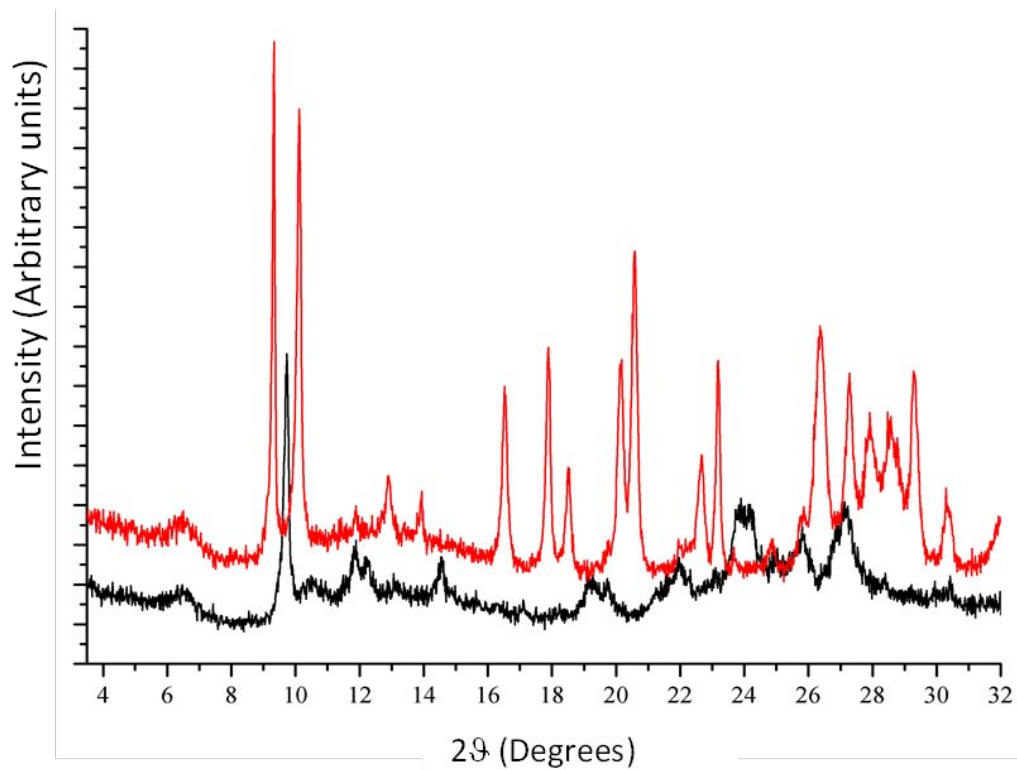
Figure S11. X-ray powder diffraction profiles of compound Pt(ppy)K collected during cooling: anhydrous form measured at 420 K (black) and hydrated form measured at 310 K (red).
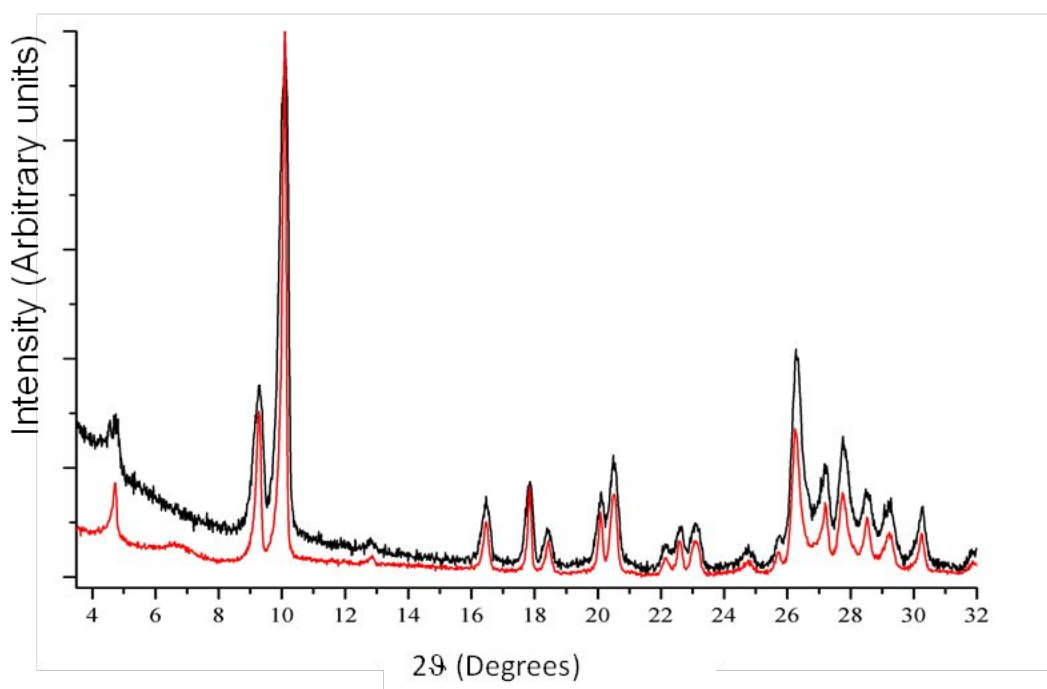
Figure S12. X-ray powder diffraction profiles of compound Pd(ppy)K• collected before (black) and after (red) the exposure to 100% HR H_2O vapors. The FWHM of the peak at $2\vartheta=10°$ is 0.34 for the black and 0.14 for the red profile.
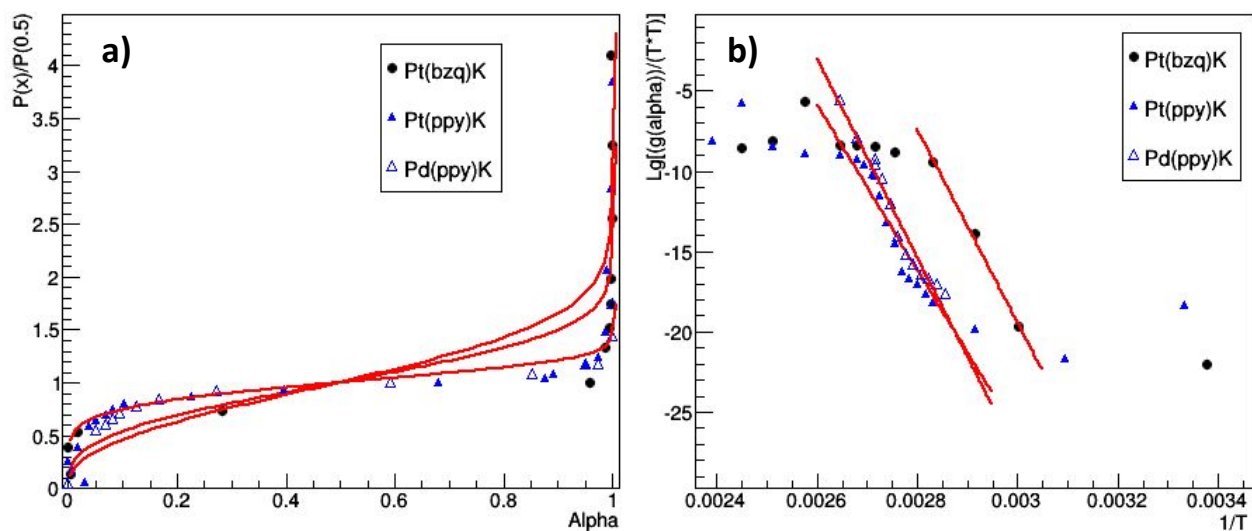
Figure S13. Kinetic analysis of the reaction coordinate extracted from variable-temperature X-ray powder diffraction profiles. Masterplot fit with the Avrami-Eroféev model (a) and Coats and Redfern fit of the kinetic equation (b).
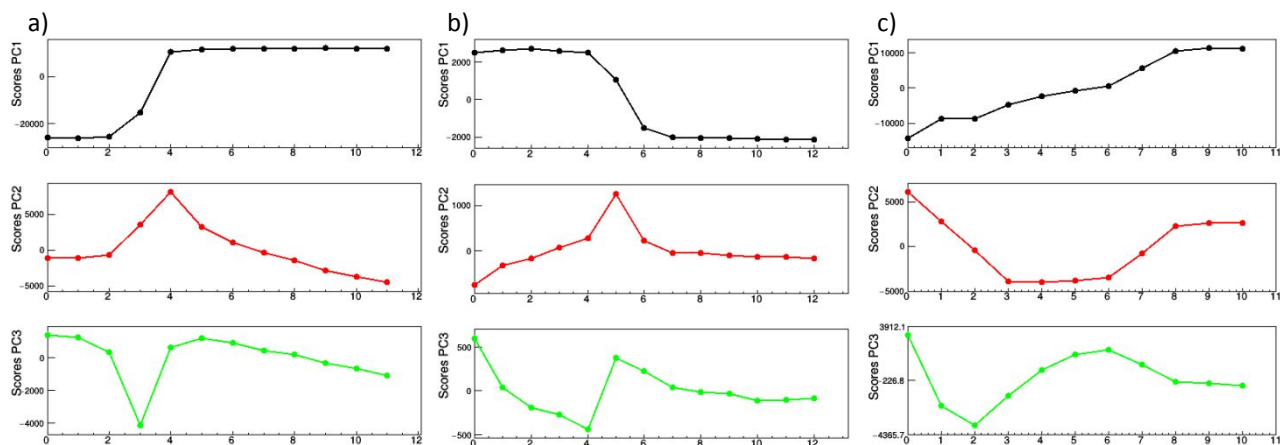
Figure S14. Results of the PCA applied to variable-temperature X-ray powder diffraction profiles. PCA scores as a function of measurement number of the first three principal components for Pt(bzq) (a), Pt(ppy) (b) and Pd(ppy) (c).

Section 5. *In situ* pair distribution function: multivariate analysis
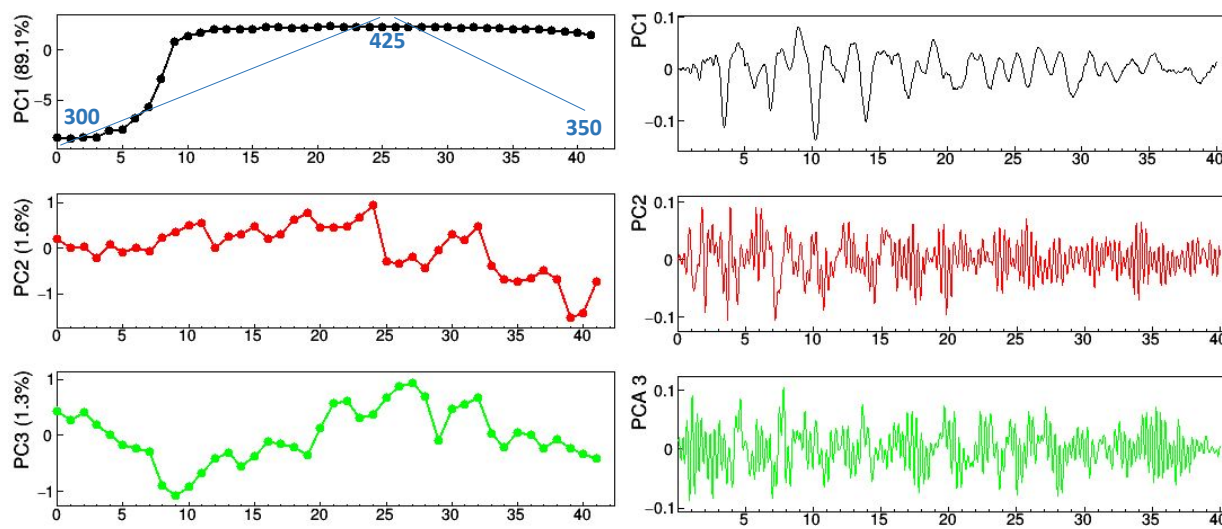
Figure S15. Results of the PCA applied to *in situ* PDF data of compound Pt(bzq)K. PCA scores as a function of measurement number (left) and PCA loadings as a function of the interatomic distance in Angstrom (right) of the three first principal components. The percentage of total data variance explained by each principal component is reported as vertical title in the scores plot. The temperature ramp with its relevant values (in K) is sketched on PC1 scores plot.
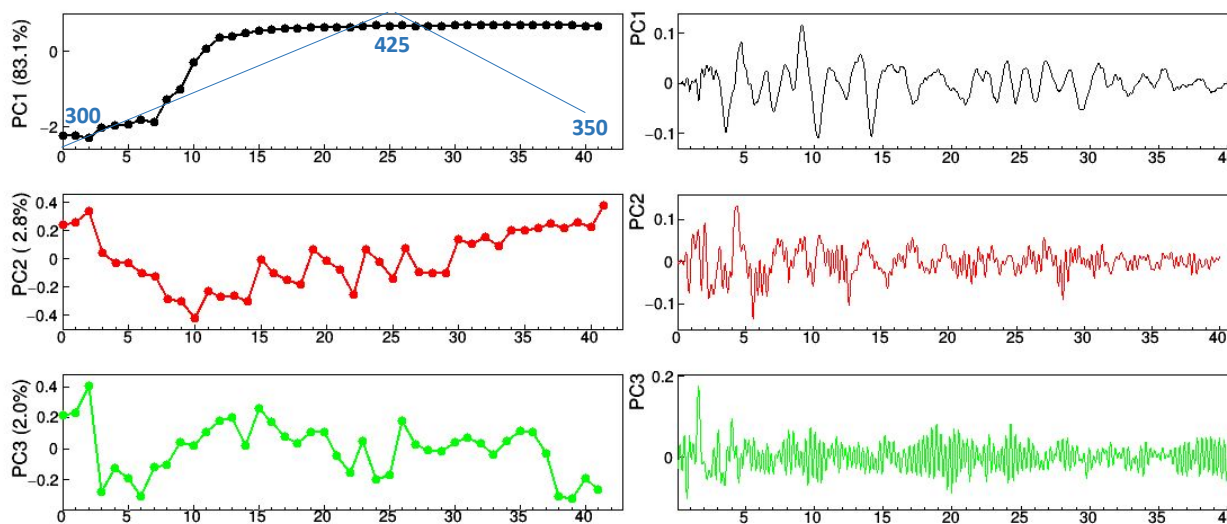
Figure S16. Results of the PCA applied to *in situ* PDF data of compound Pd(bzq)K. PCA scores as a function of measurement number (left) and PCA loadings as a function of the interatomic distance in Angstrom (right) of the three first principal components. The percentage of total data variance explained by each principal component is reported as vertical title in the scores plot. The temperature ramp with its relevant values (in K) is sketched on PC1 scores plot.
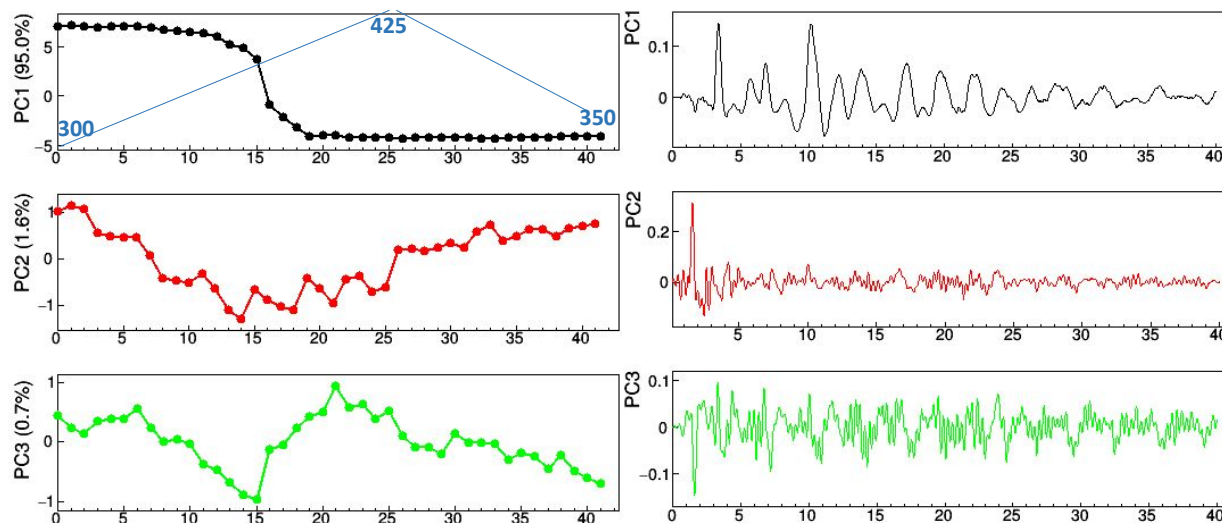
Figure S17. Results of the PCA applied to *in situ* PDF data of compound Pt(ppy)K. PCA scores as a function of measurement number (left) and PCA loadings as a function of the interatomic distance in Angstrom (right) of the three first principal components.The percentage of total data variance explained by each principal component is reported as vertical title in the scores plot. The temperature ramp with its relevant values (in K) is sketched on PC1 scores plot.
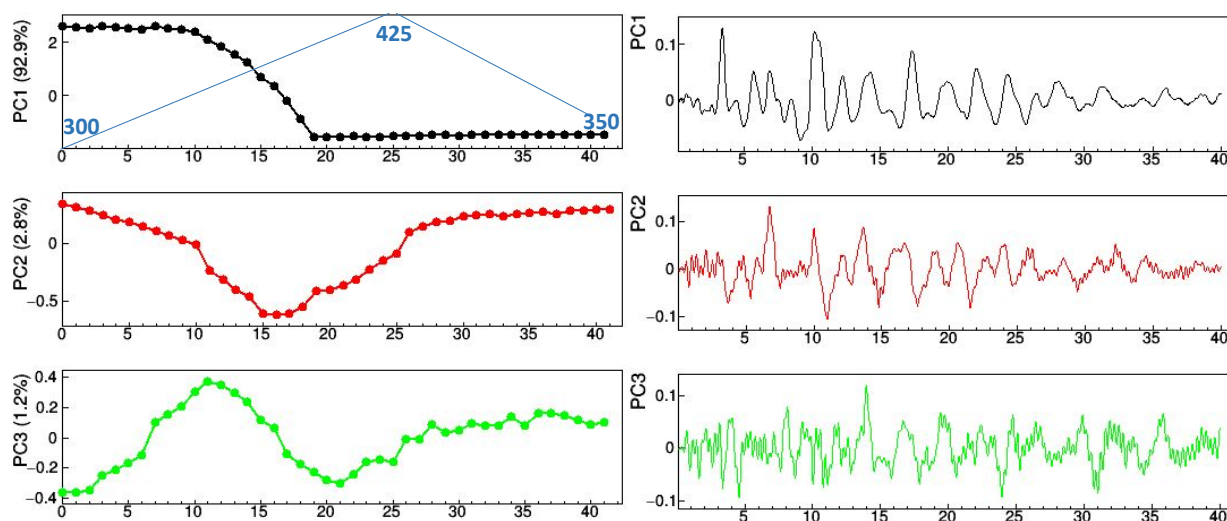
Figure S18. Results of the PCA applied to *in situ* PDF data of compound Pd(ppy)K. PCA scores as a function of measurement number (left) and PCA loadings as a function of the interatomic distance in Angstrom (right) of the three first principal components. The percentage of total data variance explained by each principal component is reported as vertical title in the scores plot. The temperature ramp with its relevant values (in K) is sketched on PC1 scores plot.
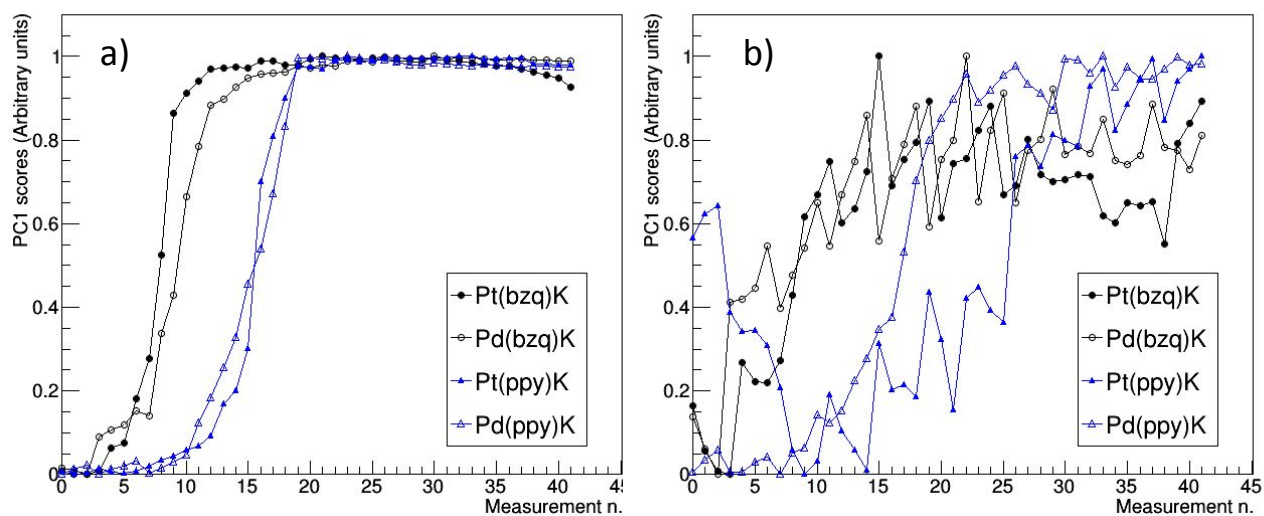
Figure S19. Comparison of scores of the first principal component (PC1), as calculated by PCA applied to PDF profiles restricted to interatomic distances higher (a) and lower (b) than 3 Å (b). Scores are arbitrarily normalized by scaling between 0 and 1.
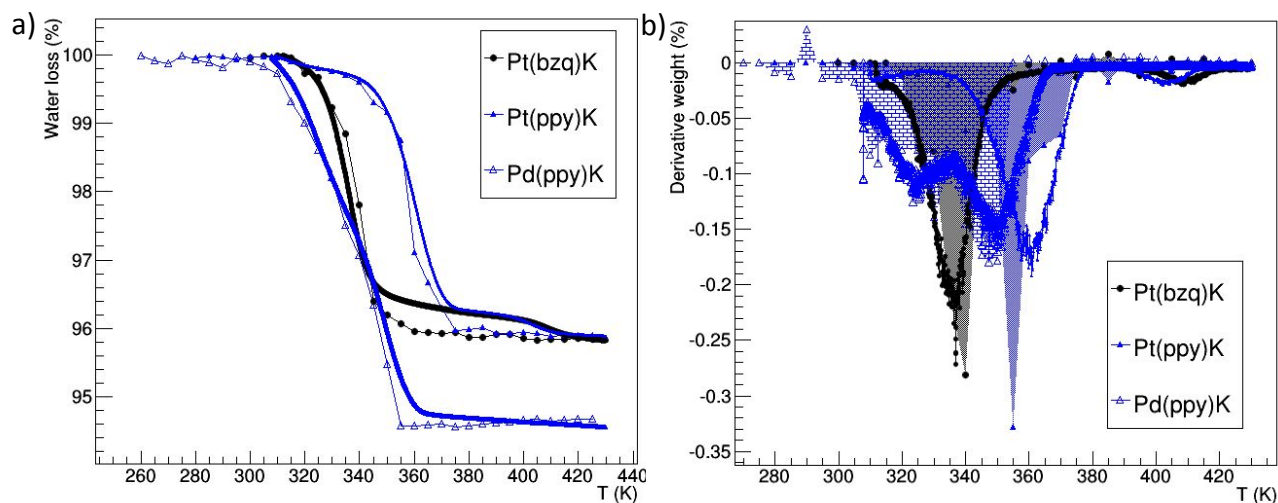
Figure S20. Weight loss (a) and its derivative (b) as determined by TGA (full lines) superposed to the PC1 scores (a) and its derivative (b) obtained from PCA applied to PDF data. PC1 scores have been rescaled to match the minimum and maximum value of the TGA curve in the temperature range covered by PDF measurements. Moreover, PC1 scores of Pt(ppy) and Pd(ppy) have been shifted by -15 K and -35 K, respectively.

Section 6. *In situ* pair distribution function: structural refinement
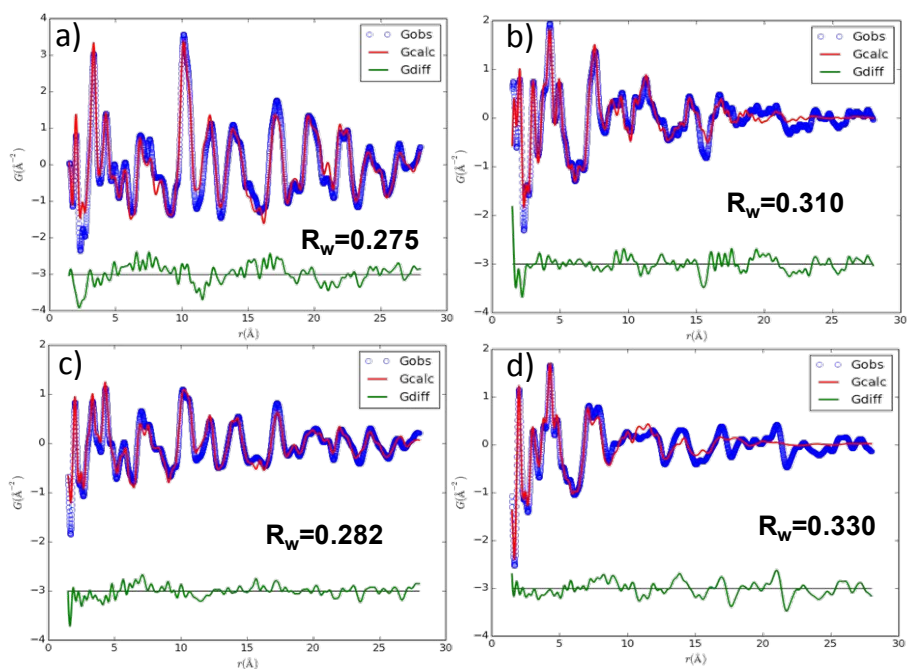
Figure S21. Results of the structural refinement for pair distribution function data of Pt(ppy)K at 300 K (a) and 450 K (b) and of Pd(ppy)K at 300 K (c) and 450 K (d). Experimental (blue dots), calculated (red line) and difference (green line) PDF values are show, and the weighted agreement factor between model and data (R_w) is reported. Only data in the fitting range between 1.5 Å and 28 Å are shown.
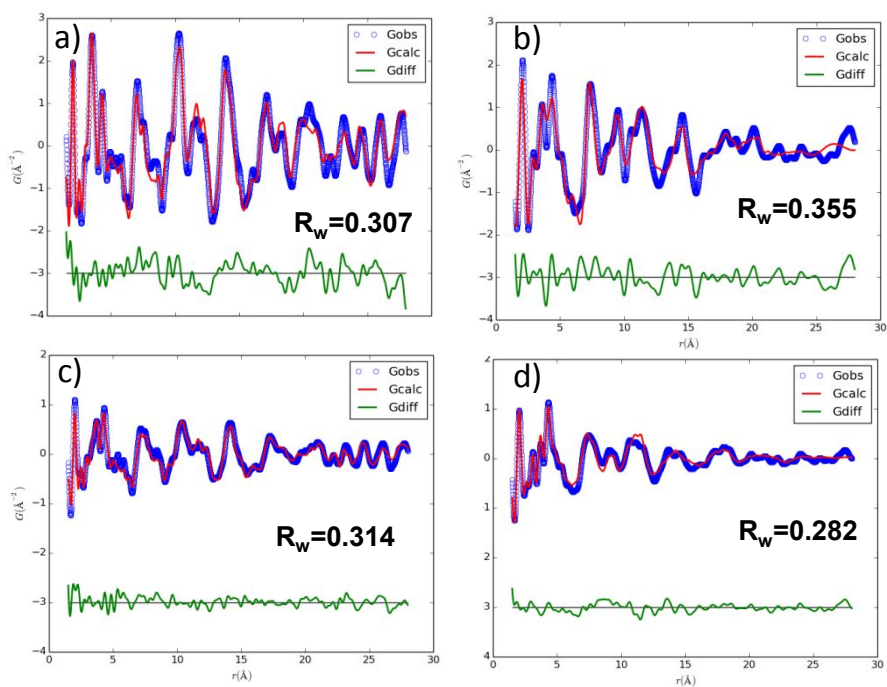
Figure S22. Results of the structural refinement for pair distribution function data of Pt(bzq)K at 300 K (a) and 450 K (b) and of Pd(bzq)K at 300 K (c) and 450 K (d). Experimental (blue dots), calculated (red line) and difference (green line) PDF values are show, and the weighted agreement factor between model and data (R_w) is reported. Only data in the fitting range between 1.5 Å and 28 Å are shown.

Table S2. Relevant distances and angles involving the metal ion Pd-(II)/Pt(II) (M) and the potassium counterion in structural models refined against 300 K (left) and 450 K (right) PDF data.

Compound	M-M (Å)	M-M-M (°)	M-K (Å)	(K-K)a (Å)	(K-K)b (Å)
Pt(ppy)K	3.4 → 3.9	178 → 136	4.2 → 4.2	4.9 → 4.3	4.2 → 4.1
Pd(ppy)K	3.4 → 3.9	179 → 134	4.2 → 4.2	5.0 → 4.4	4.2 → 4.3
Pt(bzq)K	3.5 → 3.9	167 → 162	4.5 → 4.3	4.7 → 4.7	3.9 → 4.2
Pd(bzq)K	3.5 → 3.9	170 → 166	4.5 → 4.2	4.8 → 4.6	4.2 → 4.1

Section 7. X-ray absorption spectroscopy
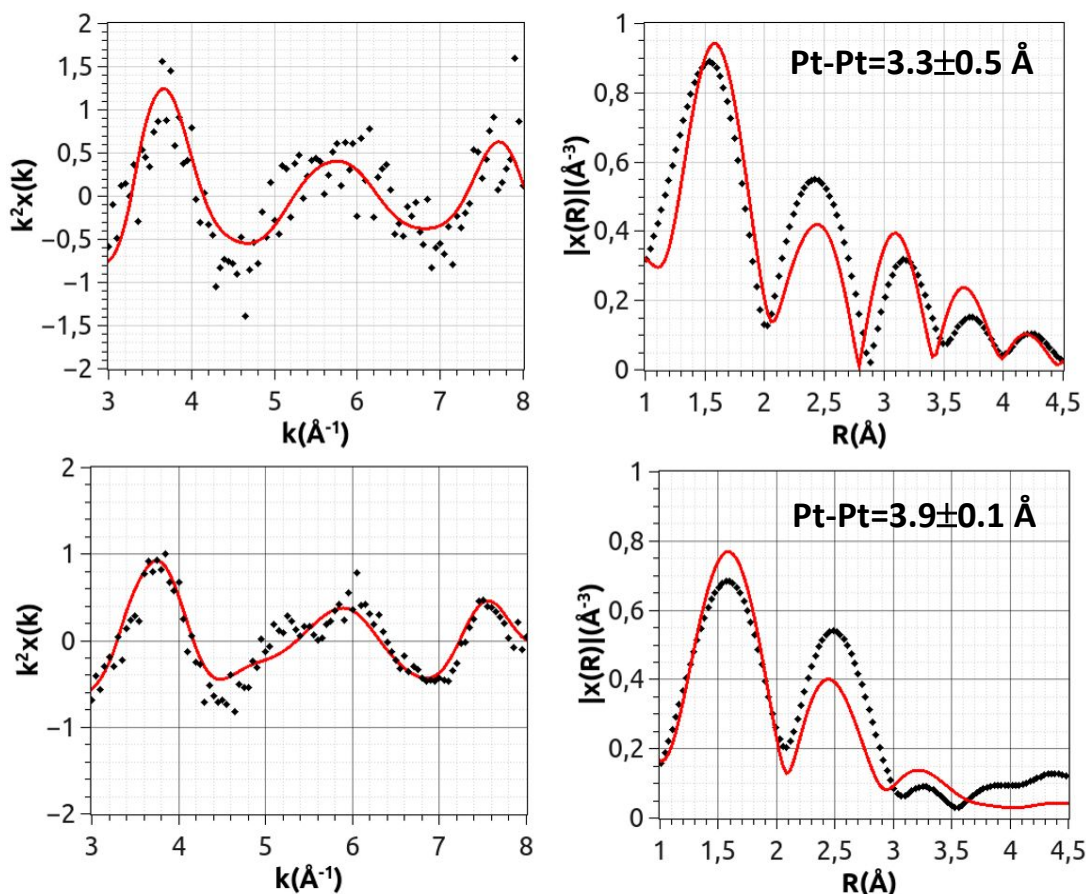
Figure S23. X-ray absorption spectroscopy analysis applied to Pt(bzq)K at low (top row) and high (bottom row) temperature: normalized XAS signal (left) and its radial distribution (right). The best-fit values of the Pt-Pt distance are shown.

APPENDIX B

SUPPORTING INFORMATION

Structure-Mechanical Relationships in Polymorphs of Organic Semiconductor (C4-NT3N)

Chiara Cappuccino,† Luca Catalano,§ Francesco Marin,† Ghada Dushaq,§ Gijo Raj,§ Mahmoud Rasras,§ Rachid Rezgui,§ Massimo Zambianchi,‡ Manuela Melucci,‡ Pače Naumov,§ Lucia Maini†**

† Dipartimento di Chimica "G. Ciamician", via Selmi 2, Università di Bologna, 40126 Bologna, Italy

§ New York University Abu Dhabi, P.O. Box 129188, Abu Dhabi, United Arab Emirates

‡ Consiglio Nazionale delle Ricerche-Istituto per la Sintesi Organica e la Fotoreattivita, (CNR-ISOF), via P. Gobetti 101, 40129 Bologna, Italy

Supporting Information

Structure-Mechanical Relationships in Polymorphs of Organic Semiconductor (C4-NT3N)

Chiara Cappuccino,† Luca Catalano,§ Francesco Marin,† Ghada Dushaq,§ Gijo Raj,§ Mahmoud Rasras,§ Rachid Rezgui,§ Massimo Zambianchi,‡ Manuela Melucci,‡ Panče Naumov,§* Lucia Maini†*

† Dipartimento di Chimica "G. Ciamician", via Selmi 2, Università di Bologna, 40126 Bologna, Italy

§ New York University Abu Dhabi, P.O. Box 129188, Abu Dhabi, United Arab Emirates

‡ Consiglio Nazionale delle Ricerche-Istituto per la Sintesi Organica e la Fotoreattivita, (CNR-ISOF), via P. Gobetti 101, 40129 Bologna, Italy

Table of Contents

Optical microscopy

Figure SI1. Crystals of the β phase with satellite crystals of the α phase. The image was taken with an optical microscope under a UV lamp (365 nm) at 100-fold magnification.

Powder diffraction

The two polymorphs were characterised by XRPD using the synchrotron facility at the PSI institute. It was performed an experiment at variable temperature (VT-XRPD) in order to detect any possible conversion upon thermal annealing (figure SI2).

From the collected patterns, it is visible that the sample undergoes a transition between 180°C and 195°C from the α to the β phase. Around 180°C (orange line in figure SI2), the pattern starts to change and contains peaks ascribable both to α and β phases, hint that the transition has begun, while at 195°C the pattern is comparable to the β phase, with a slight shift in the peaks position due to the thermal expansion effect. After the cooling of the sample, the diffractogram remains unchanged and the transition seems irreversible.
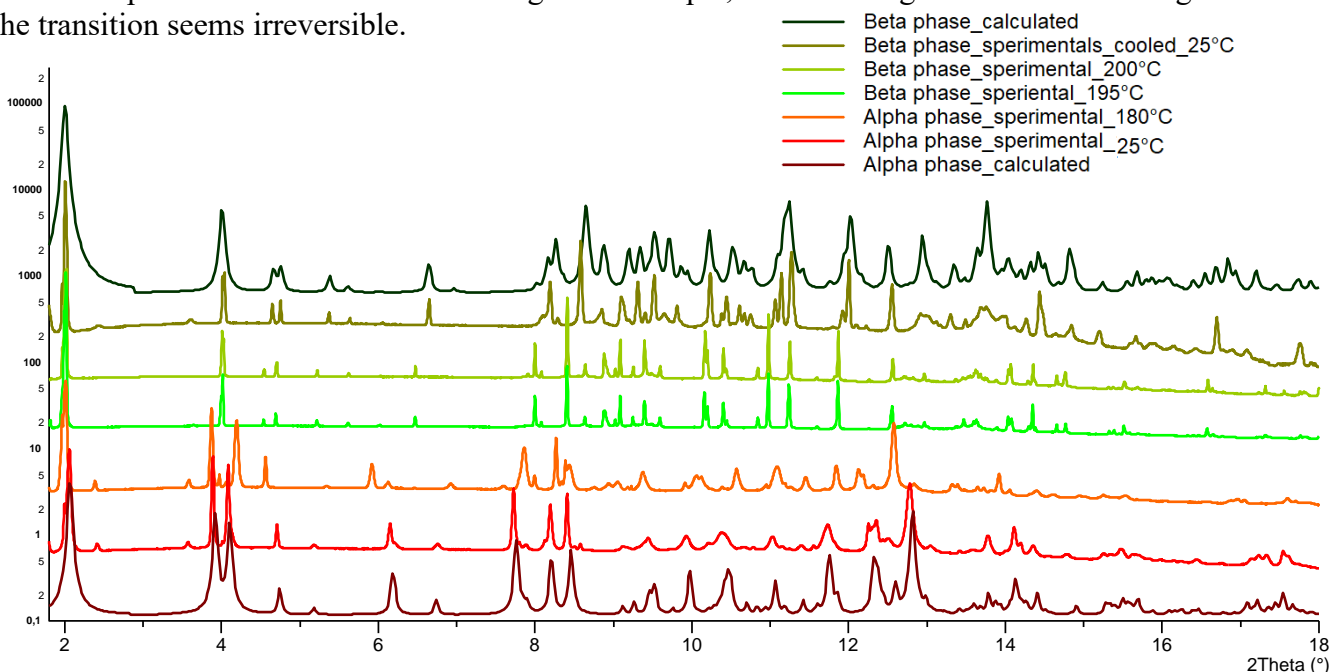
Figure SI2. Powder diffractograms of C4-NT3N (logaritmic scale), α phase, collected at different temperature, compared with the calculated diffractograms of the α (dark red line on the bottom) and β (dark green line on the top) phases, λ= 775375(2) Å.

Thermal analysis
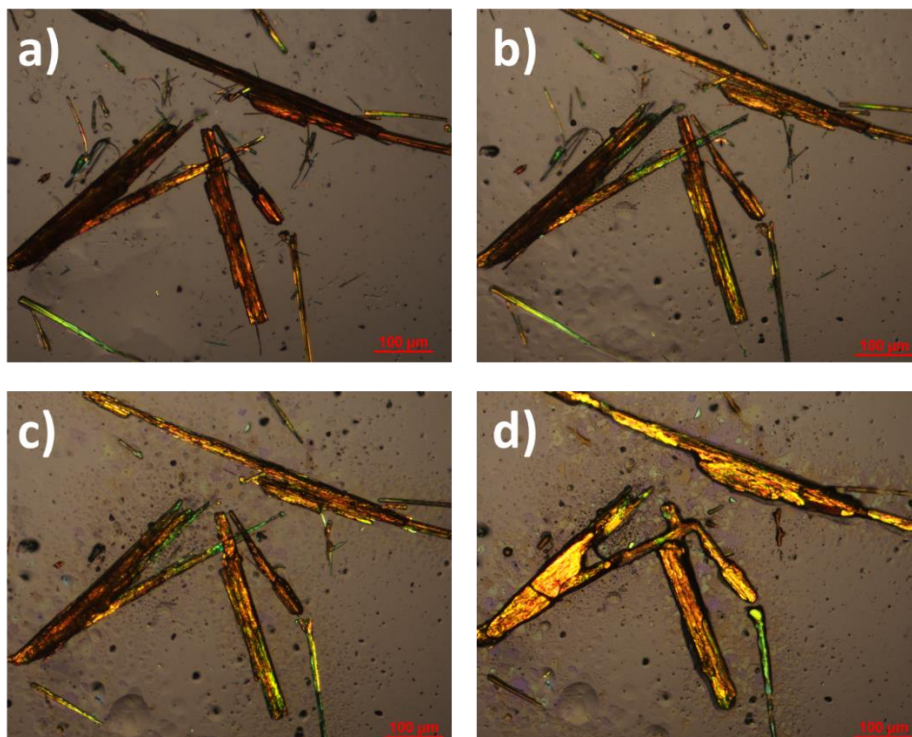
Figure SI3. Hot-stage microscopy of α phase during the thermal annealing. a) 26°C; b) 210°C, beginning of the transition from α to β; c) 217°C, end of the solid-state transition; d) 228°C, beginning of the melting. The image was taken with an optical microscope with polarizer and analyser were placed at 90° at 100-fold magnification
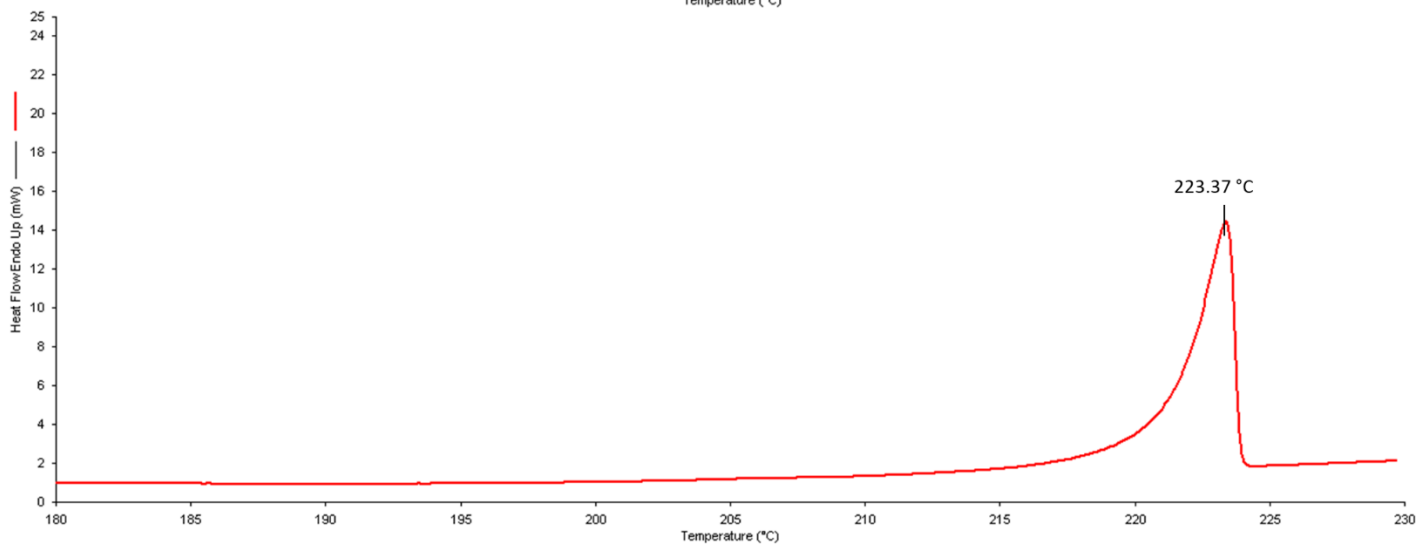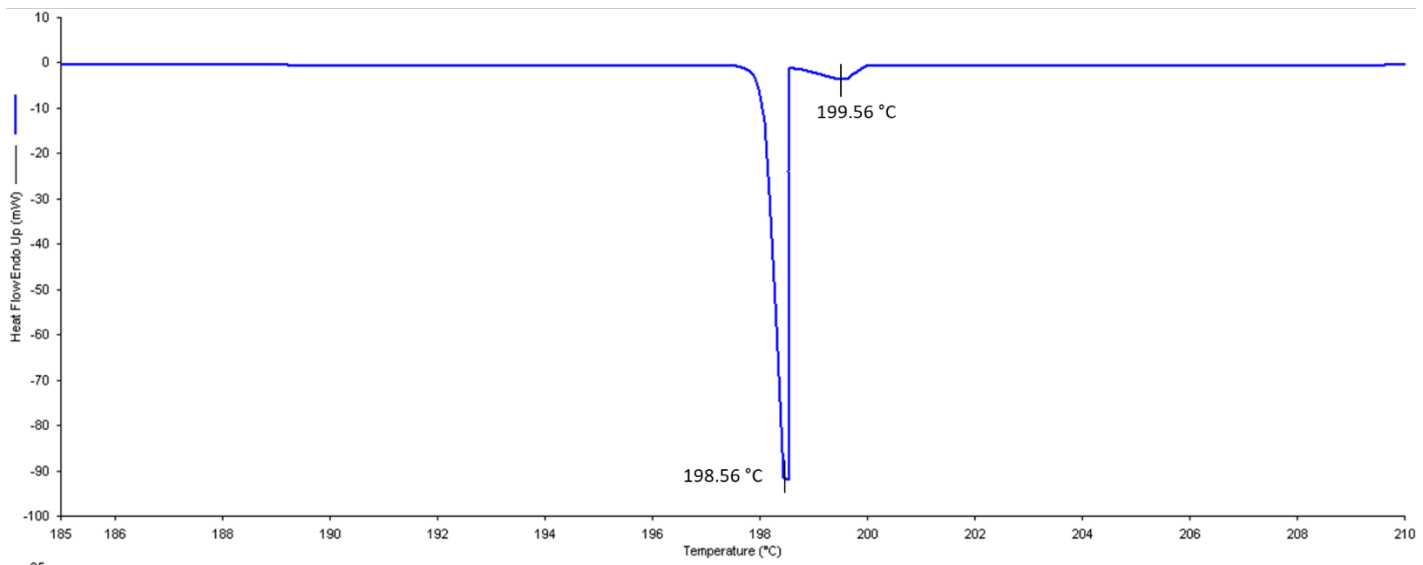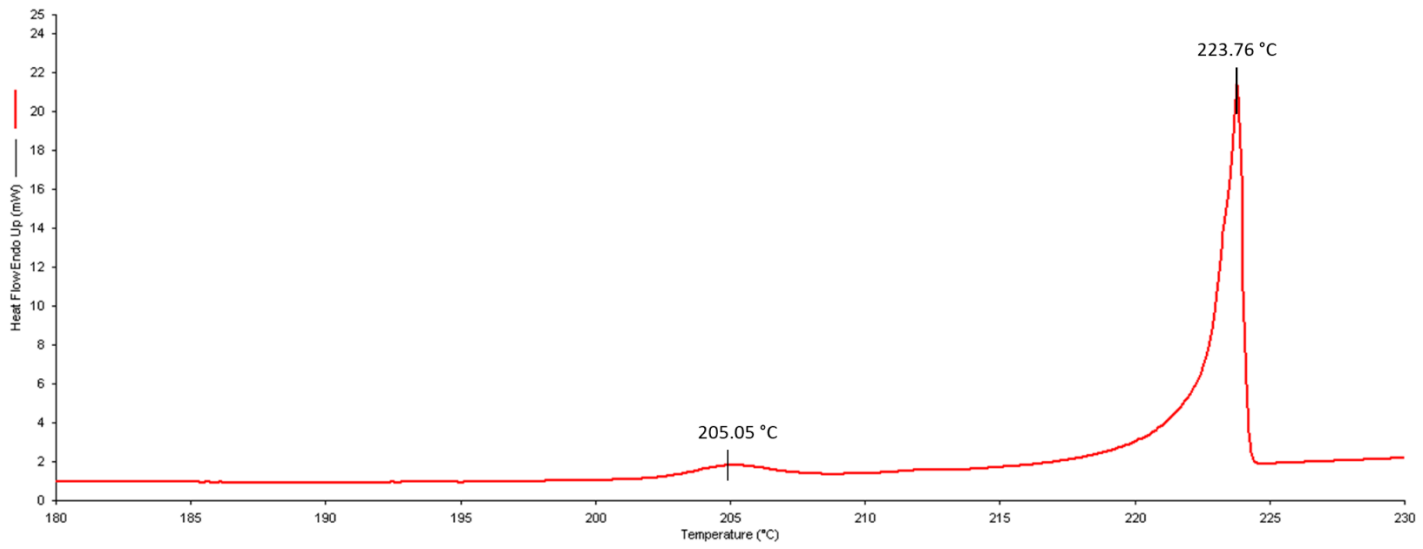
Figure SI4. DSC analysis of C4-NT3N α phase, heating, cooling and second heating.

Estimation of the intermolecular interactions

For the α phase, the interactions of a central molecule with the 13 nearest molecules were calculated (figure SI5), obtaining the values described in Table SI1.
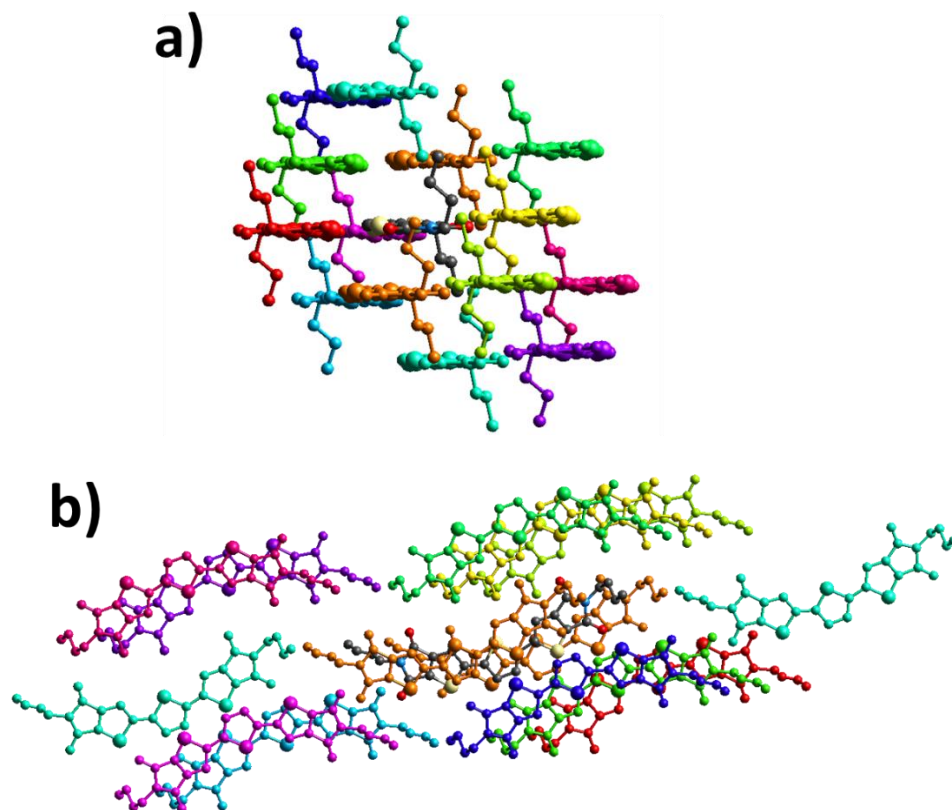
Figure SI5. View of the cluster of molecules of α phase used for the interaction energies calculation. a) view along the π-π interaction; b) View perpendicular to the molecular plane. The central molecule is marked with the atom specific colours (C=grey; O=red; N=blue; S=yellow), the surrounding molecules are marked by an identification colour.

Table SI1. Interaction energies for α phase (kJ/mol). The colours represent the corresponding molecule in figure SI5.

	N. molecules	Distance (Å)	E_ele	E_pol	E_dis	E_rep	E_tot
	2	4.83	-12.0	-2.7	-117.6	52.4	-77.4
	1	12.06	-32.0	-7.7	-19.7	22.3	-37.3
	1	9.42	-3.1	-4.7	-42.6	20.5	-28.0
	1	18.86	-16.6	-6.1	-15.2	9.8	-26.6
	1	10.96	-2.3	-3.0	-27.4	8.7	-21.9
	1	16.49	-7.5	-4.9	-20.8	9.7	-21.7
	1	8.86	-2.4	-2.2	-14.1	3.0	-14.1
	1	8.88	-0.0	-0.3	-8.6	0.7	-7.4
	1	8.71	0.0	-9.0	0.0	0.0	-5.8
	1	19.28	0.4	-0.3	-7.6	1.3	-5.6
	1	21.64	-0.2	-0.0	-2.7	0.0	-2.6
	2	23.89	-0.8	-0.1	-6.1	5.2	-2.2

For the β phase, the interactions of a central molecule with the 13 nearest molecules were calculated (figure SI6), obtaining the values described in Table SI2. To simplify the calculation, the internal disorder was removed, using only the *syn-anti* configuration, which is the configuration with highest occupancy within the crystal structure.
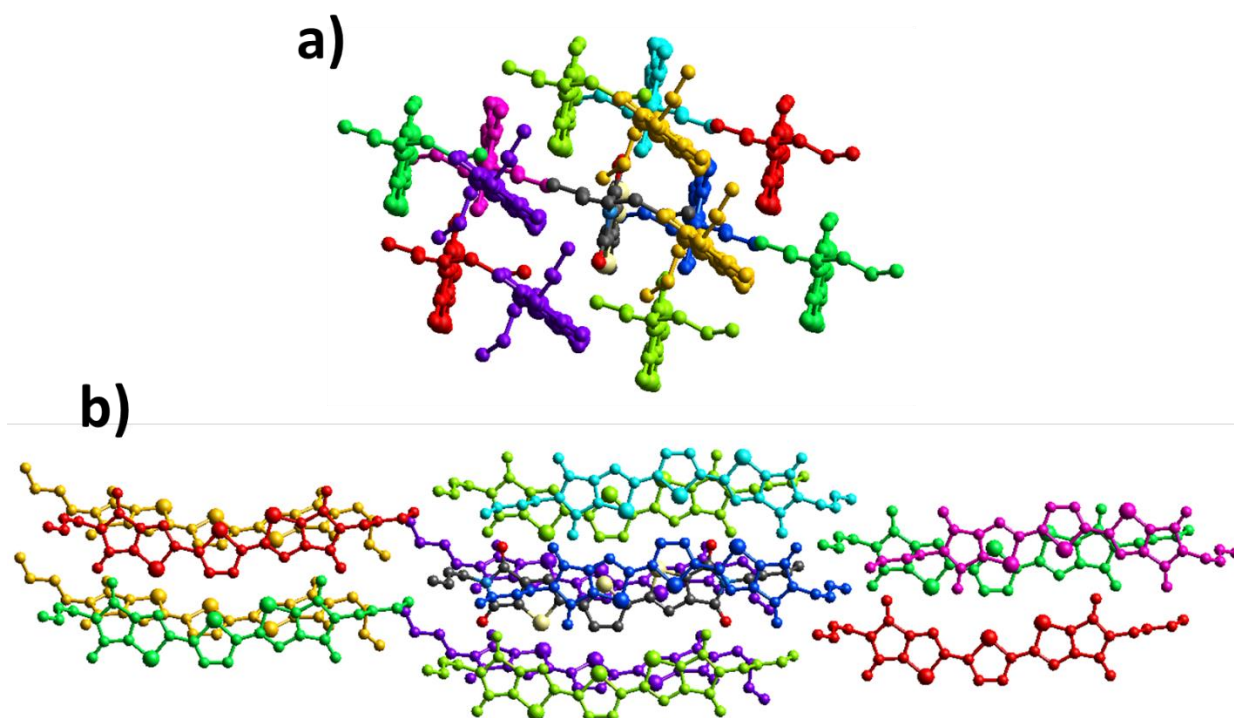
Figure SI6. View of the cluster of molecules of β phase used for the interaction energies calculation. a) view along the π-π interaction, with the details of the herringbone arrangement; b) View perpendicular to the molecular plane of the central molecule. The central molecule is marked with the atom specific colours (C=grey; O=red; N=blue; S=yellow), the surrounding molecules are marked by an identification colour.

Table SI2. Interaction energies for β phase (kJ/mol). The colours represent the corresponding molecule in figure SI6.

	N. molecules	Distance (Å)	E_ele	E_pol	E_dis	E_rep	E_tot
	1	5.78	-13.8	-1.6	-98.1	49.5	-63.4
	1	7.35	-48.3	-13.6	-40.3	-38.9	-62.9
	2	5.25	-11.3	-7.7	-72.8	35.9	-53.1
	2	5.62	-16.7	-6.6	-59.1	31.1	-49.3
	2	23.13	-0.5	-0.1	-5.9	2.6	-3.8
	2	22.94	-0.4	-0.0	5.2	1.7	-3.7
	2	23.61	-0.6	-0.0	-5.6	3.1	-3.1
	1	26.96	-0.7	-0.1	-4.7	5.4	-0.6

Crystal phase indexing

The face indexing has been performed with the software CrysalisPro, from the crystals used for the SCXRD. The indexing obtained presents one face with unusual *hkl* index, due to the imperfect fracture of the crystals chosen for the SCXRD.

The α crystals present a needle-like shape; with a preferential growing along the π-π interaction (figure SI7), that is the direction of the stronger intermolecular interaction.
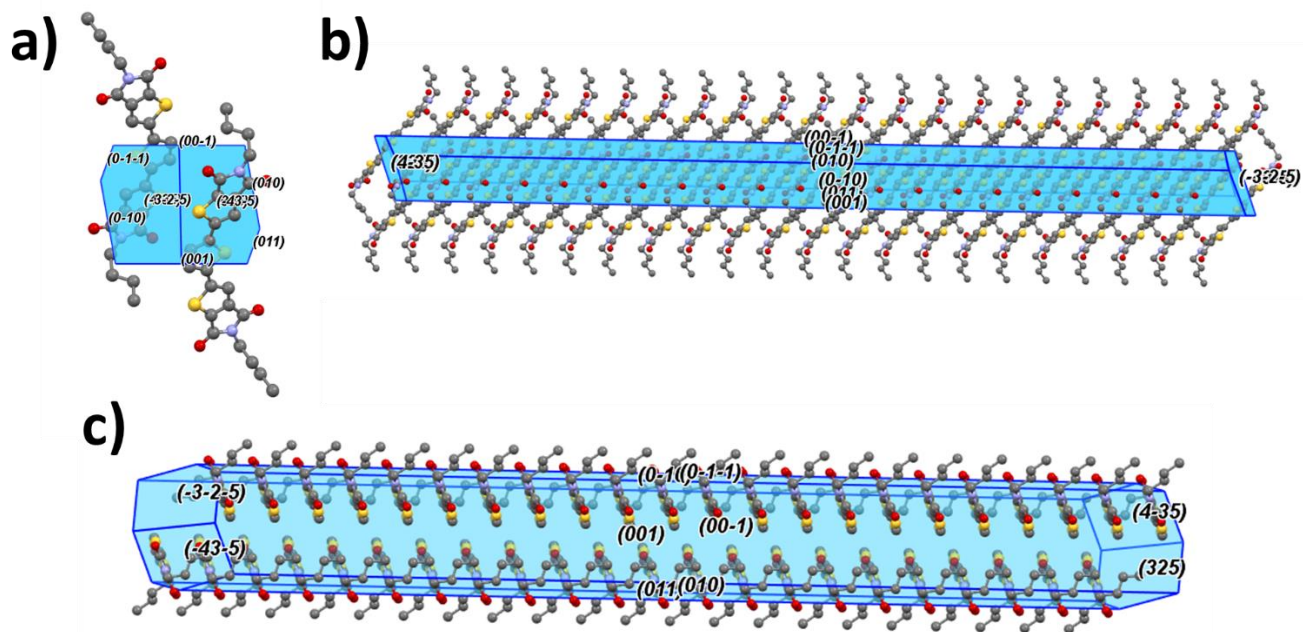
Figure SI7. Crystal morphology of α phase correlated with the crystal structure. a) View along *a* axis; b) view along *b* axis; c) view parallel to the columnar stacks.
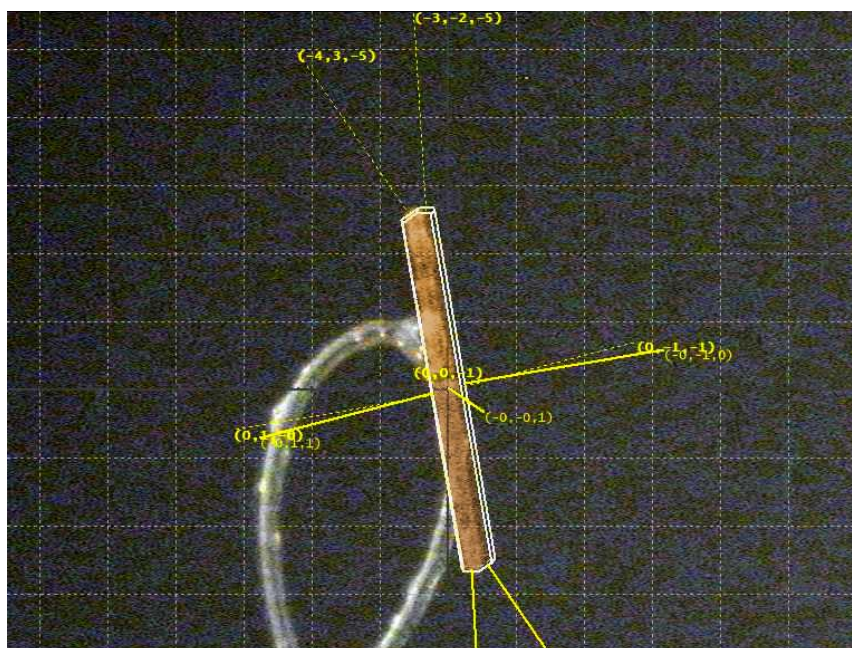
Figure SI8. Face indexing process of the α crystal, using the software CrysalisPro.

The β crystals present a plate-like shape. The structure of the morphology reflects the layered structure with a preferential grow in the direction of the π-π interaction and the herringbone (figure SI9). In the view along the b axis, is visible the wafer-like structure characteristic of the β phase.
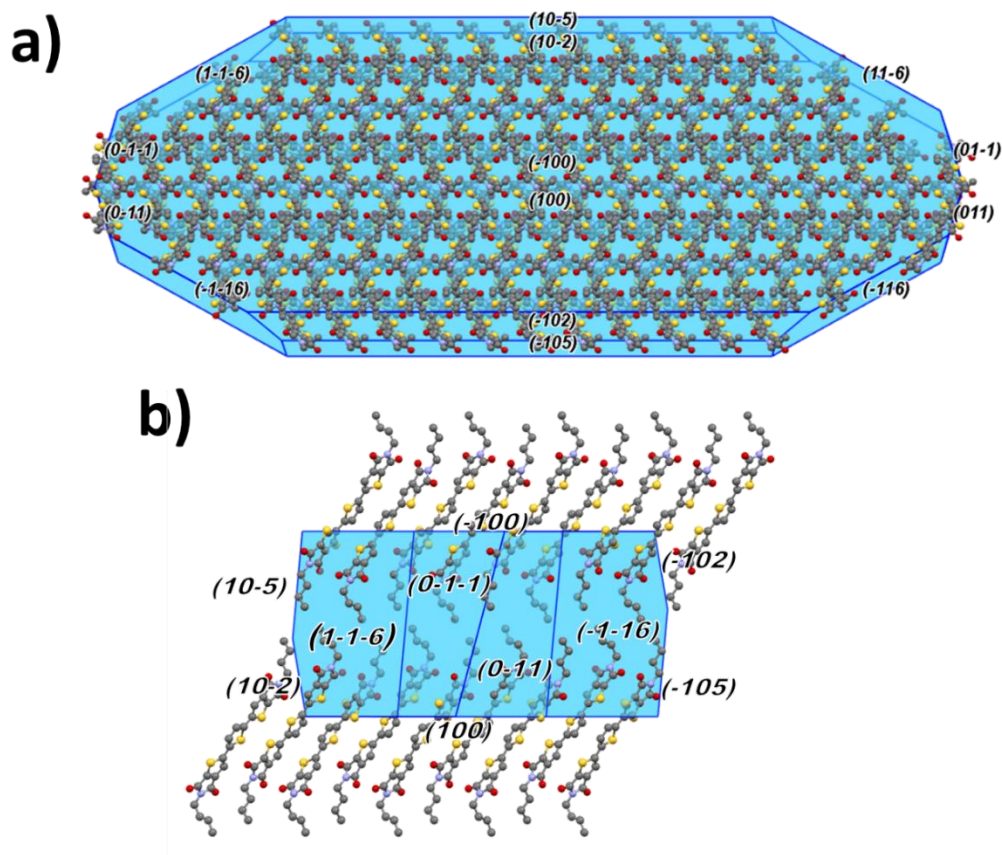
Figure SI9. Crystal morphology of β phase correlated with the crystal structure. a) View along *a* axis; b) view along *b* axis.

Figure SI10. Face indexing process of the β crystal, using the software CrysalisPro.
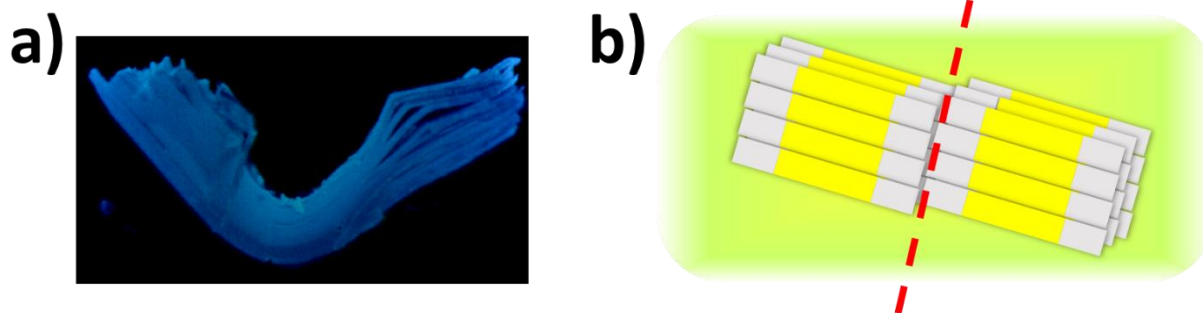
Figure SI11. The delamination of a β crystal after the deformation could be caused by the slipping of different layer, parallel to the (100) crystal face; where the intermolecular interactions are weaker.

AFM nanoindentation
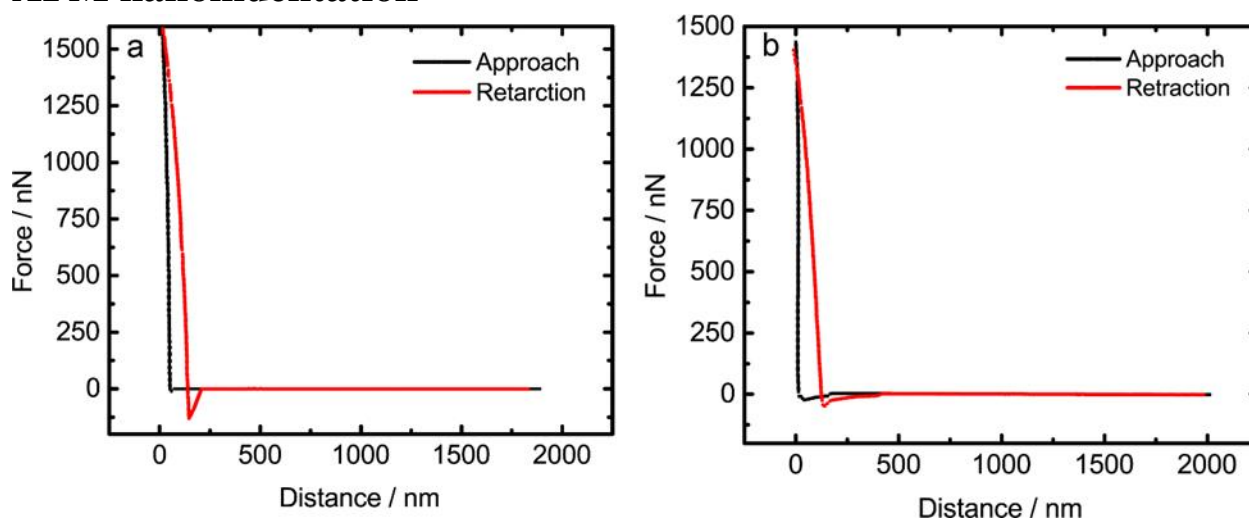
Figure SI12: Representative AFM force-distance profiles obtained on a) Elastic crystal (α polymorph), and b) plastic crystal (β polymorph).

Confocal fluorescence microscopy
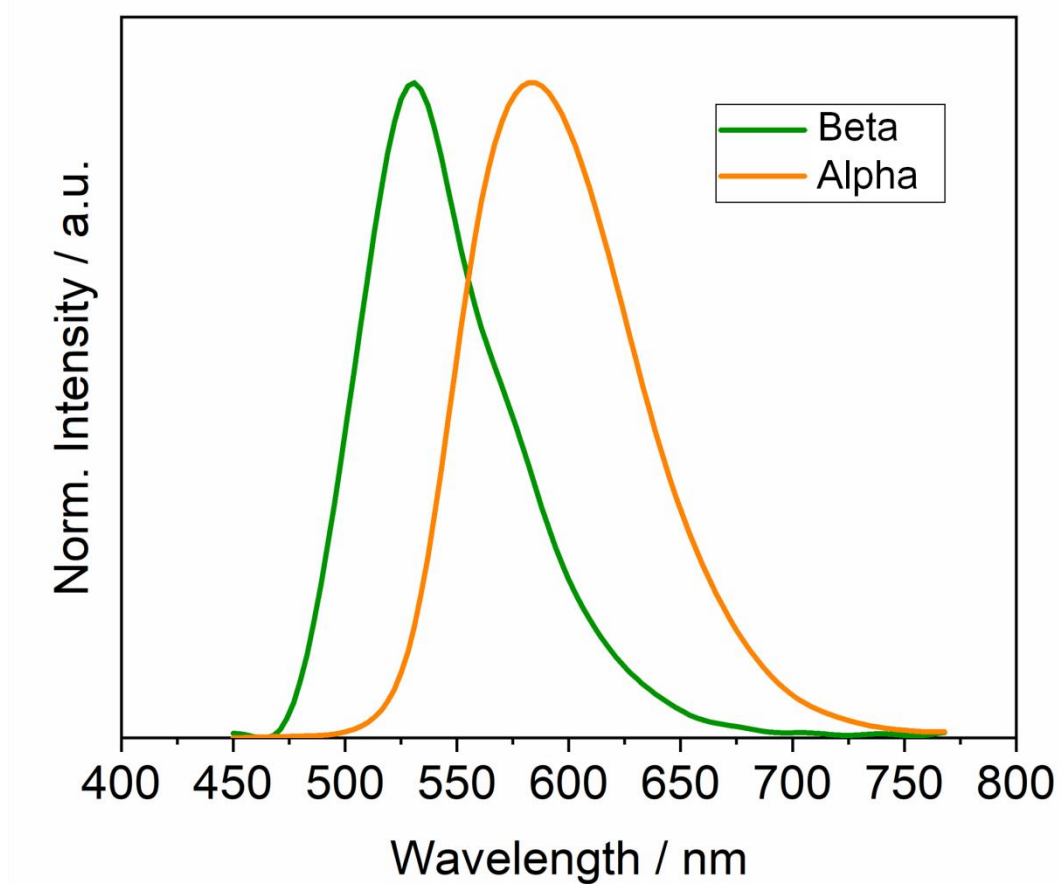
Figure SI13: Normalized emission spectra of α and β polymorphs obtained from confocal fluorescence analysis with 405 nm excitation.

APPENDIX C

SUPPLEMENTARY INFORMATION

Thorough investigation on the high-temperature polymorphism of dipentyl-perylenediimide: thermal expansion vs polymorphic transition.

Francesco Marin[a], Serena Tombolesi[a], Tommaso Salzillo*[b], Omer Yaffe[b], Lucia Maini*[a]

[a]Dipartimento di Chimica "G. Ciamician", via Selmi 2, Università di Bologna, 40126 Bologna, Italy
[b]Department of Chemical and Biological Physics, Weizmann Institute of Science, Herzl Street 234, 76100 Rehovot, Israel

Supplementary Information
Thorough investigation on the high-temperature polymorphism of dipentyl-perylenediimide: thermal expansion vs polymorphic transition.

Francesco Marin[a], Serena Tombolesi[a], Tommaso Salzillo*[,b], Omer Yaffe[b], Lucia Maini*[,a]

[a]Dipartimento di Chimica "G. Ciamician", via Selmi 2, Università di Bologna, 40126 Bologna, Italy

[b]Department of Chemical and Biological Physics, Weizmann Institute of Science, Herzl Street 234, 76100 Rehovot, Israel

Table of contents

Solubility

The solubility of PDI-C$_5$ in the solvents used in this work was extrapolated from its absorption spectra in a

saturated solution.
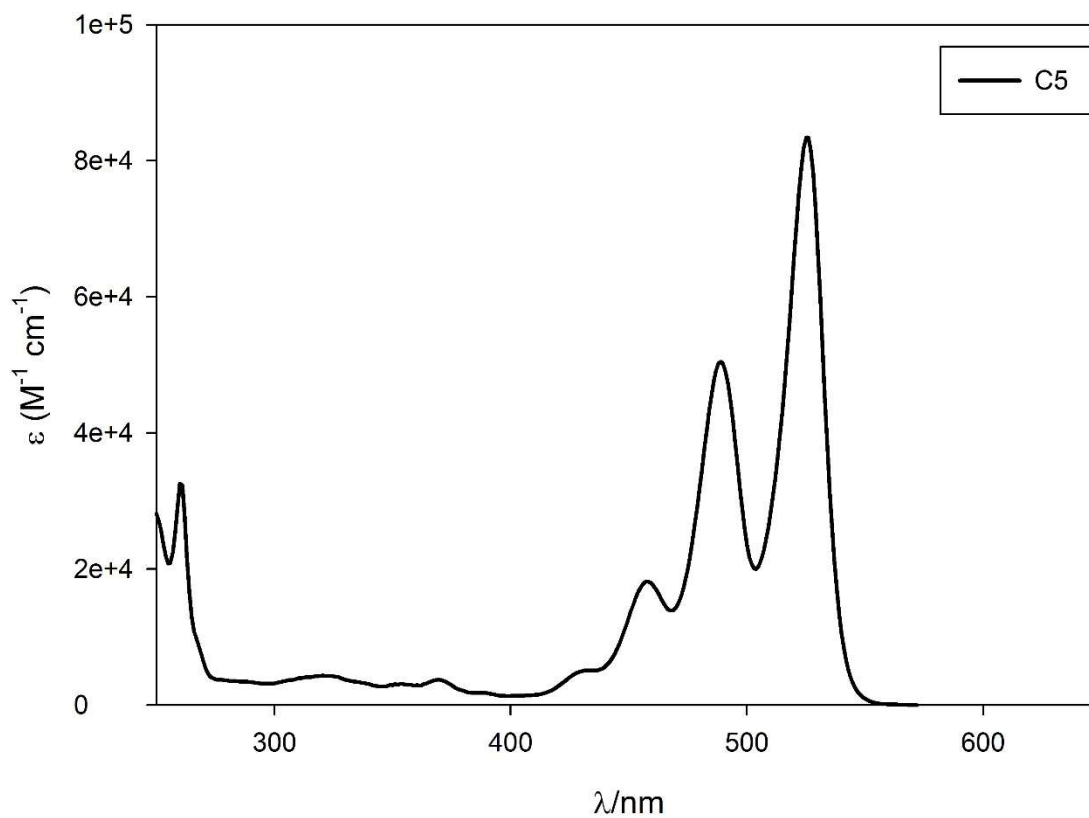
Figure S1. Absorption spectra of PDI-C$_5$ in CHCl3 to determine the maximum solubility in the solvent. Concentration of PDI-C$_5$ in solution: C = 2.2×10^{-5} M.

NMR Spectroscopy
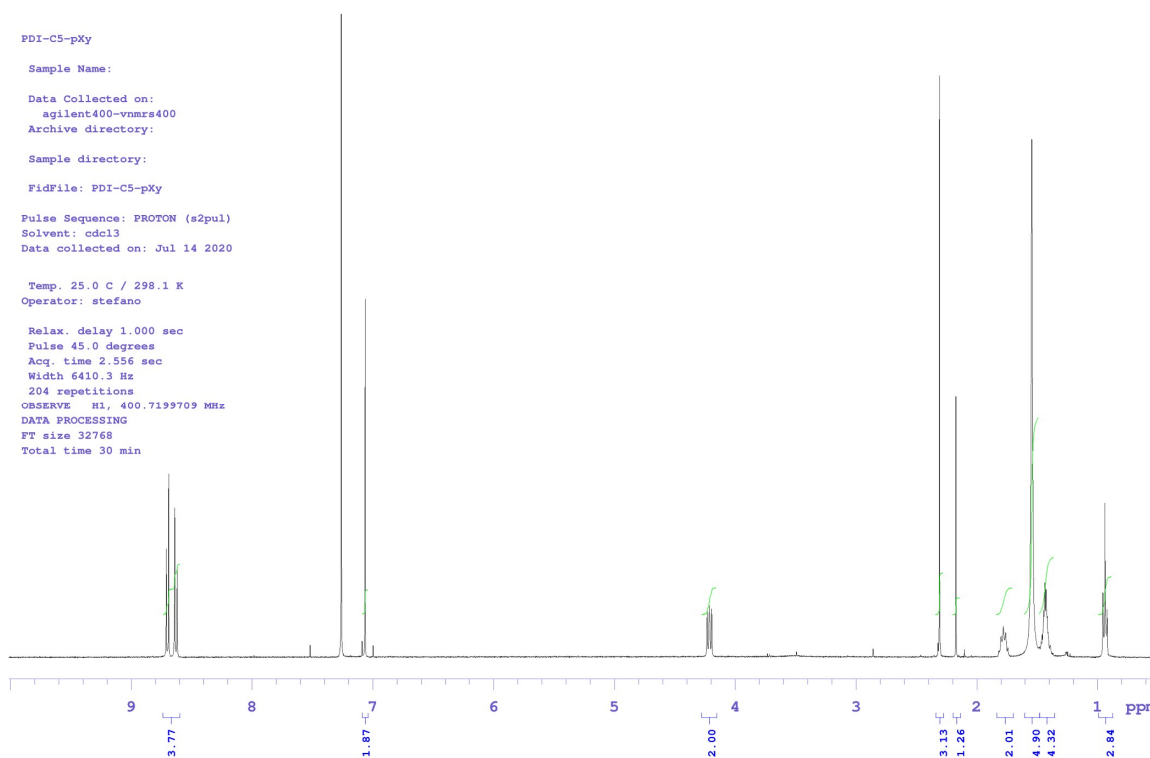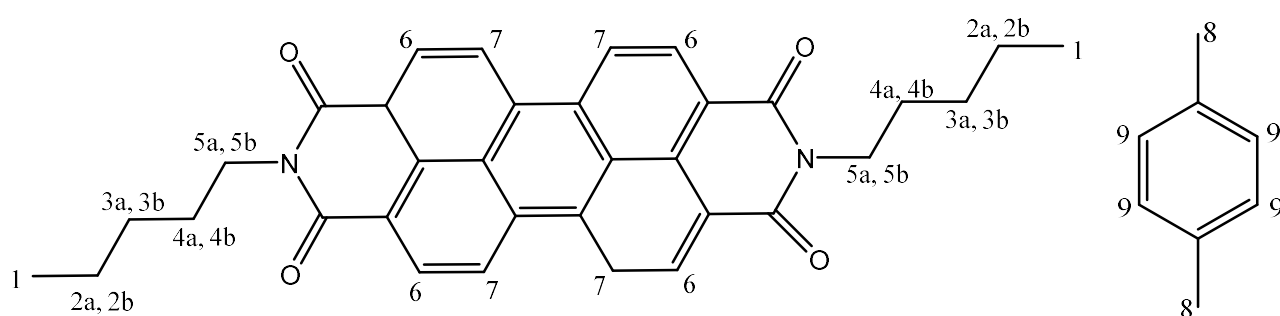
Figure S2. NMR spectra of PDI-C$_5$-pxy solvate form.

^{1}H-NMR (300 MHz, CDCl$_3$, 298K): δ 0.9 ppm (m, 6H, H1), 1.4-1.5 ppm (m, 8H, H2a-H2b-H3a-H3b), 1.8 ppm (m, 4H, H4a-H4b), 2.17 ppm (acetone used for washing crystals after filtering), 2.3 ppm (m, 6H, H8), 4.2 ppm (m, 4H, H5a-H5b), 7.0 ppm (m, 4H, H9), 7.26 ppm (hydrogen of CHCl$_3$ present in small quantity in the solvent), 8.6 ppm (m, 8H, H6-H7).
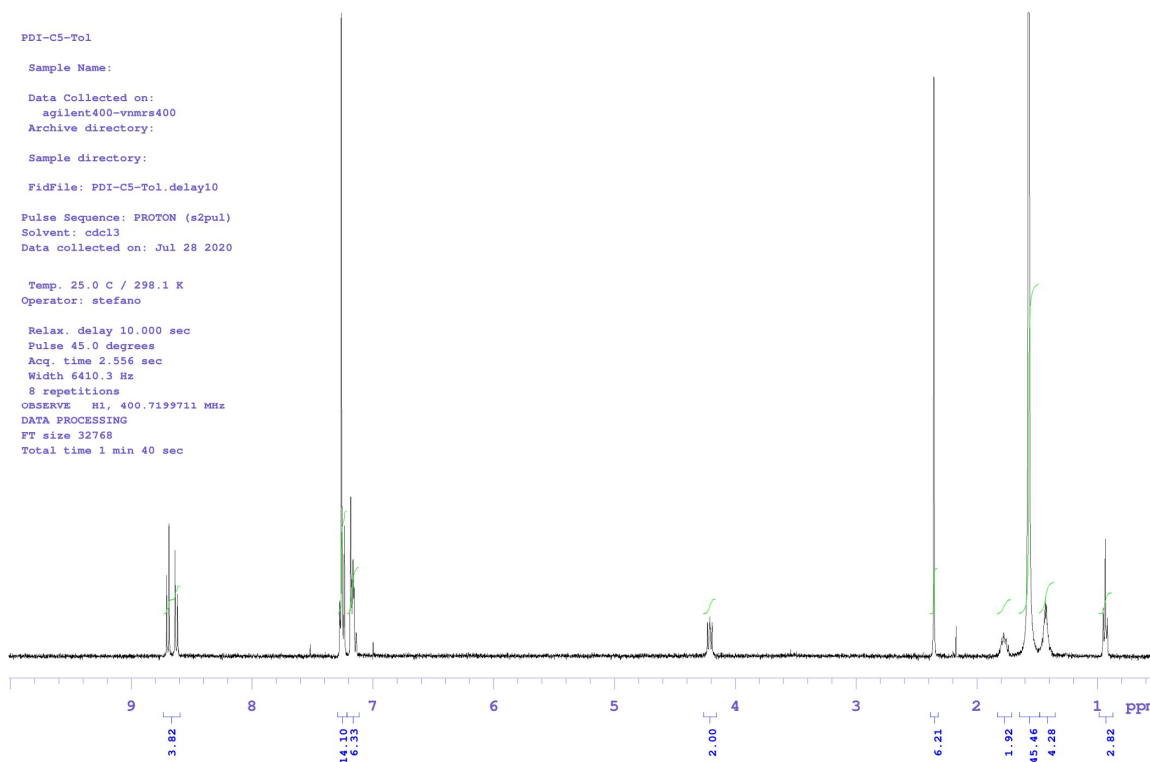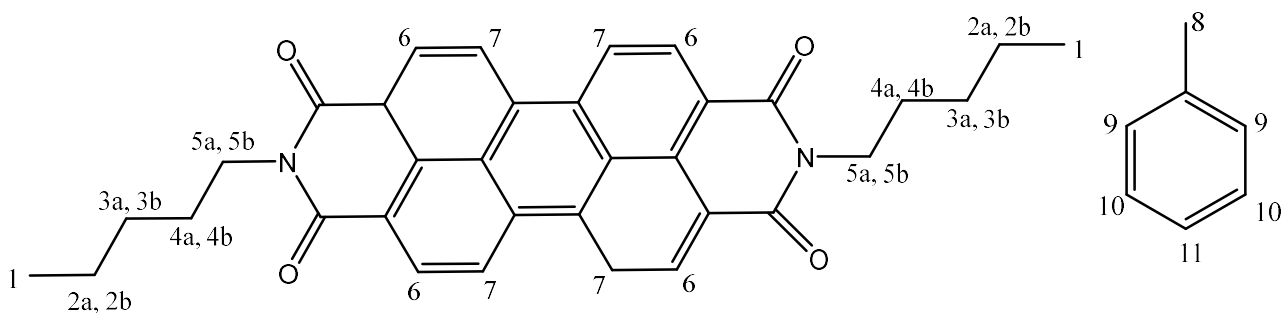
Figure S3. NMR spectra of PDI-C$_5$-tol solvate form.

^{1}H-NMR (300 MHz, CDCl$_3$, 298K): δ 0.9 ppm (m, 6H, H1), 1.4-1.6 ppm (m, 8H, H2a-H2b-H3a-H3b), 1.8 ppm (m, 4H, H4a-H4b), 2.17 ppm (acetone used for washing crystals after filtering), 2.3 ppm (m, 3H, H8), 4.2 ppm (m, 4H, H5a-H5b), 7.1-7.3 ppm (m, 5H, H9-H10-H11), 7.26 ppm (hydrogen of CHCl$_3$ present in small quantity in the solvent), 8.7 ppm (m, 8H, H6-H7).

X-ray Crystallography
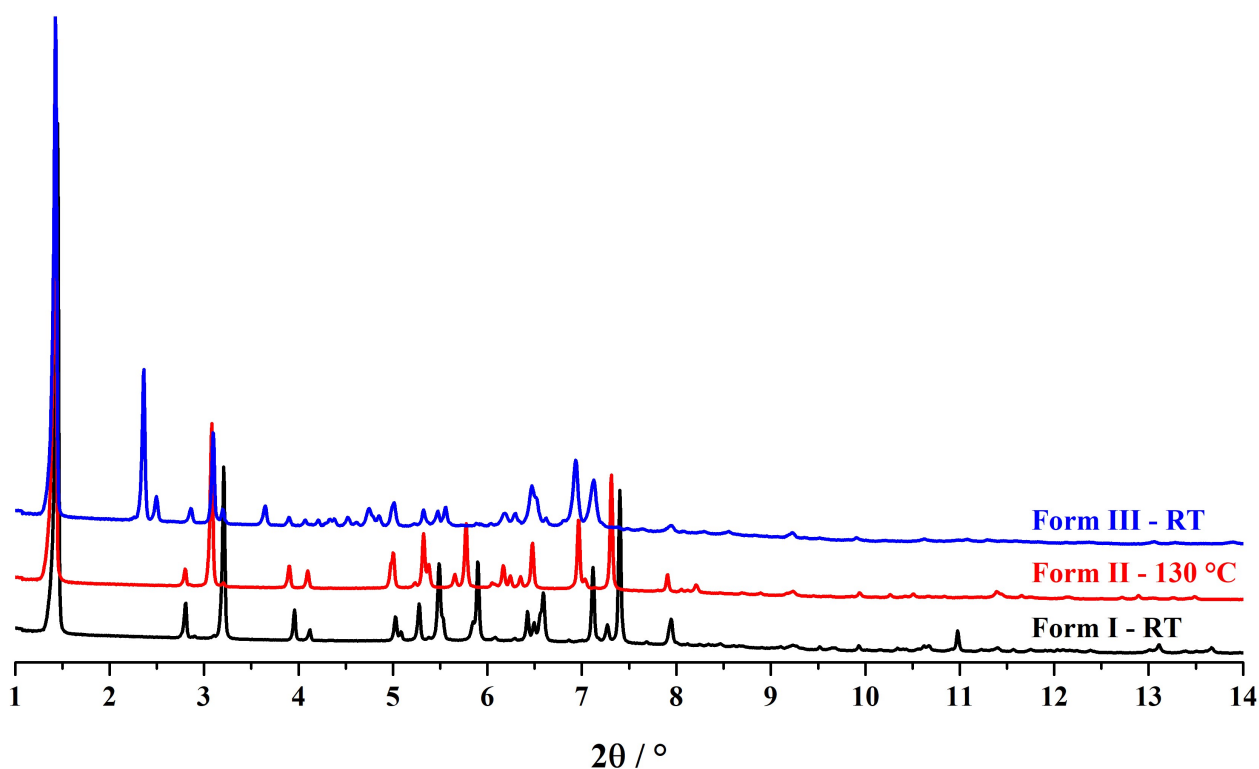
Figure S4. PXRD pattern (λ = 0.41235 Å) of the three PDI-C$_5$ crystal forms I (in black, collected at RT), II (in red, collected at 130 °C for structure solution) and III (in blue, collected at RT for structure solution).

The Rietveld refinement plot used to determine the crystal structures of form II and form III of PDI-C$_5$ from synchrotron powder data are reported. Form II crystal structure was determined at 131 °C, whereas form III crystal structure was determined at room temperature after cooling. Lamda and zero error were refined against the Si standard at RT. The background was described with Chubychev polynomial and the glass capillary modelled with 2 peaks at 2θ= 6.00° and 2θ= 7.79°. No correction for preferential orientation was applied.
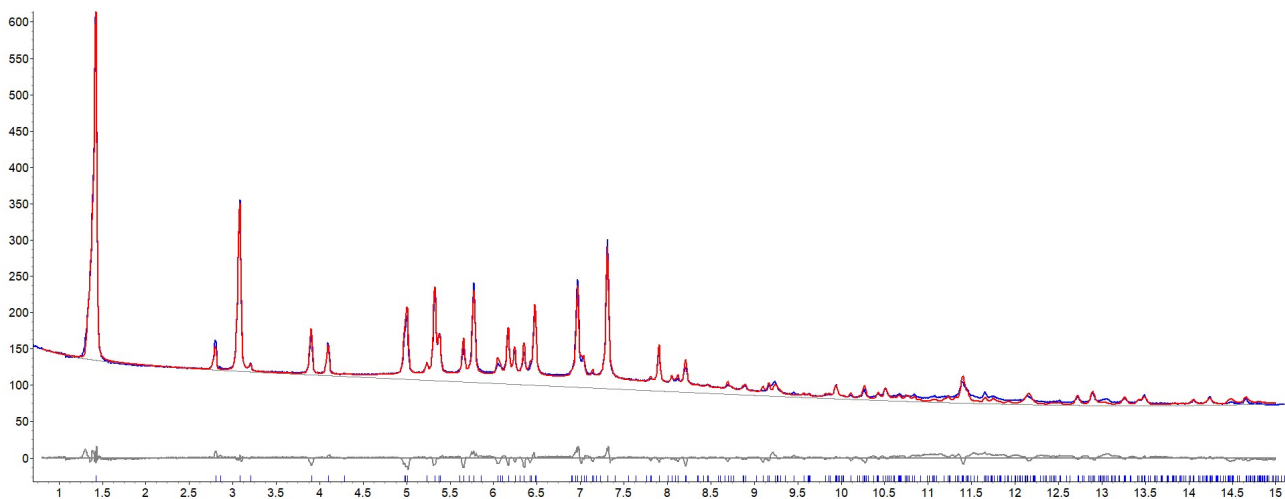
Figure S5. Rietveld refinement of form II at 131 °C. In blue is the experimental powder pattern, in red the calculated powder pattern and in grey is the difference pattern. Intensity is plotted in square root.
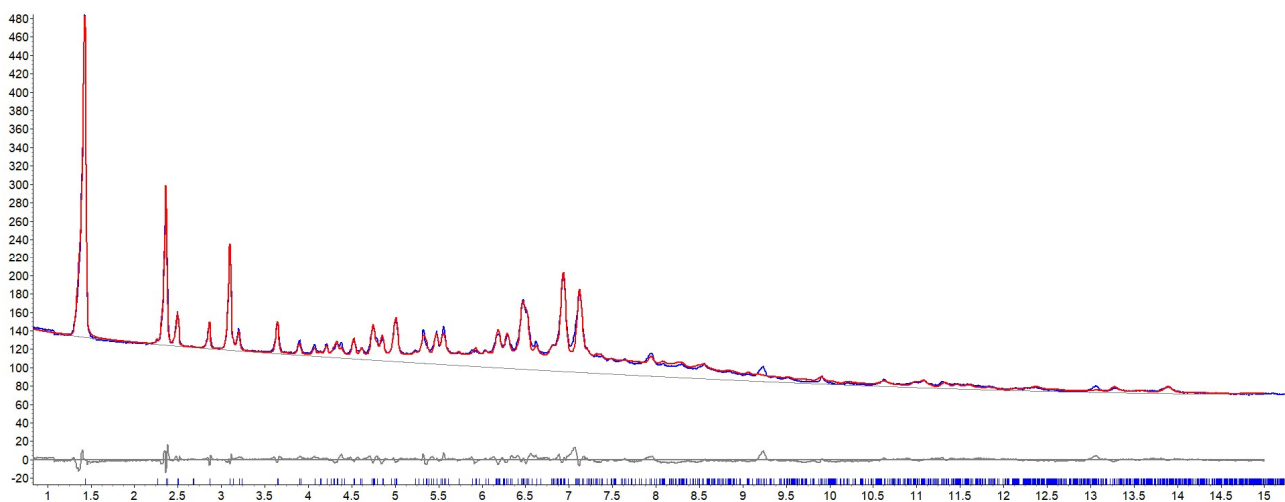
Figure S6. Rietveld refinement of form III at room temperature. In blue is the experimental powder pattern, in red the calculated powder pattern and in grey is the difference pattern. Intensity is plotted in square root.

Energy Frameworks
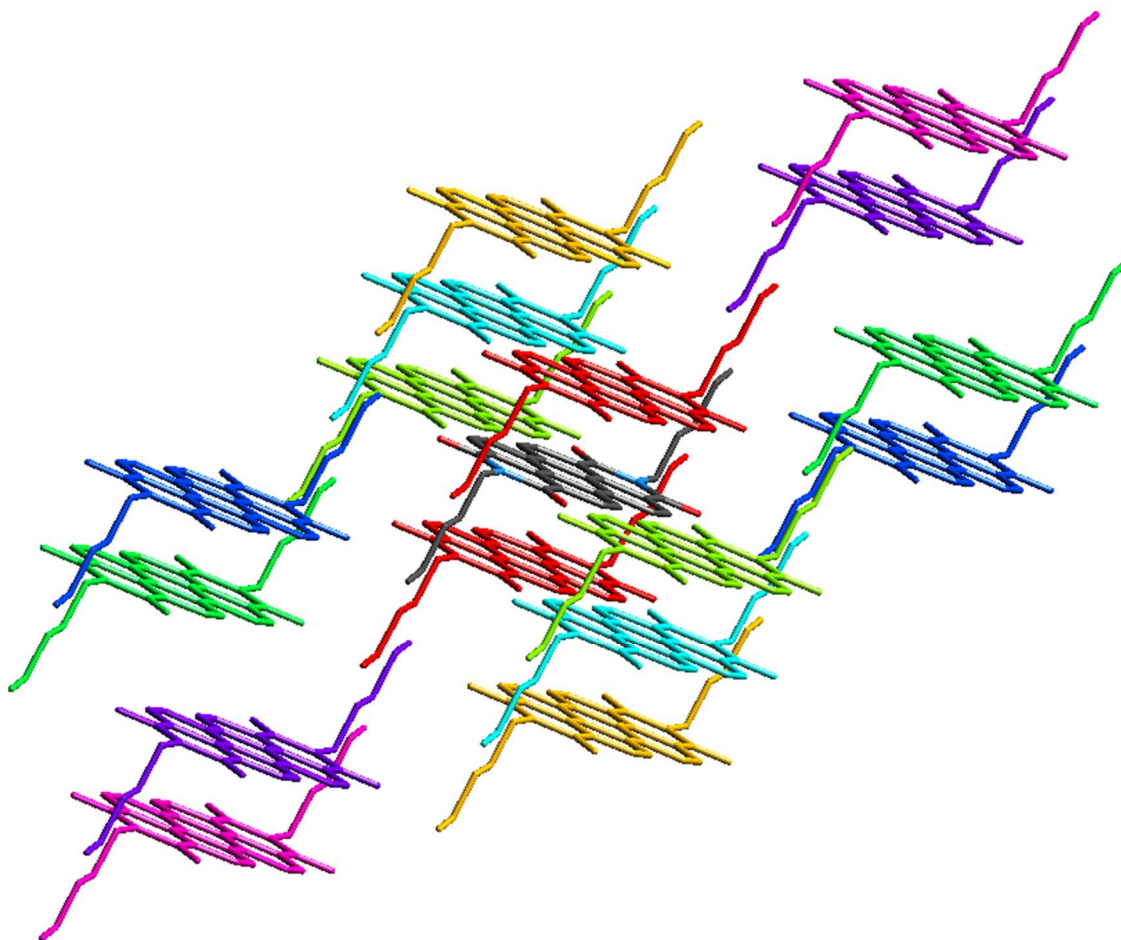
Figure S7. View of the cluster of molecules of form I used for the interaction energies calculation. The central molecule is marked with the atom specific colours (C=grey; O=red; N=blue), the surrounding molecules are marked by an identification colour. Hydrogens are omitted for clarity.

Table 1. Interaction energies for PDI-C$_5$ form I (kJ/mol). The colours represent the corresponding molecule in Figure S7. Total energies are the sum of the four energy components, scaled appropriately (see

Table **2**)

Id. colour	N. molecules	Distance (Å)	E_ele	E_pol	E_dis	E_rep	E_tot
🔴	2	4.75	-16.9	-2.3	-177.4	95.6	-115.0
🟧	2	8.48	-1.2	-1.4	-16.4	2.5	-15.0
🟢	2	12.02	-18.1	-4.7	-16.3	16.2	-26.8
🟩	2	19.75	-2.0	-1.4	-22.4	9.9	-16.5
🟦	2	9.25	-12.9	-6.4	-62.3	37.7	-49.4
🔵	2	21.83	-0.5	-0.1	-10.2	4.4	-6.8
🟣	2	26.09	-0.9	-0.0	-5.5	4.2	-3.2
🟪	2	24.56	-0.2	-0.0	-2.4	0.6	-2.0

Table 2. Scale factors for the different contributions to calculate total energy for interaction energies.

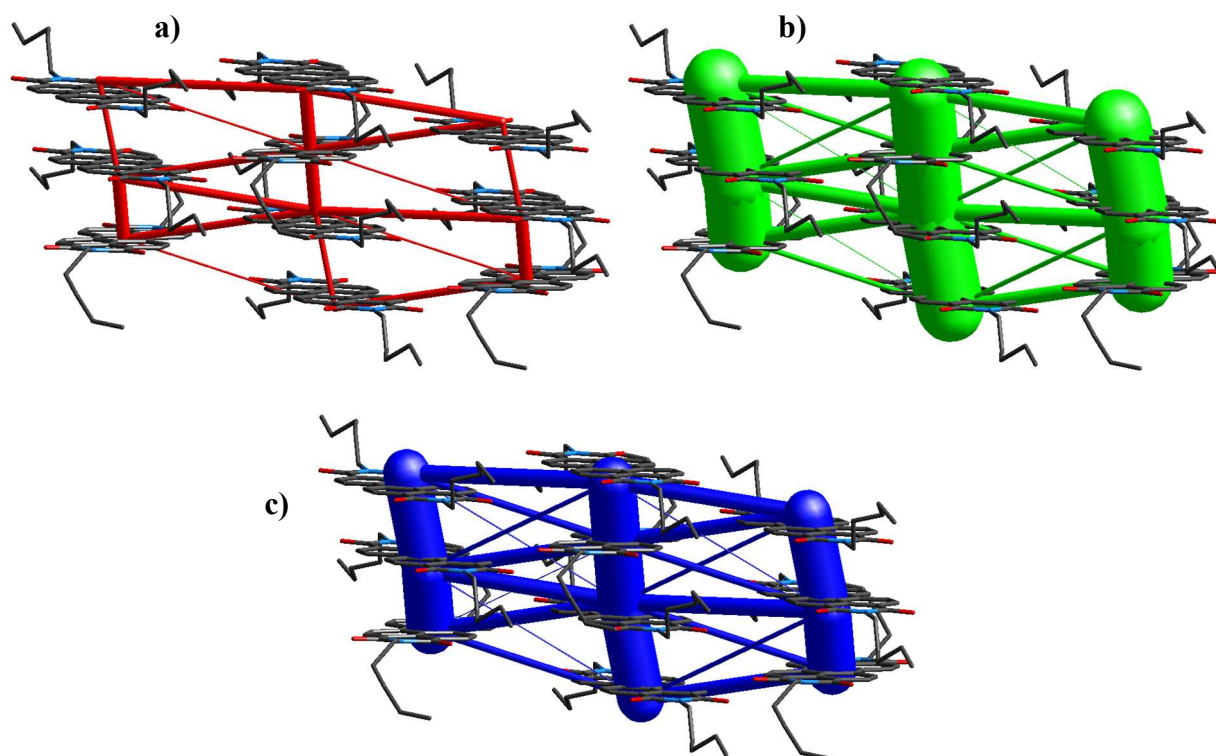| k_ele	k_pol	k_disp	k_rep
1.057	0.740	0.871	0.618
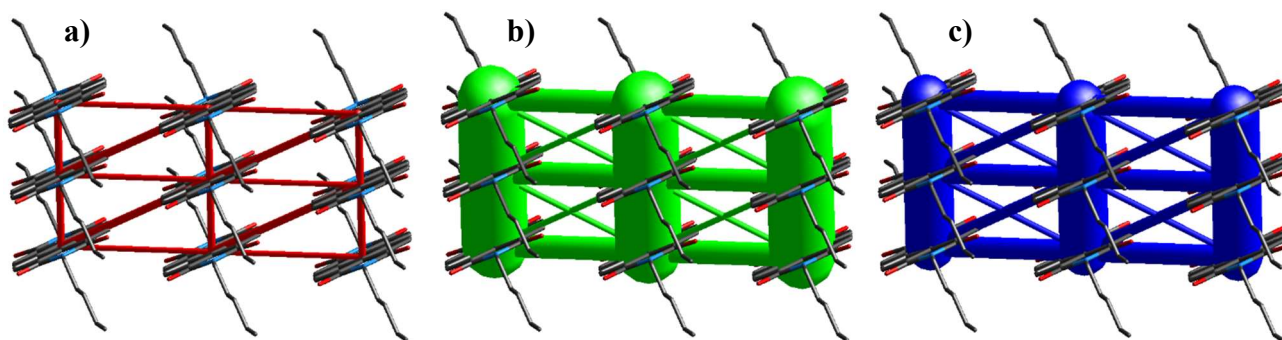
Figure S8. Graphic representation of the energy framework in PDI-C$_5$ form I calculated with CystalExplorer. The thickness of the lines is directly correlated with the intensity of the interaction. (a) electrostatic energy framework (red); (b) dispersion energy framework (green); (c) total energy framework (blue).
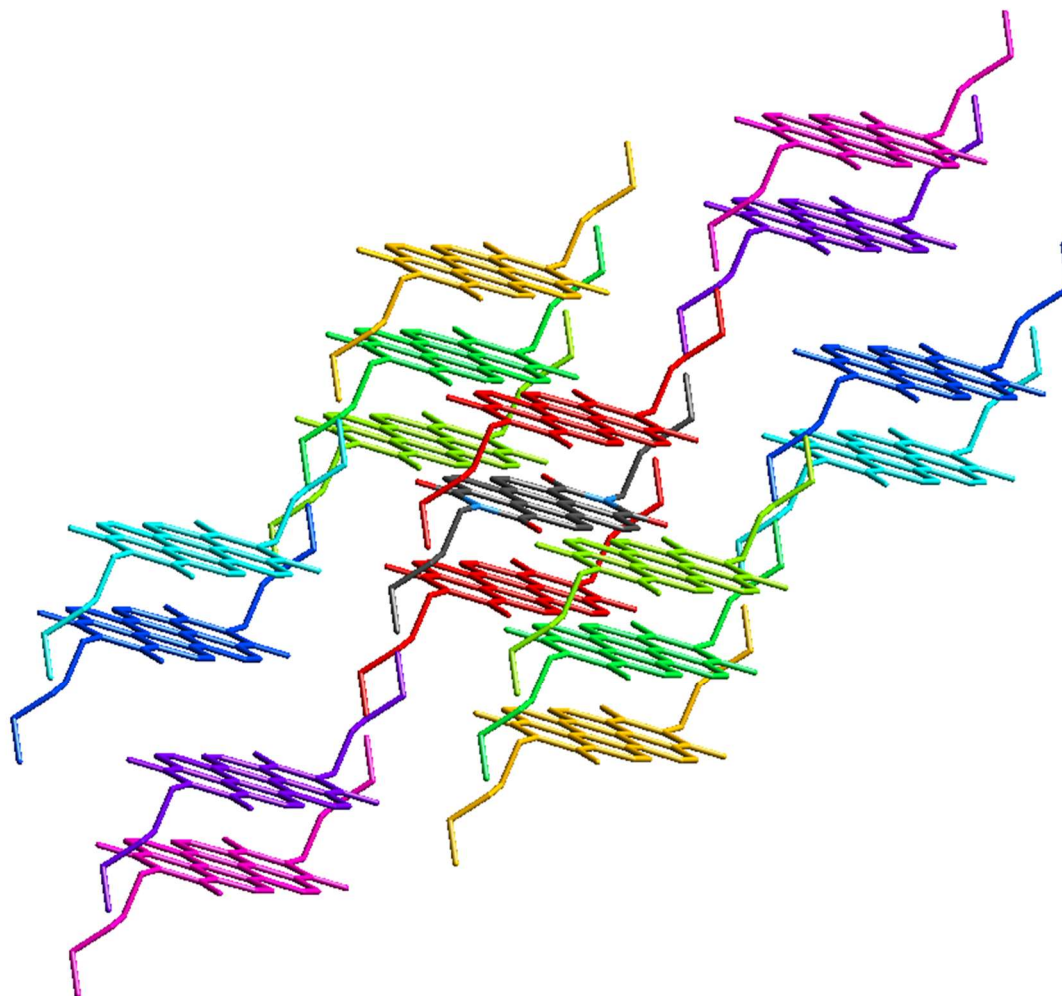
Figure S9. View of the cluster of molecules of form II used for the interaction energies calculation. The central molecule is marked with the atom specific colours (C=grey; O=red; N=blue), the surrounding molecules are marked by an identification colour. Hydrogens are omitted for clarity.

Table 3. Interaction energies for PDI-C$_5$ form II (kJ/mol). The colours represent the corresponding molecule in Figure S9. Total energies are the sum of the four energy components, scaled appropriately (see Table 2)

Id. colour	N. molecules	Distance (Å)	E_ele	E_pol	E_dis	E_rep	**E_tot**
red	2	4.85	-13.5	-2.2	-164.8	78.2	-111.1
orange	2	8.53	-0.3	-1.3	-13.1	2.1	-11.3
green	2	11.93	-18.7	-4.8	-16.5	16.3	-27.6
green	2	9.17	-10.1	-5.0	-50.3	30.6	-39.2
cyan	2	21.29	-0.6	-0.1	-8.5	2.0	-6.9
blue	2	19.23	-5.3	-1.4	-20.0	15.3	-14.6
purple	2	25.04	-2.3	-0.0	-6.7	8.3	-3.1
magenta	2	23.58	-1.3	-0.0	-6.1	5.6	-3.3
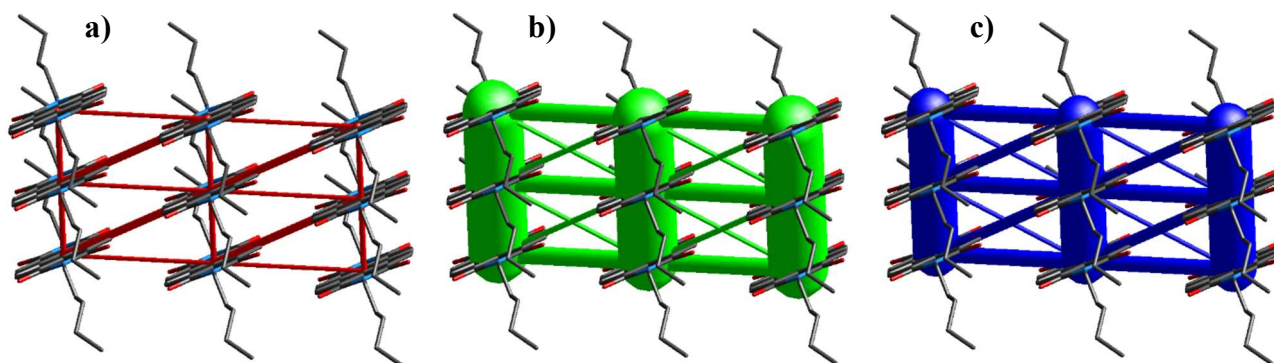
Figure S10. Graphic representation of the energy framework in PDI-C$_5$ form II calculated with CystalExplorer. The thickness of the lines is directly correlated with the intensity of the interaction. (a) electrostatic energy framework (red); (b) dispersion energy framework (green); (c) total energy framework (blue).
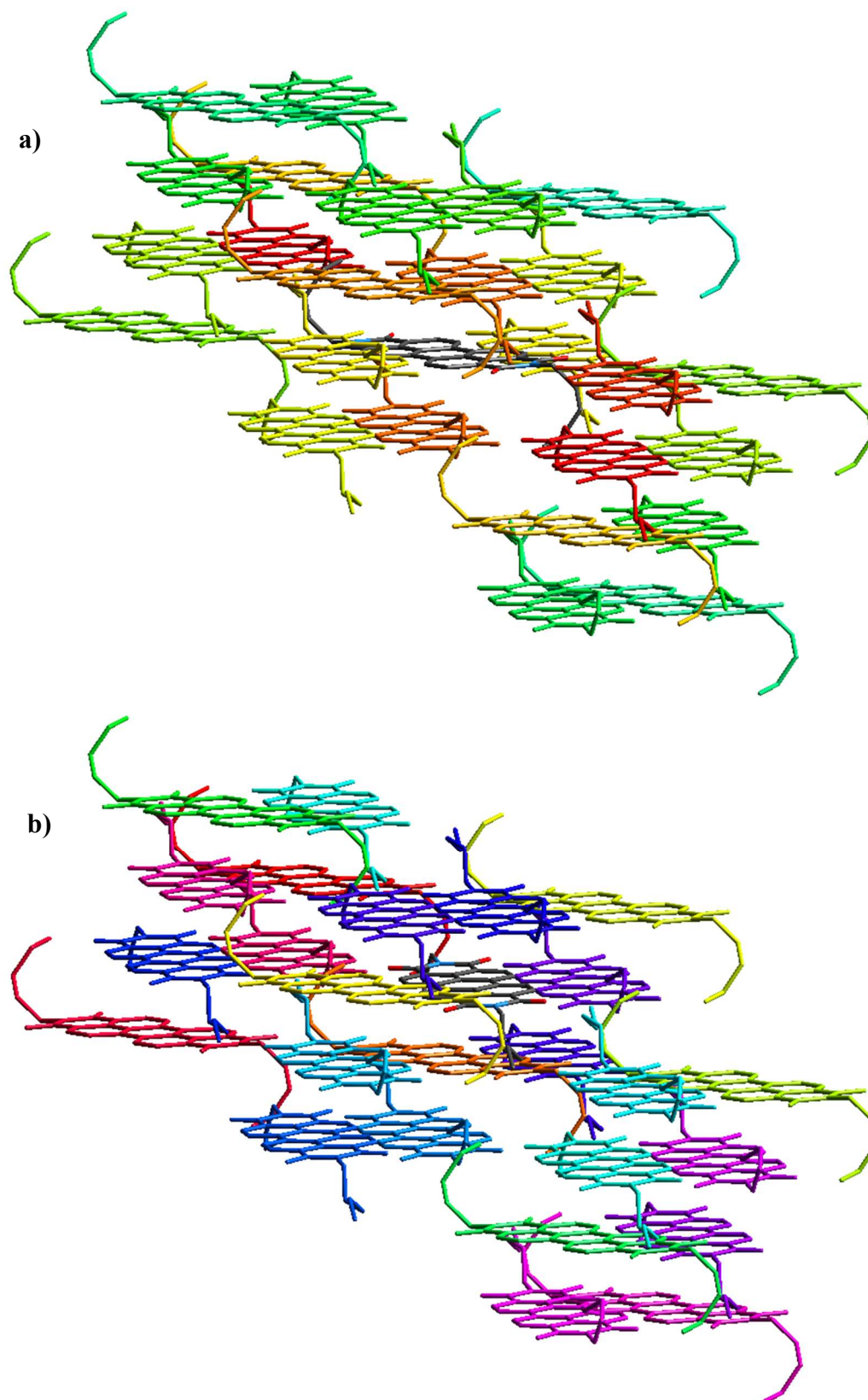
Figure S11. View of the cluster of molecules of form III used for the interaction energies calculation. The central molecule is marked with the atom specific colours (C=grey; O=red; N=blue), the surrounding molecules are marked by an identification colour. Hydrogens are omitted for clarity. (a) Central molecule is the one with alkyl chains in trans configuration; (b) Central molecule is the one with alkyl chains in cis configuration.

Table 4. Interaction energies for PDI-C$_5$ form III (kJ/mol), calculated respect to the molecule with alkyl chains in trans configuration. The colours represent the corresponding molecule in Figure S11a. Total energies are the sum of the four energy components, scaled appropriately (see

Table **2**).

Id. colour	N. molecules	Distance (Å)	E_ele	E_pol	E_dis	E_rep	E_tot
	2	24.10	-0.5	-0.0	-3.4	1.7	-2.5
	1	25.38	-0.1	-0.0	-0.2	0.0	-0.3
	2	3.63	-28.6	-6.4	-171.3	117.1	-111.8
	1	12.31	-0.9	-0.1	-1.4	0.0	-2.2
	2	22.96	-0.0	-0.0	-0.3	0.0	-0.3
	2	10.57	-17.1	-5.2	-39.8	36.3	-34.1
	2	10.82	-5.0	-2.1	-14.3	2.3	-17.8
	2	17.94	-9.5	-2.7	-19.9	30.4	-10.5
	2	19.51	-0.3	-0.1	-10.5	1.6	-8.6
	1	8.01	-0.0	-0.1	-6.7	0.0	-6.0
	1	14.75	-0.3	-0.0	-1.3	0.0	-1.5
	2	17.44	-0.7	-0.6	-8.3	2.3	-7.0
	2	22.35	-2.4	-0.0	-6.2	8.4	-2.7
	2	17.41	-0.3	-0.0	-5.6	0.4	-5.0
	1	11.62	1.2	-0.1	-1.6	0.0	-0.2

Table 5. Interaction energies for PDI-C$_5$ form III (kJ/mol), calculated respect to the molecule with alkyl chains in cis configuration. The colours represent the corresponding molecule in Figure S11b. Total energies are the sum of the four energy components, scaled appropriately (see

Table **2**).

Id. colour	N. molecules	Distance (Å)	E_ele	E_pol	E_dis	E_rep	E_tot
	1	24.10	-0.5	-0.0	-3.4	1.7	-2.5
	1	3.63	-28.6	-6.4	-171.3	117.1	-111.8
	1	10.57	-17.1	-5.2	-39.8	36.3	-34.1
	1	10.82	-5.0	-2.1	-14.3	2.3	-17.8
	1	17.94	-9.5	-2.7	-19.9	30.4	-10.5
	1	17.44	-0.7	-0.6	-8.3	2.3	-7.0
	1	22.35	-2.4	-0.0	-6.2	8.4	-2.7
	2	22.96	-0.4	-0.0	-5.0	0.8	-4.3
	1	23.65	-0.3	-0.0	-6.3	1.4	-5.0
	1	9.91	-18.5	-6.0	-41.6	35.6	-38.2

	1	7.26	-3.5	-0.2	-30.6	16.2	-20.5
	1	11.62	-1.0	-0.1	-2.5	0.0	-3.4
	1	19.51	0.1	-0.0	-0.6	0.0	-0.4
	1	4.42	-12.7	-2.9	-176.2	98.4	-108.2
	2	12.31	-0.7	-0.5	-12.7	1.7	-11.1
	1	11.20	-19.3	-7.5	-46.0	42.5	-39.8
	1	17.41	-0.3	-0.0	-0.5	0.0	-0.7
	1	17.02	-0.2	-0.0	-1.3	0.0	-1.3
	1	22.33	-0.2	-0.0	-0.5	0.0	-0.6
	1	18.13	-0.2	-0.0	-0.3	0.0	-0.5
	1	18.20	0.2	-0.0	-1.1	0.0	-0.7
	1	25.71	-0.1	-0.0	-2.0	0.1	-1.8
	1	21.57	-0.2	-0.0	-0.7	0.0	-0.8

Figure S12. Graphic representation of the energy framework in PDI-C$_5$ form III calculated with CystalExplorer. The thickness of the lines is directly correlated with the intensity of the interaction. (a) electrostatic energy framework (red); (b) dispersion energy framework (green); (c) total energy framework (blue).

Thermogravimetrical analysis (TGA)
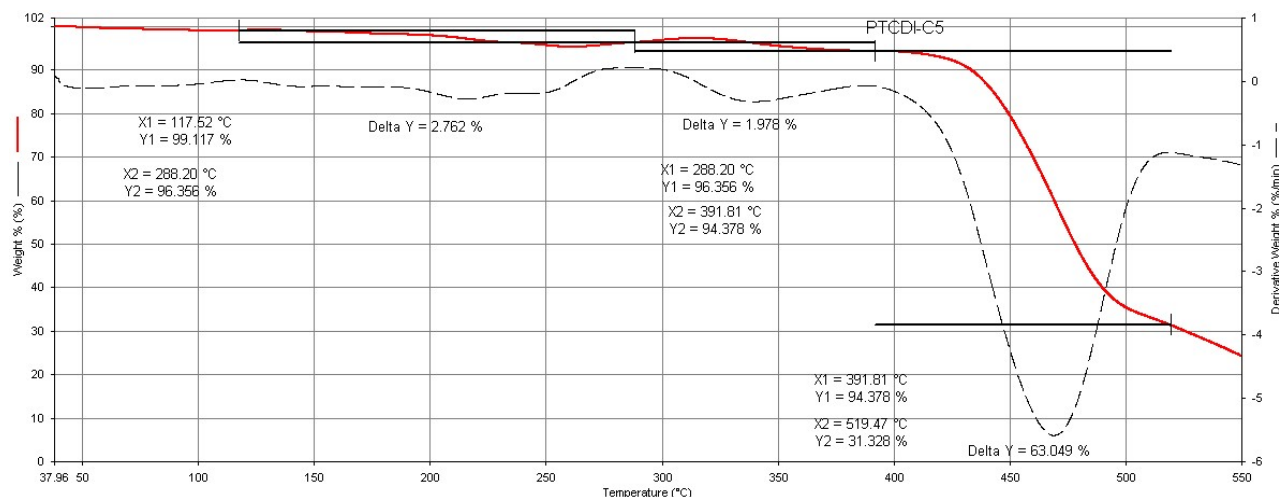
Figure S13. Thermogravimetrical analysis of PDI-C$_5$ in the temperature range RT – 550°C.

The TGA curve shows that the compound is thermally stable up to 400°C, then one weight loss step is observed.

Differential Scanning Calorimetry (DSC)
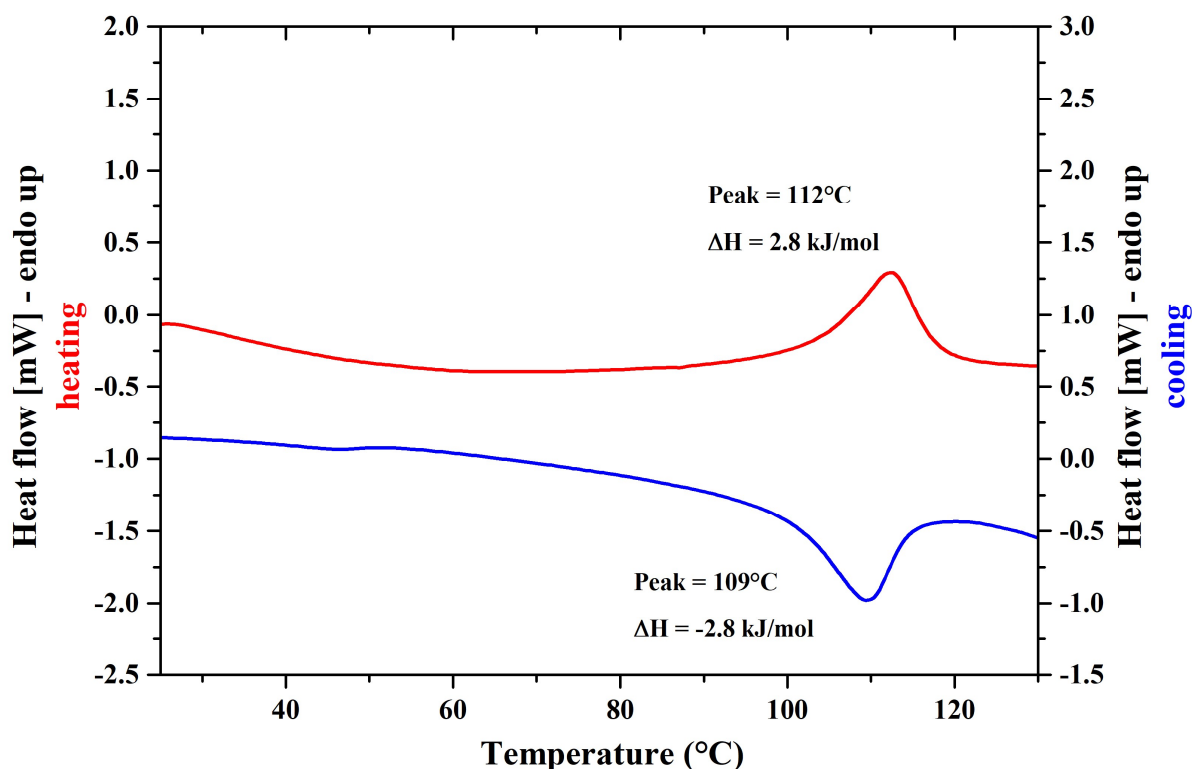
Figure S14. Differential Scanning Calorimetry of PDI-C$_5$, measured in the temperature range RT - 140 °C with a 20 °C/min heating rate, in both heating (red curve) and cooling (blue curve). An endothermic event is observed in heating at 112 °C, while an exothermic event is observed at 109 °C upon cooling with the same DH of transition, indicating that this transition is fully reversible.
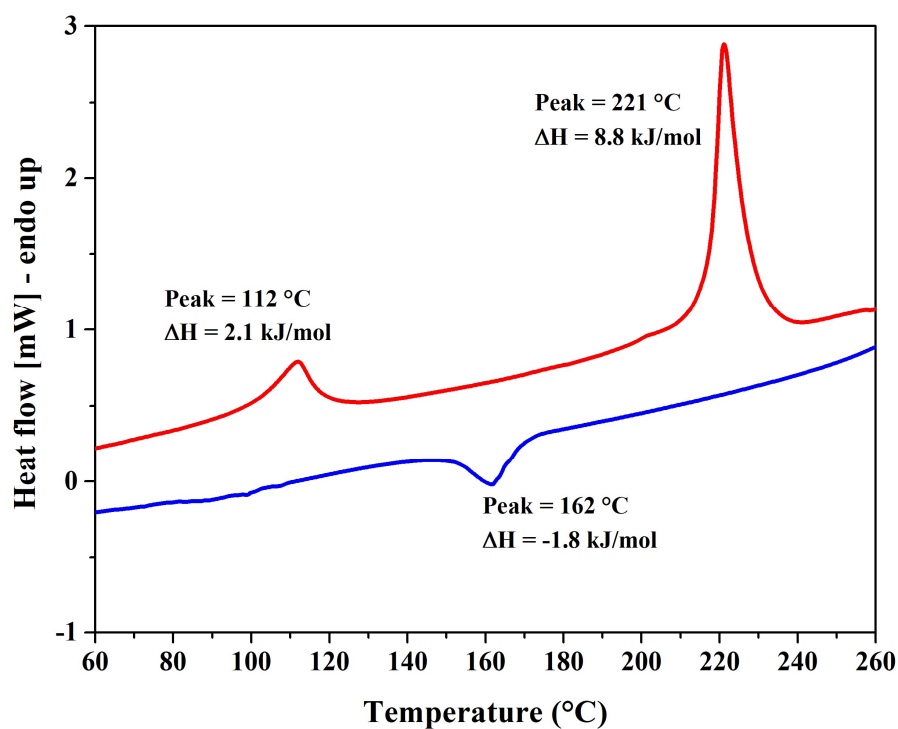
Figure S15. Differential Scanning Calorimetry of PDI-C$_5$, measured in the temperature range RT - 280 °C with a 20 °C/min heating rate, in both cooling and heating. Two endothermic events are observed in heating with peak at 112 and 221 °C respectively, while only one exothermic event is observed at 162 °C upon cooling.

Variable Temperature X-ray Powder Diffraction (VTXRPD)
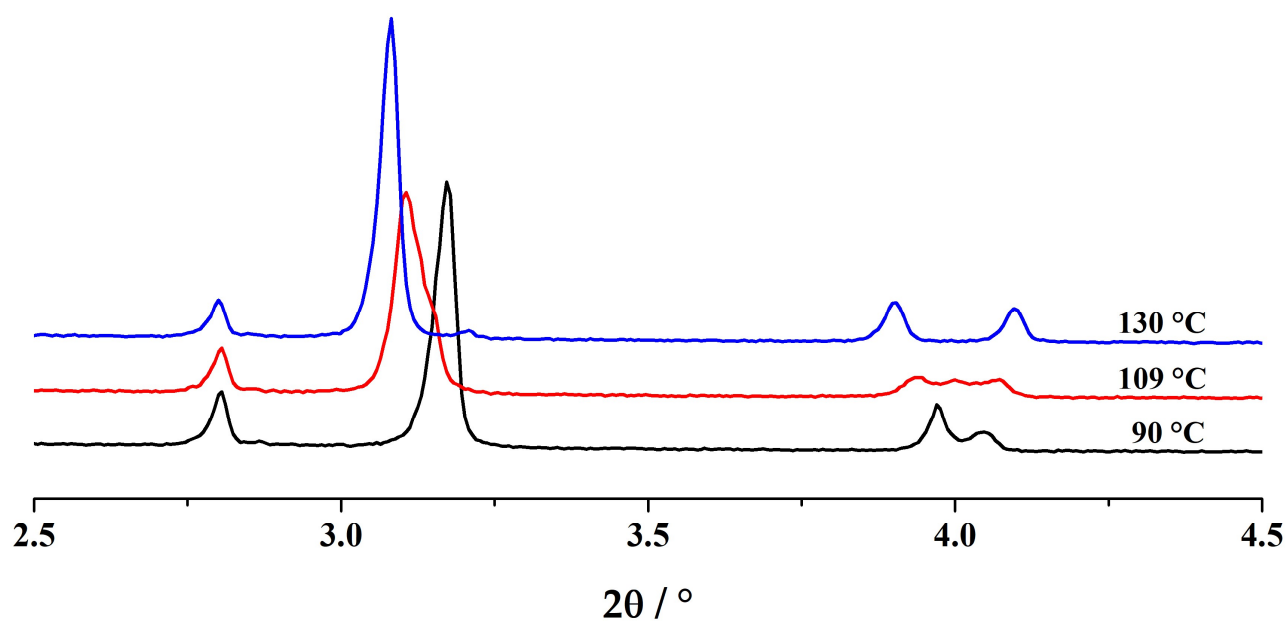
Figure S16. Variable temperature X-ray powder diffraction patterns of the material in the temperature range of the transition I-II. At 90 °C only form I is present (black); at 109 °C a mixture of form I and II is present (in red); at 130 °C all form I converted to form II.
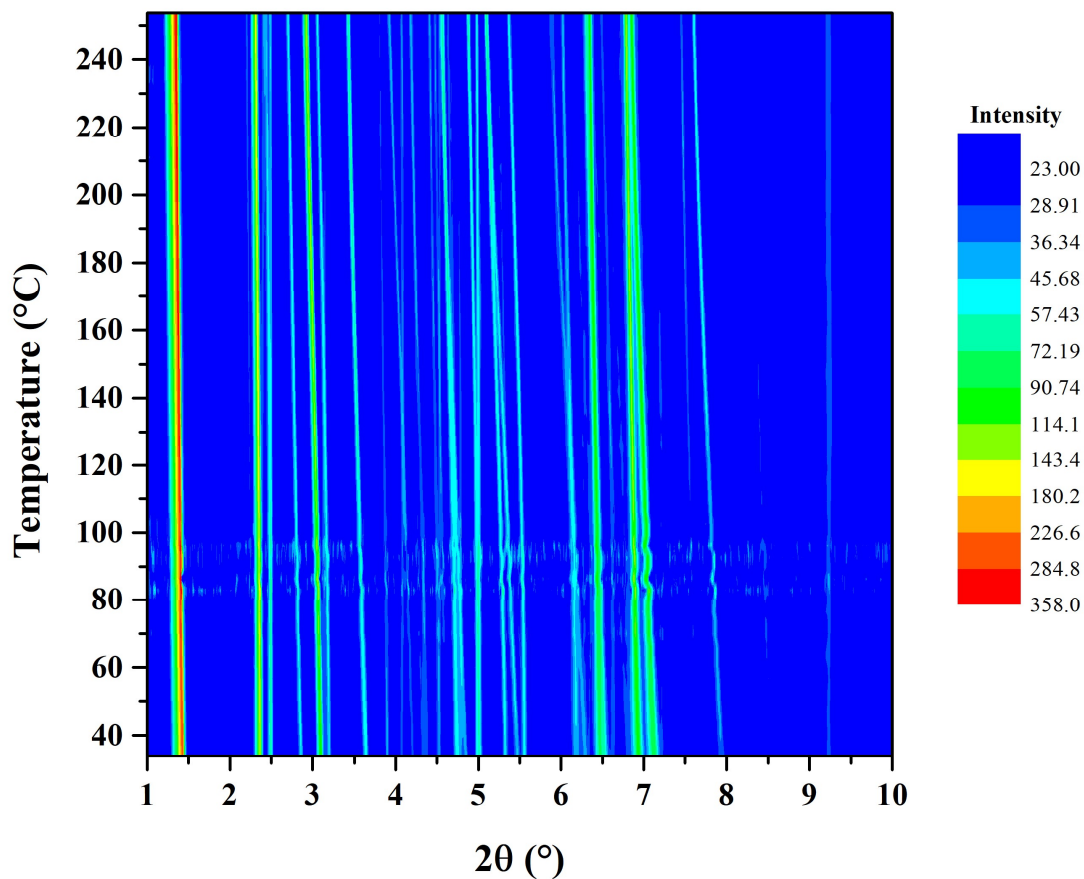
Figure S17. VTXRPD experiment of PDI-C$_5$ upon cooling. No changes that could be linked to phase transition are observed, indicating that form III was isolated at room temperature. Intensity is plotted in square root scale for clearness's sake.

Sequential Rietveld refinement was carried out using VTXRD data of the three separate forms. The sequential Rietveld refinement was performed according to the method described in the Durham Topas tutorial on "Sequential Rietveld Refinement of Multiple Data Sets". The variation of the crystal structure parameters of the three forms with temperature obtained by this method is reported here. Furthermore, the variation of the alkyl chain torsion angles with increasing temperature is reported for form I and form II, showing the different alkyl chain conformation.
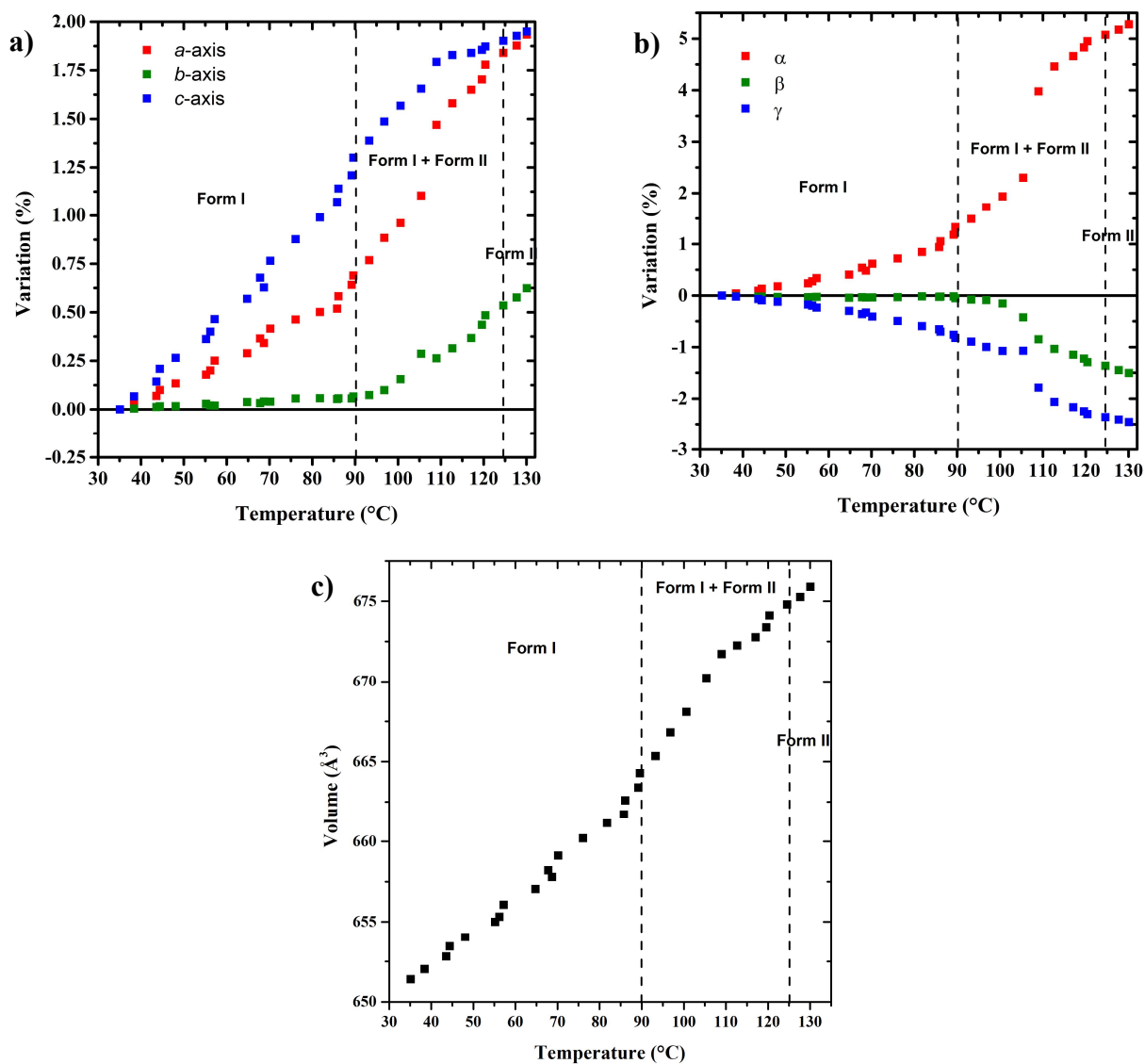
Figure S18. Sequential Rietveld refinement of PDI-C$_5$ form I, variation of unit cell parameters in the temperature range 35 – 130 °C. a) Variation in percentage of unit cell a-axis (red), b-axis (green) and c-axis (blue) with T; b) Variation in percentage of unit cell α (red), β (green) and γ (blue) angles with T; c) Variation of volume with T. The discontinuity in the trend of unit cell parameter with temperature, which indicates the transition to form II, is observed in the temperature range 90 – 125 °C (highlighted by the dashed lines).

The variation of the alkyl chain conformation with temperature in form I and II was reported using four torsion angles (see Figure S19).
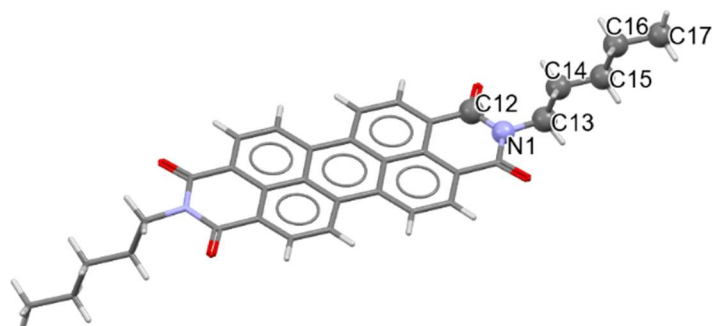
Torsion 1 = C12-N1-C13-C14

Torsion 2 = N1-C13-C14-C15

Torsion 3 = C13-C14-C15-C16

Torsion 4 = C14-C15-C16-C17

Figure S19. Torsion angles used to describe alkyl chain conformation at different temperatures.
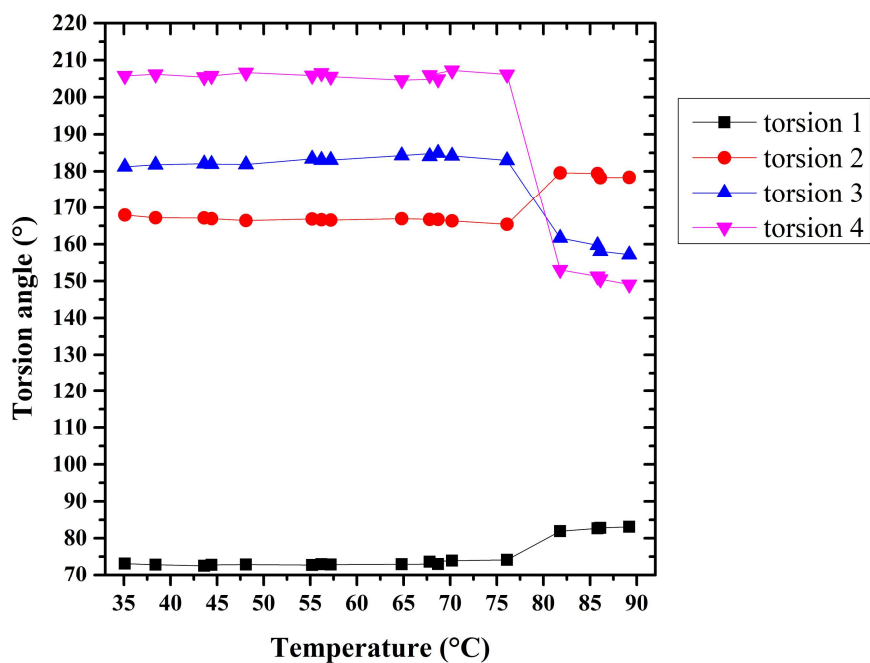
Figure S20. Variation of torsion angles of PDI-C5 form I alkyl chains with temperatures in the rang 35-90 °C. The four torsion angles change only slightly up to 75 °C, and after that temperature a drastic change is observed in all the torsion angles.
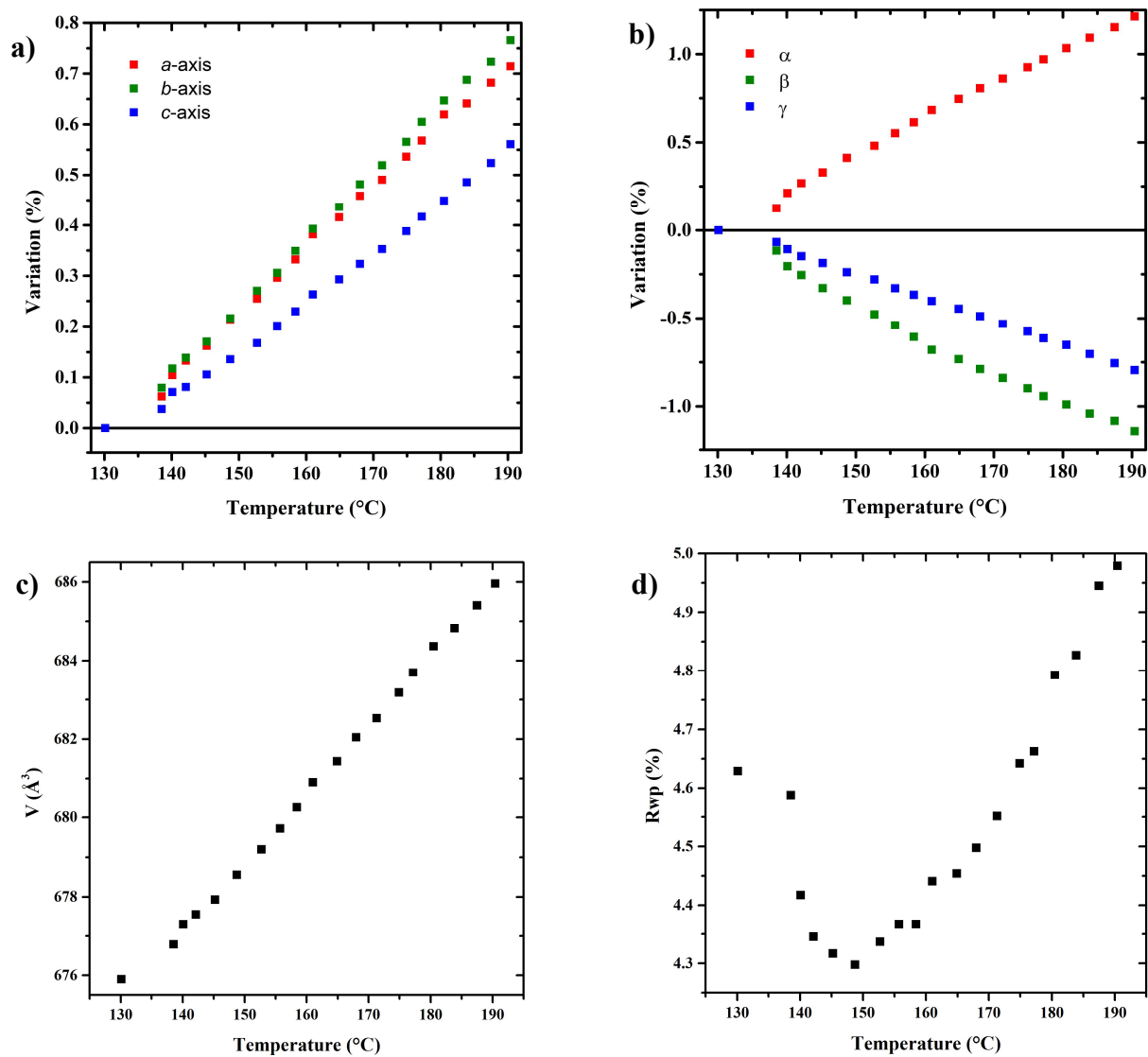
Figure S21. Sequential Rietveld refinement of PDI-C₅ form II, variation of unit cell parameters in the temperature range 130 – 190 °C. a) Variation in percentage of unit cell a-axis (red), b-axis (green) and c-axis (blue) with T; b) Variation in percentage of unit cell α (red), β (green) and γ (blue) angles with T; c) Variation of volume with T; d) Variation of R$_{wp}$ with T.
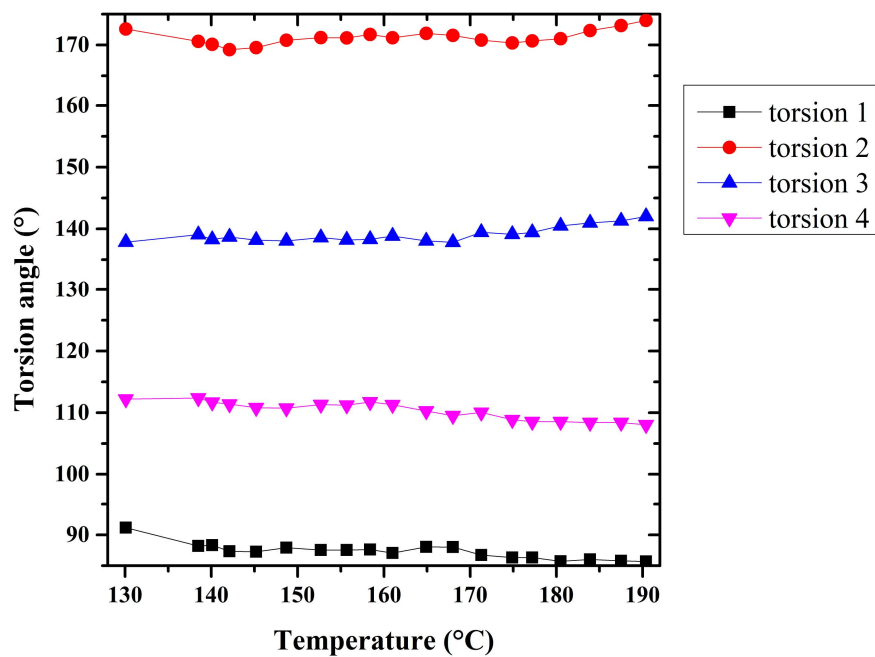
Figure S22. Variation of torsion angles of PDI-C$_5$ form II alkyl chains with temperatures in the range 130-190 °C. The four torsion angles change only slightly in the whole temperature range considered. The torsion angles are labelled as in Figure S19.
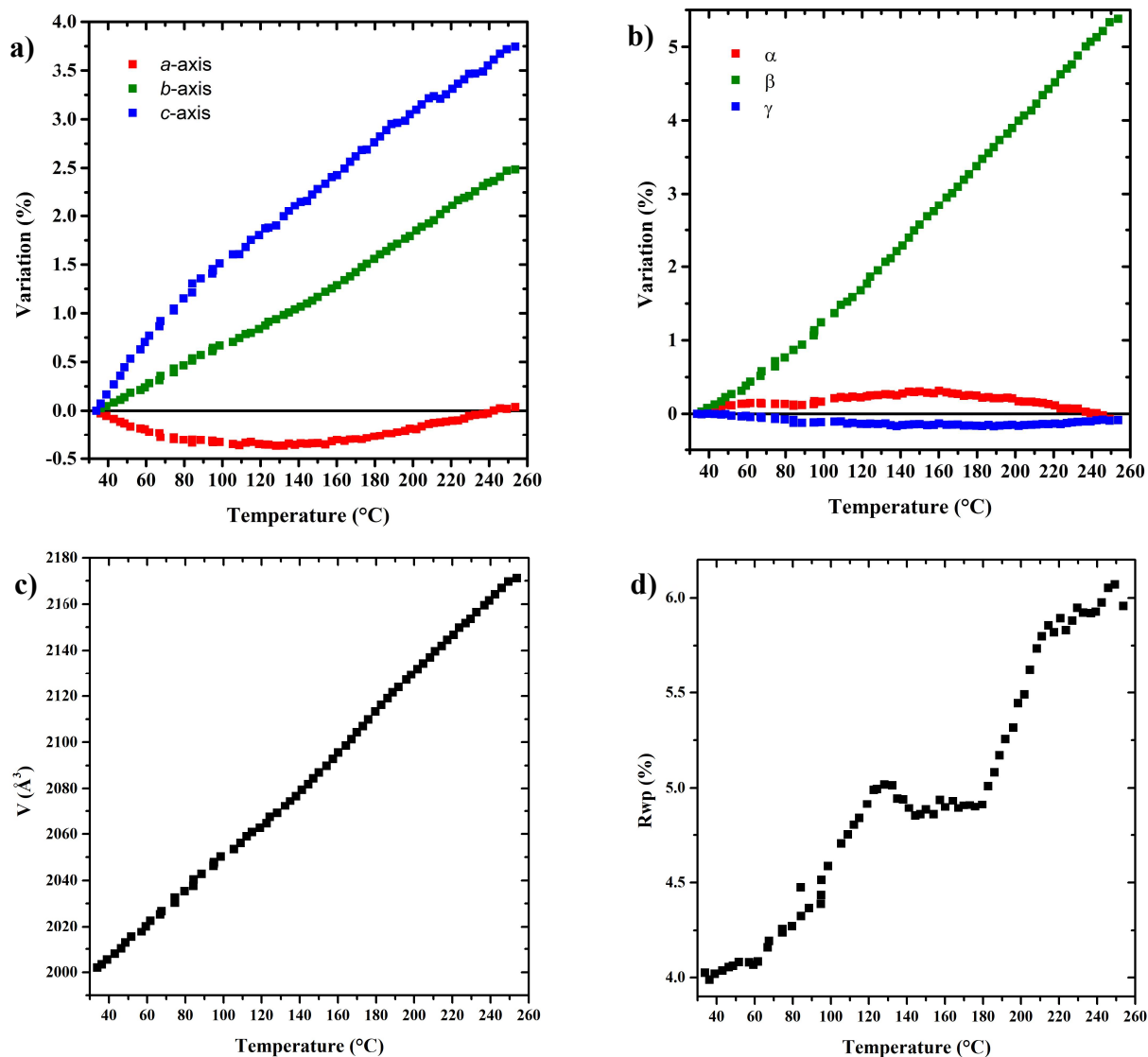
Figure S23. Sequential Rietveld refinement of PDI-C$_5$ form II, variation of unit cell parameters in the temperature range 35-225 °C. The VTXRPD data collected upon cooling form III to room temperature were used for this refinement. a) Variation in percentage of unit cell a-axis (red), b-axis (green) and c-axis (blue) with T; b) Variation in percentage of unit cell α (red), β (green) and γ (blue) angles with T; c) Variation of volume with T; d) Variation of R$_{wp}$ with T.

Thermal Expansion

The variation of unit cell parameters with temperature of the three forms were used to investigate their thermal expansion. The variation of the three principal axes with temperature is reported for the three forms, showing that in the temperature range considered the linear approximation holds.
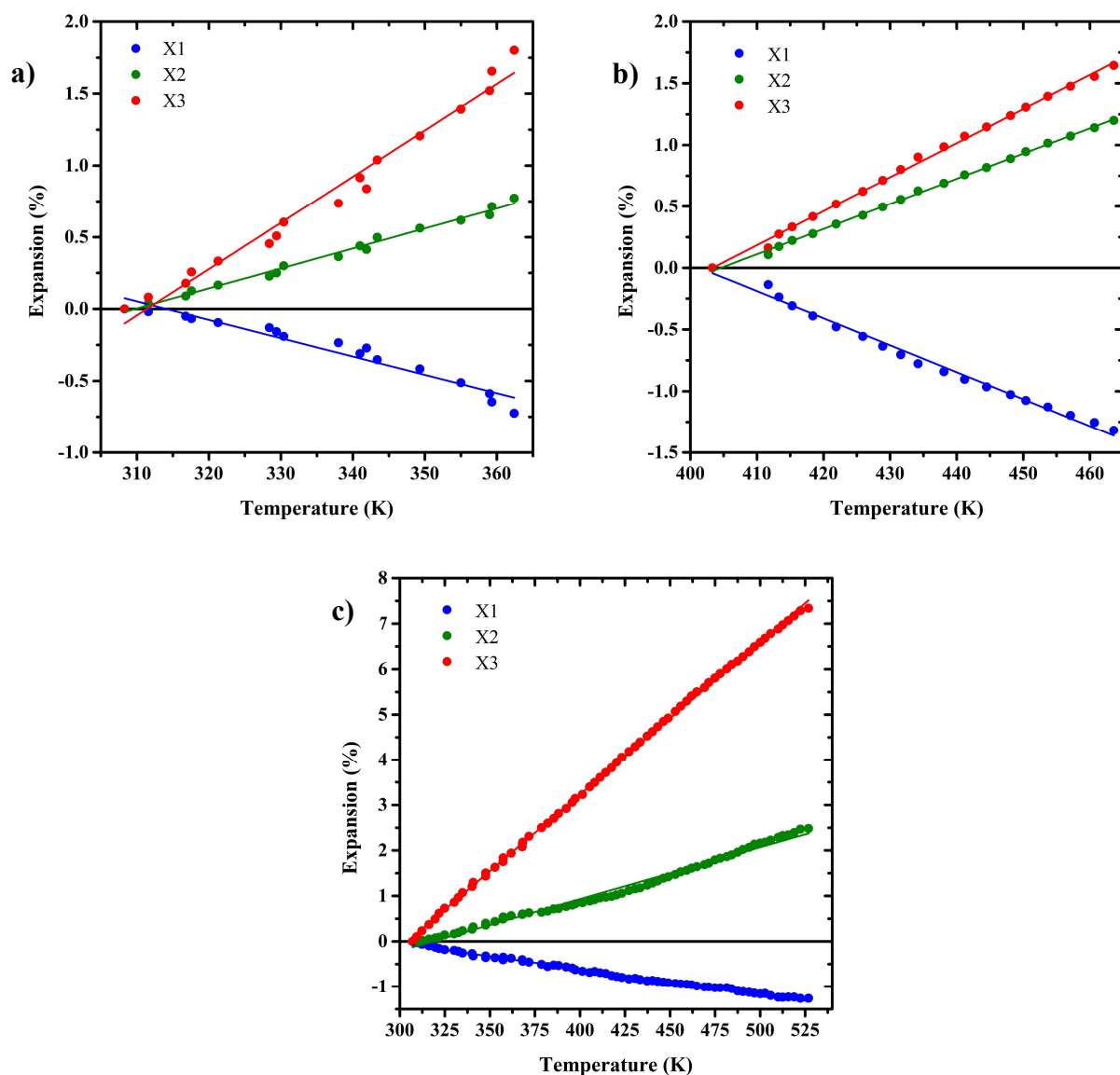
Figure S24. Variation (%) of the three principal axes X_1 (in blue), X_2 (in green), and X_3 (in red) with temperature in the three forms: a) form I; b) form II; c) form III. The linear approximation holds in the temperature range considered.

The orientation of the principal axes within the structure is reported in Figure S25.
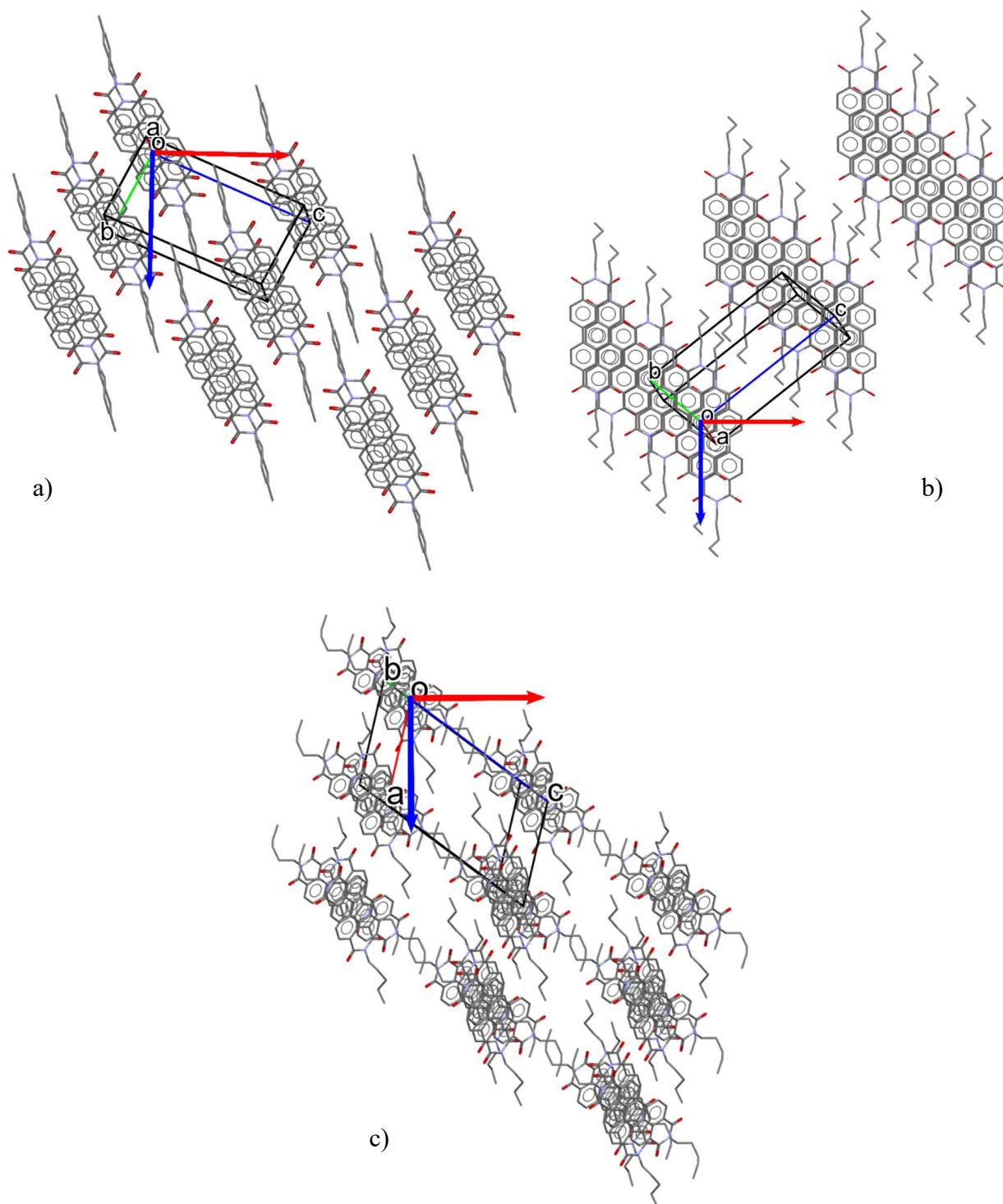
Figure S25. Packing of the structures a) form I, b) form II and c) form III with indicated the orientation of the thermal expansion principal axes calculated by PASCal: X$_2$ is perpendicular to the figure, while X$_1$ is indicated by the blue arrow and X$_3$ is indicated by the red arrow.

Raman Spectroscopy
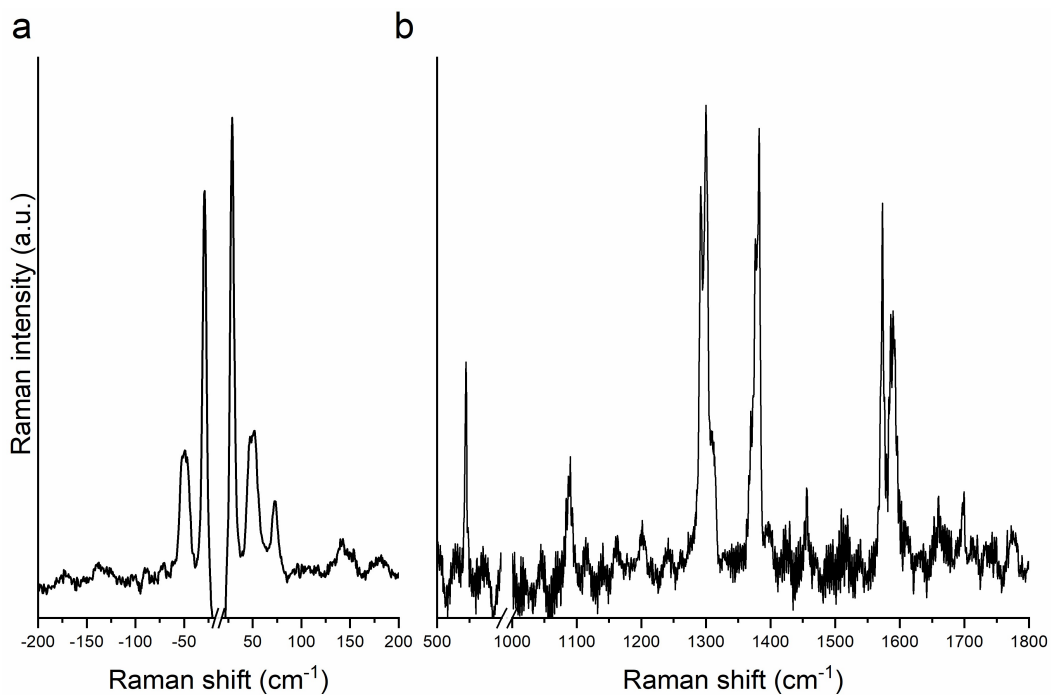
Figure S26. Raman spectra at room temperature of PDI-C$_5$ in the low frequency range (a) showing Stokes and anti-Stokes peaks and in the high frequency range (b).
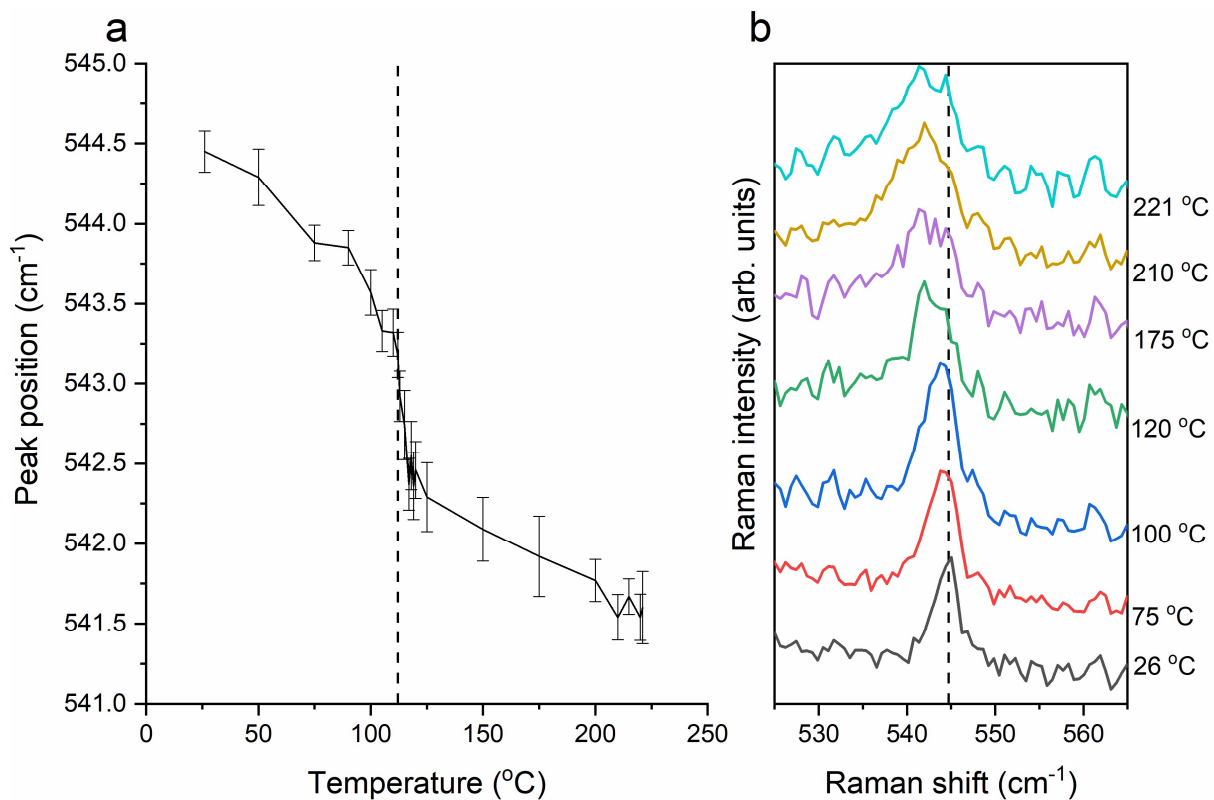
Figure S27. Intramolecular peak position as a function of the temperature (a) and corresponding Raman spectra (b).
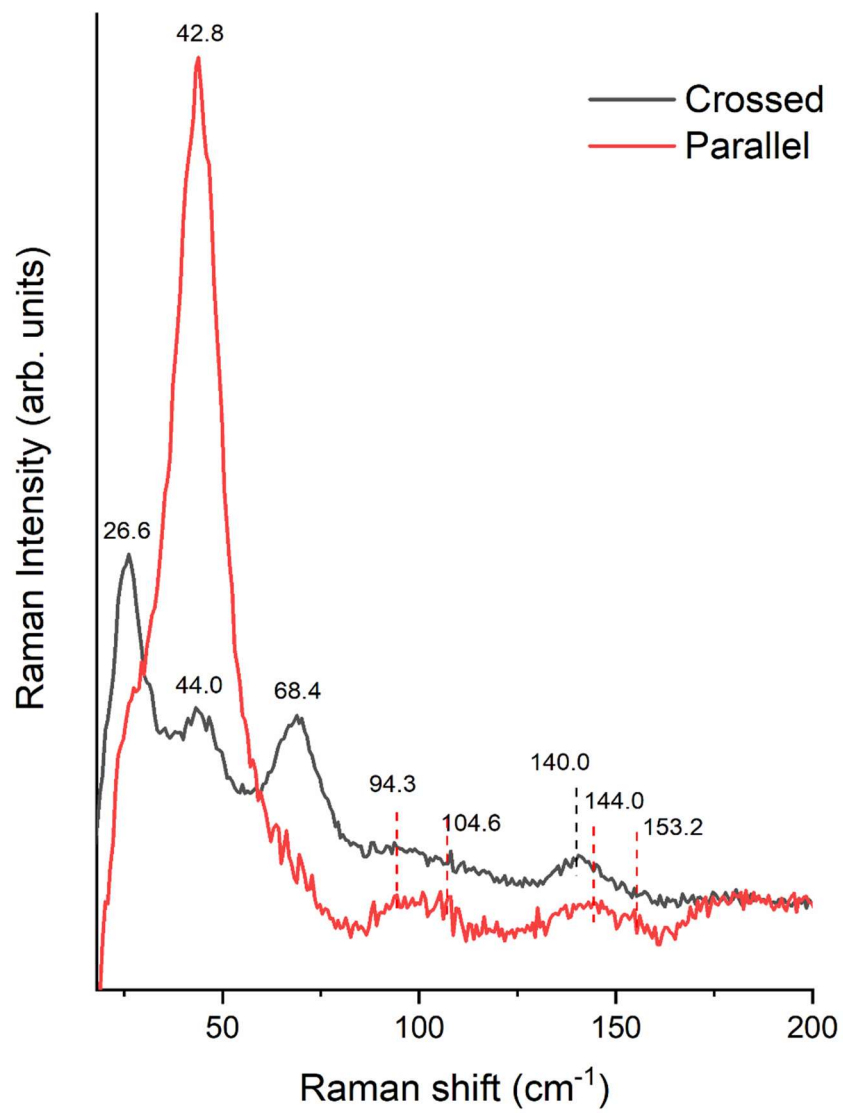
Figure S28. Polarized Low-frequency spectra of PDI-C$_5$ form III.

APPENDIX D

SUPPLEMENTARY INFORMATION

Exploring Polymorphic Landscape of PDI-Cn at variable Temperature and Pressure

Thermogravimetric analysis (TGA)

The thermal stability of the different PDI-Cn was investigated by TGA, showing that all the PDI-Cn are thermally stable up to 400 °C, where degradation occurs.

PDI-C5
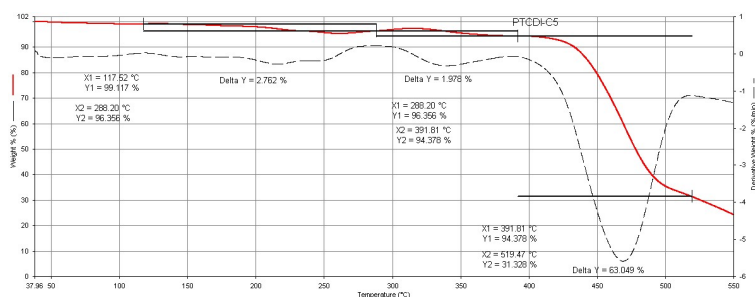
Figure S1. TGA curve of PDI-C5, a single degradation step is observed above 400 °C.

PDI-C6
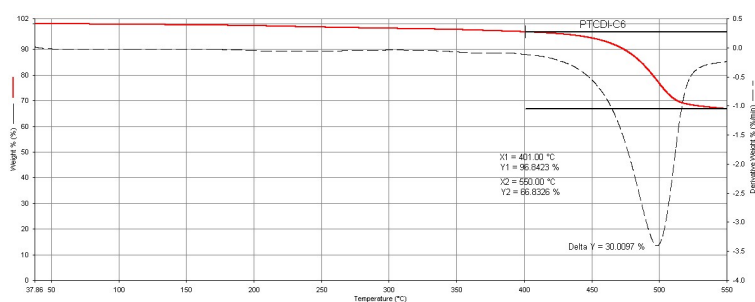
Figure S2. TGA curve of PDI-C6, a single degradation step is observed above 400 °C.

PDI-C7
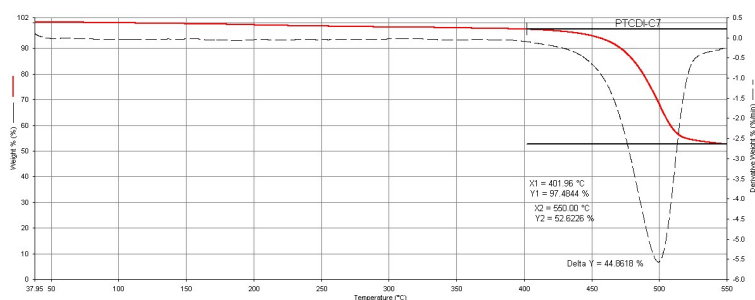
Figure S3. TGA curve of PDI-C7, a single degradation step is observed above 400 °C.

PDI-C8
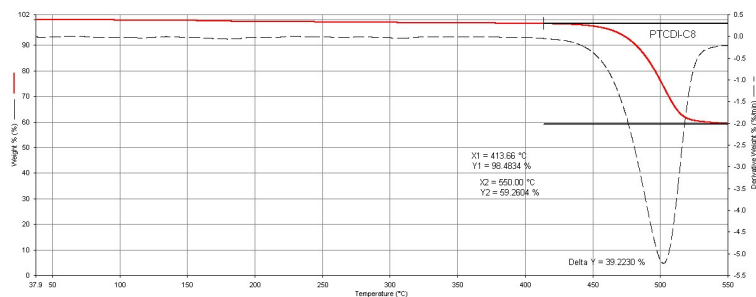
Figure S4. TGA curve of PDI-C8, a single degradation step is observed above 400 °C.

Indexing of high-temperature polymorphs

The patterns of PDI-Cn high-temperature polymorphs were indexed with TOPAS5[1] or EXPO[2]; the best crystal cell obtained was refined with a Pawley refinement with TOPAS5.

PDI-C6 form III
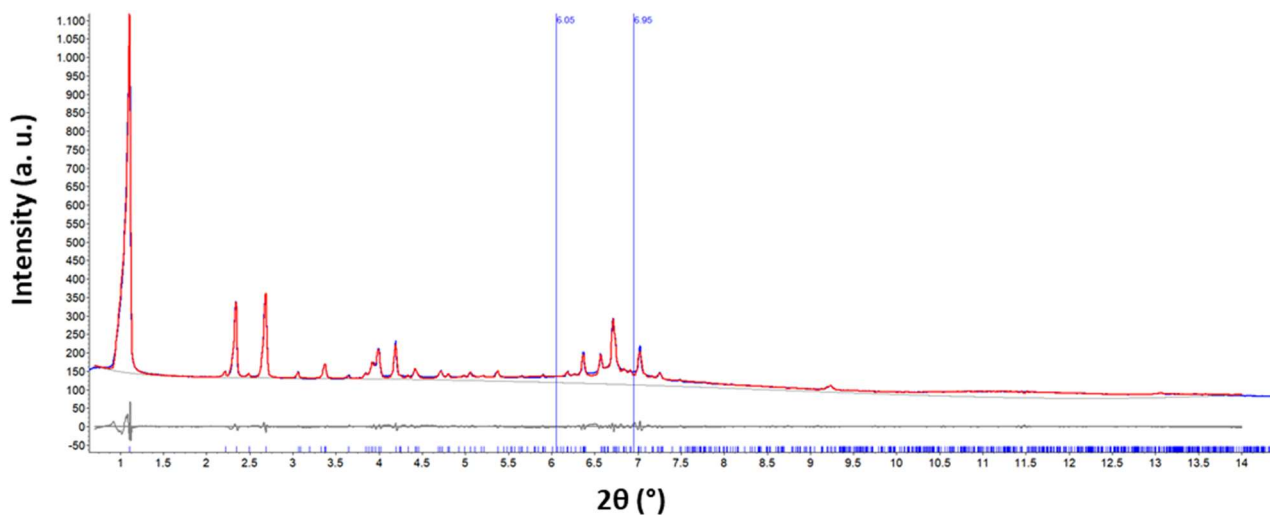
Figure S5. Pawley refinement of PDI-C6 at 265 °C. In blue is the experimental pattern, in red is the calculated pattern and in grey is the difference pattern. The blue lines at 6.05 and 6.95 of 2θ correspond to the two peaks used to describe the glass capillary contribution. The intensity is reported in square root for the sake of clarity.

PDI-C7 form II
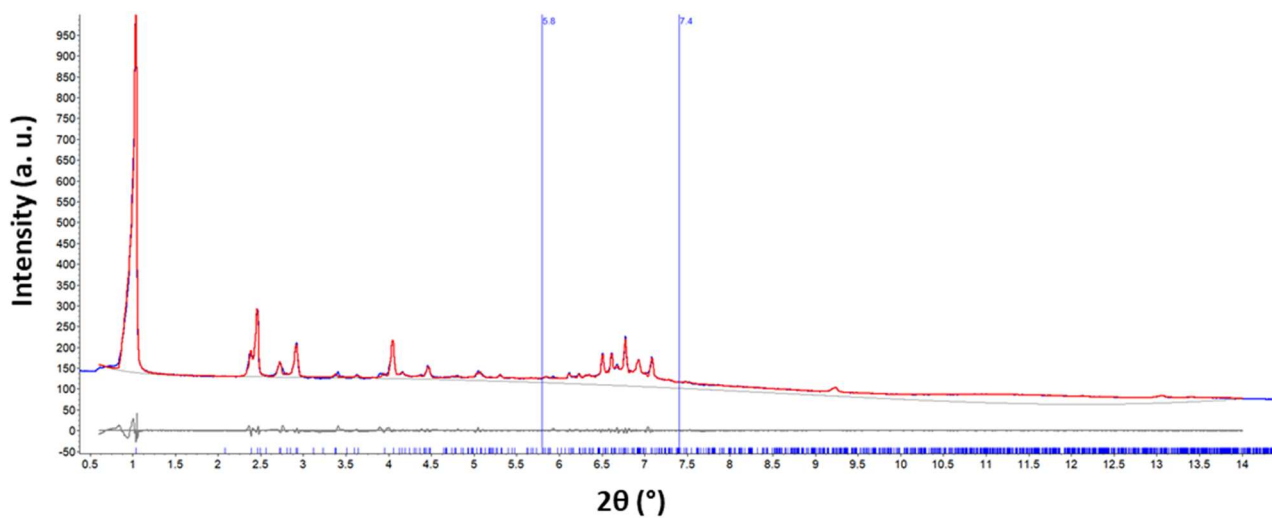
Figure S6. Pawley refinement of PDI-C7 at 218 °C. In blue is the experimental pattern, in red is the calculated pattern and in grey is the difference pattern. The blue lines at 5.8 and 7.4 of 2θ correspond to the two peaks used to describe the glass capillary contribution. The intensity is reported in square root for the sake of clarity.

PDI-C7 form III
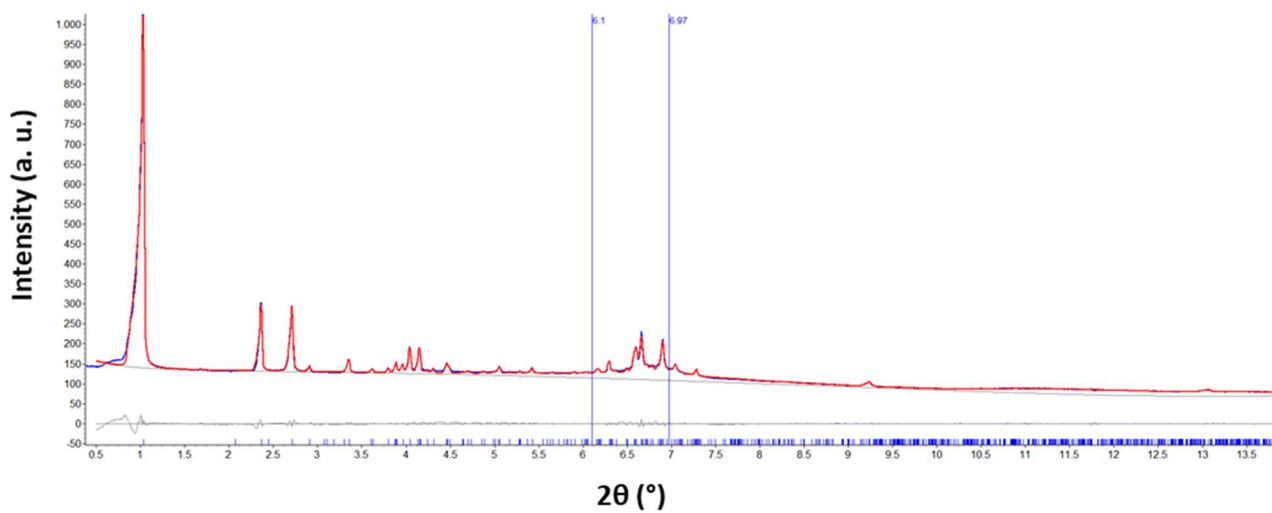
Figure S7. Pawley refinement of PDI-C7 at 255 °C. In blue is the experimental pattern, in red is the calculated pattern and in grey is the difference pattern. The blue lines at 6.1 and 6.97 of 2θ correspond to the two peaks used to describe the glass capillary contribution. The intensity is reported in square root for the sake of clarity.

PDI-C8 form II
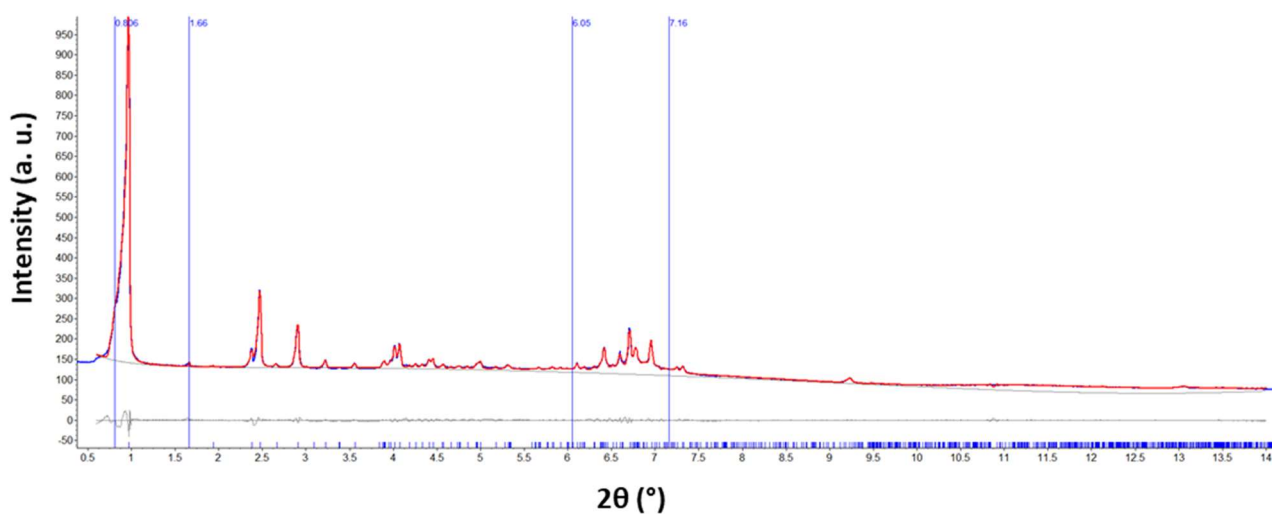
Figure S8. Pawley refinement of PDI-C8 at 224 °C. In blue is the experimental pattern, in red is the calculated pattern and in grey is the difference pattern. The blue lines at 0.806 and 1.660 of 2θ correspond to peaks of another phase present, these peaks grow when the temperature is further increased; the blue lines at 6.1 and 6.97 of 2θ corresponds to the two peaks used to describe the glass capillary contribution.

Pressure-dependent UV-Vis absorption spectra

Pressure-dependent UV-Vis absorption spectra of the PDI-Cn upon releasing pressure.

PDI-C5
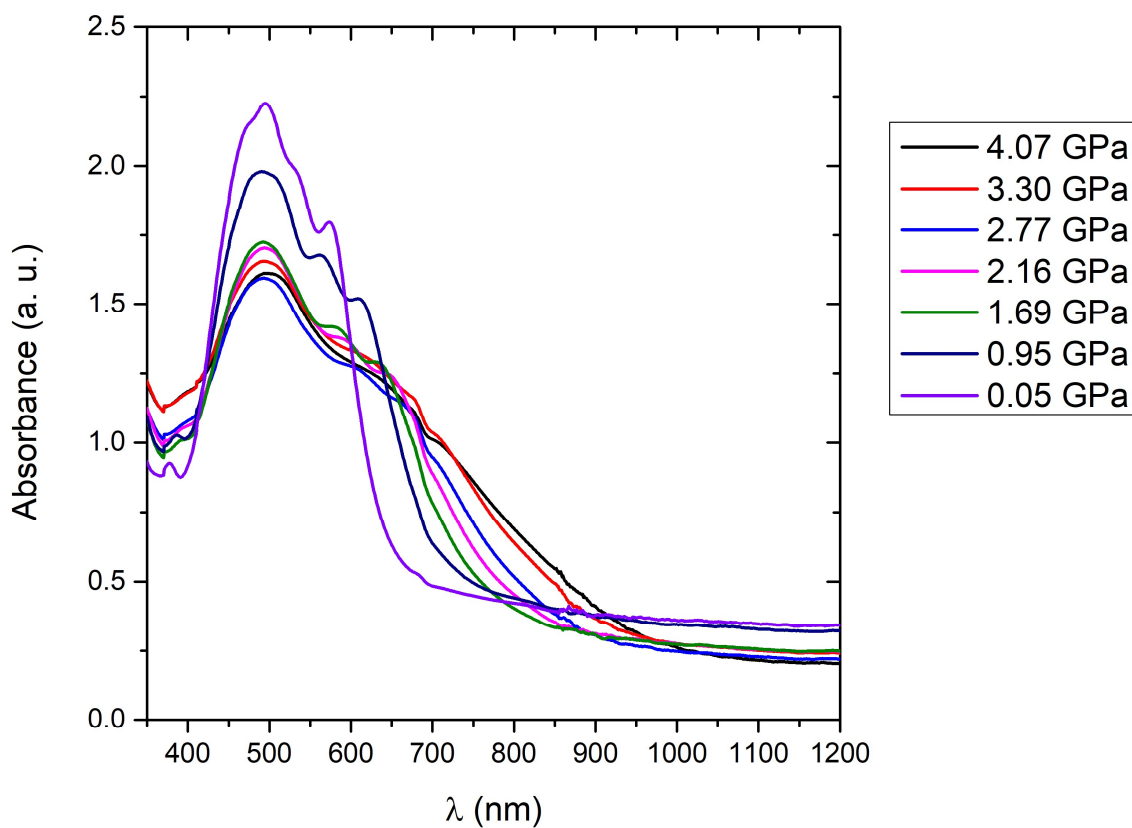
Figure S9. UV-Vis-NIR absorption spectra of PDI-C5 upon releasing pressure.
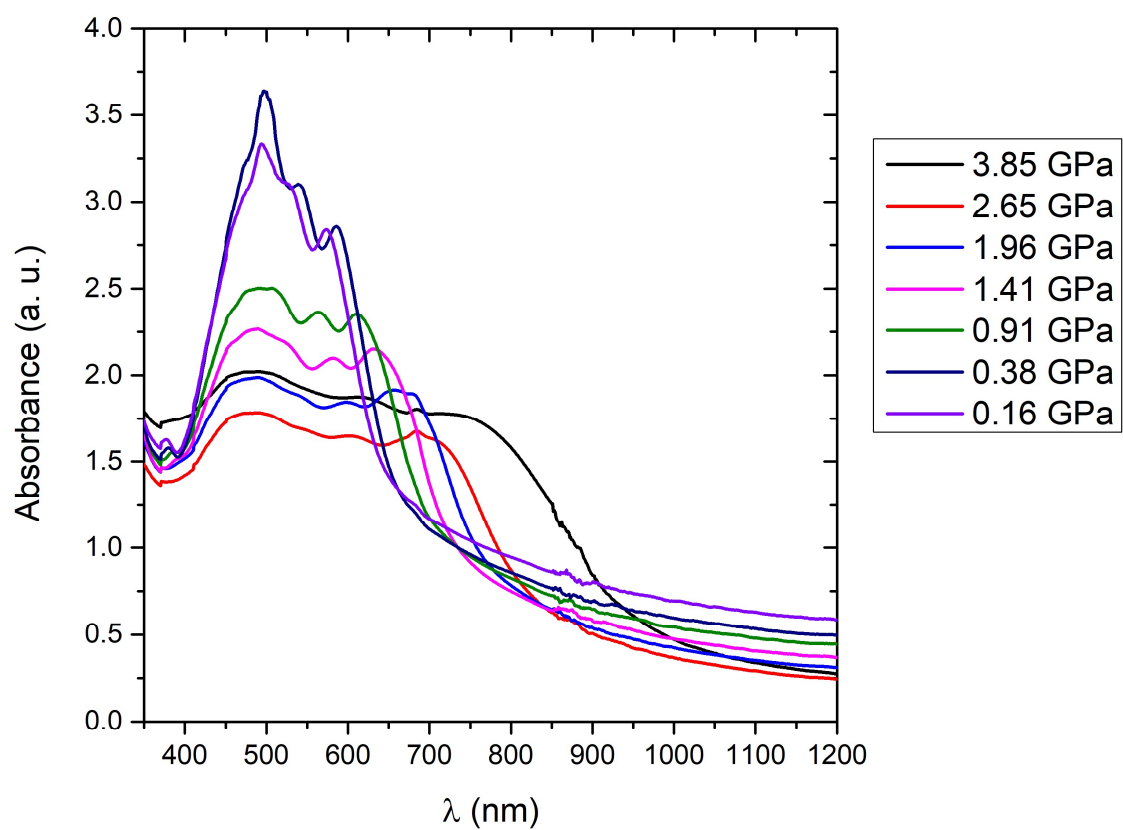
PDI-C6

Figure S10. UV-Vis-NIR absorption spectra of PDI-C6 upon releasing pressure.

PDI-C7
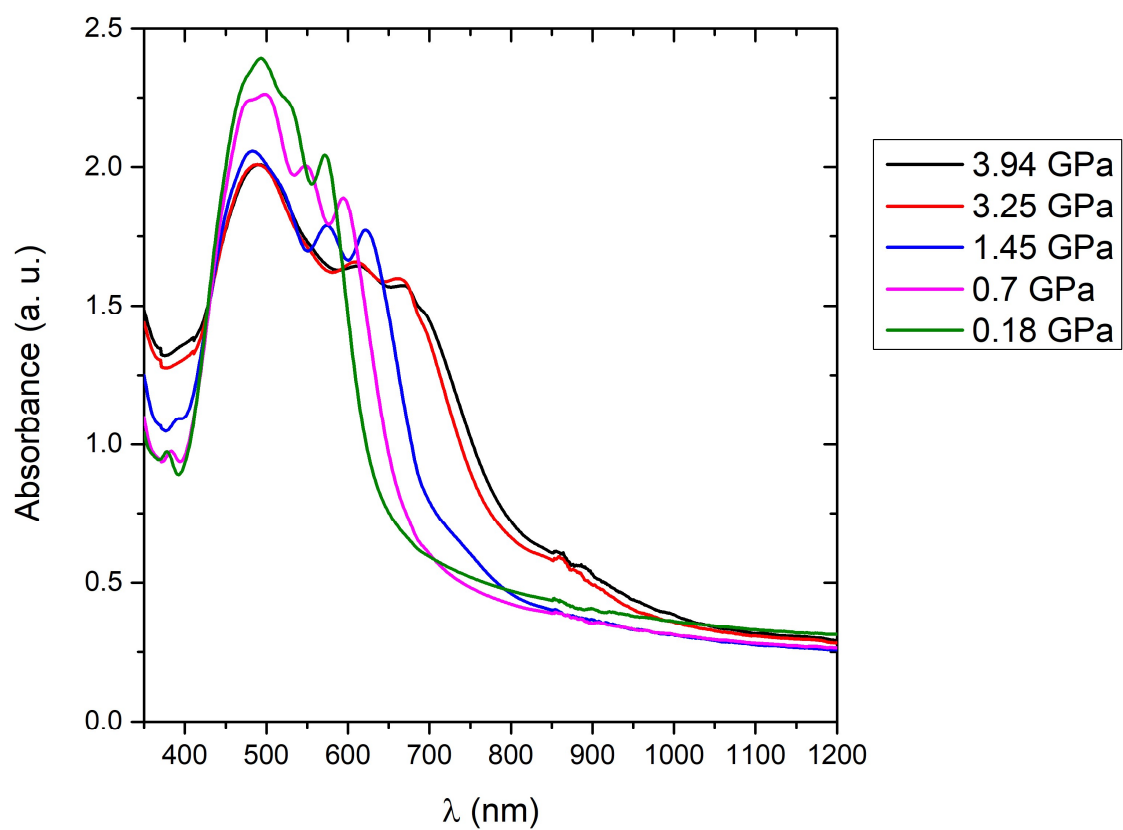
Figure S11. UV-Vis-NIR absorption spectra of PDI-C7 upon releasing pressure.
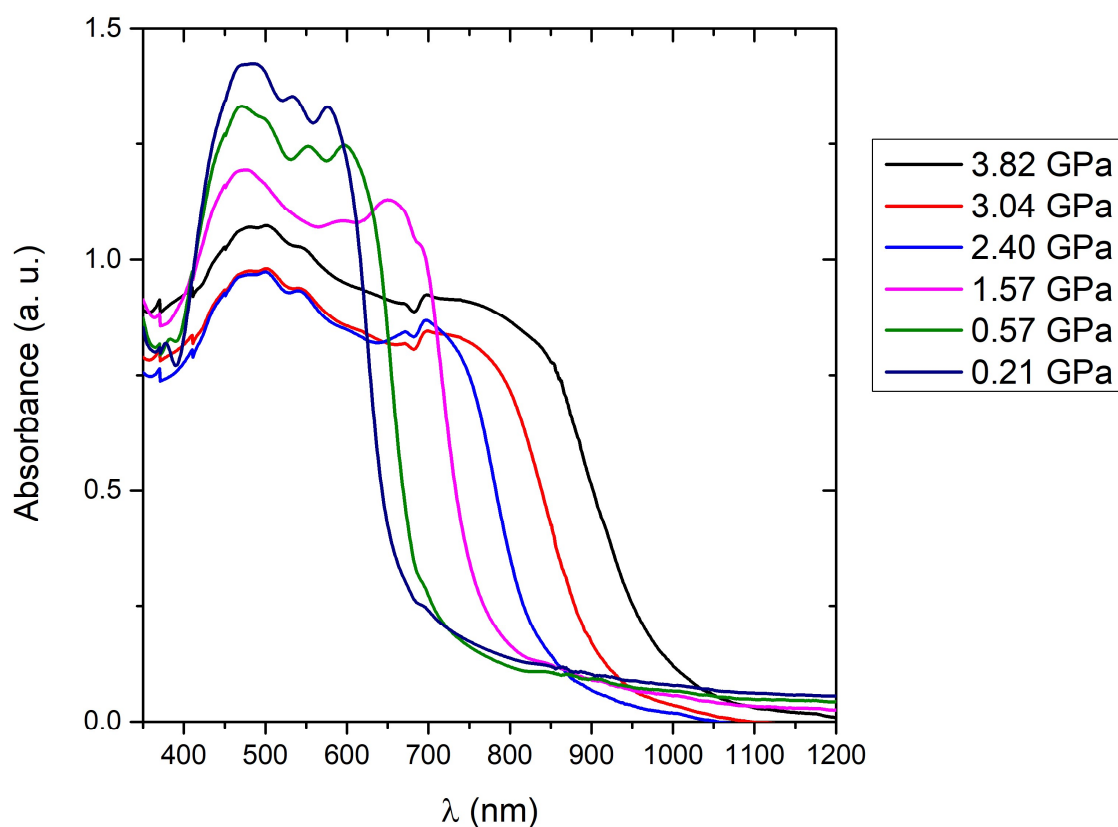
PDI-C8

Figure S12. UV-Vis-NIR absorption spectra of PDI-C8 upon releasing pressure.

REFERENCES

(1)   Coelho, A. A. TOPAS and TOPAS-Academic: An Optimization Program Integrating Computer Algebra and Crystallographic Objects Written in C++: An. *J. Appl. Crystallogr.* **2018**, *51* (1), 210–218.

(2)   Altomare, A.; Cuocci, C.; Giacovazzo, C.; Moliterni, A.; Rizzi, R.; Corriero, N.; Falcicchio, A. EXPO2013: A Kit of Tools for Phasing Crystal Structures from Powder Data. *J. Appl. Crystallogr.* **2013**, *46* (4), 1231–1235.

APPENDIX E

SUPPLEMENTARY INFORMATION

Self-Organizing Maps as a data-driven approach to reveals the variety of packing motives of PDI derivatives

Francesco Marin[a], Alessandro Zappi[,a], Dora Melucci[a], Lucia Maini*[a]*

[a]Dipartimento di Chimica "G. Ciamician", via Selmi 2, Università di Bologna, 40126 Bologna, Italy

In the present paragraph, we present the procedure and outcomes of the SOM analysis.[1] As already stated in the main text, the SOM analyses were carried out with the package SOMEnv[2] of the R environment. Here we present the SOM calculated with map dimensions 10 x 6, but the results are analogous for all the other calculated maps.

The dataset is composed of 142 objects (crystal structures) and 17 numeric variables (described in the main text). The computation starts by choosing the map dimensions and shape, in this case, a rectangular map composed of 60 units divided into 10 rows and 6 columns.[3] The first step of the computation produces an output as the one reported in Figure S1 in which the map is shown, and the dimension of the black filling is proportional to the number of objects in each unit. At this stage, it is not really important to know how many objects are assigned to each unit, it is most of all interesting to observe that there are regions of the map that are more populated than others and that there are also some empty units.
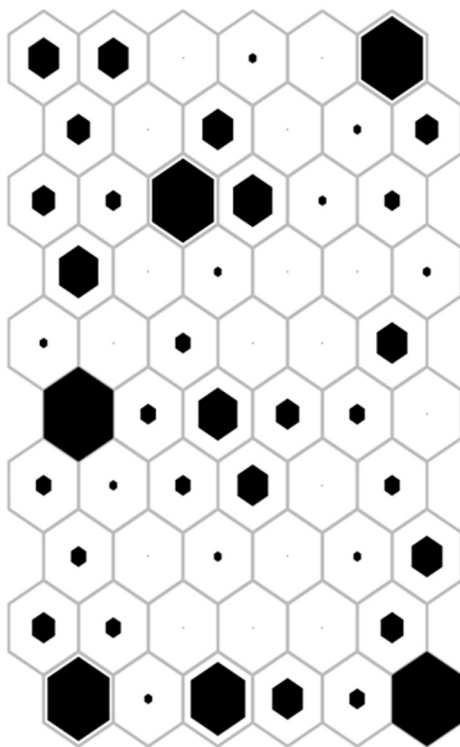
Figure S1. SOM map reporting the number of objects assigned to each unit: black fillings are proportional to the number of objects.

The second important output of this first stage is reported in Figure S2. It concerns the role of variables in the SOM computation. The filling of the hexagons, in this case, is proportional to the basic statistic of each variable: black colour represents higher quartiles in that region for that variable, white colour represents lower quartiles. This means that the objects assigned to a certain region of the map have higher or lower (median) values for that variable, based on the colour reported in Figure S2. From this graph, it is possible to evaluate some features of the variables. In particular, if two or

more variables show similar graphs, they would probably have the same general behaviour, *i.e.* they are strongly correlated. In the case shown in Figure S2, for example, the variables $d_{\pi\text{-}\pi}$ (called d.p.p in Figure S2), M/L (ML) and S have very similar SOM graphs, thus these can be considered correlated.
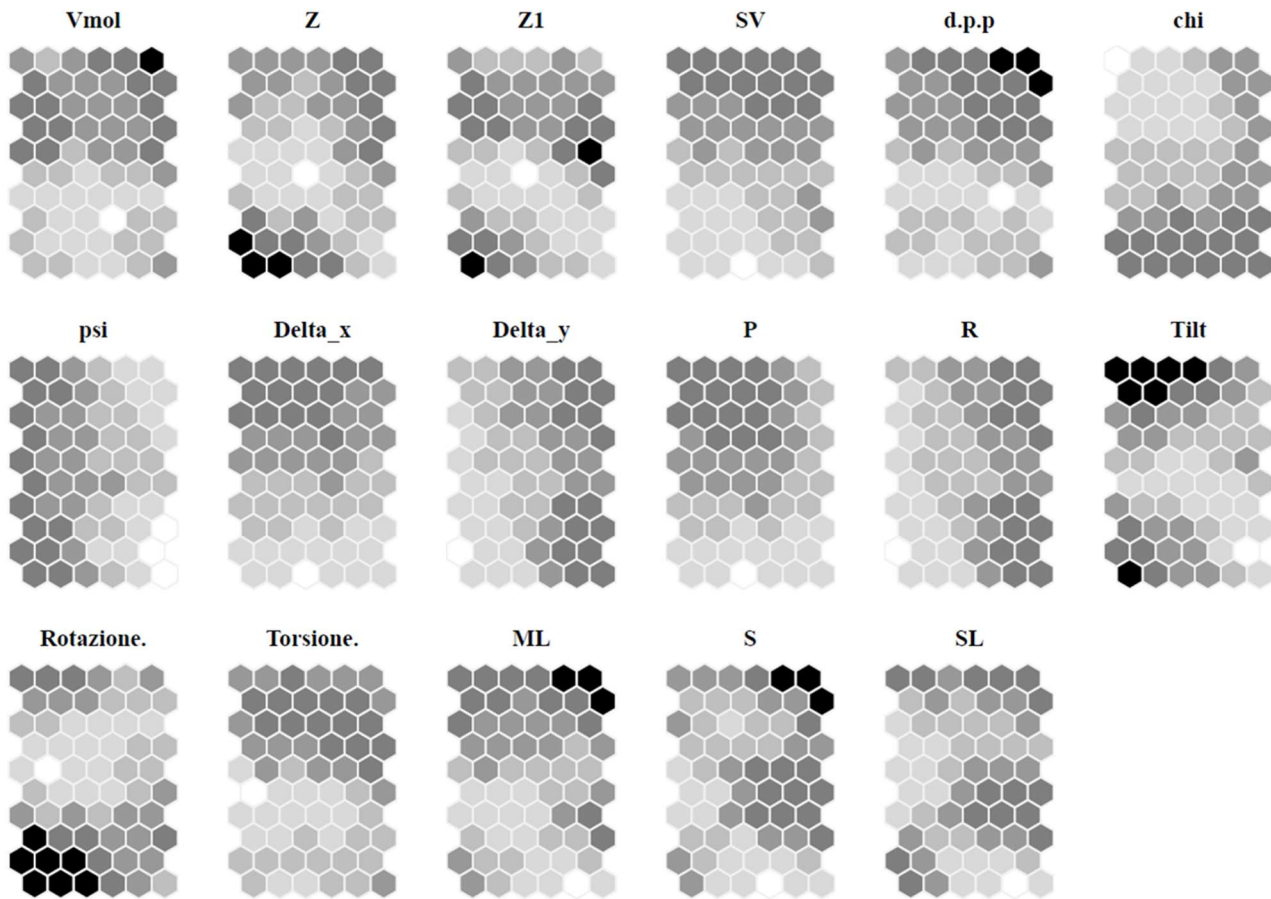

Figure S2. Variable's behaviour in the SOM analysis. Black and white colours represent respectively higher and lower quartiles of each variable in each map region.

Other graphical output (not shown) can be produced by SOMEnv graphical user interface to evaluate the model stability.

From the map shown in Figure S1, a K-means cluster analysis can be computed, using the units as starting data.[4] In this case, the maximum number of possible clusters (k) has to be decided as input data and the algorithm calculates the optimal number of clusters from k=2 to the decided maximum k. The optimization is based on minimization of the DB-index,[5] as explained in the main text. In the present work, k_{max} was always put as 8. For the map presented in this paragraph, the optimal number of cluster results to be 5. The graphical output produced by SOMEnv is reported in Figure S3. Figure S3 shows the same map reported in Figure S1, but the colours represent the clusters to which each unit is assigned. Based on these clusters, the computations and the discussion reported in the main text were carried out.
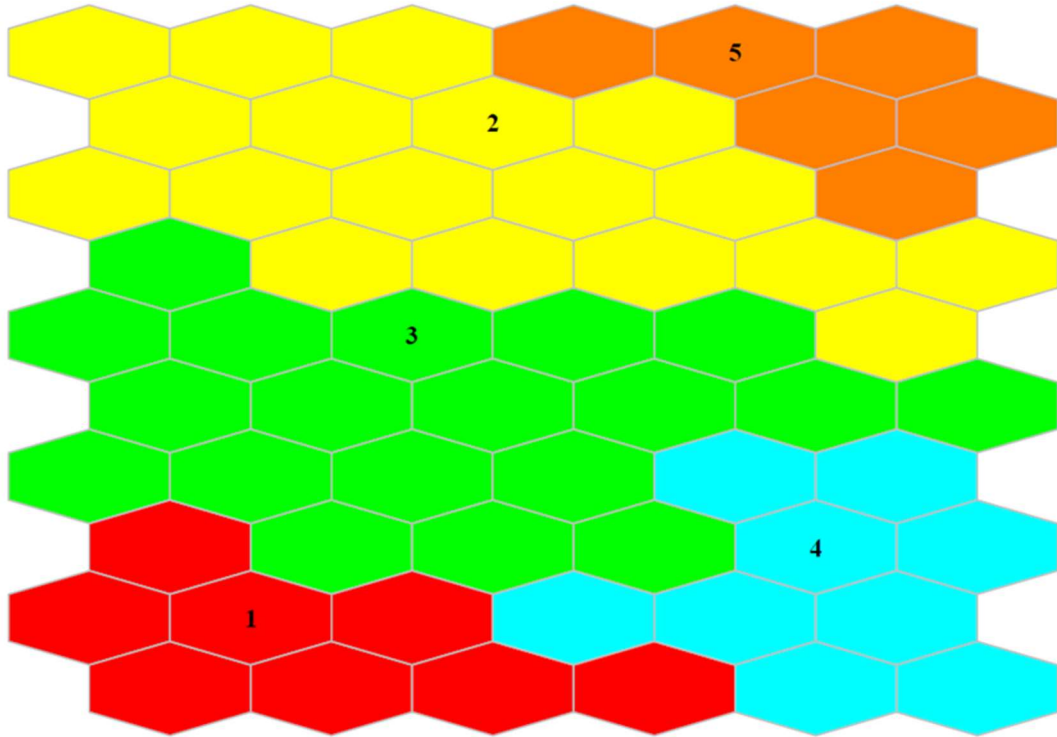
Figure S3. SOM map divided by colours after K-means cluster analysis. The units in which cluster-number is placed indicates the cluster centroids.

Also in this case, the role of variables in the clustering step can be graphically evaluated by the plot reported in Figure S4. In this case, boxplots of auto-scaled variables (each original data is subtracted to its column-mean and the result divided by the column standard deviation) are reported for each cluster. From these graphs, it can be argued which variables are the most characteristic of each cluster. In the example shown, Cluster 3 (in green in Figure S3) have no particular characteristic variables, while Cluster 4 (in light blue) is mainly characterized by variables χ (chi), Δy (Delta_y), and R.
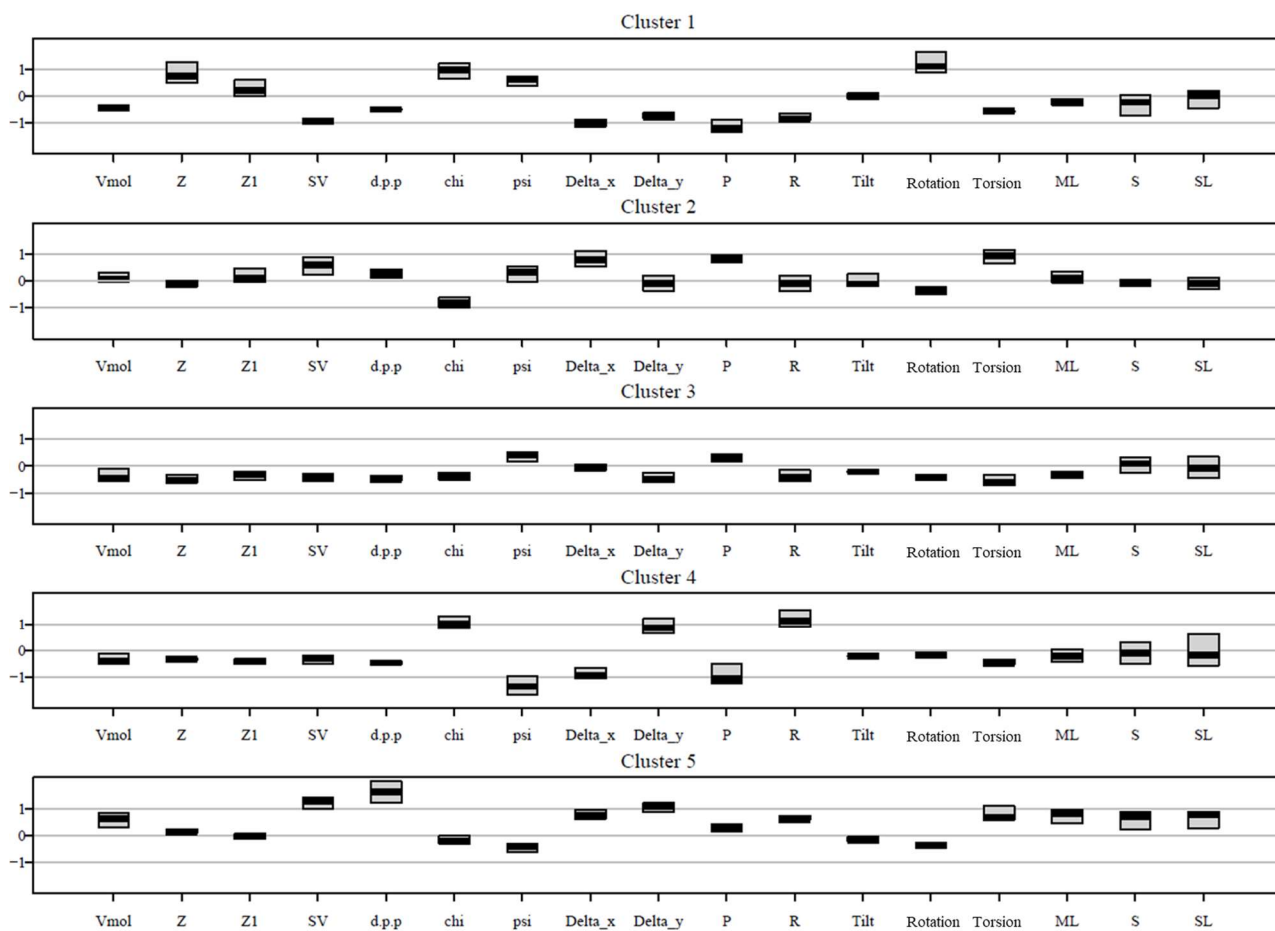
Figure S4. Boxplots of variables for each cluster. Higher median values indicate more characteristic variables for the corresponding cluster.

The boxplots showing the variation of the variables in the six packing families not reported in the main text are reported here. In the boxplots, the variation range of each variable is plotted for each family, and these can give information about the range and distribution of each variable within the family. The use of boxplots is helpful to identify the families' most important characteristics.
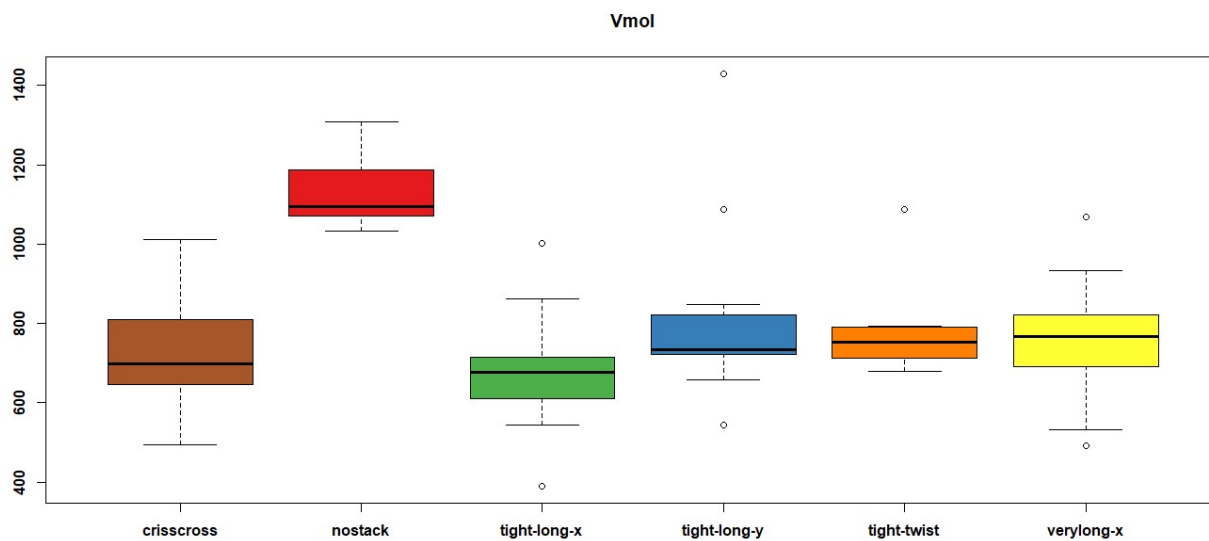
Figure S5. Boxplot of the molecular volume (V_{mol}) distribution among the identified families.
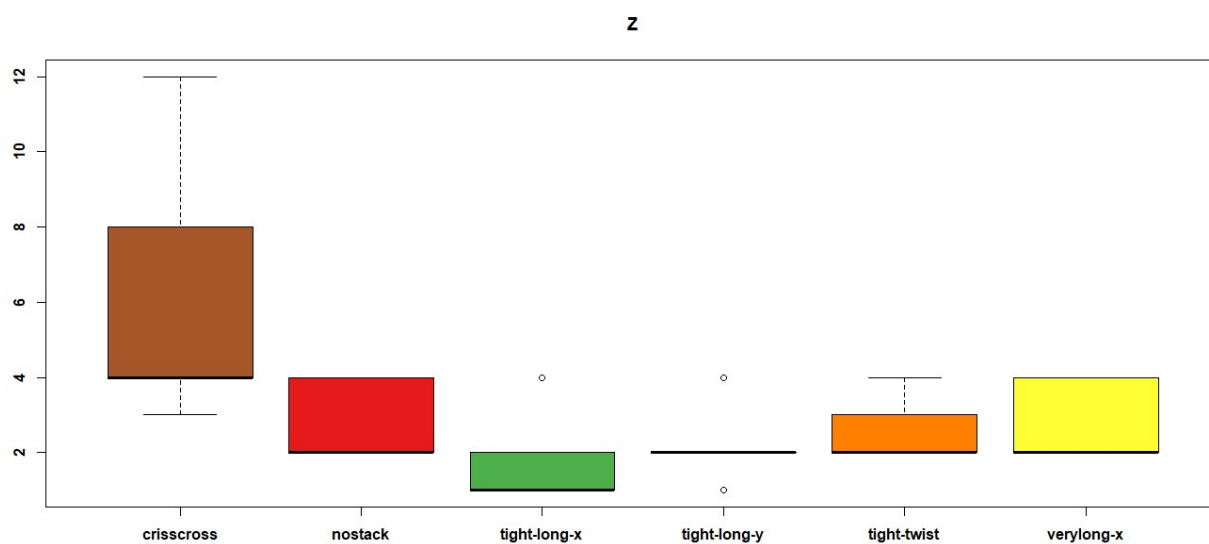
Figure S6. Boxplot of the number of molecules in the unit cell (Z) distribution among the identified families.
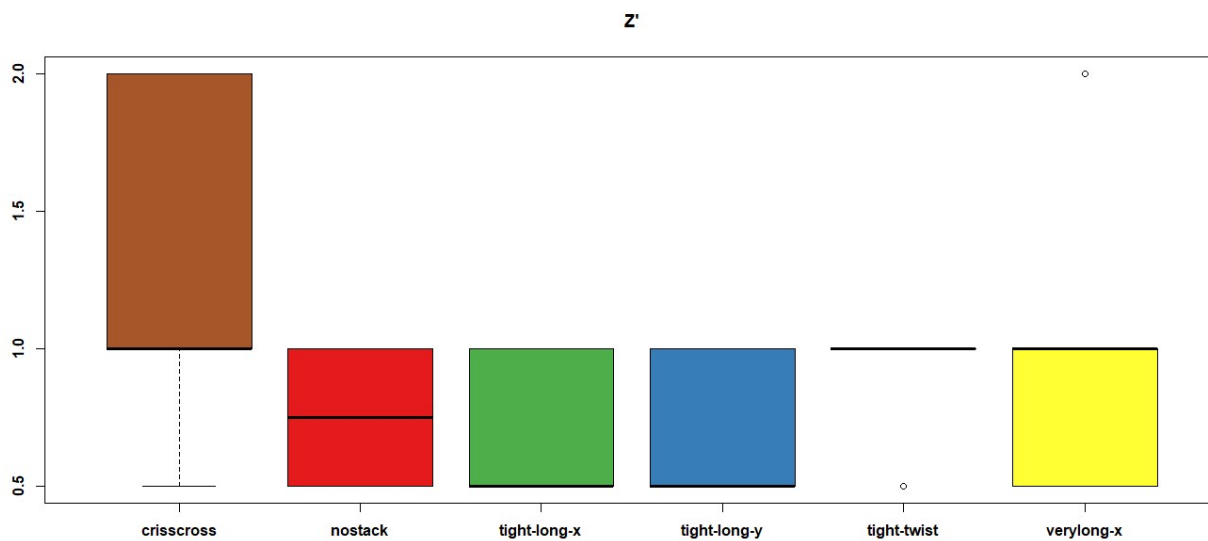
Figure S7. Boxplot of the number of molecules in the asymmetric unit (Z') distribution among the identified families.
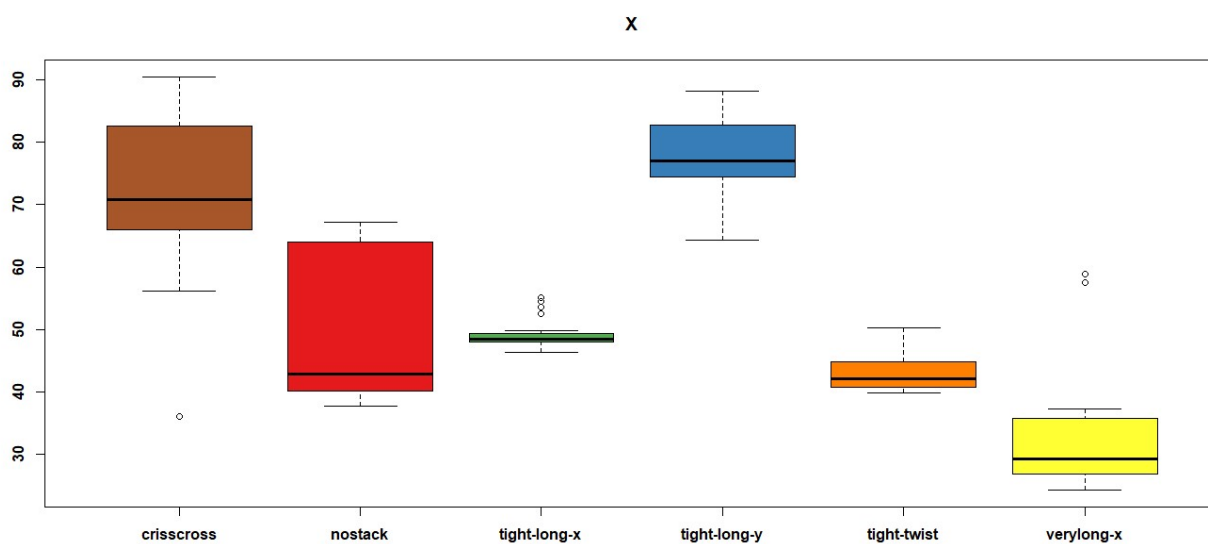
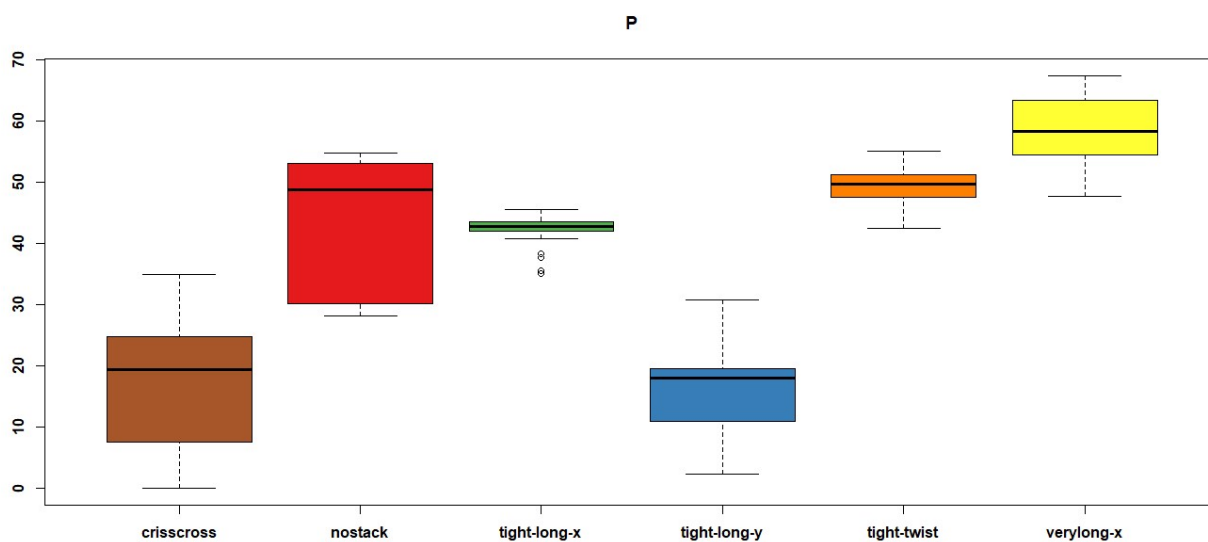Figure S8. Boxplot of the angles of the direction cosines of the SV with the perylene x-axis (χ) distribution among the identified families.

139
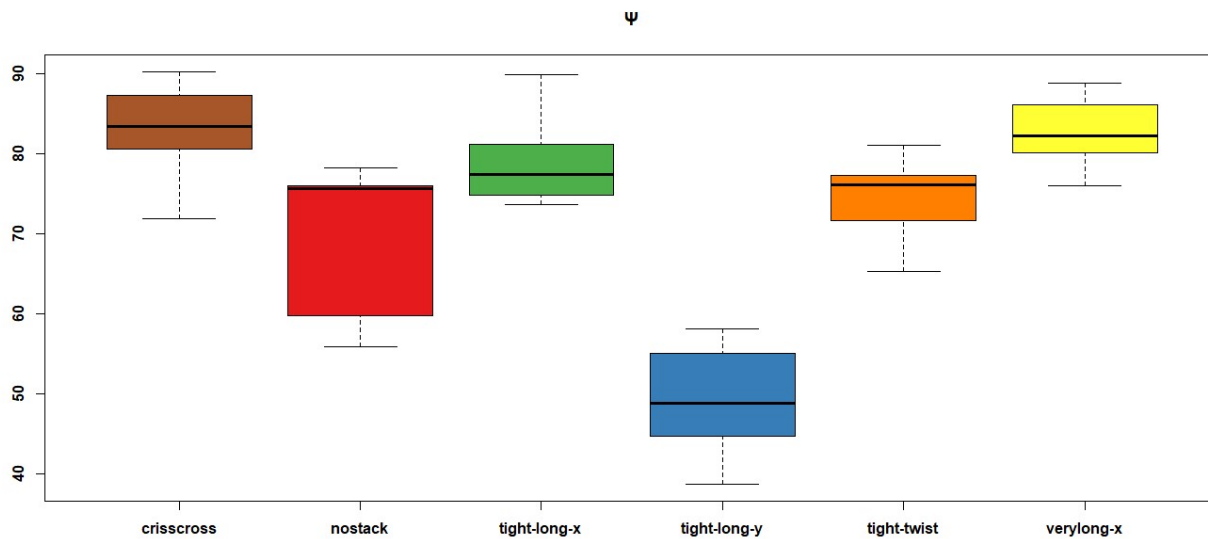
Figure S9. Boxplot of the angles of the direction cosines of the SV with the perylene y-axis (ψ) distribution among the identified families.

Figure S10. Boxplot of the pitch angles (P) distribution among the identified families.
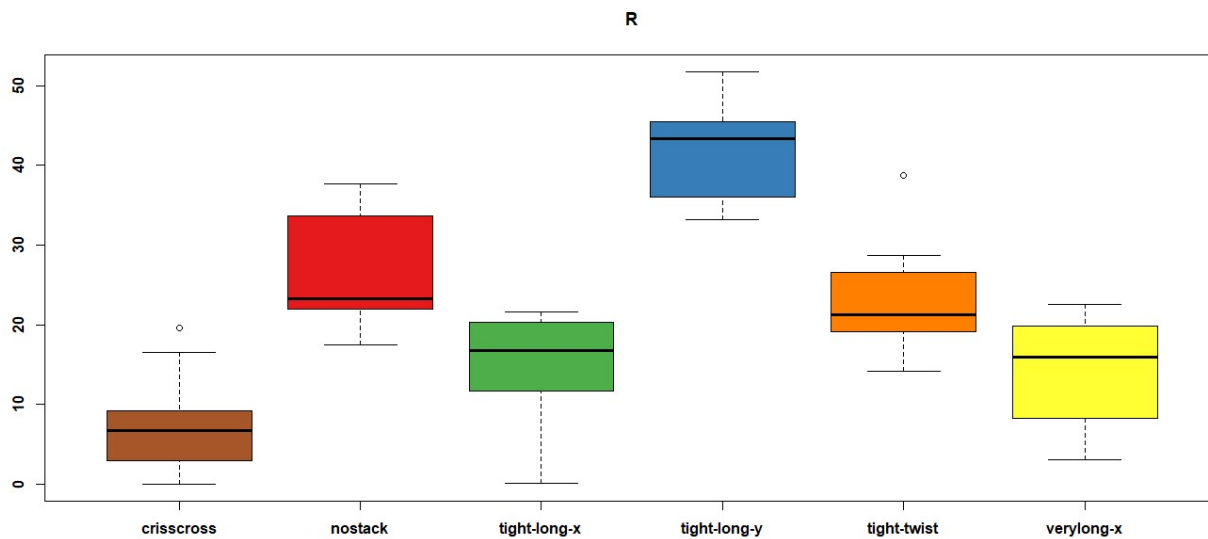
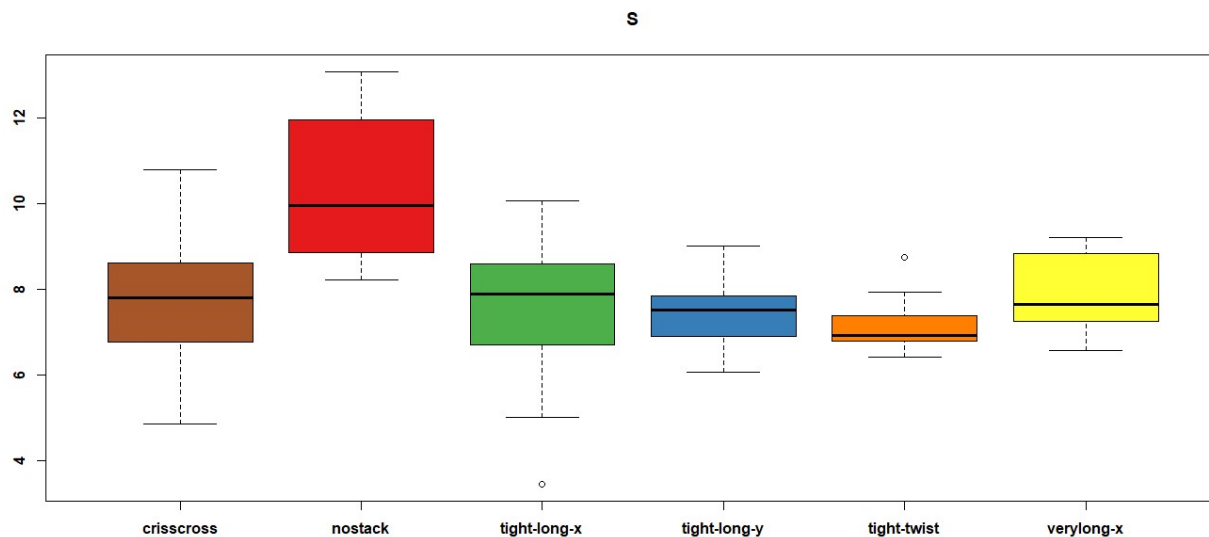Figure S11. Boxplot of the roll angles (R) distribution among the identified families.
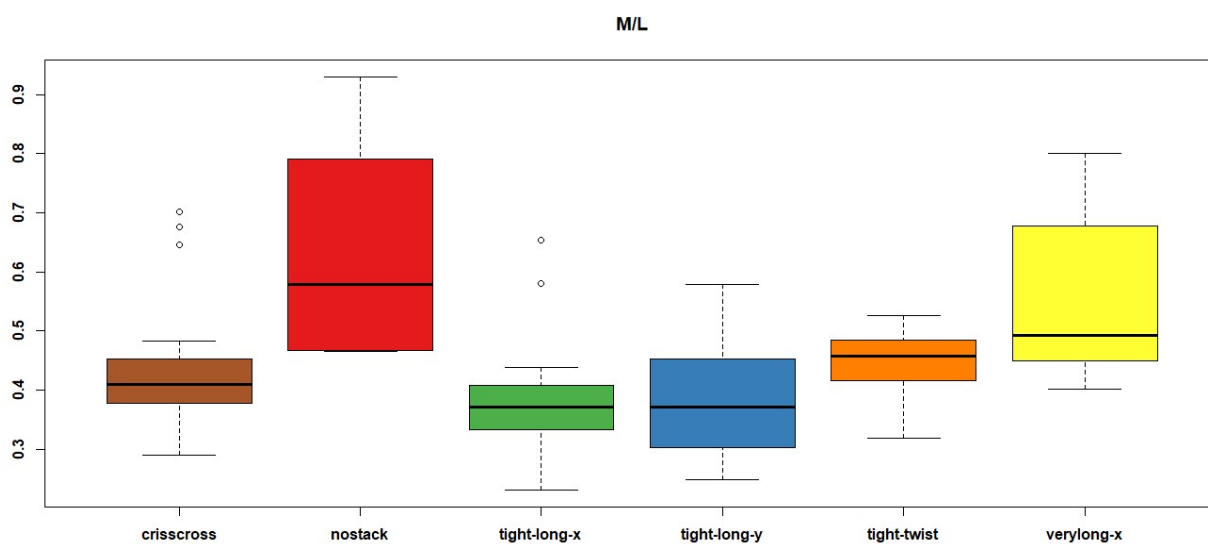
Figure S12. Boxplot of the aspect ratio of the molecule described as enclosed in a rectangular box, with here showed the ratio of the medium and long box axes (M/L) distribution among the identified families.

Figure S13. Boxplot of the aspect ratio of the molecule described as enclosed in a rectangular box, with here showed the length of the short box axis (S) distribution among the identified families.
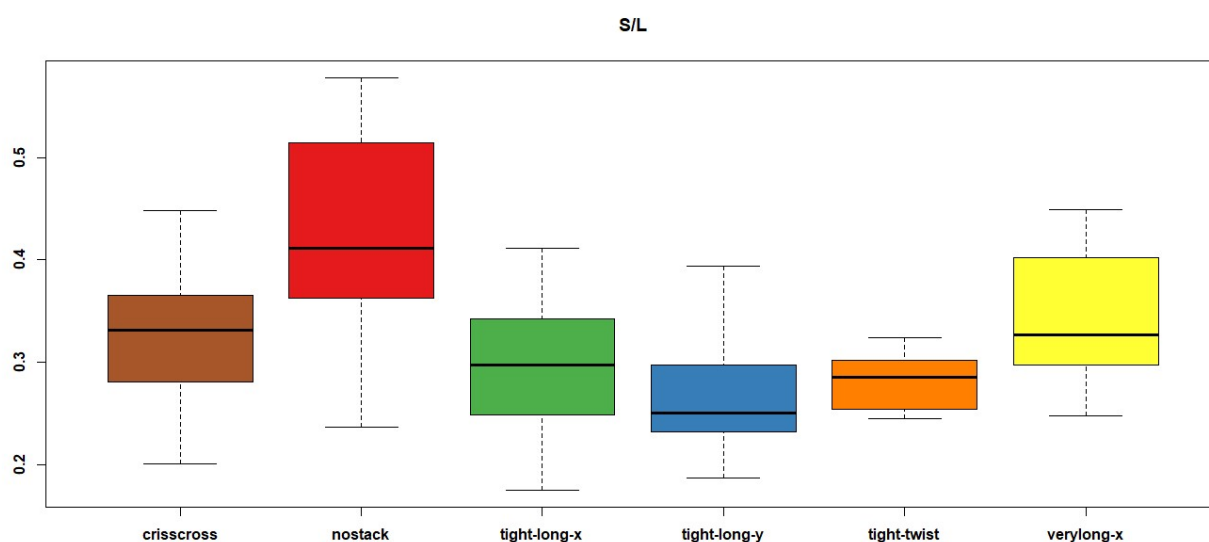

Figure S14. Boxplot of the aspect ratio of the molecule described as enclosed in a rectangular box, with here showed the ratio of the short and long box axes (S/L) distribution among the identified families.

The result of SOM grouping visualized using the PCA scores plot are shown, with the *extra* divided into the 5 small groups. The scores of PC1 vs PC2 are shown, the colour of the scores correspond to the group in which each object was categorized.
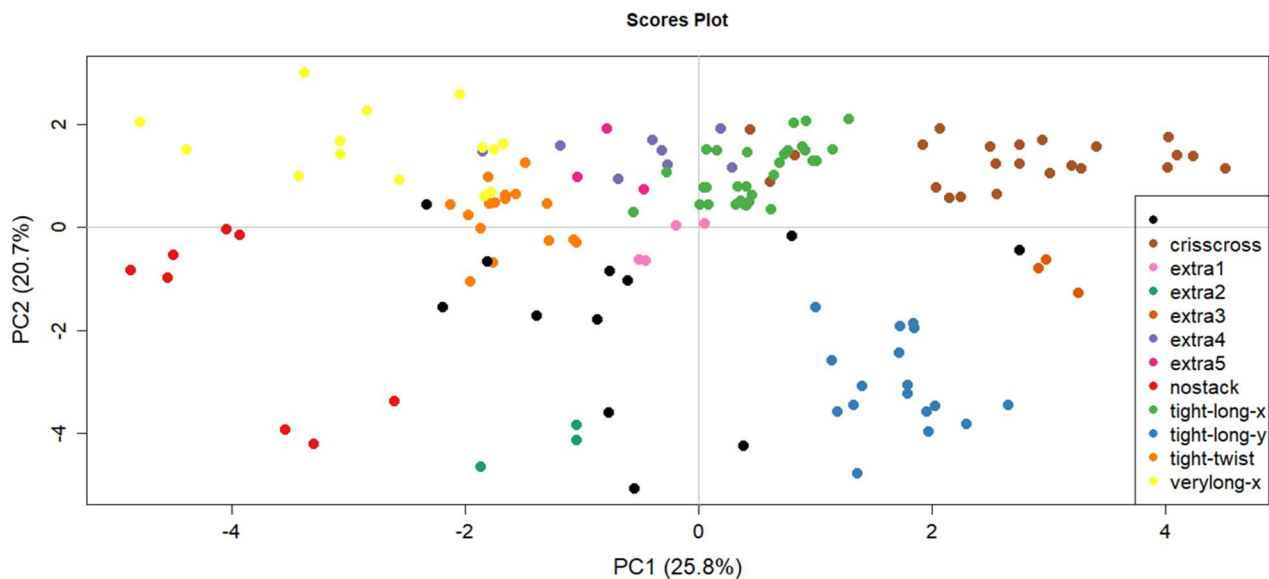
Scores Plot

Figure S15. PC1-PC2 scores plot obtained by PCA, with the scores categorized by the group they belong to. In particular, the 6 major families are shown, and the extra is divided into the respective 5 small groups. With extra1 in pink; extra2 in dark green; extra3 in dark orange; extra4 in purple; extra5 in violet.

The packing of YIWMEY, which is one of the two objects displaying dipole-π interaction between the perylene core and the carbonyl oxygen of the closest molecule, is shown as an example.
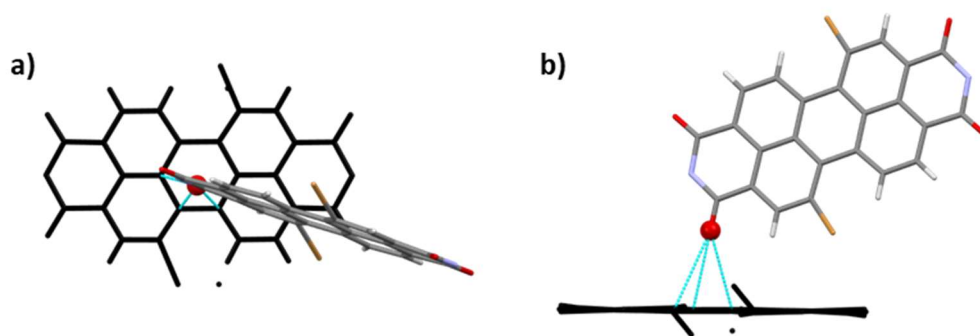

Figure S16. Dipole-π interaction in YIWMEY packing; a) viewed along z-direction; b) viewed along x-direction.

By looking only at the objects substituted at the core, we observe that most of them are found at negative PC1 of the scores plot where the π-π stacking interactions between perylene cores becomes weaker and other type of interactions becomes dominant.
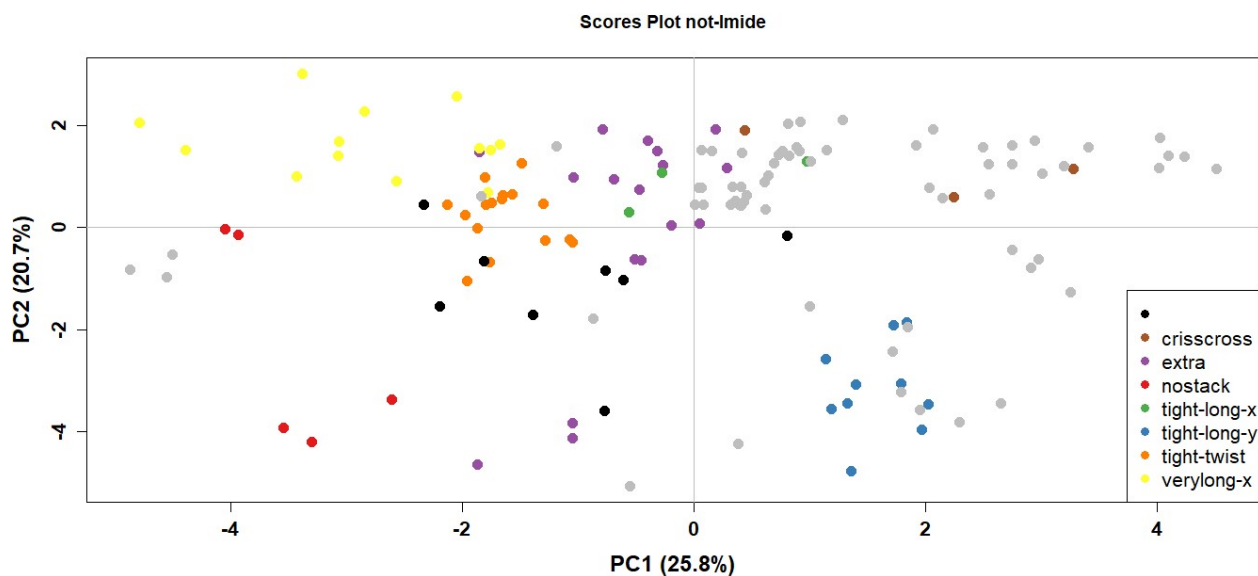
Scores Plot not-Imide

Figure S17. PC1-PC2 scores plot obtained by PCA, with the *bay*-, *ortho*-, and *bay*- and *ortho*-substituted objects categorized by the family they belong to by the colour. The *imide*-substituted objects are coloured in grey. Most of the *core*-substituted objects are at negative PC1 values, where the π-π stacking interactions between perylene cores becomes weaker and other type of interactions becomes dominant.

REFERENCES

(1)   Kohonen, T. The Self-Organizing Map. *Neurocomputing* **1998**, *21* (1), 1–6.

(2)   Licen, S.; Franzon, M.; Rodani, T.; Barbieri, P. SOMEnv: An R Package for Mining Environmental Monitoring Datasets by Self-Organizing Map and k-Means Algorithms with a Graphical User Interface. *Microchem. J.* **2021**, *165*, 106181.

(3)   Nakagawa, K.; Yu, Z.-Q.; Berndtsson, R.; Hosono, T. Temporal Characteristics of Groundwater Chemistry Affected by the 2016 Kumamoto Earthquake Using Self-Organizing Maps. *J. Hydrol.* **2020**, *582*, 124519.

(4)   Everitt, B. S.; Landau, S.; Leese, M. *Cluster Analysis*, 5th ed.; Wiley Publishing, 2011.

(5)   Davies, D. L.; Bouldin, D. W. A Cluster Separation Measure. *IEEE Trans. Pattern Anal. Mach. Intell.* **1979**, *PAMI-1* (2), 224–227.